Ph D. Dissertation *2018. 09*

Development of Novel Luminescent Crystalline Materials of Gold(I) Complexes with Stimuli-Responsive Properties

Hokkaido University

Graduate School of Chemical Science and Engineering

Organoelement Laboratory

Mingoo Jin

Table of Contents

Chapter 1.

General Introduction

1.1. External Stimuli Responsive Luminescence of Solid-State Molecular Materials

In general, organic and organometallic compounds exhibiting luminescence properties in solid-state have possessed π-conjugated moiety. The π-conjugated moiety can induce intermolecular interactions such as π–π stacking and CH–π interactions, and result formation of rigid and ordered assembled structure. In other words, such resulted molecular packed structures are desired to be "static". On the other hand, there are possibility to induce structural changes to ordered molecular assemblies composed of the organic or organometallic molecules having π-conjugated moieties by applying an external stimulus such as heat, pressure, gas, solvent, etc (Figure 1). The alteration is useful to create "dynamic" functional materials, which change their luminescence properties and without chemical decomposition.[1] Research on these materials has rapidly grown over the past decade due to the strong interest in the underlying fundamental mechanisms, and the potential applications for sensors, memories, informational displays, and security features.[1]

Luminescence properties of many fluorescent solid-state compounds are significantly influenced by their molecular arrangements and molecular conformation because their electronical environment, ruling the photophysical properties, is correlated to their inter- and intra-molecular interactions.[2] Thus, rearrangement of the molecular packing and change of the molecular conformation of such materials via external stimuli can be utilized to alter their photophysical properties.[1,2] However, it is still issued how to control and design the phase transition of ordered assembled structure such as crystal. In addition, controlling the luminescence properties in solid phase is also difficult subject because inter-intra molecular structure control of the luminophore in solid-phase is very challenge and solid-phase can easy to experience some unexpected energy transfer, generally disturbing the luminescence control.

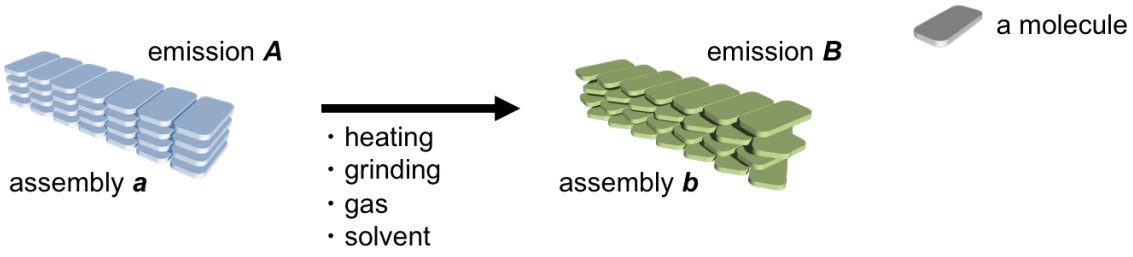

Figure 1. Representation of the external stimulation-induced luminescence change of solid-state molecular materials.

For development of the stimulus responsive solid-state materials, generating multiple phases and interconversion between the phases should be designed. In the case of molecular crystals, molecular structure determines the formation and properties of the crystals, as well as molecular arrangement, conformation, and dynamics. Thus, molecular design toward forming multiple crystal structures and inducing phase transitions could be considered as *not impossible*. Several molecular design concepts and over the few hundreds of examples have been reported. In this section, several representative pioneering examples will be described. Sagara, Kato, and Araki *et al* have reported several stimuli responsive materials with luminescence alteration by combining rigid π-conjugation group, hydrogen bonding site, and alkyl group for forming variable structures.[3] For example, the 1,3,6,8-tetraphenylpyrene derivative **1** was reported to exhibit mechano-responsive luminescence and phase recovery through heating (Figure 2a).[3a] Tang and co-workers have built the mechano- and thermo-stimuli responsive crystalline phase corresponding the emission properties change through introducing alkyl group into the aggregation-induced emissive luminophoric core unit tetraphenylethylene (TPE), representing as **2** (Figure 2b).[4] Several gold complexes have been reported to show mechano-, thermo-, and solvent-responsive luminescence properties.[5] Ito, H. *et al* have reported several examples of mechano-responsive luminescent crystals with thermal or solvent responsive luminescence alterations through aryl gold(I) isocyanide complexes.[6] For instance, the gold(I) complex **3** forms a blue emitting powder crystals which shows drastic luminescence color change from blue to yellow.[6a] In addition, the blue emitting phase can be recovered by adding CH_2Cl_2 solvent (Figure 2c). The gold(I) complex **4**, possessing nitrogen atoms, which is modified from the molecular structure of **3** exhibits various range of luminescence color changes through grinding, heating, and addition of the acetone corresponding to the crystal structure changes (Figure 2d).[6b] In these cases, the intermolecular metal-metal interactions, so called aurophilic interactions, and π stacking or CH-π interactions of aryl groups work for key factors of switching luminescence properties corresponding to solid-state phase transitions.[6]

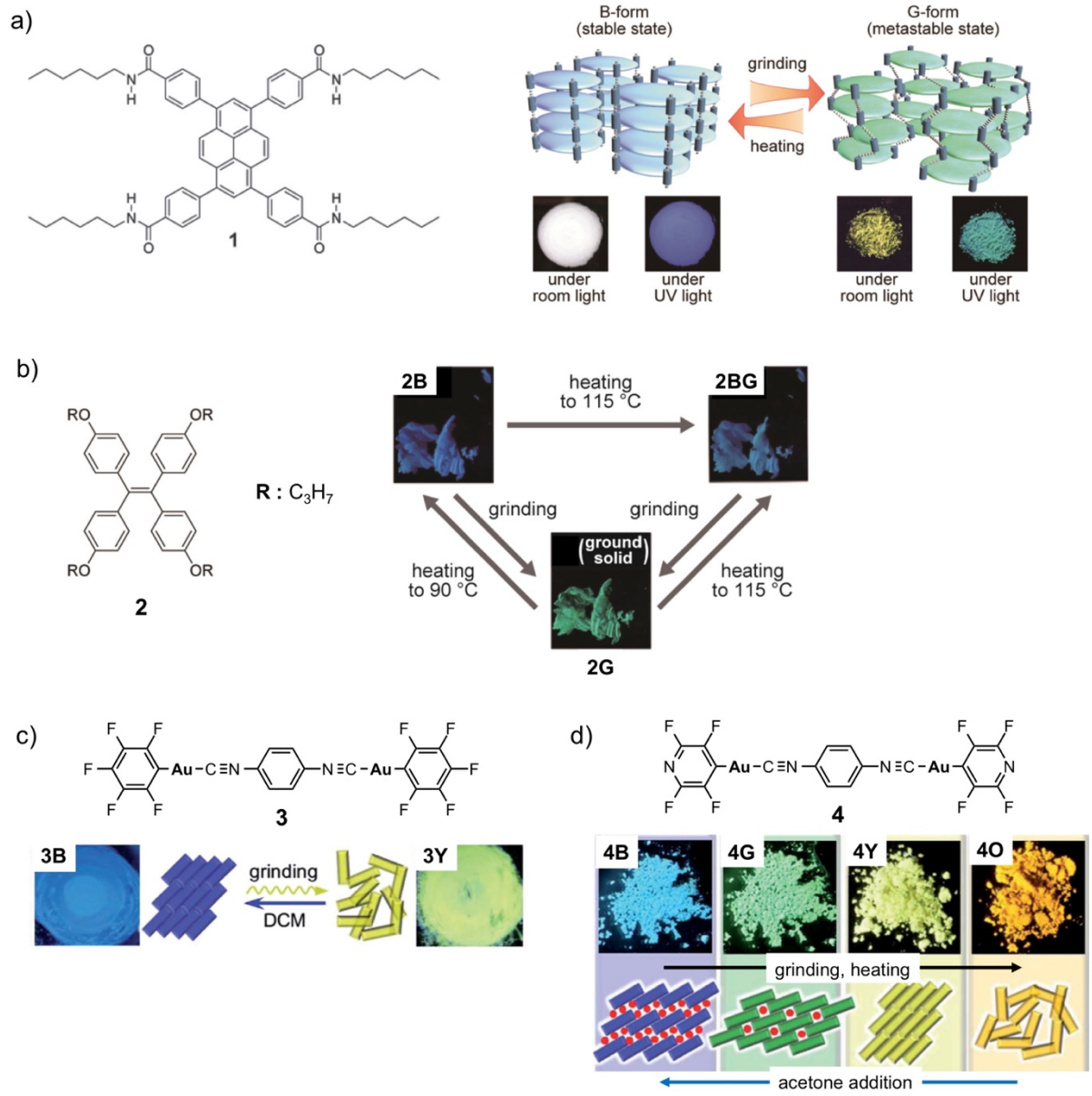

Figure 2. Several designed molecular concepts and examples of external stimulus-responsive luminescence corresponding to the crystal structure transformation.

Most of the stimuli-response properties can only be observed where the stimulation is applied. However, luminescent single crystals of the phenyl-phenyl gold(I) isocyanide complex **5**[7a] and some of derivate[7b] can change their luminescence by remote mechanical stimulation as shown in Figure 3. Through rapid and slow recrystallization, the gold(I) isocyanide complex **5** forms a blue luminescence single crystal I_b and yellow luminescence single crystal II_y, respectively (Figure 3a). When a small pit was made on a single crystal of I_b using a thin needle, a tiny spot showing yellow luminescence appeared on the spot of the crystal, indicating that mechanically induced phase transition from I_b to II_y occurred at the position of mechanical stimulation

(Figure 3b). Interestingly, the yellow-emitting area was gradually spread over the entire single crystal within several hours. This effect was shown to be caused by a single-crystal to single-crystal (SCSC) phase transition that was accompanied by a change of the luminescence color. Also, the same SCSC transformation is achieved by contacting a crystal II_y to other crystals I_b (Figure 3c). The observed spreading of the yellow-emitting II_y phase was named as "molecular domino" effect, because a locally applied mechanical stress was able to trigger the transformation throughout the entire crystal. Indeed, the thermodynamic stability of the two polymorphs associate the direction of the SCSC transition from thermodynamically unstable phase I_b to stable phase II_y. Through the single crystal XRD analyses and photophysical properties of I_b and II_y, it is revealed that the formation of aurophilic interaction induced the red-shifted emission (Figure 3d–e).

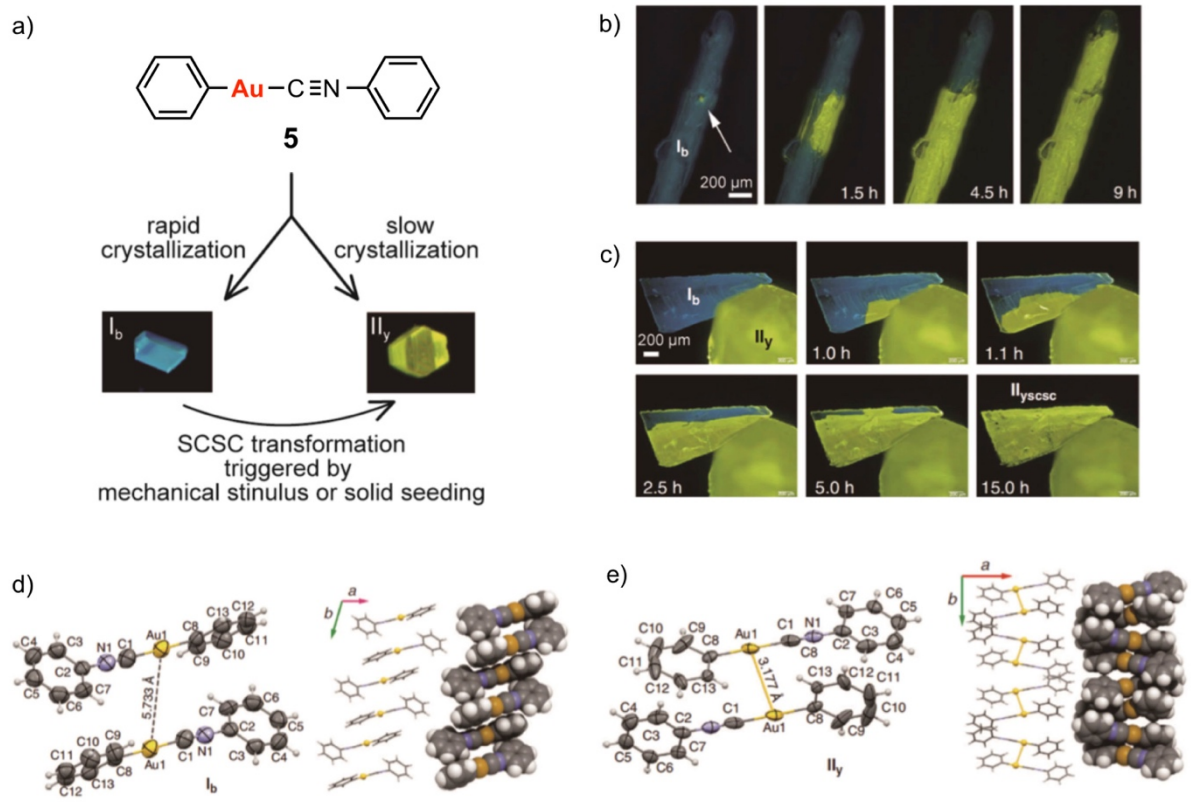

Figure 3. Luminescent molecular dominos via single-crystal to single-crystal (SCSC) phase transition.[7a] a) Procedure to obtain two different crystals of **5** and scheme of the SCSC transformation. b) picking-induced and c) seeding-triggered SCSC transformations of **5**. Crystal structures of d) I_b and e) II_y.

1.2. Luminescence Properties of Gold(I) Complexes

Luminescence properties of gold(I) complexes can originate from ligands, especially their geometry around the gold atom, or from the presence of metal-metal interaction so called aurophilic interaction.[8] In other word, it can be displayed by transitions between orbital of metal center and orbitals of the ligands (usually among *p* orbitals), or in transition involving both metal and ligands, where these can act as donors or acceptors of electronic density (charge transfer transition).[9] In general, gold(I) complexes has formed the linear geometry around the gold(I) atom center. This coordination condition usually results an energy distribution that the LUMO is composed mainly of the *p* orbitals from the ligands and the HOMO is composed of the *p* orbital from the ligands or d_z^2 orbital from the gold(I) atom as shown in figure 4. Thus, the luminescence properties usually originate from π-π* transition or metal-to-ligand charge transfer (MLCT) (Figure 4a). However, some geometry conditions having a distance of two gold atoms < 3.50 Å, so called aurophilic interaction, results in destabilization of d_z^2 orbitals in the gold(I) atoms, forming $d_z^2\sigma^*$ orbital, and the newly formed $d_z^2\sigma^*$ orbital act as the HOMO. Consequently, the luminescence with aurophilic interaction is displayed through metal-metal-to-ligand charge transfer (MMLCT) exhibiting phosphorescence and has lower HOMO-LUMO energy gap (Figure 4b). In addition, formation of aurophilic interactions generally induce higher emission intensity.[8] According to these features, the electronic environment of gold(I) complex can easily be influenced by internal or external changes, molecular conformations, the dipole moment of neighboring systems, and alternative molecular arrangements. Consequently, the luminescence properties can be altered by such the change of external or internal environment of the gold(I) complex.

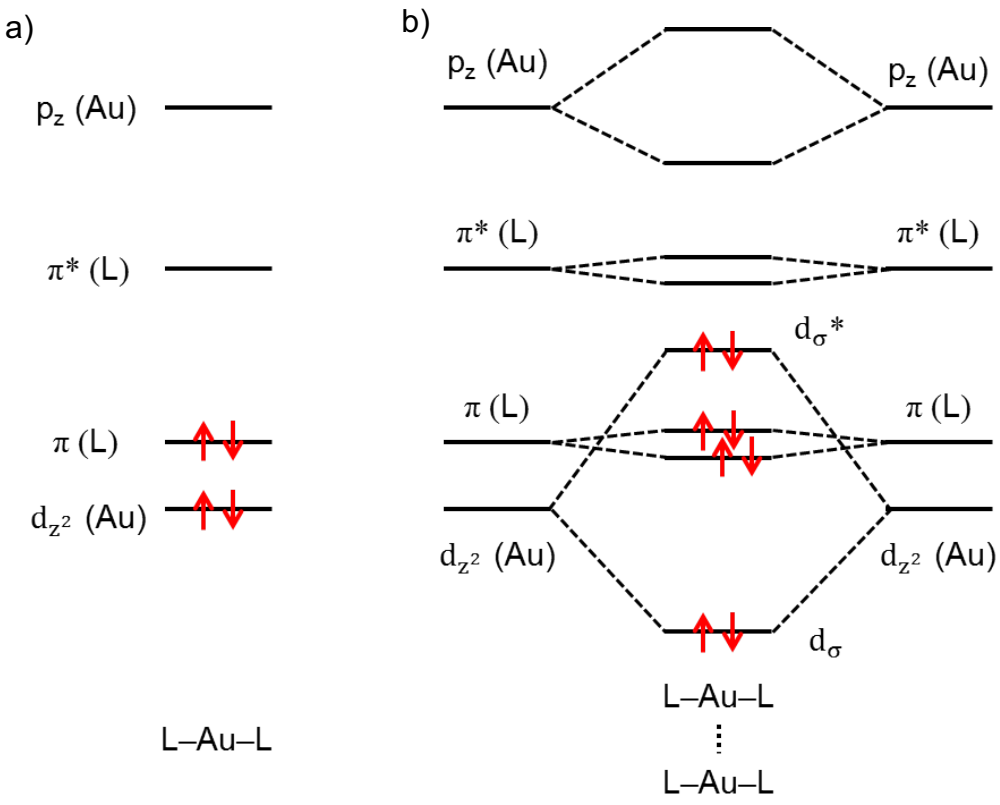

Figure 4. Schematic representation of molecular orbitals of gold complex when it is a) monomer and b) forms aurophilic interaction.

1.3. Conditions for Crystal-to-Crystal / Single-Crystal-to-Single-Crystal Transformation

There are several types of the solid-state phase transition when some solid sample changed to different solid structure by controlling external conditions such as light, temperature, pressure, chemical gradients.[1] The category can be described as below.

a. Crystal-to-Amorphous
b. Crystal-to-Crystal
c. Single Crystal-to-Single Crystal
d. Amorphous-to-Crystal

In the phase transitions involving amorphous phase (a and d), it is impossible to have concise structural information in the solid samples, thus, hard to understand underlying mechanism of the phase transition with physical properties changes. By contrast, if the phase transition is undergoing (b) Crystal-to-Crystal or (c) Single Crystal-to-Single Crystal transition, we can have precise information of the crystal structure change in terms of powder and single crystal X-ray diffraction analyses. Because of the huge benefit, design and control of Crystal-to-Crystal[6c-d,10] or Single Crystal-to-Single Crystal[7,11] phase transition via external stimulus has been intensely researched. Even the high development of the crystal engineering, it is still difficult to predict or design these types of phase transitions for molecular crystalline phase. Especially, realization of the Single Crystal-to-Single Crystal transformation would be major challenge because exposing single crystals to external or internal forces by applying some stimulations generally results in the loss of single crystallinity.[11m]

Several conditions to realize and control the Crystal-to-Crystal or the Single Crystal-to-Single Crystal transformations have been discussed despite there is no rational rule.[11m-n] First, the sample should be able to form multiple crystal structures, in other word, to show polymorphism. Second, reasonable energy barrier between the polymorphs should be formed for interconversion. Third, thermodynamic stability of the crystalline phase should be characterized because many cases of these phase transitions undergo from thermodynamically unstable phase to stable phase. These three factors should be intensely considered when the molecular or material blue-print is designed for the Crystal-to-Crystal or the Single Crystal-to-Single Crystal phase transitions.

1.4. Features of Biaryl Group

In this section, biaryl group possessing two aryl plans connected by C-C bonding will be focused. In 2,2'-disubstituted biphenyl compounds (Figure 5a), the rotation around the single bond between the phenyl groups is restricted to some extent by the steric repulsion between the two substituents. The reported dihedral angles between the phenyl rings of the 2,2'-disubstituted biphenyl structure ($\theta_{Biphenyl}$, Figure 5a) range from 30° to 60°.[12] This indicates that a structure change with various $\theta_{Biphenyl}$ is possible with small free energy loss. Such a structure with restricted freedom may enable structural variation of the crystalline phases.

As shown in Figure 5b, 2,2'-disubstituted binaphtyl compounds can exhibit stable axial chirality as (*R*)- and (*S*)-conformations. In the case of 2-mono-substituted biphenyl compounds, the structure can adopt (*M*)- or (*P*)-conformations based on their helical chirality (Figure 5b). In solution, these (*M*)- or (*P*)-conformers rapidly interconvert between each other, but in the solid state, the conformer should be fixed in (*M*)- or (*P*)-conformation by the intermolecular interactions between neighboring molecules. These chiral structures in the solid state should be helpful to construct chiral crystal and design control of the chirality of crystal.

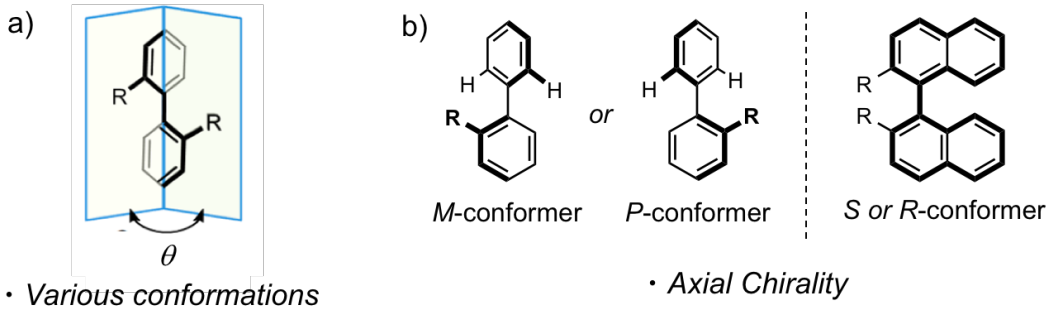

Figure 5. a) Dihedral angle of biphenyl moiety (θ). b) Helical and axial chirality of biaryl groups.

1.5. Chirality of Molecular Crystal and Wallach's Rule

In dealing with chirality in relation to crystal structures, it is essential to distinguish between three different objects that may be either chiral or achiral. The three manners is determined from 1) the molecular components of the crystal, 2) the crystal structure itself, and 3) the symmetry group of the crystal structure, *viz.*, its space group.[13] Technically, if the crystal structure shows chiral space groups (the 65 Sohcke space groups) with near the zero value of the frack parameter confirmed by single crystal XRD analysis, the crystal structure can be defined as chiral crystal structure.[13] In this section, the case of molecular crystals will be mainly described. The Table 1 summarize the collation of observations concerning the existence of chiral and achiral crystal structures formed from chiral (enantiomerically pure or racemate) or achiral molecules.[13]

Table 1. Restrictions on the formation of chiral and achiral crystal structures from chiral or achiral molecules.[13]

	Achiral crystal structure	Chiral crystal structure
Achiral molecules	Permitted	Permitted
Chiral molecules – enantiomerically pure	Forbidden	Permitted
Chiral molecules – racemate	Permitted	Permitted

Achiral molecules can have possibility to form both achiral and chiral crystal structures because the chirality can be decided by not only intra molecular structure but also inter molecular assembled structure. As the similar reason, racemic molecules could form achiral or chiral structures. However, enantiomerically pure molecules which do not undergo racemate process are forbidden to form achiral crystal structure because the homo-chiral molecular structure cannot allow to form inversion or encounter symmetry in its crystal structure.

Wallach's Rule

Wallach's rule is experimental tendency regarding chirality of crystal and their physical property such as density of the unit cell. For instance, the density of crystal phases with chiral space groups denoted in "chiral crystals" is lower than that of crystals with centrosymmetric space groups denoted in "achiral crystals" (Figure 6a).[14] In addition, the polymorph having a high density is generally thermodynamically stable because of high dense molecular packing. As shown in Figure 6b, the chiral crystal of *L*-mandelic acid and the achiral (racemic) crystal of the corresponded racemic compounds can be one of good example following the Wallach's

rule.[14c] Through these tendency between chiral crystals and the physical properties, it is suggested that Wallach's rule can serve as an empirical guide for the understanding of polymorph stability.

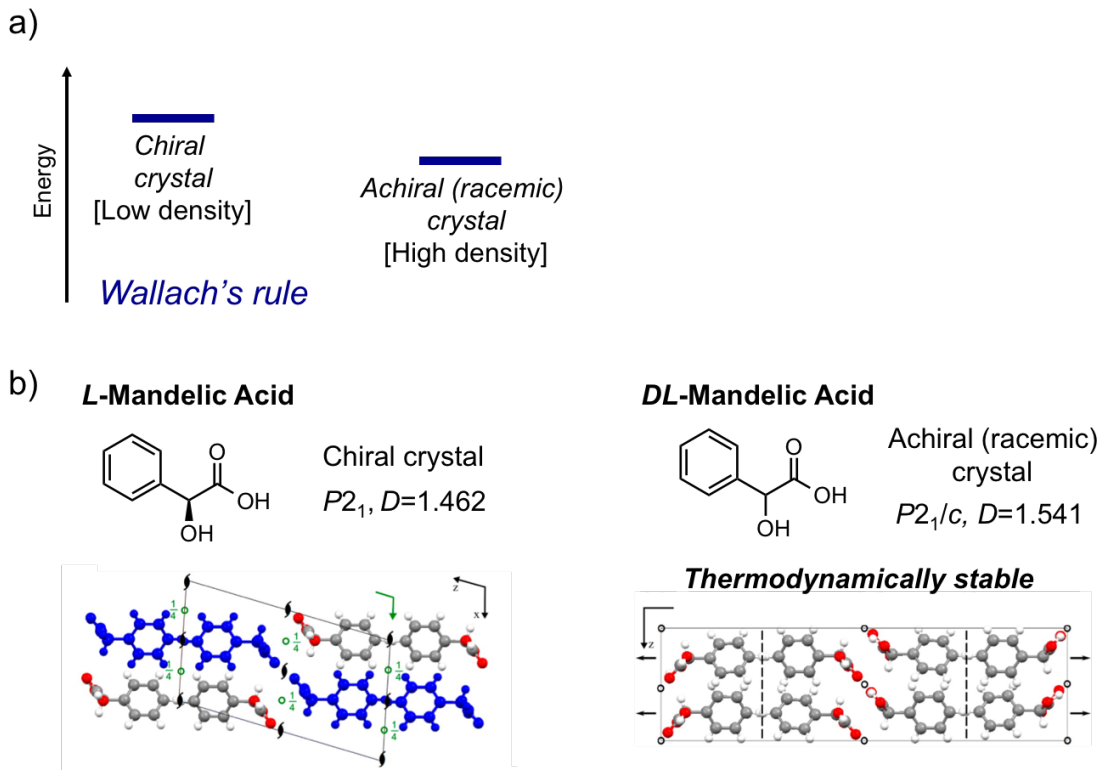

Figure 6. a) Schematic representation of Wallach's rule. b) Example crystals of following Wallach's rule.

1.6. Amphidynamic Crystal

Molecular crystals are highly ordered three-dimensional assembly of molecules aggregated together by relatively weak non-bonding interactions. Generally, molecular crystals are assembled into close packing arrangements that minimize the amount of empty space, consequently, molecules are forced to decrease their individual degrees of freedom in the crystals. In search of an insight into molecular freedom in the assembled phase, the relationship between molecular motion and long-range phase order may help us to understand the correlation as illustrated in Figure 7.[15] With a measure of phase order on the vertical axis and a measure of motion on the horizontal axis, liquid phase is located in the bottom right corner of the plot. Liquids have very low long-range order and each molecule exhibits rapid full molecular rotation, rendering them homogeneous on the time average. On the other hand, molecular crystals are characterized by their rigidity, homogeneity, periodicity, and their macroscopic anisotropy.[15] Molecular crystals have long-range order and only the small-amplitude molecular displacements associated with lattice vibrations, illustrated as the top left corner of the plot. Following the concept in the above, plastic-crystal or liquid crystal can be described as in the plot.

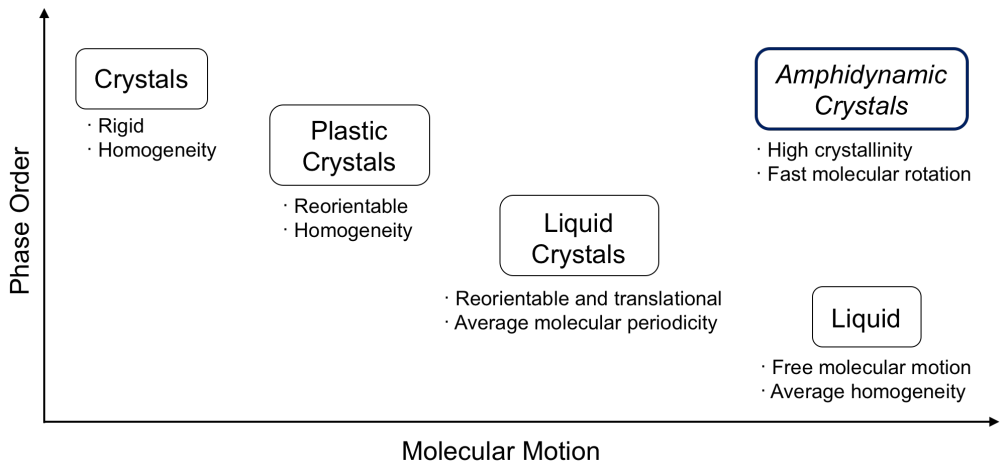

Figure 7. Plot of phase order versus molecular motion with schematic representation of each assembly phase.[15b]

Molecular structure determines the formation and properties of plastic and liquid crystals, as well as their dynamics. The fact suggests that suitable molecular structures can be designed to form a highly ordered rigid lattice which is also working for supporting rapid motion of well-designed moiety. The crystals, representing on the top right corner, can be constrained to

specific lattice positions while other components exhibit rapid molecular motion. As suggested by the presence of a rigid ordered component and a highly mobile component, this phase has been defined as “amphidynamic” crystal. This newly investigated class of solid phase has been considered as providing many interesting opportunities in materials science.[15]

When investigate these type of the crystals, we can have precise crystal structure information from single crystal XRDs. However, the result from the single crystal XRD analysis give no direct information for molecular dynamics in the crystal. Thus, coupling of complementary techniques that span much wider range of frequencies, such as variable-temperature solid-state NMR (CP-MAS, wide-line analysis of ^{2}H spin echo and T1 spin-lattice relaxation) can provide access to the amplitude and frequency of motion, as well as the energy of activation of the dynamic process within the crystal lattice.[15]

For the construction of amphidynamic crystals, the components working as static frames designed to support the dynamic portions of the system should be needed. Highly mobile components, defined as rotator, may be isolated from each other, and may have free volume around itself within the crystal lattice. The stator should connect to the rotators through suitable axles that support their rotary motion, or through pivots that support an oscillatory movement. Based on these idea, several molecular or material designs for constructing the amphidynamic crystals have been reported such as macroscopic gyroscopes, metal-organic frameworks (MOFs), mesoporous organosilicas, organic cages and porous aromatic framworks.[15c] Focusing on molecular crystals, macroscopic gyroscopes, possessing rotator, axel, and stator, have provided the promising designs for the realization of amphidynamic crystals (Figure 8a).[15] In particular, Garcia-Garibay M.A. and co-workers have revealed that dumbbell-shaped molecules designed for having gyroscope properties could form many types of amphidynamic crystals (Figure 8b).[15a-b]

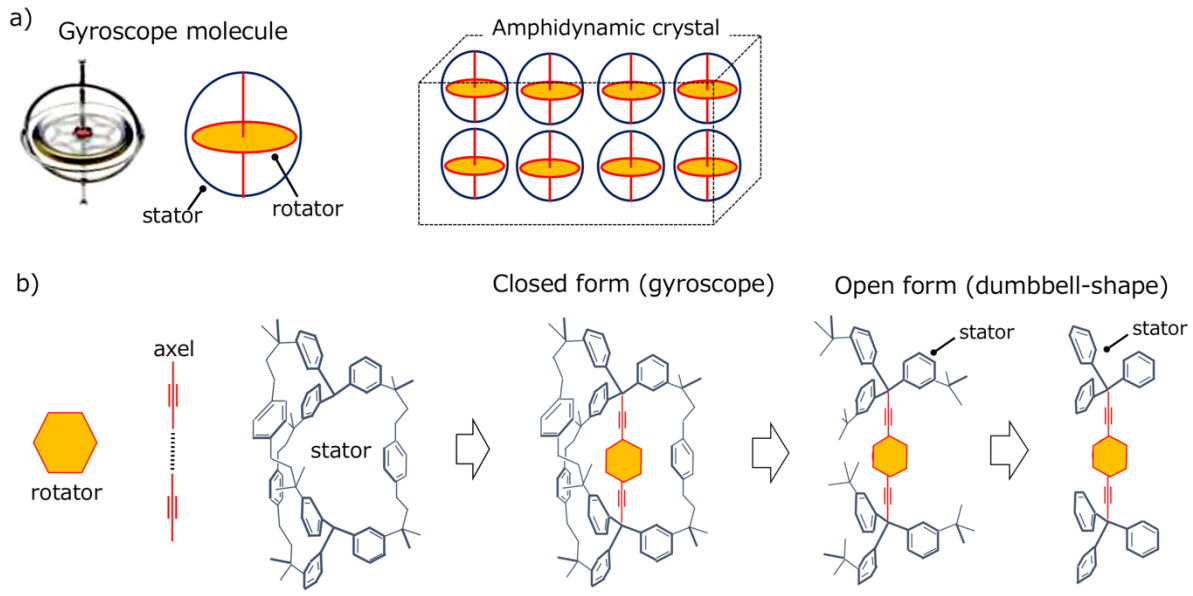

Figure 8. a) Gyroscope molecule for forming amphidynamic crystal. b) Molecular design for gyroscope molecule.

Several functions in solid-phase taking advantage of amphidynamic crystals have been reported. For instance, amphidynamic crystals from MOFs or porous framework have free volume around the rotators. Thus, small molecules such as gas or vapor can easy to be included in the crystal lattice. Through the inclusion of the molecules, the rotation of the rotator should be slowdown. Taking advantage of this concept, several amphidynamic crystals as "molecular sensors" monitored by rotator dynamics change have been investigated using the periodic mesoporous-organosilica (PMOs) by Sozzani and co-workers (Figure 9a).[16] Kitagawa S. and co-workers have investigated the gas adsorption properties of MOFs system with the rotation properties of the ligands (Figure 9b).[17] When the rotator possesses high dipolar moment, the rotation in the amphidynamic crystals can response to external electric field. Garcia-Garibay M.A. and co-workers have revealed that external electric field which is generated from alternating current can interact with the rotation of the high dipolar rotator in the crystals (Figure 9c).[18a-b] Recently, several examples of such dipolar rotors have been reported, based on molecular crystals,[18] mesoporous hybrid materials[19] and MOFs[20]. It is worth to note that the dielectric phenomena associated to dipolar rotors can be tuned and switched by applying external electric field to the amphidynamic crystals or by temperature change.[15c] Recently, control of the conjugation environment with luminescence properties has been challenged using amphidynamic crystalline system. Garcia-Garibay M.A. *et al.* have reported the conjugation control through molecular rotation of dumbbell-shaped organic molecules (Figure

9d).[21] Dinca and co-workers have reported that luminescence of the MOFs possessing a tetraphenylethylene (TPE) moiety in ligand can exhibit luminescence intensity change through degree of inclusion of NH_3 molecules in the MOF framework which associate to rotation of the phenyl rings in the TPE (Figure 9e).[22] However, it has been still challenging subject that material design for fine control of solid-state luminescence properties because tuning the electronical environment (or conjugation system) in solid-phase is difficult.

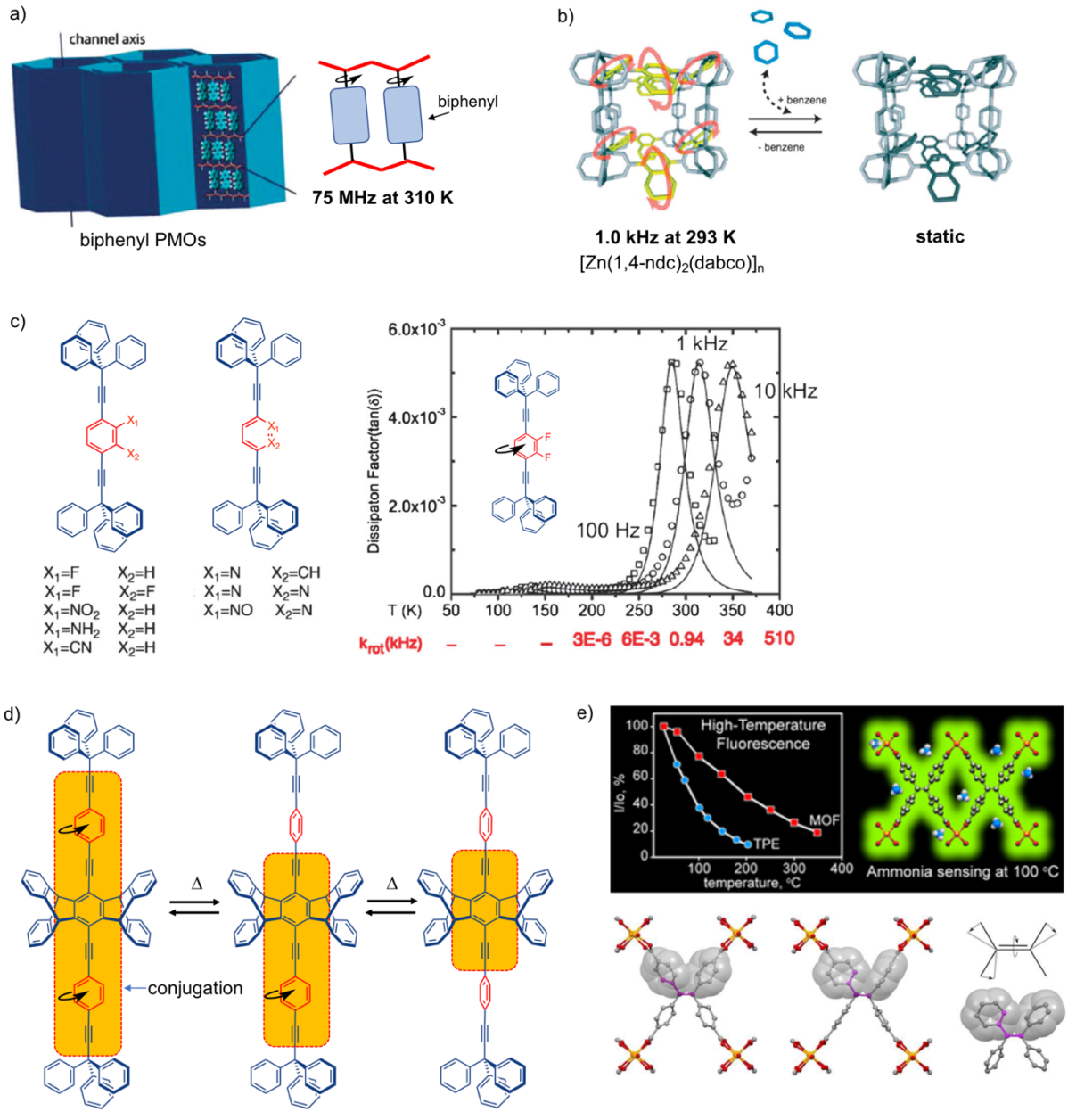

Figure 9. Several examples of amphidynamic crystals possessing functional properties.

1.7. Molecular Design in the Ph. D. Dissertation

In this Ph. D. studies, several novel molecular strategies for controlling molecular arrangement and altering molecular conformation in solid-phase have been performed toward rational material design of external stimuli-responsive luminescence. In the chapter 2, the author focused on a feature of biaryl moiety that have a high chance to take a various dihedral angle in solid-phase. From this property, formation of multiple polymorphs with distinct emission properties were purposed. At the chapter 3 and 4, chirality of crystal has been approached for controlling molecular arrangement of crystals and corresponded emission properties through taking advantage of axial chirality of molecules. In the chapter 3, homo-chiral and racemic gold(I) isocyanide complexes possessing binaphthyl moiety were designed for comparing mechano-responsive luminescence properties with molecular arrangement alterations between homo-chiral crystal and racemic crystal. The strategy aimed for using different molecular packing when they were different in chirality of crystal. The chapter 4 had challenged for achieving interconvertible system with emission properties alteration between chiral and racemic (or achiral) crystals through external stimulations. For this concept, *o*-substituted biphenyl gold(I) isocyanide complex which could form *P*- and *M*- type of helically chiral molecular structures has been designed. In the chapter 5, minorly tuned molecular structure from the above biphenyl gold(I) complex that possess CF_3- group and one naphthyl moiety on biaryl group has been synthesized for adding further functional properties such as polarity response. From the chapter 2 to 5, hybrid gold(I) isocyanide complexes and biaryl moiety was main molecular design concept for controlling molecular arrangement in solid-phase. On the other hand, the chapter 6 have focused on molecular rotation in solid-phase because molecular rotation could be termed as conformational change. For achieving this proposal, dumbbell shaped molecular structure possessing rotator and stators was hybrid with luminescent gold complex which its emission properties were easy to be changed by external electronical environment change.

1.8. References

1. (a) Sagara, Y.; Yamane, S.; Mitani, M.; Weder, C.; Kato, T. *Adv. Mater.* **2016**, *28*, 977. (b) Anthony, S. P. *ChemPlusChem* **2012**, *77*, 518.
2. Mutai, T.; Satou, H.; Araki, K. *Nat. Mater.* **2005**, *4*, 685.
3. (a) Sagara, Y.; Mutai, T.; Yoshikawa, I.; Araki, K. *J. Am. Chem. Soc.* **2007**, *129*, 1520. (b) Sagara, Y.; Komatsu, T.; Ueno, T.; Hanaoka, K.; Kato, T.; Nagano, T. *Adv. Funct. Mater.* **2013**, *23*, 5277. (c) Sagara, Y.; Komatsu, T.; Terai, T.; Ueno, T.; Hanaoka, K.; Kato, T.; Nagano, T. *Chem. Eur. J.* **2014**, *20*, 10397.
4. Wang, J.; Mei, J.; Hu, R.; Sun, J. Z.; Qin, A.; Tang, B. Z. *J. Am. Chem. Soc.* **2012**, *134*, 9956.
5. (a) Assefa, Z.; Omary, M. A.; McBurnett, B. G.; Mohamed, A. A.; Patterson, H. H.; Staples, R. J.; Fackler, J. P. *Inorg. Chem.* **2002**, *41*, 6274. (b) Grey, J. K.; Butler, I. S.; Reber, C. *Inorg. Chem.* **2003**, *42*, 6503. (c) Lee, Y.A.; Eisenberg, R. *J. Am. Chem. Soc.* **2003**, *125*, 7778. (d) Schneider, J.; Lee, Y.A.; Pérez, J.; Brennessel, W. W.; Flaschenriem, C.; Eisenberg, R. *Inorg. Chem.* **2008**, *47*, 957.
6. (a) Ito, H.; Saito, T.; Oshima, N.; Kitamura, N.; Ishizaka, S.; Hinatsu, Y.; Wakeshima, M.; Kato, M.; Tsuge, K.; Sawamura, M. *J. Am. Chem. Soc.* **2008**, *130*, 10044. (b) Seki, T.; Ozaki, T.; Ohkura, T.; Asakura, K.; Sakon, A.; Uekusa, H.; Ito, H. *Chem. Sci.* **2015**, *6*, 2187. (c) Yagai, S.; Seki, T.; Aonuma, H.; Kawabuchi, K.; Karatsu, T.; Okura, T.; Sakon, A.; Uekusa, H.; Ito, H. *Chem. Mat.* **2015**, *28*, 1, 234. (d) Seki, T.; Takamatsu, Y; Ito, H. *J. Am. Chem. Soc.* **2016**, *138*, 6252.
7. (a) Ito, H.; Muromoto, M.; Kurenuma, S.; Ishizaka, S.; Kitamura, N.; Sato, H.; Seki, T. *Nat. Commun.* **2013**, *4*, 2009. (b) Seki, T.; Sakurada, K.; Ito, H. *Angew. Chem., Int. Ed.* **2013**, *52*, 12828. (c) Seki, T.; Sakurada, K.; Muromoto, M.; Seki, S.; Ito, H. *Chem.–Eur. J.* **2016**, *22*, 1968.
8. (a) Schmidbaur, H. in Gold - *Progress in Chemistry, Biochemistry and Technology*, John Wiley & Sons, Inc., New York, 1999. (b) Schmidbaur, H.; Graf, W.; Muller, G. *Angew. Chem., Int. Ed.* **1988**, *27*, 417. (c) Balch, A. L. *Gold Bull.* **2004**, *37*, 45. (d) Pyykkö, P. *Angew. Chem., Int. Ed.* **2004**, *43*, 4412. (e) Katz, M. J.; Sakai, K.; Leznoff, D. B. *Chem. Soc. Rev.* **2008**, *37*, 1884. (f) Schmidbaur, H.; Schier, A. *Chem. Soc. Rev.* **2008**, *37*, 1931. (g) Laguna, A. *Modern Supramolecular Gold Chemistry*, Wiley-VCH; John Wiley distributor, Weinheim, Germany, 2008.

9. *Optoelectronic Properties of Inorganic Compounds*, Roundhill, D. M.; Fackler, J. P., Jr., Plenum, New York, 1999, 195–226.
10. (a) Yoon, S.-J.; Chung, J. W.; Gierschner, J.; Kim, K. S.; Choi, M.-G.; Kim, D.; Park, S. Y. *J. Am. Chem. Soc.* **2010**, *132*, 13675. (b) Harada, N.; Abe, Y.; Karasawa, S.; Koga, N. *Org. Lett.* **2012**, *14*, 6282. (c) Abe, Y.; Karasawa, S.; Koga, N. *Chem.–Eur. J.* **2012**, *18*, 15038. (d) Yagai, S.; Okamura, S.; Nakano, Y.; Yamauchi, M.; Kishikawa, K.; Karatsu, T.; Kitamura, A.; Ueno, A.; Kuzuhara, D.; Yamada, H.; Seki, T.; Ito, H. *Nat. Commun.* **2014**, *5*, 4013. (e) Seki, T.; Sakurada, K.; Ito, H. *Chem. Commun.* **2015**, *51*, 13933.
11. (a) Li, F. F.; Zhang, L.; Gong, L. L.; Yan, C. S.; Gao, H. Y.; Luo, F. *Dalton Trans.* **2017,** *46*, 338. (b) Lim, S. H.; Olmstead, M. M.; Balch, A. L. *Chem. Sci.* **2013**, *4*, 311. (c) Zeng, M.-H.; Tan, Y.-X.; He, Y.-P.; Yin, Z.; Chen, Q.; Kurmoo, M. *Inorg. Chem.*, **2013**, *52*, 2353. (d) Huang, R.-W.; Wei, Y.-S.; Dong, X.-Y.; Wu, X.-H.; Du, C.-X.; Zang, S.-Q.; Mak, T. C. W. *Nat. Chem.* **2017,** *9*, 689. (e) Lim, S. H.; Olmstead, M. M.; Balch, A. L. *J. Am. Chem. Soc.* **2011**, *133*, 10229. (f) Liu, G.; Liu, J.; Liu, Y.; Tao, X. *J. Am. Chem. Soc.* **2014**, *136*, 590. (g) Liu, J.; Liu, G.; Liu, Y.; Zheng, X.; Han, Q.; Ye, X.; Tao, X. *Chem. Asian J.* **2016**, *11*, 1682. (h) Karothu, D. P.; Weston, J.; Desta, I. T.; Naumov, P. *J. Am. Chem. Soc.* **2016**, *138*, 13298. (i) Liu, G. F.; Liu, J.; Ye, X.; Nie, L. N.; Gu, P. Y.; Tao, X. T.; Zhang, Q. C. *Angew. Chem. Int. Ed.* **2017,** *56,* 198. (j) Takamizawa, S.; Miyamoto, Y. *Angew. Chem. Int. Ed.* **2014,** *53,* 6970. (k) Takasaki, Y.; Takamizawa, S. *Chem. Commun.* **2015**, *51*, 5024. (l) Takamizawa, S.; Takasaki, Y. *Angew. Chem. Int. Ed.* **2015,** *54,* 4815. (m) Naumov, P.; Bharadwaj, P. K. *CrystEngComm* **2015,** *17*, 8775. (n) Chaudhary, A.; Mohammad, A.; Mobin, S. M. *Cryst. Growth Des.* **2017,** *17*, 2893.
12. (a) Grein, F. *J. Phys. Chem. A* **2002**, *106*, 3823. (b) Grein, F. *Theor. Chem. Acc.* **2003**, *109*, 274.
13. (a) Flack, H. D. *Helvetica Chemica Acta*, **2003**, *86*, 905.
14. (a) Wallach, O. *Liebigs Ann. Chem.* **1895**, *286*, 90. (b) Brock, C. P.; Schweizer, W. B.; Dunitz, J. D. *J. Am. Chem. Soc.* **1991**, *113*, 9811. (c) Marciniak, J.; Michal, A.; Weizhao, C.; Andrzej, K. *J. Phys. Chem. C.* **2014**, *118*, 4309.
15. (a) Vogelsberg, C. S.; Garcia-Garibay, M. A. *Chem. Soc. Rev.* **2012**, *41*, 1892. (b) Khuong, T. A. V.; Nuñez, J. E.; Godinez, C. E.; Garcia-Garibay, M. A. *Acc. Chem. Res.* **2006**, *39*, 413. (c) Catalano, L.; Naumov, P. *CrystEngComm*, **2018**, in press.

16. (a) Comotti, A.; Bracco, S.; Valsesia, P.; Beretta, M.; Sozzani, P. *Angew. Chem. Int. Ed.* **2010**, *49*, 1760. (b) Bracco, S.; Comotti, A.; Valsesia, P.; Chmelka, B. F.; Sozzani, P. *Chem. Commun.* **2008**, *0*, 4798.
17. (a) Kitagawa, S.; Kitaura, R.; Noro, S.-I. *Angew. Chem. Int. Ed.* **2004**, *43*, 2334. (b) Inukai, M.; Fukushima, T.; Hijikata, Y.; Ogiwara, N.; Horike, S.; Kitagawa, S. *J. Am. Chem. Soc.* **2015**, *137*, 12183. (c) Seo, J.; Matsuda, R.; Sakamoto, H.; Bonneau, C.; Kitagawa, S. *J. Am. Chem. Soc.* **2009**, *131*, 12792.
18. (a) Dominguez, Z.; Khuong, T. A. V.; Sanrame, C. N.; Dang, H.; Nuñez, J. E.; Garcia-Garibay, M. A. *J. Am. Chem. Soc.* **2003**, *125*, 8827. (b) Horansky, R. D.; Clarke, L. I.; Winston, E. B.; Price, J. C.; Karlen, S. D.; Jarowski, P. D.; Santillan, R.; Garcia-Garibay, M. A. *Phys. Rev. B* **2006**, *74*, 14302. (c) Akutagawa, T.; Koshinaka, H.; Sato, D.; Takeda, S.; Noro, S.-I.; Takahashi, H.; Kumai, R.; Tokura, Y.; Nakamura, T. *Nat. Mater.* **2009**, *8*, 342. (d) Setaka, W.; Yamaguchi, K. *J. Am. Chem. Soc.* **2013**, *135*, 14560.
19. Bracco, S.; Beretta, M.; Cattaneo, A.; Comotti, A.; Falqui, A.; Zhao, K.; Rogers, C.; Sozzani, P. *Angew. Chem. Int. Ed.* **2015**, *54*, 4773.
20. (a) Winston, E.B.; Lowell, P.J.; Vacek, J.; Chocholoušová, J.; Michl, J.; Price, J. C. *Phys. Chem. Chem. Phys.* **2008**, *10*, 5188. (b) Devautour-Vinot, S.B.; Maurin, G.; Serre, C.; Horcajada, P.; Da Cunha, D.P.; Guillerm, V.; De Souza Cosa, E.; Taulelle, F.; Martineau, C. *Chem. Mater.* **2012**, *24*, 2168.
21. Hughs, M.; Jimenez, M.; Khan, S. I.; Garcia-Garibay, M. A. *J. Org. Chem.* **2013**, *78*, 5293.
22. (a) Shustova, N. B.; McCarthy, B. D.; Dincă, M. *J. Am. Chem. Soc.* **2011**, *133*, 20126. (b) Shustova, N. B.; Ong, T.-C.; Cozzolino, A. F.; Michalis, V. K.; Griffin, R. G.; Dincă, M. *J. Am. Chem. Soc.* **2012**, *134*, 15061.

Chapter 2.

Introduction of a Biphenyl Moiety for a Solvent Responsive Aryl Gold(I) Isocyanide Complex with Reactivation by Mechanical Stimulation

2.1. Introduction

Solid-state emitting materials that can change their emission properties in response to environmental changes attract much attention for application in sensors.[1] Alteration of the emission properties of solid materials is often caused by changes in molecular assembly states, which further perturb electronic states important for emitting properties.[2] In particular, compounds that display an emission color change upon exposure to volatile solvents are promising for applications in detection.[3] This is because visual observation of a material's emission properties can easily inform us of the existence of specific substances, including harmful volatile chemical substances.[4] However, there are several issues that limit general use of solvent-responsive compounds. For example, uptake of solvents is often required for these compounds to change their emission properties. In many cases, detection relies on the specific intermolecular interactions between solvent-responsive compounds and solvents. Thus, a single compound only tends to be able to detect a limited number of solvents.[5] Moreover, to allow repeated use of these compounds, removal of included solvents is required, which typically involves increasing temperature and reduced pressure.[4d] It is important to design solid–state emitting materials that can discriminate multiple volatile materials and be reused following an easy reactivation procedure to remove the volatile compounds after their detection. Moreover, for many emission materials used for solvent detection, their molecular-level structures in the recognition process are unknown. This hampers the understanding of detailed detection mechanisms, which is critical for the further design of these materials. Detailed structure analysis by single-crystal X-ray diffraction (XRD) is required to elucidate the detection mechanisms of solvent-responsive emissive materials.

We have explored solid-state emissive gold complexes that change their emission color in response to mechanical stimulation and solvent addition. Compared with halogenated[6] and alkynyl[7] gold isocyanide complexes, aryl gold isocyanide complexes have seldom been studied.[8] In 2008, we reported the pioneering mechanochromic aryl gold isocyanide complex **1**, which shows a mechano-induced emission color change from blue (**1B**) to yellow (**1Y**, Figure 1a and b).[9] Addition of CH_2Cl_2 to **1Y** induces the reversible phase transition back to the original **1B** that does not contain solvent molecules (Figure 1b). This finding stimulated the study of luminescent mechanochromism.[10] Structurally related tetrafluoropyridyl gold isocyanide complex **2** (Figure 1a) shows more prominent phase transitions than **1** in response to mechanical stimulation and solvent addition.[11] As-prepared solid **2Y** displaying yellow emission undergoes phase transitions to form **2B** (blue emission) and **2G** (green emission) by

immersion in acetone and subsequent evaporation, respectively (Figure 1c). The resulting **2G** shows mechanochromism, affording an orange-emitting amorphous **2O** phase that does not contain solvent molecules (Figure 1c). In this mechanochromism, the transformation from **2G** to **2O** upon grinding is caused by amorphization during solvent release.

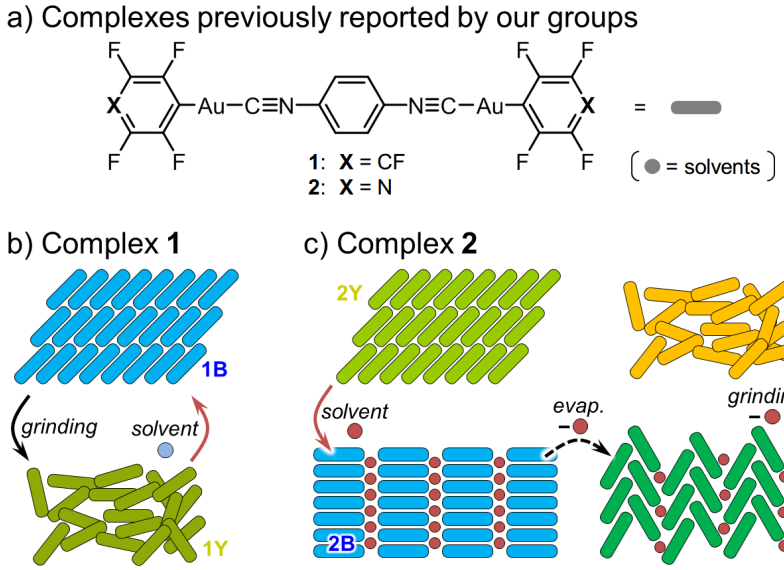

Figure 1. a) Structures of **1** and **2**. Schematic illustration of the phase transitions of b) **1** and c) **2** induced by mechanical stimulation and solvent addition.

On the basis of our previous studies, we envisioned that aryl gold isocyanide complexes are a promising candidate for solid-state emitting materials that can response to volatile molecules. Our intensive studies[9,11,12] have revealed that aryl gold isocyanide complexes tend to form multiple crystalline structures with different emission colors. Under appropriate external stimuli, these crystal structures change to various other structures in an interconvertible manner.[11,12d,e,13] The structural changes include the modification of intermolecular interactions (Au···Au, Au/π, and CH/π interactions) and their conformation (dihedral angle between the aromatic ring on Au and that in the isocyanide ligand $\theta_{\text{Isocyanide}}$). Addition of solvent often causes changes in the solid-state structures of aryl gold isocyanide complexes. In the study of complex **2**, simple grinding releases acetone molecules,[11] suggesting that grinding to induce solvent release can be used as a reactivation process.[14] We anticipated that the further structure design of aryl gold isocyanide complexes will enable the development of solvent-responsive emitting compounds that show grinding-induced reactivation of solvent detection properties even after solvent release.

As a new design of aryl gold isocyanide complex, we focus here on the 2,2'-substituted biphenyl structure. In 2,2'-disubstituted biphenyl compounds (Figure 2a), the rotation around the single bond between the phenyl groups is restricted to some extent by the steric repulsion between the two substituents. The reported dihedral angles between the phenyl rings of the 2,2'-disubstituted biphenyl structure (θ_{Biphenyl}, Figure 2a) range from 30° to 60°.[15] As preliminary attempt, we calculated the potential energy surface of a model compound **M** as a simple gold isocyanide complex possessing biphenyl structure to investigate the rotation of the single bond between two phenyl rings (PBEPBE/SDD; Figure 2b). We obtained a shallow potential energy curve ($\Delta E < 2$ kJ mol^{-1} within the range of $\theta_{\text{Biphenyl}} = 40°–80°$) with an energy minimum at 63.5°. This indicates that a large structure change with various θ_{Biphenyl} is possible with very small free energy loss. Such a structure with restricted freedom may enable structural variation of the crystalline phases of biphenyl gold complexes.[16] In addition, 2,2'-disubstituted biphenyl compounds can adopt (*R*)- and (*S*)-conformations based on their axially chiral biphenyl structure (Figure 2c). In solution, these conformers rapidly interconvert between each other, but in the solid state, the conformer should be fixed in (*R*)- or (*S*)-conformation by the intermolecular interactions between neighboring molecules. These chiral structures in the solid state should be helpful to discriminate the stereochemical composition of chiral molecules. We prepared gold isocyanide complex **3** (Figure 3a) in which a biphenyl structure is included between two aryl gold(I) isocyanide moieties as a "bridging" unit that can adopt various structures. Because of the restricted freedom of its 2,2'-disubstituted biphenyl moiety, it is expected that **3** will be able to form multiple solid structures favorable for solvent detection.

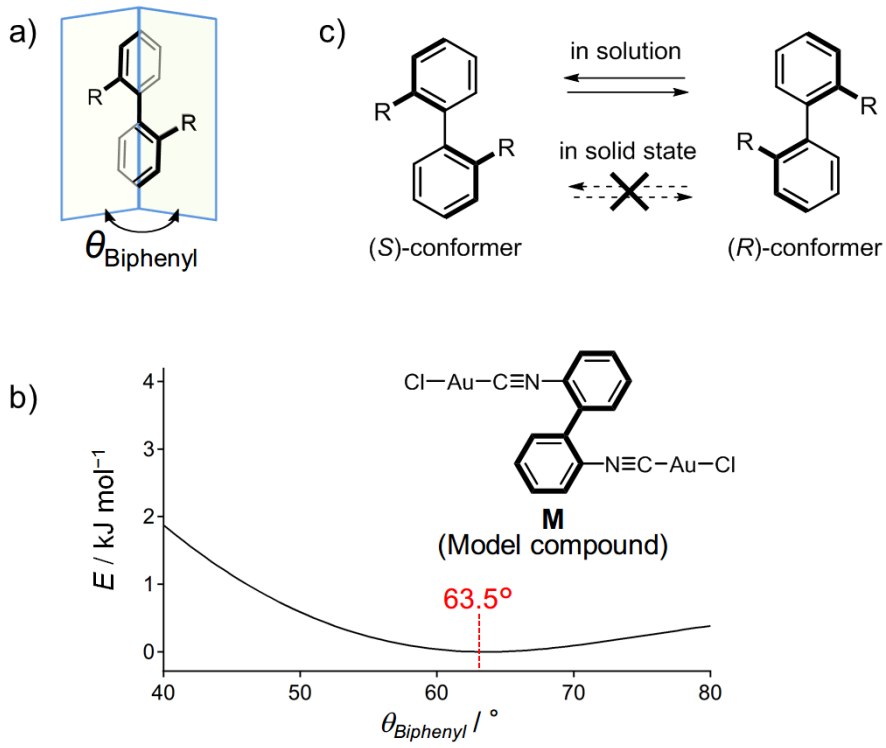

Figure 2. a) Dihedral angles (θ_{Biphenyl}) of 2,2'-disubstituted biphenyl compounds. b) Potential energy surface of 2,2'-disubstituted biphenyl gold isocyanide complex **M** for the rotation of the two benzene rings of the biphenyl group. c) A 2,2'-disubstituted biphenyl structure with (*R*)- and (*S*)-conformations.

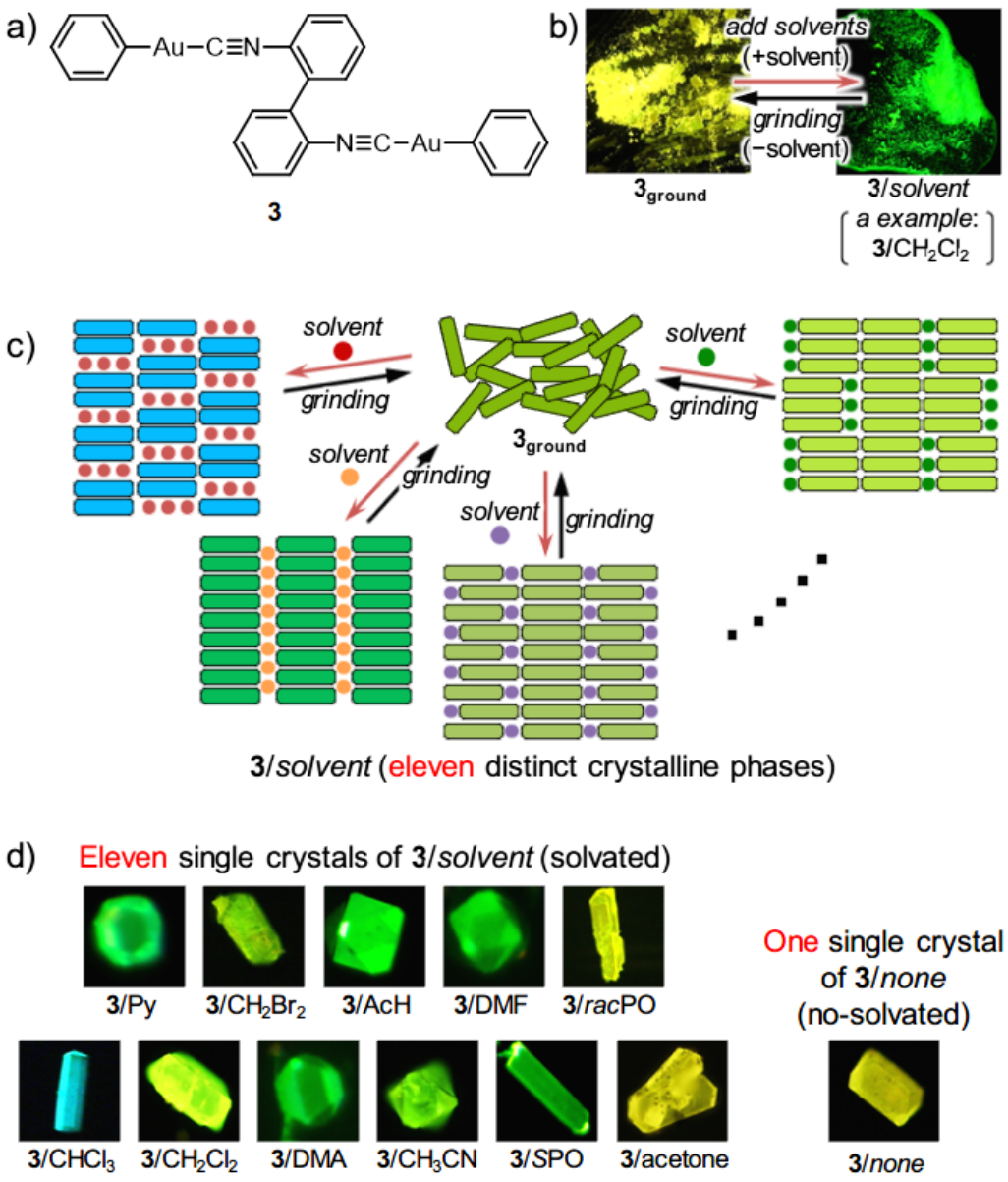

Figure 3. a) Structure of **3**. b) Photographs of the powder forms of $\mathbf{3}_{\mathbf{ground}}$ and **3**/CH_2Cl_2 taken under UV light. c) Schematic illustration of the phase transitions of **3** induced by mechanical stimulation and solvent addition. Rectangles and circles denote **3** and solvent, respectively. d) Photographs of eleven single crystals of **3** with solvent (**3**/*solvent*) and one single crystal of **3** without solvent (**3**/*none*) taken under UV light.

Herein, we report a gold(I) isocyanide complex **3** possessing a biphenyl group that forms eleven different crystal structures **3**/*solvent* with solvent molecules exhibiting different emission maxima (Figure 3). The as-prepared form of complex **3** ($\mathbf{3}_{\mathbf{ground}}$) does not contain any solvent molecules. Addition of various solvents to $\mathbf{3}_{\mathbf{ground}}$ followed by drying under ambient

conditions affords eleven different **3**/*solvent* structures, where *solvent* corresponds to added solvents as follows: $CHCl_3$, pyridine (Py), CH_2Cl_2, CH_2Br_2, dimethylacetamide (DMA), acetaldehyde (AcH), CH_3CN, DMF, (*S*)-propylene oxide (*S*PO), *rac*-propylene oxide (*rac*PO), or acetone (Figure 3b and c). These eleven **3**/*solvent* materials exhibited broad emission spectra with maxima ranging from 490 to 580 nm depending on the type of solvent. Mechanical stimulation of **3**/*solvent* induces amorphization and solvent release to recover the $\mathbf{3_{ground}}$ phase (Figure 3b). The resulting $\mathbf{3_{ground}}$ phase can again transform to **3**/*solvent* with an emission color change. This indicates the reactivation of the solvent-responsive properties of **3** through mechanical stimulation. To investigate the structure–property relationship of **3**/*solvent*, single crystals of **3** are prepared and a dozen single crystals of **3**, eleven **3**/*solvent* and one solvent-free **3**/*none*, are obtained (Figure 3d). Single-crystal structure analyses indicate that each crystal of **3**/*solvent* contains solvent molecules and their molecular arrangements vary from each other. Detailed comparison of various crystallographic parameters and optical properties indicates that multiple crystal structural factors affect the optical properties of **3**. Although several compounds that can form various solvated polymorphs have been reported,[17] **3** exhibits the largest number of solvated, crystallographically solved polymorphs with distinct emission properties to date.[18]

2.2. Results and Discussion

2.2.1. Synthesis.

Complex **3** was prepared from 2,2'-diaminobiphenyl according to a previously reported procedure[11,13] with some modification (Figure 4 and Supporting Information, SI). **3** was purified by column chromatography and recrystallization from $CHCl_3$ to afford blue-emitting crystallites (denoted as **3**/$CHCl_3$, Figure 4). Following a typical vacuum drying process, a small amount of $CHCl_3$ (approx. 1 equiv) could not be eliminated from the product. However, grinding the resulting crystals afforded the analytically pure product without solvent contamination. The structure of **3** was characterized by nuclear magnetic resonance (NMR) spectroscopy, high-resolution mass spectrometry, and elemental analysis (see the experimental section). Because the final purification process of **3** to eliminate solvent molecules is grinding, we call the resulting powder sample $\mathbf{3_{ground}}$ (Figure 4).

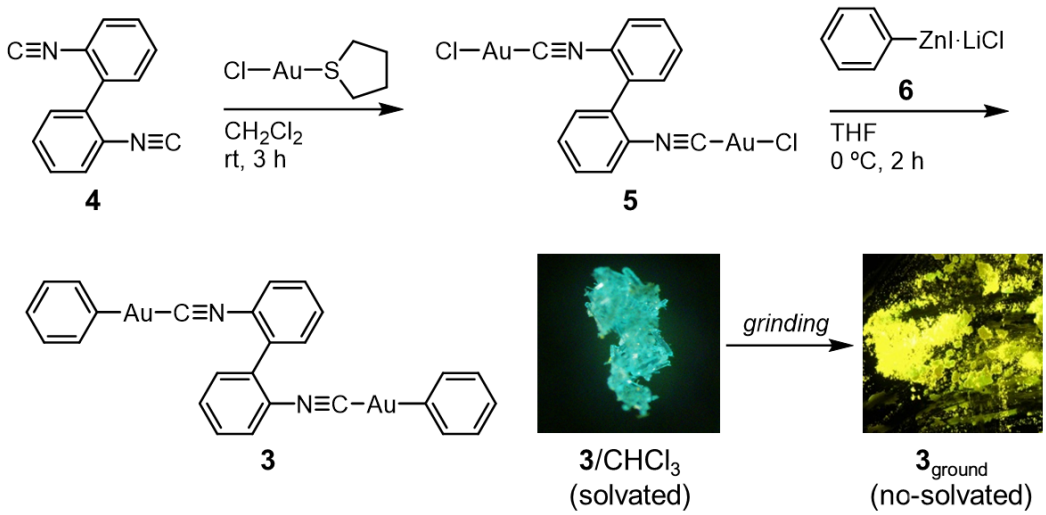

Figure 4. Synthesis of **3** and preparation of $\mathbf{3_{ground}}$. Photographs of **3**/$CHCl_3$ and $\mathbf{3_{ground}}$ were taken under UV light.

2.2.2. Emission Color Changes Induced by Solvent Addition and Grinding

We first examined emission spectral changes of $\mathbf{3_{ground}}$ upon addition of various solvents. The emission spectrum of $\mathbf{3_{ground}}$ following excitation at 365 nm exhibited a broad band with its emission maximum $\lambda_{em,max}$ at 578 nm (black dashed line in Figure 5b).[19,20] We next added various solvents to $\mathbf{3_{ground}}$, and then allowed the solvents to evaporate under ambient conditions. Emission spectra of the resulting powders were recorded under excitation at 365 nm. In this experiment, we used both common organic solvents and various volatile compounds. We obtained eleven different emission spectra for the samples exposed to eleven types of solvents ($CHCl_3$ Py, CH_2Cl_2, CH_2Br_2, DMA, AcH, CH_3CN, DMF, *S*PO, *rac*PO, and acetone), as illustrated in Figure 5b. We call the eleven resulting powders **3**/*solvent*, where *solvent* is an added solvent (Figure 5). It should be noted that complete dissolution is not required in the conversion from $\mathbf{3_{ground}}$ to **3**/*solvent*: immersion of $\mathbf{3_{ground}}$ in the specific solvents afforded **3**/*solvent* after solvent evaporation. All spectra of **3**/*solvent* are broad with distinct $\lambda_{em,max}$ that range from 490 to 580 nm (Figure 5b and S4).[21] For example, the addition of $CHCl_3$ to yellow-emitting $\mathbf{3_{ground}}$ led to an emission color change to blue-emitting powder **3**/$CHCl_3$ with $\lambda_{em,max}$ of 490 nm (Figure 5). We obtained eight green-emitting powders, **3**/Py, **3**/CH_2Cl_2, **3**/CH_2Br_2, **3**/DMA, **3**/AcH, **3**/CH_3CN, **3**/DMF, and **3**/*S*PO, upon the individual addition of eight types of solvents (Figure 5a). These green-emitting powders show different $\lambda_{em,max}$ that range from 530 to 566 nm (Figure 5b). When *rac*PO or acetone was added to $\mathbf{3_{ground}}$, only slight emission color changes were visually confirmed. The resulting yellow-emitting **3**/*rac*PO and **3**/acetone display yellow emission with $\lambda_{em,max}$ of 576 and 580, respectively (Figure 5b). One important characteristic of **3** is the different emission properties of green-emitting **3**/*S*PO and yellow-emitting **3**/*rac*PO with $\lambda_{em,max}$ of 566 and 576 nm, respectively; these two samples are distinguishable from each other by observation under UV light (Figure 5a). This indicates that **3** can act as a solid-state indicator for the stereochemical composition of propylene oxide.

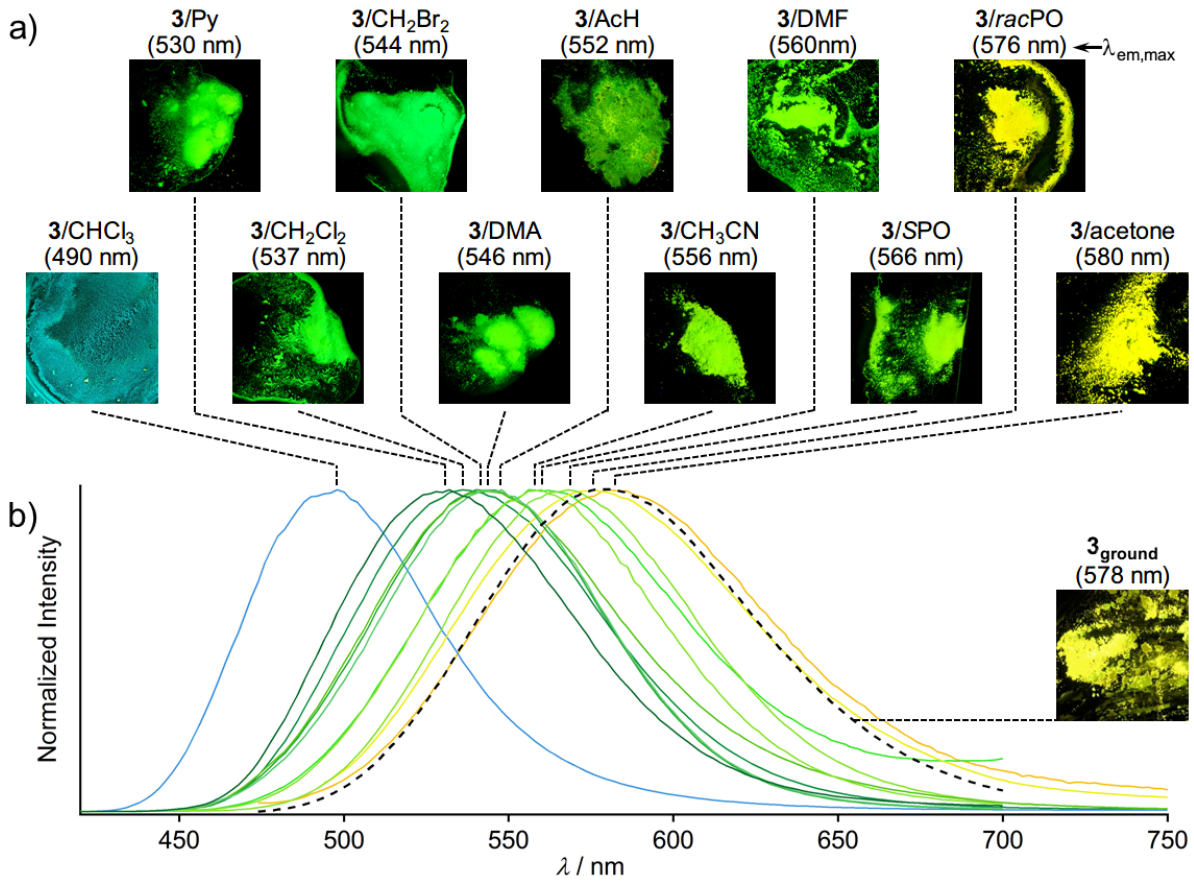

Figure 5. a) Photographs of eleven **3**/*solvent* samples taken under UV illumination. $\lambda_{em,max}$ are shown in parentheses. b) Emission spectra of eleven **3**/*solvent* samples (colored solid lines) and $\mathbf{3}_{\mathbf{ground}}$ (black dotted line) excited at 365 nm. Inset is a photograph of $\mathbf{3}_{\mathbf{ground}}$ taken under UV illumination.

Powder XRD analyses indicate that **3**/*solvent* have crystalline structures that differ from each other and $\mathbf{3}_{\mathbf{ground}}$ is amorphous. The lack of features in the powder XRD pattern of $\mathbf{3}_{\mathbf{ground}}$ reveals that it is amorphous (black line in Figure 6). As discussed above, this amorphous phase is the solvent-free form. Contrary to this, all eleven powders of **3**/*solvent* exhibit intense diffraction patterns, as shown in Figure 6. This indicates that **3**/*solvent* all have crystalline nature, even though the powders of **3**/*solvent* are prepared simply by adding a solvent to amorphous $\mathbf{3}_{\mathbf{ground}}$ and letting the solvent evaporate under ambient conditions. Careful inspection of the powder XRD patterns of the eleven **3**/*solvent* samples confirmed that the peak positions are different from each other (Figure 6). This observation suggests that the crystal structures of the resulting **3**/*solvent* are different from each other and depend on the solvent added to induce the phase transition of $\mathbf{3}_{\mathbf{ground}}$. NMR spectroscopy indicates that all **3**/*solvent* contain solvent molecules inside the crystalline lattices (Figure S5). These results imply that

the formation of different crystalline structures of **3**/*solvent* and solvent inclusion is responsible for their varied emission properties.

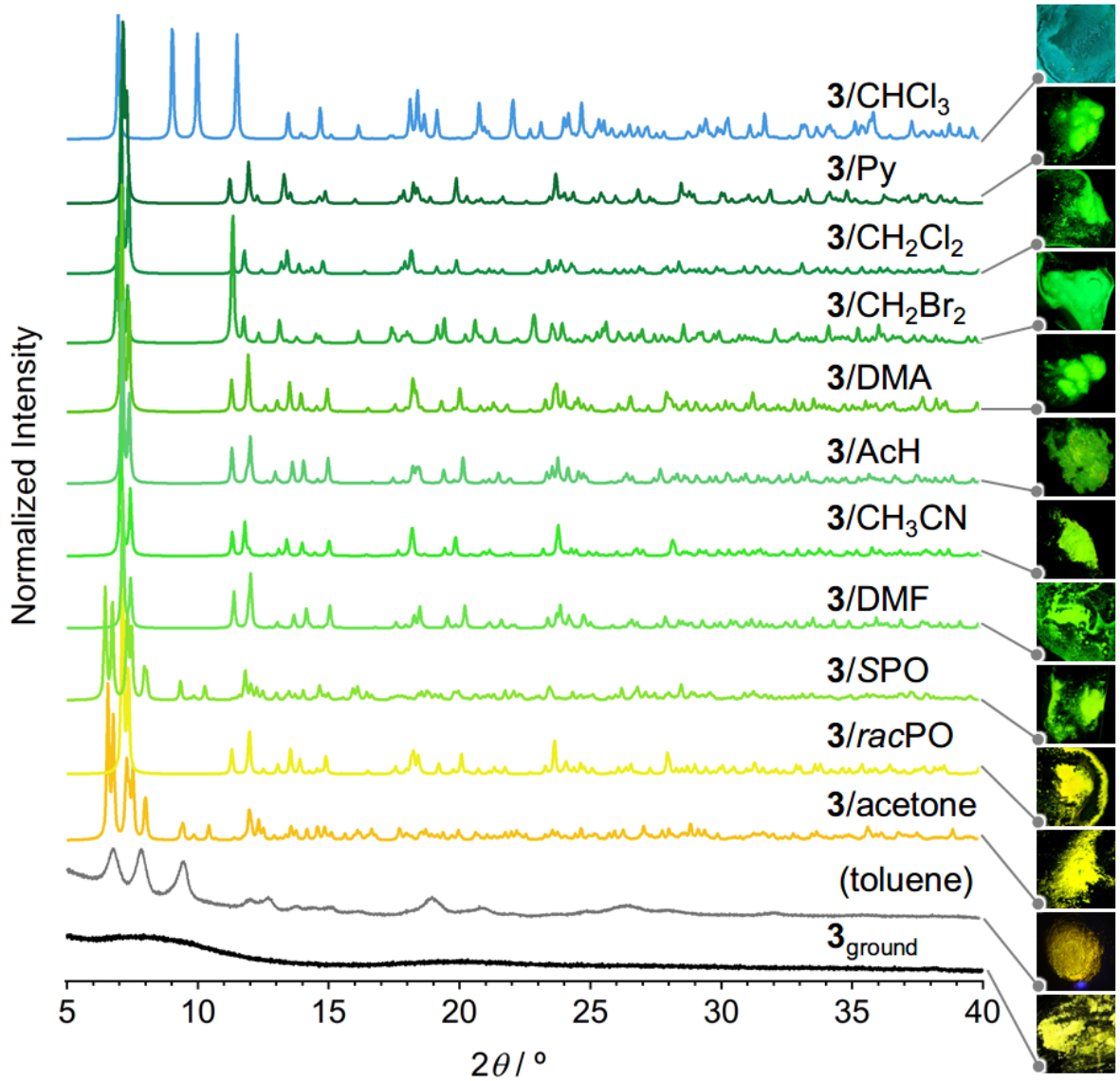

Figure 6. Powder XRD patterns of eleven powder samples of **3**/*solvent*, the powder treated with toluene [denoted as "(toluene)"], and ground powder $\mathbf{3}_{\text{ground}}$.

When other solvents not listed in the previous paragraph were added to $\mathbf{3}_{\mathbf{ground}}$, no detectable emission color changes were observed in the resulting powders. We also added 25 other different volatile compounds to $\mathbf{3}_{\mathbf{ground}}$,[22] but no emission color change was observed; the yellow emission mostly remained. XRD measurements of the resulting powders imply that the addition of these solvents does not induce distinctive changes in molecular arrangement of **3**. For example, the XRD patterns of the powders obtained after treatment with toluene exhibit several peaks with very low intensity (grey line in Figure 6). These weak diffraction peaks indicate that toluene only induces partial crystallization of **3**. Such diffraction patterns with low

intensity were also obtained after $\mathbf{3}_{\mathbf{ground}}$ was treated with benzene, trichloroethene, and THF (Figure S6). Meanwhile, the powders of **3** obtained after treatment with hexane or MeOH exhibited diffraction patterns with almost no peaks that were similar to that of $\mathbf{3}_{\mathbf{ground}}$ (Figure S6).[23] We speculate that the above solvents that do not induce emission color changes of **3** cannot form the corresponding solvated crystals with **3**, so $\mathbf{3}_{\mathbf{ground}}$ remains after solvent addition.

Mechanical stimulation can eliminate solvent molecules from **3**/*solvent* to allow reuse of **3** for solvent detection, which is more convenient than other reactivation processes. Grinding eleven samples of **3**/*solvent* using a spatula or ball milling regenerates yellow-emitting powder $\mathbf{3}_{\mathbf{ground}}$ irrespective of the type of solvent in **3**/*solvent* (Figure S7, S8 and Table S2).[20] The powder XRD patterns of $\mathbf{3}_{\mathbf{ground}}$ obtained after grinding of **3**/*solvent* are featureless, indicating that all $\mathbf{3}_{\mathbf{ground}}$ sample are amorphous (Figure S9). These amorphous phases of $\mathbf{3}_{\mathbf{ground}}$ do not include solvent molecules, as shown by NMR spectroscopy and thermogravimetric analyses (TGA, Figure S10 and S11), indicating solvent release is induced by mechanical stimulation.[24] The resulting $\mathbf{3}_{\mathbf{ground}}$ again exhibited various emission color changes upon addition of specific solvents to form **3**/*solvent*. Thus, sequential emission color changes through multiple mechanical grinding/solvent addition processes is possible. Figure 7a presents the emission color changes of a single sample. Initially, $\mathbf{3}_{\mathbf{ground}}$ shows an emission color change from yellow to green upon CH_2Cl_2 addition. Yellow emission can then be recovered by mechanical stimulation (reactivation), which changes to blue upon addition of $CHCl_3$. After reactivation of yellow-emitting $\mathbf{3}_{\mathbf{ground}}$, addition of *S*PO affords green-emitting **3**/*S*PO. Further grinding again recovers $\mathbf{3}_{\mathbf{ground}}$ (yellow emission), and green emission is observed again upon adding CH_2Cl_2 (Figure 7a). Attempts to remove the included solvent from $\mathbf{3}_{\mathbf{ground}}$ at high temperature under reduced pressure, which is a common method to remove solvent, results in partial removal of the solvent from **3**/*solvent* samples (Figure 7a, i). The resultant samples are not amorphous and differ from $\mathbf{3}_{\mathbf{ground}}$ (Figure S12). For example, **3**/CH_2Cl_2 was treated at 70 °C under reduced pressure, which results in an emission color change from green to yellow (Figure 7b, i). NMR spectroscopy and powder XRD measurements reveal that the resulting powders remain moderate crystallinity and contain residual CH_2Cl_2 (Figure S12).[25] Importantly, the resulting powder does not show an emission color change upon $CHCl_3$ addition (Figure 7b, ii), indicating that heating under reduced pressure does not effectively reactivate the solvent-responsive properties of **3** compared with mechanical stimulation.

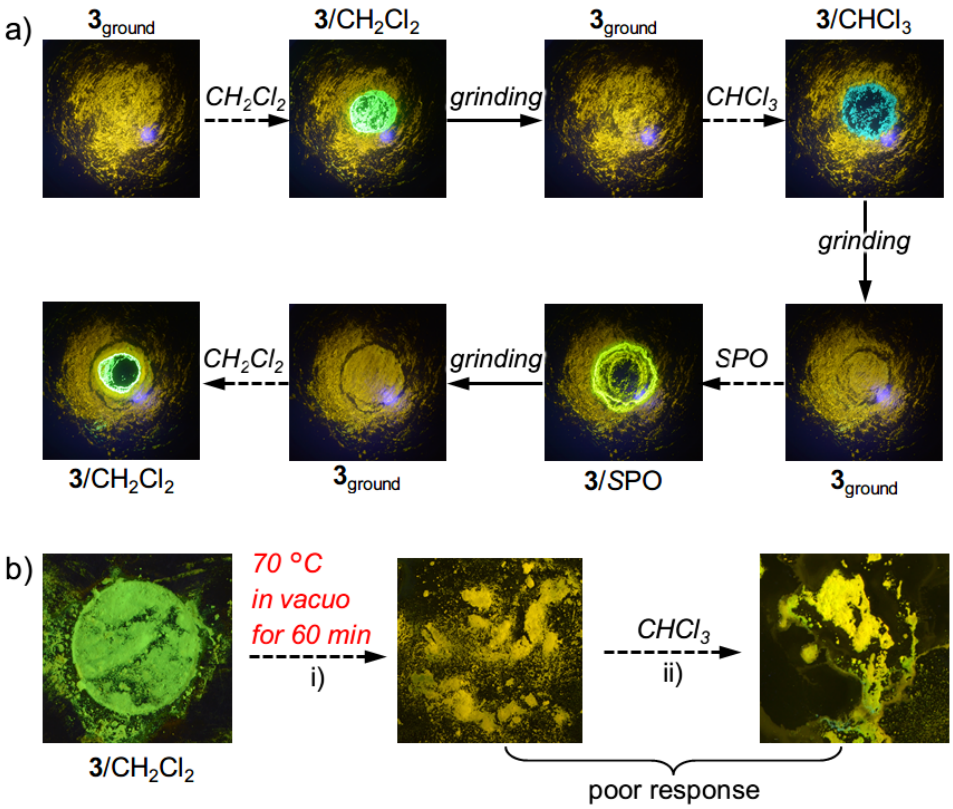

Figure 7. a) Sequential interconversion between **3**/*solvent* and $\mathbf{3}_{ground}$ through repeated solvent addition and mechanical grinding processes. Photographs are taken under UV light. b) Photographs of **3**/CH_2Cl_2 i) before and after heating under reduced pressure, and ii) after addition of $CHCl_3$ taken under UV light. The powder obtained by heating/evacuation does not show a clear emission color change.

2.2.3. Single-Crystal Structure Analyses

To obtain precise structural information about the **3**/*solvent* samples, we prepared single crystals corresponding to their powder forms. After repeated trials, we obtained eleven different single crystals of **3**/*solvent* by recrystallization from eleven solvents (Figure 8a and S13–S23, and Table 1 and S3). Typical conditions to prepare single crystals of **3**/*solvent* are as follows: **3** was dissolved in a solvent to induce inclusion, and then stored for 12 h in a freezer at −25 °C to give single crystals of **3**/*solvent*. Emission colors (Figure S24) and excitation/emission spectra (Figure S25) of the single crystals of **3**/*solvent* are very similar to those of the powders prepared by addition and evaporation of the same solvents. In addition, simulated powder patterns derived from these single crystals of **3**/*solvent* match the XRD patterns of the powder forms (Figure S26). These results clearly indicate that the molecular arrangements of the single crystals correspond to those of the powder forms of **3**/*solvent*. All **3**/*solvent* samples contain solvent molecules used in the recrystallization (0.25–1 equiv; Table 1), which is consistent with the NMR spectra of the powder forms of **3**/*solvent* (Figure S5). In addition, when trichloroethene was used for recrystallization of **3**, a single crystal of **3**/*none* without any solvent molecules formed (blue dotted squares in Figure 8 and Table 1).[26] As shown in Figure 8b, the dozen single-crystal structures of **3**, eleven **3**/*solvent* and one **3**/*none*, are different from each other (crystallographic parameters are listed in Table S3).

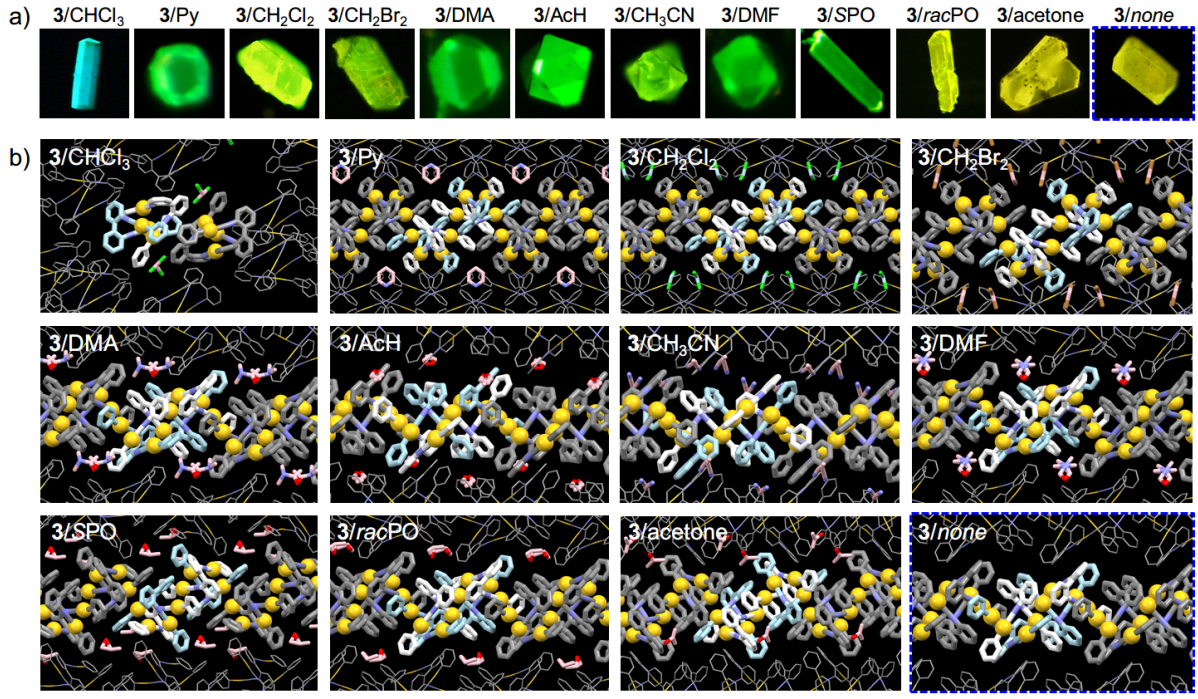

Figure 8. a) Photographs of eleven single crystals of **3**/*solvent* taken under UV illumination. b) Single-crystal structures of eleven **3**/*solvent* samples. H atoms are omitted for clarity. Further detail description is provided in SI. Photographs and the single crystal structure of **3**/*none* are also shown in the blue dashed squares (see text for more detail).

Table 1. Summary of the Molar Composition of **3** and Solvent and Au··· Au and π···π Distances of Single-Crystal Structures of **3**/solvent and **3**/none.

	Solvents		Monomer		Intra-dimer	Inter-dimer		Other
3/*solvent*	**3**:solvent[a]/ -	Volume[b,c] / %	$\theta_{Biphenyl}$[d] / °	$\theta_{Isocyanide}$[d] / °	Au···Au distance[e] / Å	Au···Au distance[e] / Å	π···π distance[e,f] / Å	Density / g cm^{-3}
3/$CHCl_3$	1:1	18.6	57.22	13.49	3.191	(8.156)	-	2.221
3/Py	1:0.5	5.8	50.84	5.77	3.189	3.517	3.298	2.201
3/CH_2Cl_2	1:1	15.0	52.72	7.55	3.206	3.566	3.309	2.247
3/CH_2Br_2	1:1	15.8	51.64	7.27	3.216	3.527	3.312	2.458
3/DMA	1:0.5	12.7	52.55	4.41	3.212	3.527	3.347	2.208
3/AcH	1:0.5	12.6	51.96	5.08	3.212	3.516	3.352	2.151
3/CH_3CN	1:1	12.7	55.93	4.73	3.221	3.498	3.381	2.183
3/DMF	1:0.5	4.9	51.93	4.93	3.194	3.485	3.284	2.226
3/SPO	1:1	2.7	51.78	9.28	3.193	3.426	3.248	2.119
3/*rac*PO	1:0.25	3.1	53.21	4.38	3.218	3.504	3.322	2.123
3/acetone	1:0.25	9.5 (2.9 %)[c]	52.20	21.62	3.134	3.493	3.414	2.120
3/*none*	1:0	0	51.57	6.87	3.185	3.527	3.305	2.317

[a]Measured in molar ratio. [b]Volume% occupied by included solvent molecules within the unit cell volume. [c]Volume% of voids within the unit cell are listed in parentheses. [d]Average dihedral angles found are listed. [e]The average distances found are listed, and standard deviation is omitted. [f]Distances for [f]Distances for π···π stacking interactions are measured between one phenyl plane and one of the carbon atoms in a phenyl ring.

As a representative example of a single-crystal structure of **3**/*solvent*, the single-crystal structure of **3**/CH_2Cl_2 is shown in Figure 9 and S14. We found that **3**/CH_2Cl_2 crystallized into monoclinic space group *I*2/*a* (Table S3). The simulated powder pattern derived from the **3**/CH_2Cl_2 single crystal matches the experimental XRD pattern of the powder form of this complex (Figure S26). As illustrated in Figure 9a, the gold complexes in **3**/CH_2Cl_2 form a dimeric structure containing three intermolecular Au···Au interactions with Au···Au distance of 3.164, 3.291, and 3.164 Å (Figure 9a). The two molecules in each dimer adopt the same conformational enantiomer, as shown in Figure 9a. The dimers in **3**/CH_2Cl_2 further interact with neighboring ones through aurophilic and slipped π–π stacking interactions (Au···Au and π···π distances of 3.566 and 3.309 Å, respectively; Figure 9b). Between the two gold atoms of the dimers, there is an inversion center (denoted as a purple square in Figure 9). These intermolecular interactions between the dimers afford an infinite columnar motif (Figure 8b and 9c). Adjacent dimers always include molecules with the opposite conformational enantiomers. Thus, the columns consist of an alternating sequence of dimers with the opposite

conformational enantiomers in which the chiral structures of complexes are ···*RRSSRRSS*··· (Figure 9c). The neighboring columns (see green and light-blue columns in Figure 9d) align parallel to each other. Included CH_2Cl_2 molecules (**3**:CH_2Cl_2 = 1:1) are located between columns and display CH/π interactions with a distance of 2.381 Å (Figure 9e).

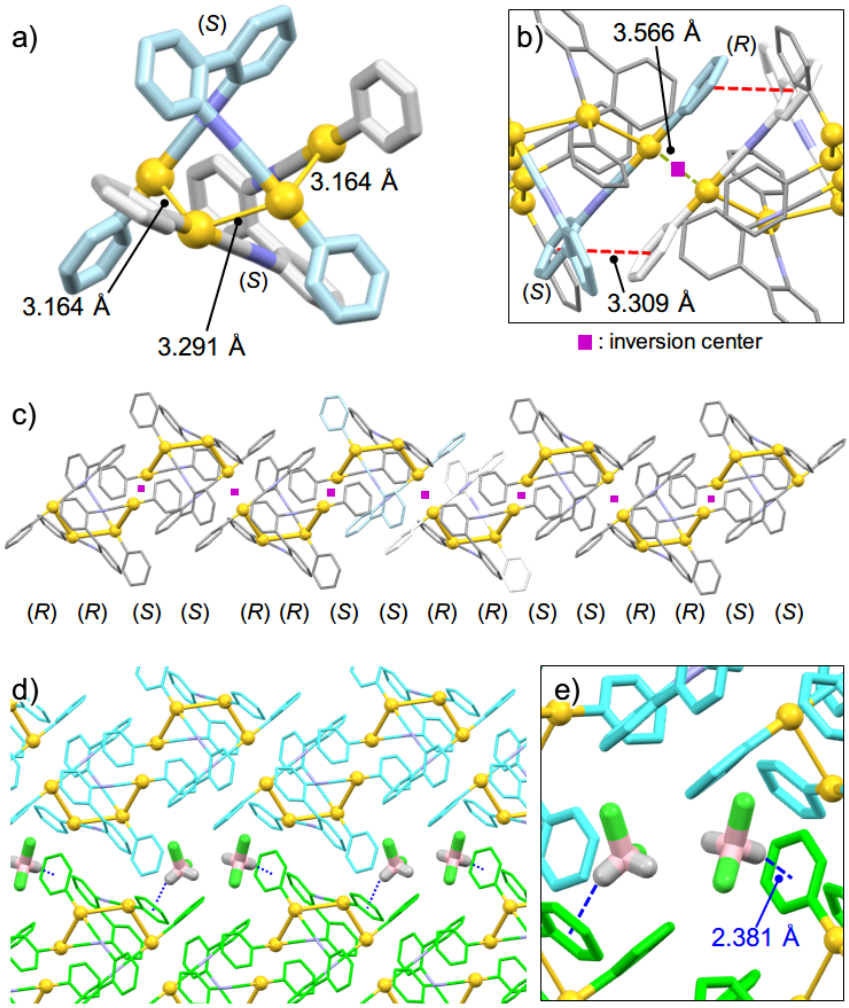

Figure 9. Single-crystal structure of **3**/CH_2Cl_2 showing a) the dimer arrangement, b) the intermolecular interactions between the dimers, c) 1D column structure, and d and e) the solvent molecules located between the columns. H atoms of **3** are omitted and gold atom is represented by yellow ball for clarity. The inversion center is denoted as a purple square. In d) and e), molecules in one column are colored in light-blue and ones in its neighboring column are colored in light-green. More detailed crystalline structures are shown in Figure S14.

Nine other single-crystal structures of **3**/*solvent*, excluding **3**/$CHCl_3$, show structural characteristics similar to that of **3**/CH_2Cl_2 (Figure S13–S23). We summarize selected crystallographic information and parameters obtained from the single crystals of **3**/*solvent* in Table 1 and S3, respectively. In addition to **3**/CH_2Cl_2, the nine complexes **3**/Py, **3**/CH_2Br_2, **3**/DMA, **3**/AcH, **3**/CH_3CN, **3**/DMF, **3**/*S*PO, **3**/*rac*PO, and **3**/acetone form a homochiral dimer structure (*SS* or *RR*) in which molecules form three aurophilic bonds. Table 1 reveals that the average Au···Au distances within the dimer of ten **3**/*solvent* crystals, excluding **3**/$CHCl_3$, range from 3.134 to 3.218 Å (see also Figure S14–S23). These dimers form columnar structures through aurophilic (Au···Au distances range from 3.426 to 3.566 Å) and π–π stacking interactions (π···π distances range from 3.248 to 3.381 Å) to form extended 1D columnar motifs (Figure 8b and Table 1) with arrangements of ···*RRSSRRSS*··· (*vide supra*). Between the columns of **3**/*solvent*, 0.25–1 equiv of solvent molecules are accommodated (Figure 8b and Table 1). Although these characteristics of the single-crystal structures of **3**/*solvent* are similar to each other, they are not the same single-crystal structures. The powder patterns simulated from these single-crystal structures are different from each other (Figure S27). In addition, as local crystallographic information, Figure 10 compares the dimer conformations derived from the eleven single crystals of **3**/*solvent* with one phenyl ring at a fixed position, confirming their distinct conformations.

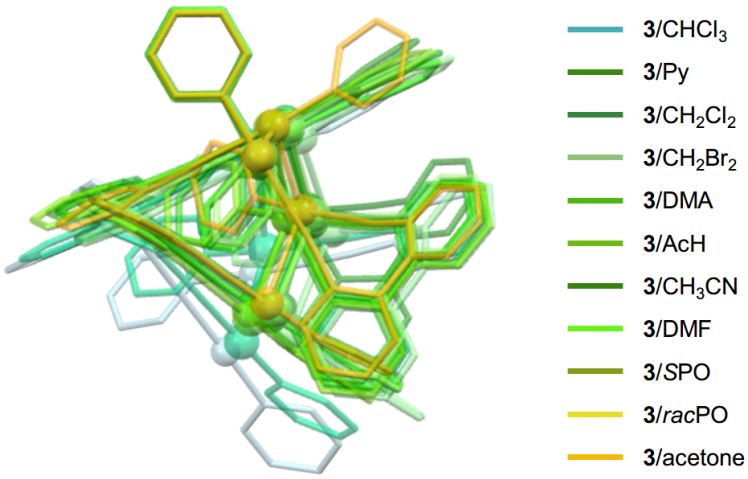

Figure 10. Comparison of the dimer conformations derived from the eleven single-crystal **3**/*solvent* structures. One phenyl ring of each of the eleven dimers is located at a fixed position.

It should be noted that the single-crystal structures of **3**/*S*PO and **3**/*rac*PO are different from each other (Figure S23 and S24, respectively). For example, the molar ratio of **3** to included *S*PO in **3**/*S*PO is 1.0, while it is 0.25 for **3**/*rac*PO (Table 1). Moreover, Au···Au distances within a dimer and between dimers in **3**/*S*PO are shorter than those observed in **3**/*rac*PO (Table 1). θ_{Biphenyl} of **3**/*S*PO is smaller than that of **3**/*rac*PO (51.78° and 53.21°, respectively), and $\theta_{\text{Isocyanide}}$ of **3**/*S*PO (9.28°) is larger than that of **3**/*rac*PO (4.38°; Table 1). This comparison of the structures of **3**/*S*PO and **3**/*rac*PO indicates that complex **3** can form different crystal structures depending on the stereochemical composition of the propylene oxide molecules, which leads to two distinct emission colors (green and yellow, respectively). Moreover, the former crystallized into chiral space group *P*1, in which the homochirality of *S*PO is expressed at the level of the packing of the crystal structure of **3**/*S*PO.

The single-crystal structure of **3**/*none* is reminiscent of those of **3**/*solvent* apart from **3**/$CHCl_3$, but there is no inclusion of solvent molecules and distinctive π–π stacking interactions are formed between columns. As mentioned above, the simple addition of trichloroethene to $\mathbf{3}_{\mathbf{ground}}$ only induces partial crystallization of **3** and the resulting powder is different from **3**/*solvent*. However, crystallization of **3** from trichloroethene solution gives the yellow-emitting single crystal **3**/*none* (Figure 3d, 8a and S28).[26] The 1D column structure of **3**/*none* is similar to that of other **3**/*solvent*, like **3**/CH_2Cl_2: a dimer structure possessing one conformational enantiomer (Figure 11a) interacts with a dimer with the opposite enantiomer through Au···Au and π–π stacking interactions (Figure 11b), which form 1D columns with sequential chiral units of ···*RRSSRRSS*··· (Figure 11c). However, different from **3**/*solvent*, there is no solvent inclusion in **3**/*none*, which is also supported by NMR spectroscopy (Figure S29). The interaction between columns of **3**/*none* is thus different from those of **3**/*solvent*. One column interacts with a neighboring column (see green and light-blue columns in Figure 11d) through slipped π–π stacking interactions between benzene rings of biphenyl moieties (π···π distances: 3.337 Å; Figure 11e).[27] The formation of distinct intermolecular interactions of complexes between columns, as well as those within columns, is a structural characteristic of **3**/*none* that is not found in **3**/*solvent*.

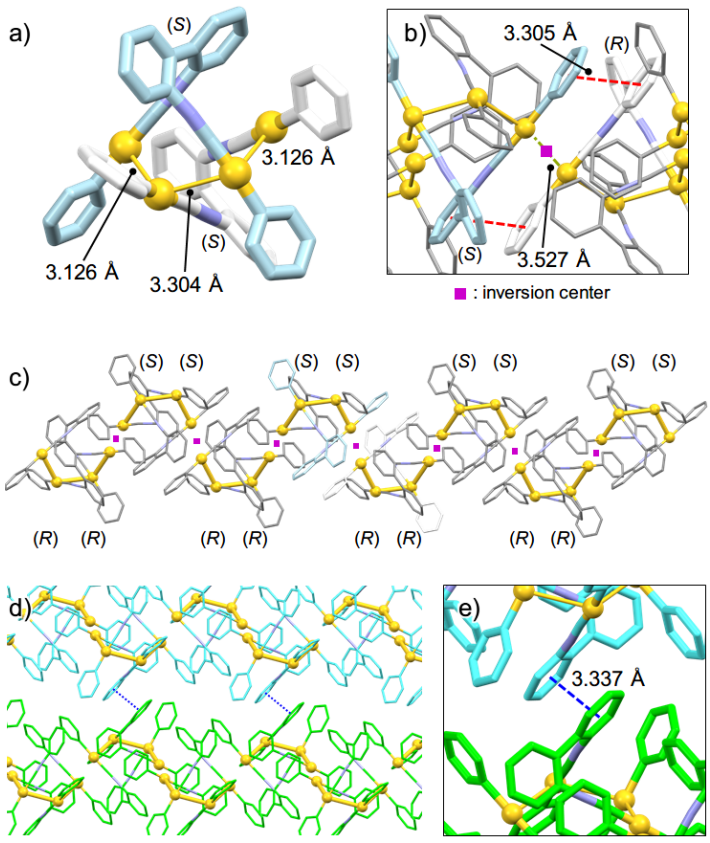

Figure 11. Single-crystal structure of **3**/*none* showing a) the dimer arrangement, b) the intermolecular interactions between the dimers, c) 1D column structure, and d and e) the intermolecular interactions between the columns. H atoms are omitted and gold atom is represented by yellow ball for clarity. The inversion center is denoted as a purple square. In d) and e), molecules in one column are colored in light-blue and ones in its neighboring column are colored in light-green. More detailed crystalline structures are shown in Figure S29.

The single-crystal structure of **3**/$CHCl_3$ is quite different from those of the other eleven single-crystal structures of **3** (Figure 12 and S13). Molecules in **3**/$CHCl_3$ form a dimer structure through aurophilic interactions with Au···Au distances of 3.148, 3.278, and 3.148 Å (Figure 12a). The chiral configuration of two molecules in each dimer is always the same; *i.e.*, *RR* or *SS*. The dimers are isolated from neighboring ones because of the presence of included $CHCl_3$ molecules (Figure 12c). The determined molar ratio of **3**:$CHCl_3$ is 1:1. As shown in 12b, the distance of CH/π interactions between a phenyl plane of **3** and an H atom of $CHCl_3$ is 2.177 Å. The isolation of dimers through the rather strong CH/π interactions with solvent molecules is not found in the other single crystals **3**/*solvent* and **3**/*none* (Figure 8b); this explain why $\lambda_{em,max}$ of **3**/$CHCl_3$ is at the shortest wavelength ($\lambda_{em,max}$ = 490 nm) of the complexes.

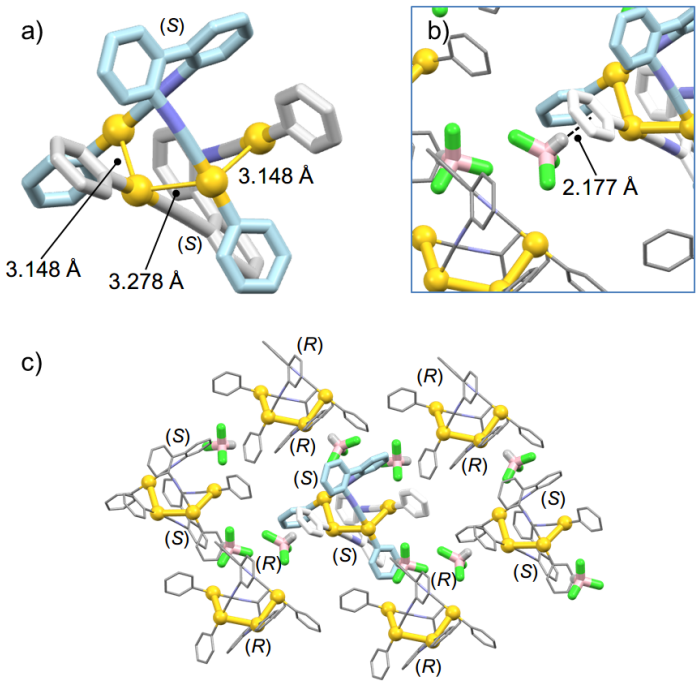

Figure 12. Single-crystal structure of **3**/$CHCl_3$ showing a) the dimer arrangement, b) the dimers and $CHCl_3$ molecules that surround one dimer unit, c) the intermolecular interactions between the dimer and $CHCl_3$. H atoms of complex **3** are omitted and gold atom is represented by yellow ball for clarity. More detailed crystalline structures are shown in Figure S13.

2.2.4. Structure–Property Relationship

Comparison of crystallographic information and optical properties of **3**/*solvent* and **3**/*none* indicates that multiple structural factors affect various emission properties. Typically, the solid-state emission properties of organic crystalline materials strongly depend on intermolecular interactions within the crystal structures.[28] We plotted various crystallographic factors of **3**/*solvent* and **3**/*none* against $\lambda_{em,max}$ (Figure 13) with the expectation that some structural factors will strongly correlate with their optical properties. It is known that aurophilic interactions decrease excitation energy, leading to red-shifted emission, and the degree of this decrease of excitation energy is more prominent when the Au···Au distance is shorter.[29] Indeed, our previously reported gold isocyanide complexes showed red-shifted emission upon the formation of aurophilic interactions.[8-9,15] In Figure 13a, we plot average Au···Au distances within the dimers ($L_{Au\cdots Au}$) of **3**/*solvent* and **3**/*none* with respect to corresponding $\lambda_{em,max}$. The random distribution of the plots indicates that $\lambda_{em,max}$ of **3**/*solvent* do not directly correlate with $L_{Au\cdots Au}$. Inter-dimer $L_{Au\cdots Au}$ and phenyl-to-phenyl distances for π···π stacking interactions ($L_{\pi\cdots\pi}$) against corresponding $\lambda_{em,max}$ are also plotted (Figure 13b). These plots are scattered, indicating there is no apparent correlation between $L_{Au\cdots Au}$ or $L_{\pi\cdots\pi}$ and $\lambda_{em,max}$. We plot $\theta_{Biphenyl}$ and $\theta_{Isocyanide}$ with respect to $\lambda_{em,max}$ of **3**/*solvent* and **3**/*none* in Figure 13c. A very weak correlation can only be found in the blue dotted plot ($\theta_{Biphenyl}$ *versus* $\lambda_{em,max}$): as $\theta_{Biphenyl}$ decreased, only a slight red shift of emission was observed. However, a clear correlation between $\theta_{Biphenyl}$ and $\lambda_{em,max}$ was not be revealed by this systematic investigation of **3**. Similarly, we cannot confirm that **3**:solvent ratio and solvent volume% in the unit cell of **3**/*solvent* and **3**/*none* are directly correlated with the corresponding $\lambda_{em,max}$ from the plots in Figure 13d. The observations in Figure 13 indicate that one specific crystallographic factor of **3**/*solvent* and **3**/*none* does not dominantly affect the optical properties of **3**. Instead, the combination of various structural factors influences the optical properties of **3**/*solvent* and **3**/*none* crystals. Quantum chemical calculation based on coordination of **3**/*solvent* does not afforded valuable information of their emission mechanism.[31] We did not find a clear structure–property relationship of **3**/*solvent* and **3**/*none* that could be used as a simple guide for material design.

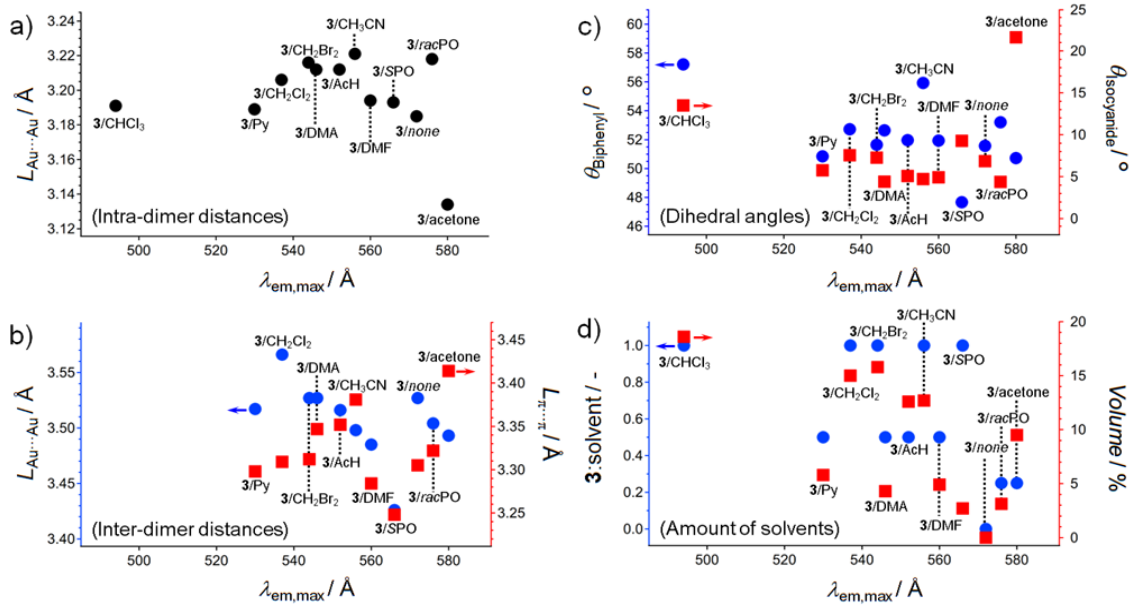

Figure 13. Plot of average Au···Au distances within a dimer ($L_{Au\cdots Au}$, a), average Au···Au distances between dimers ($L_{Au\cdots Au}$, blue circles in b), average distances of two phenyl planes between dimers ($L_{\pi\cdots\pi}$, red square in b), dihedral angles of phenyl rings in the biphenyl moiety ($\theta_{Biphenyl}$, blue circles in c), dihedral angle between the phenyl ring on Au and that in the isocyanide ligand ($\theta_{Isocyanide}$, red squares in c), **3**:solvent ratio (blue circles in d), and volume% occupied by solvents (red squares in d) *versus* the corresponding $\lambda_{em,max}$ of **3**/*solvent* and **3**/*none*.

2.3. Summary

In this report, we introduced the aryl gold isocyanide complex **3** appended with a biphenyl moiety to restrict conformational freedom. The addition of various solvents to ground powder $\mathbf{3}_{\mathbf{ground}}$ afforded eleven types of **3**/*solvent* with different emission properties ($\lambda_{em,max}$ ranging from 490 to 580 nm). The **3**/*solvent* samples contain eleven different types of solvent molecules, which are important for their varied emission properties. This indicates that **3** can be used as an indicator for various volatile organic molecules, which can be probed by examining the emission properties of **3**/*solvent*. Mechanical stimulation of **3**/*solvent* reactivated the solvent-responsive properties of **3** through the recovery of the yellow-emitting $\mathbf{3}_{\mathbf{ground}}$ as a solvent-free amorphous phase. We prepared single crystals of all eleven **3**/*solvent* corresponding to the powder forms obtained by simple solvent addition and subsequent evaporation. To the best of our knowledge, **3** is the first luminescent compound that can form a dozen fully-solved different solid structures with distinct emission properties. Comparison of the single-crystal structures revealed that crystalline structures differed from each other. We also obtained solvent-free single crystal **3**/*none*. To understand the structure–property relationships in the single crystals of **3**/*solvent* and **3**/*none*, we extracted crystallographic factors, *i.e.*, Au···Au distances, π···π stack distances, and dihedral angles of benzene rings, and plotted them with respect to corresponding $\lambda_{em,max}$. Analyses of the crystal structures of **3**/*solvent* indicated that there was not one specific structure factor that controlled the emission properties of **3**/*solvent*. Instead, the emission properties might be the result of the combination of several structure factors. We could not identify simple design guidelines to predict the emission properties of **3** from its crystal structure. However, we found that including a biphenyl moiety with restricted rotational freedom into gold isocyanide complexes enhances the ability of the gold complexes to adopt various crystal structures with different emission properties in response to solvent addition. This finding should be important for the design of emission-based solvent-responsive materials.

2.4. Experimental Section

2.4.1. General

All commercially available reagents and solvents are of reagent grade and were used without further purification unless otherwise noted. Solvents for the synthesis were purchased from commercial suppliers, degassed by three freeze-pump-thaw cycles and further dried over molecular sieves (4 Å). NMR spectra were recorded on a JEOL JNM-ECX400P or JNM-ECS400 spectrometer (^{1}H: 400 MHz; ^{13}C: 99.5 MHz) using tetramethylsilane and $CDCl_3$ as internal standards, respectively. Emission spectra were recorded on a Hitachi F-7000 spectrometer. Fluorescence microscopic spectra were recorded on a Photonic Hamamatsu PMA-12 Multichannel Analyzer. The emission quantum yields of the solid samples were recorded on a Hamamatsu Quantaurus-QY spectrometer with an integrating sphere. Emission lifetime measurements were recorded on a Hamamatsu Quantaurus-Tau spectrometer. Elemental analyses and low- and high resolution mass spectra were recorded at the Global Faculty Center at Hokkaido University. Photographs were obtained using Olympus BX51 or SZX7 microscopes with Olympus DP72, Nikon D5100 digital cameras. Thermal gravimetric analysis profiles were recorded on Bruker TG-DTA2010SAT.

2.4.2. Synthesis

*Synthesis of **5**.*

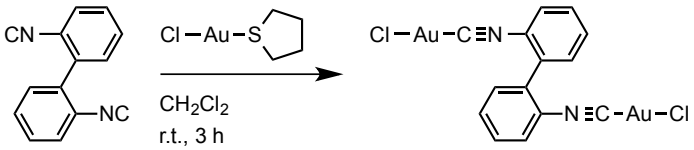

6 **5**

2,2'-Diisocyano-1,1'-biphenyl **6** (0.610 g, 3.0 mmol)[32] and chloro(tetrahydrothiophene)gold(I) (1.930 g, 6.0 mmol) were dissolved in CH_2Cl_2 (30 mL) and stirred for 3 h. The solvent was removed with a rotary evaporator under a reduced pressure. Washing with methanol gave an analytically pure white solid **5** (1.776 g, 2.7 mmol, 88 %). ^{1}H NMR (400 MHz, $CDCl_3$, δ): 7.50–7.53 (m, 2H), 7.67–7.53 (m, 2H), 7.76–7.80 (m, 4H). MS-ESI (*m*/*z*): $[M+Na]^+$ calculated for $C_{26}H_{18}Au_2N_2Na$, 690.9293; found, 690.9293. Anal. Calcd for $C_{26}H_{18}Au_2N_2$: C, 25.13; H, 1.21; N, 4.19. Found: C, 25.18; H, 1.06; N, 4.04. This compound exhibits poor solubility in common organic solvents (for example, maximum solubility in $CHCl_3$ is 2 mg/mL); therefore, ^{13}C NMR spectroscopy cannot be measured.

*Synthesis of **3**.*

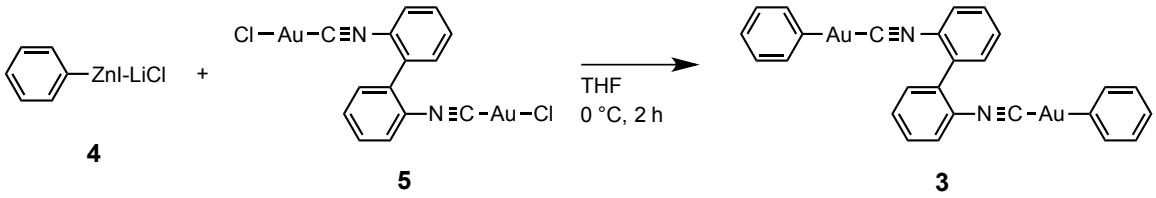

4 **5** **3**

To chlorogold(I) isocyanide complex **5** (0.334 g, 0.5 mmol) in 100 mL flask, THF (2 ml) was added under nitrogen atmosphere. After cooling to 0 °C, organozinc iodide reagent **4** in THF (1.10 ml, 1.2 mmol) was added to the mixture dropwise and stirred for 2 h.[33] The reaction was quenched by addition of a phosphate buffer solution and then extracted with CH_2Cl_2 three times and washed with H_2O and brine. The organic layers were collected and dried over $MgSO_4$. After filtration, the solvent was removed *in vacuo*. Further purification by flash column chromatography (SiO_2, $CHCl_3$/hexane = 6:1) gave a yellow and light blue solid mixture. The resulting solid was dissolved in $CHCl_3$ at 50 °C and stand in a refrigerator for 24 h, affording a light blue crystal. The resulting crystal contains $CHCl_3$ (approx. 1.0 equiv as indicated by ^{1}H NMR in CD_2Cl_2), thus denoted as **3**/$CHCl_3$. Ball milling of **3**/$CHCl_3$ for 40 min at 4600 rpm

gave an analytically pure yellow powder $\mathbf{3_{ground}}$ (0.177 g, 0.23 mmol, 47 %). ^{1}H NMR (400 MHz, CD_2Cl_2, δ): 6.98 (tt, *J* = 1.5 Hz, 7.5 Hz, 2H), 7.12 (t, *J* = 7.6 Hz, 4H), 7.29 (dd, *J* = 1.4 Hz, 7.8 Hz, 4H), 7.52 (dd, *J* = 0.8 Hz, 8.0 Hz, 2H), 7.59–7.74 (m, 6H). ^{13}C NMR (100 MHz, $CDCl_3$, □): 124.0 (*C*), 126.2 (*C*H), 127.6 (*C*H), 128.7 (*C*H), 130.8 (*C*H), 131.1 (*C*H), 131.7 (*C*H), 133.9 (*C*), 141.0 (*C*H), 162.7 (*C*), 164.3 (*C*). MS-ESI (*m*/*z*): $[M+Na]^+$ calculated for $C_{26}H_{18}Au_2N_2Na$, 775.0699; found, 775.0699. Anal. Calcd for $C_{26}H_{18}Au_2N_2$: C, 41.51; H, 2.41; N, 3.72. Found: C, 41.21; H, 2.42; N, 3.66.

2.4.3. Optical Properties of 3 in Solution Phase

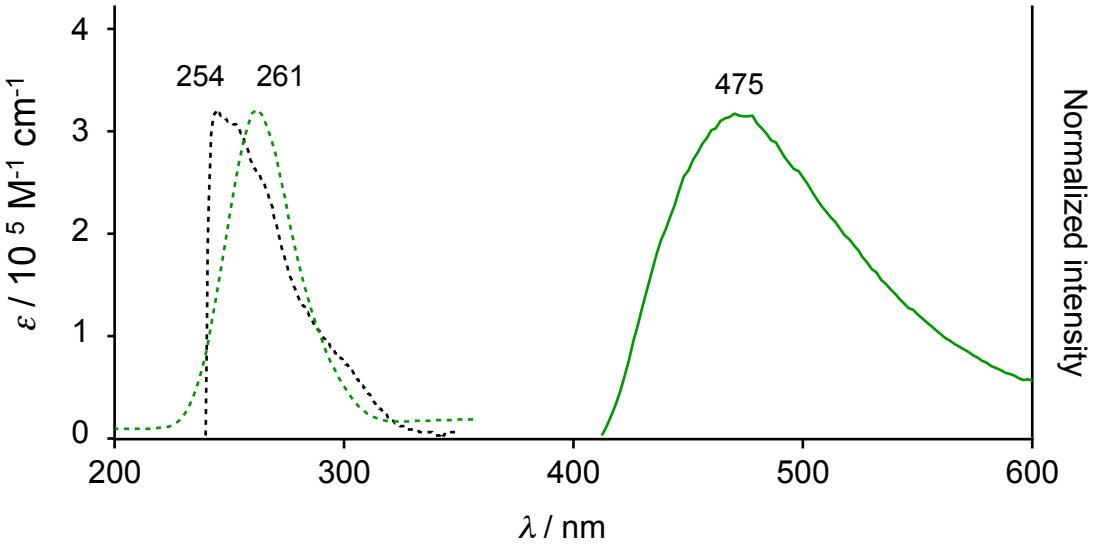

Figure S1. UV/vis absorption (dashed black line), excitation (dashed green line, λ_{em} = 475 nm), and emission spectra (solid green line, λ_{ex} = 261 nm) of **3** in $CHCl_3$ ($c = 3.6 \times 10^{-5}$ M) at room temperature.

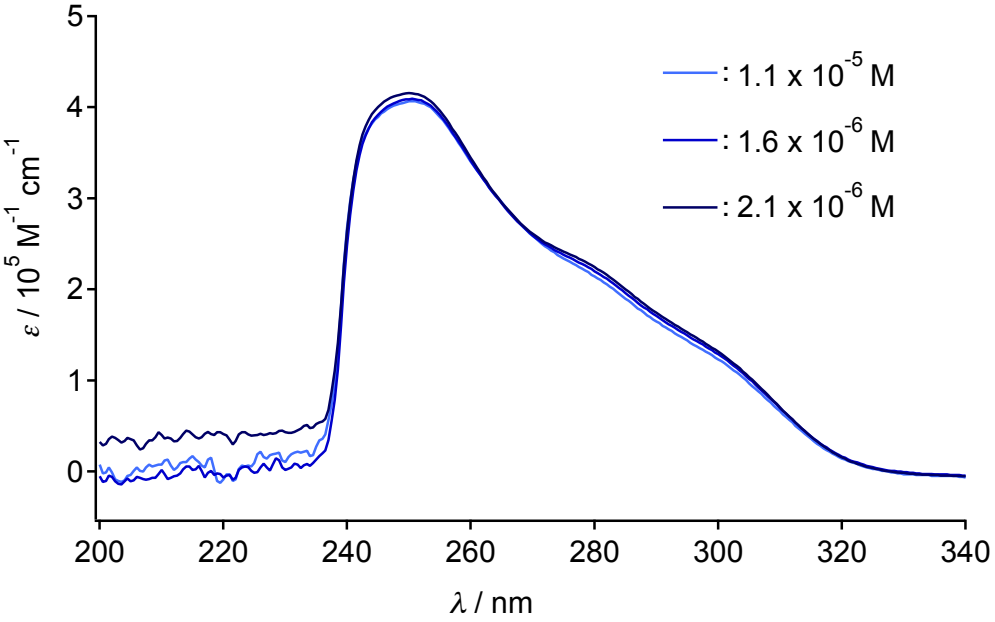

Figure S2. Concentration-dependent UV/vis absorption spectra of **3** in $CHCl_3$ at room temperature.

2.4.4. Changes of 3/*solvent* in Response to Mechanical Stimulation

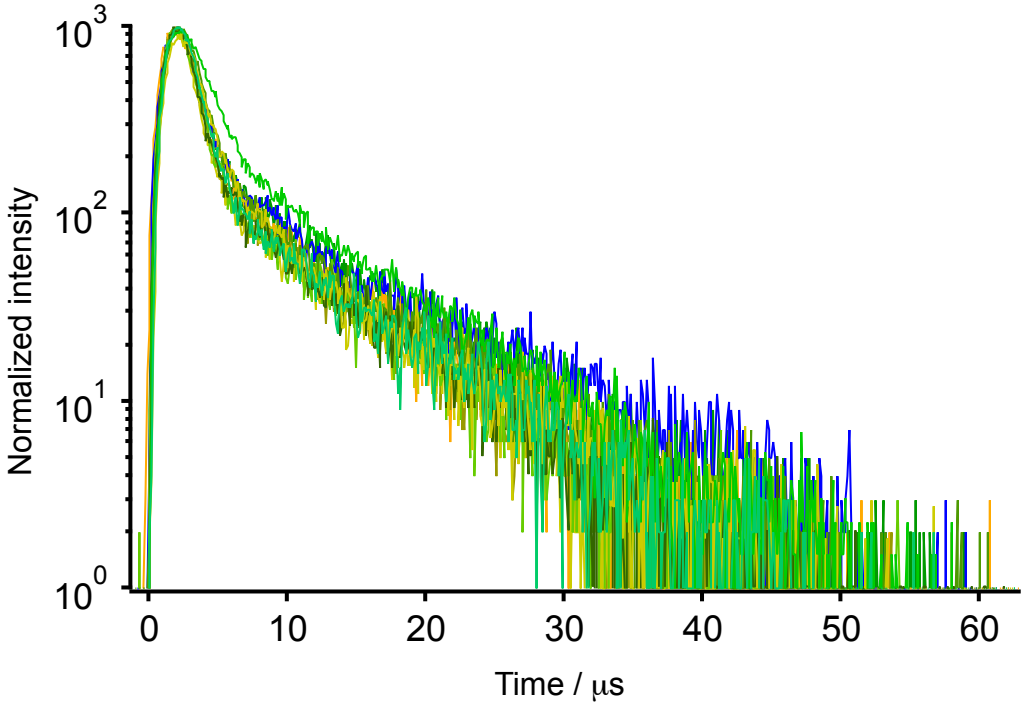

Figure S3. Emission decay profiles of **3**/$CHCl_3$, **3**/Py, **3**/CH_2Cl_2, **3**/CH_2Br_2, **3**/DMA, **3**/AcH, **3**/CH_3CN, **3**/DMF, **3**/*S*PO, **3**/*rac*PO, and **3**/acetone under excitation at 370 nm (monitored emission wavelength: 494, 530, 537, 544, 546, 552, 556, 560, 566, 574, and 580 nm, respectively).

Table S1. Photophysical properties of **3**/*solvent*.

	Φ_{em} / % (λ_{ex} / nm)	τ_{av} / μs[a,b] (λ_{em} / nm)	τ_1 / μs[a] (A / -)	τ_2 / μs[a] (A / -)
3/$CHCl_3$	2.90 (393)	6.90 (494)	1.29 (0.85)	10.71 (0.15)
3/Py	20.3 (439)	5.37 (530)	1.02 (0.85)	8.21 (0.15)
3/CH_2Cl_2	17.9 (437)	5.93 (537)	1.12 (0.82)	8.69 (0.18)
3/CH_2Br_2	7.10 (421)	5.38 (544)	1.12 (0.88)	9.08 (0.12)
3/DMA	25.6 (412)	5.86 (546)	1.72 (0.79)	8.91 (0.21)
3/AcH	13.1 (413)	5.49 (552)	1.29 (0.86)	9.21 (0.14)
3/CH_3CN	18.0 (394)	5.23 (556)	0.94 (0.80)	7.39 (0.20)
3/DMF	22.0 (371)	4.75 (560)	1.28 (0.84)	7.78 (0.16)
3/*S*PO	16.1 (394)	4.89 (566)	1.13 (0.87)	8.28 (0.13)
3/*rac*PO	18.5 (466)	5.31 (574)	1.12 (0.88)	9.14 (0.12)
3/acetone	10.1 (447)	4.73 (580)	1.10 (0.87)	7.97 (0.13)
$\mathbf{3}_{ground}$	12.6 (436)	4.88 (575)	1.46 (0.87)	8.75 (0.13)

[a]: λ_{ex} = 370 nm. [b]: $\tau_{av} = (\tau_1 A_1^2 + \tau_2 A_2^2) / (\tau_1 A_1 + \tau_2 A_2)$. All emission decay was fitted by tail fitting.

2.4.5. Solvents Response of $\mathbf{3}_{ground}$

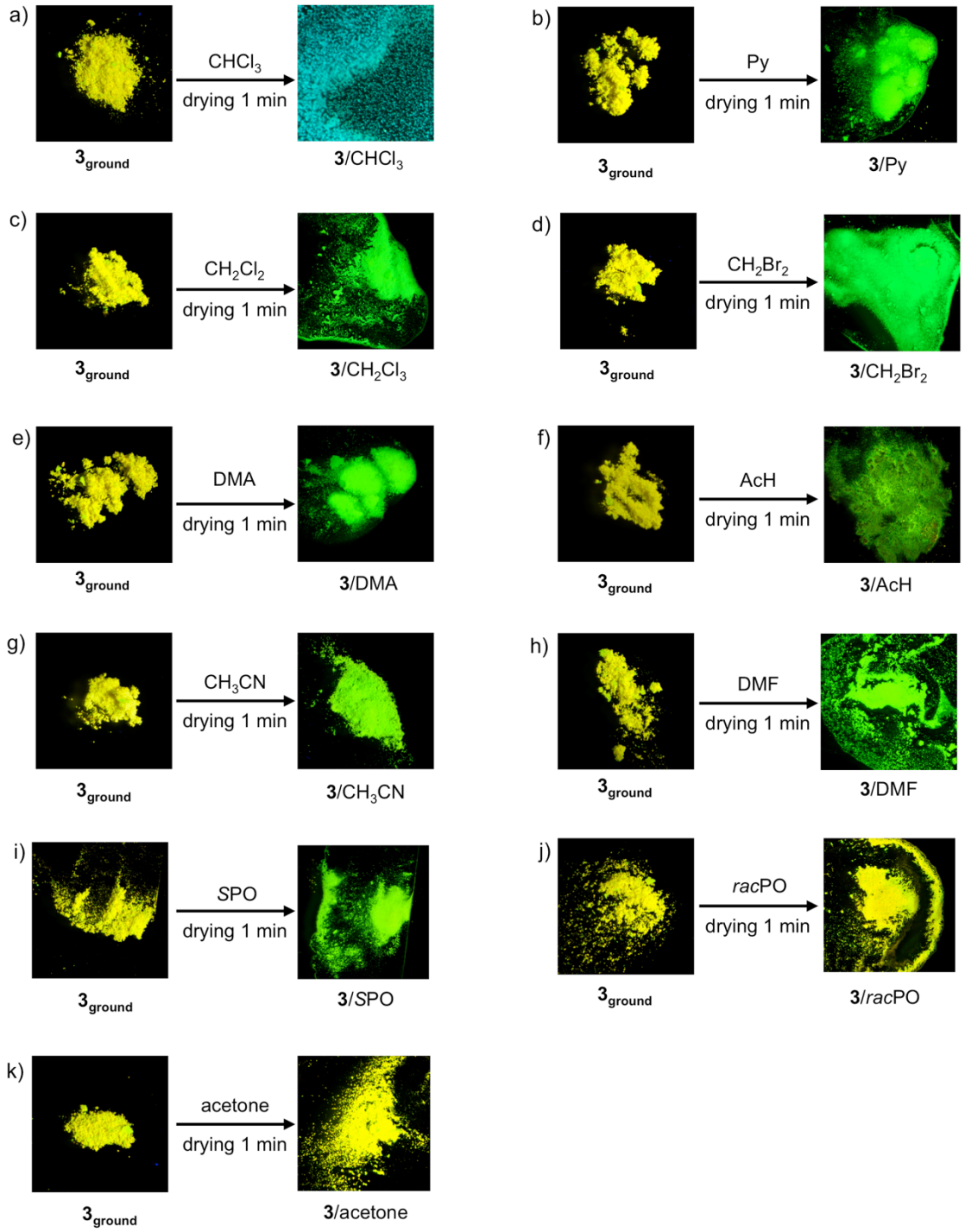

Figure S4. Photographs of emission color changes of $\mathbf{3}_{ground}$ (left-side panels) upon solvents addition to afford eleven **3**/*solvent* (right-side panels), in which **3**/*solvent* to a) **3**/$CHCl_3$, b) **3**/Py, c) **3**/CH_2Cl_2, d) **3**/CH_2Br_2, e) **3**/DMA, f) **3**/AcH, g) **3**/CH_3CN, h) **3**/DMF, i) **3**/*S*PO, j) **3**/*rac*PO, and k) **3**/acetone. All photographs are taken under UV light (λ_{ex} = 365 nm).

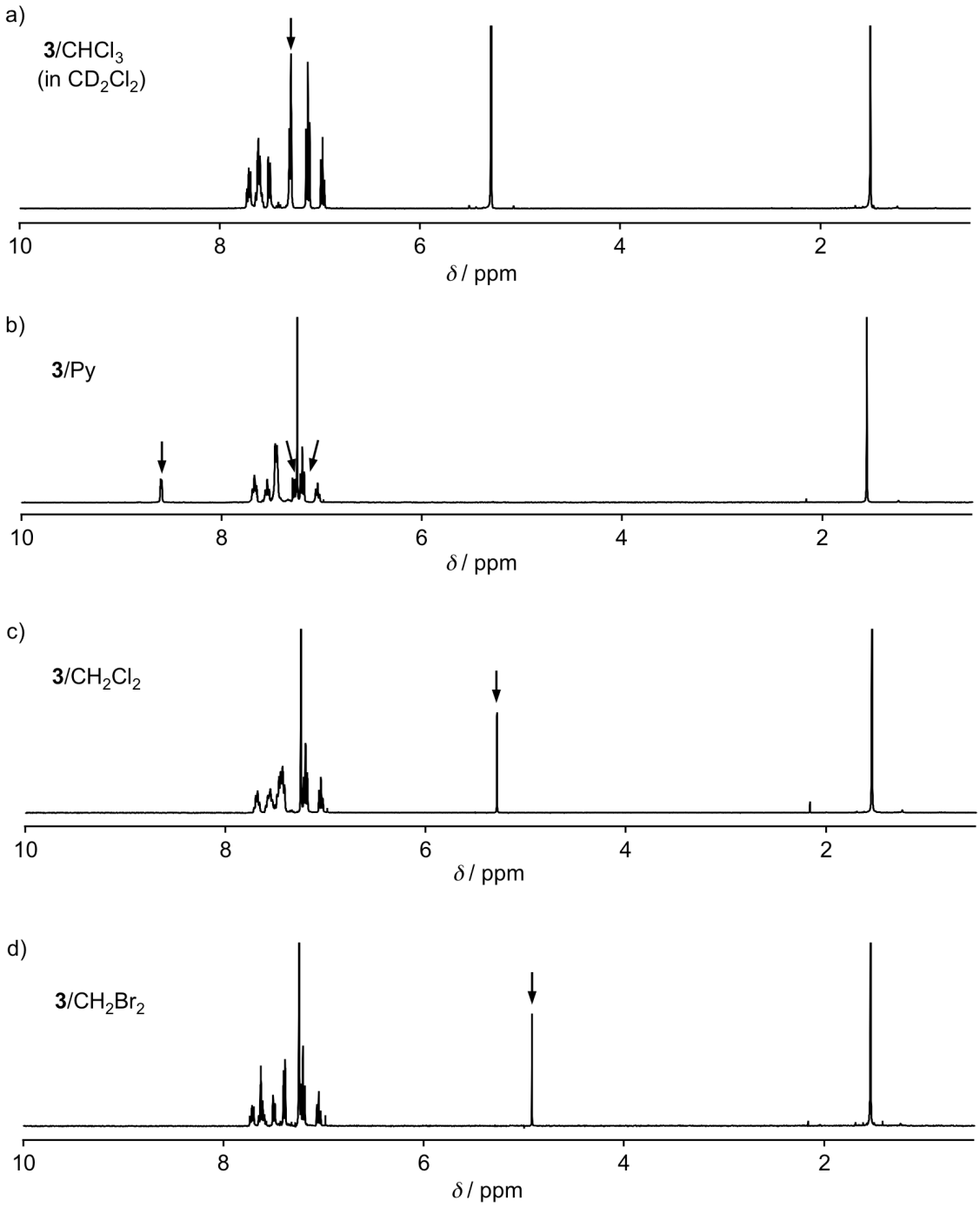
a)
3/CHCl3
(in CD2Cl2)
10
8
6
4
2
δ / ppm
b)
3/Py
10
8
6
4
2
δ / ppm
c)
3/CH2Cl2
10
8
6
4
2
δ / ppm
d)
3/CH2Br2
10
8
6
4
2
δ / ppm

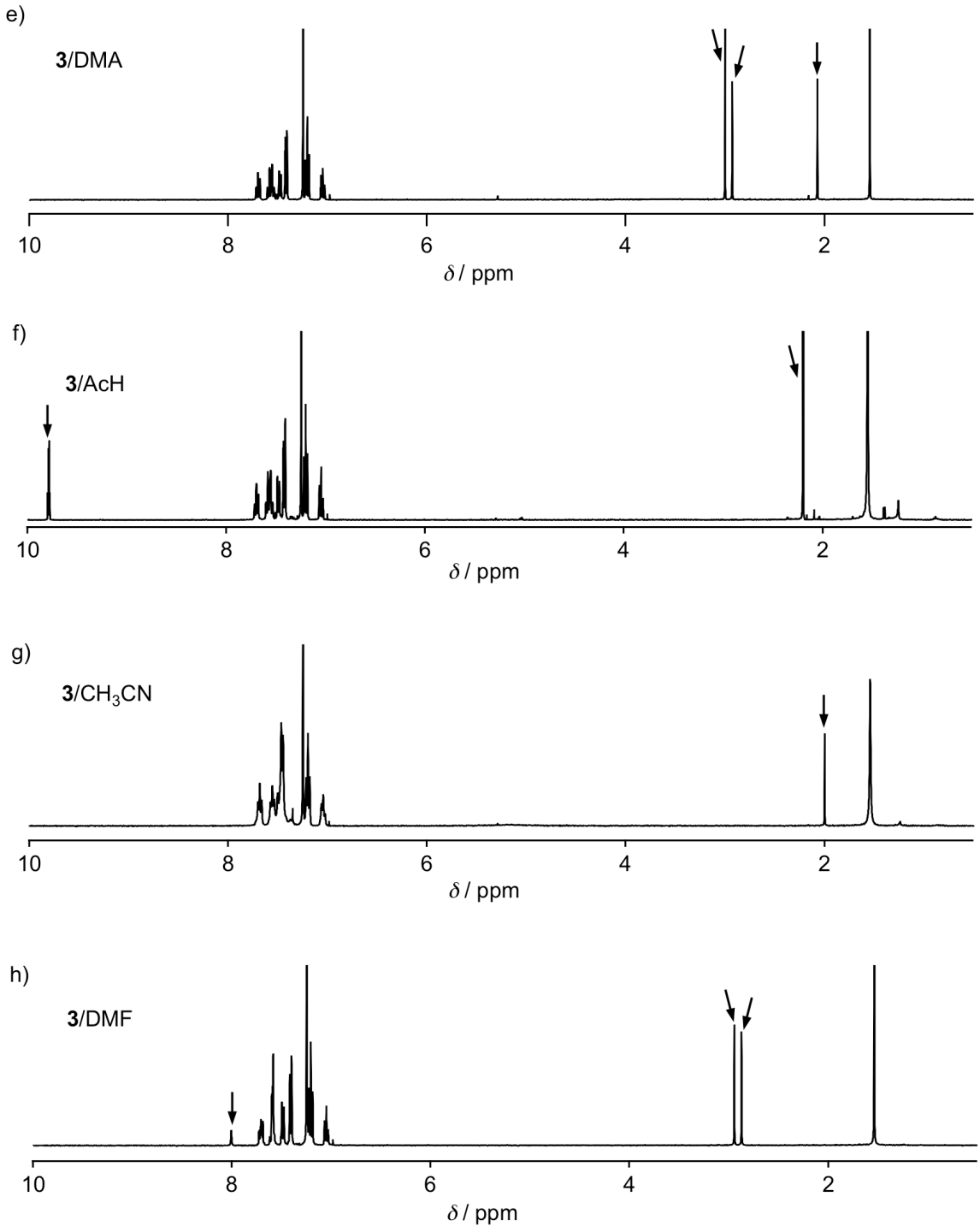
e)
3/DMA
10
8
6
4
2
δ / ppm
f)
3/AcH
10
8
6
4
2
δ / ppm
g)
3/CH3CN
10
8
6
4
2
δ / ppm
h)
3/DMF
10
8
6
4
2
δ / ppm

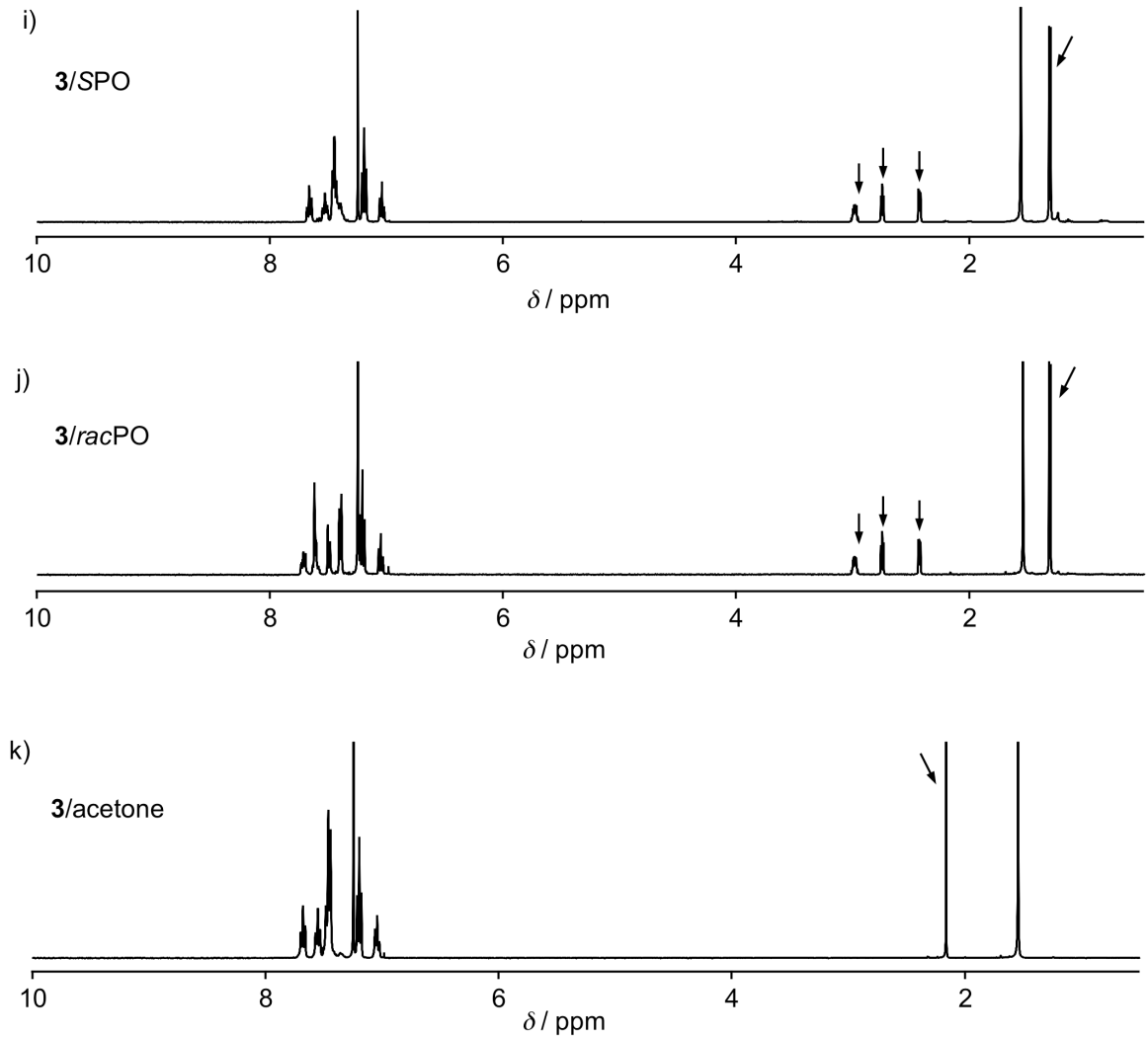

Figure S5. ^{1}H NMR spectra of a) **3**/$CHCl_3$ in CD_2Cl_2 and ten **3**/*solvent* in $CDCl_3$, in which b) **3**/Py, c) **3**/CH_2Cl_2, d) **3**/CH_2Br_2, e) **3**/DMA, f) **3**/AcH, g) **3**/CH_3CN, h) **3**/DMF, i) **3**/*S*PO, j) **3**/*rac*PO, and k) **3**/acetone are obtained by solvent addition to $\mathbf{3_{ground}}$. Arrows indicate that proton signals attributed to included solvent molecules.

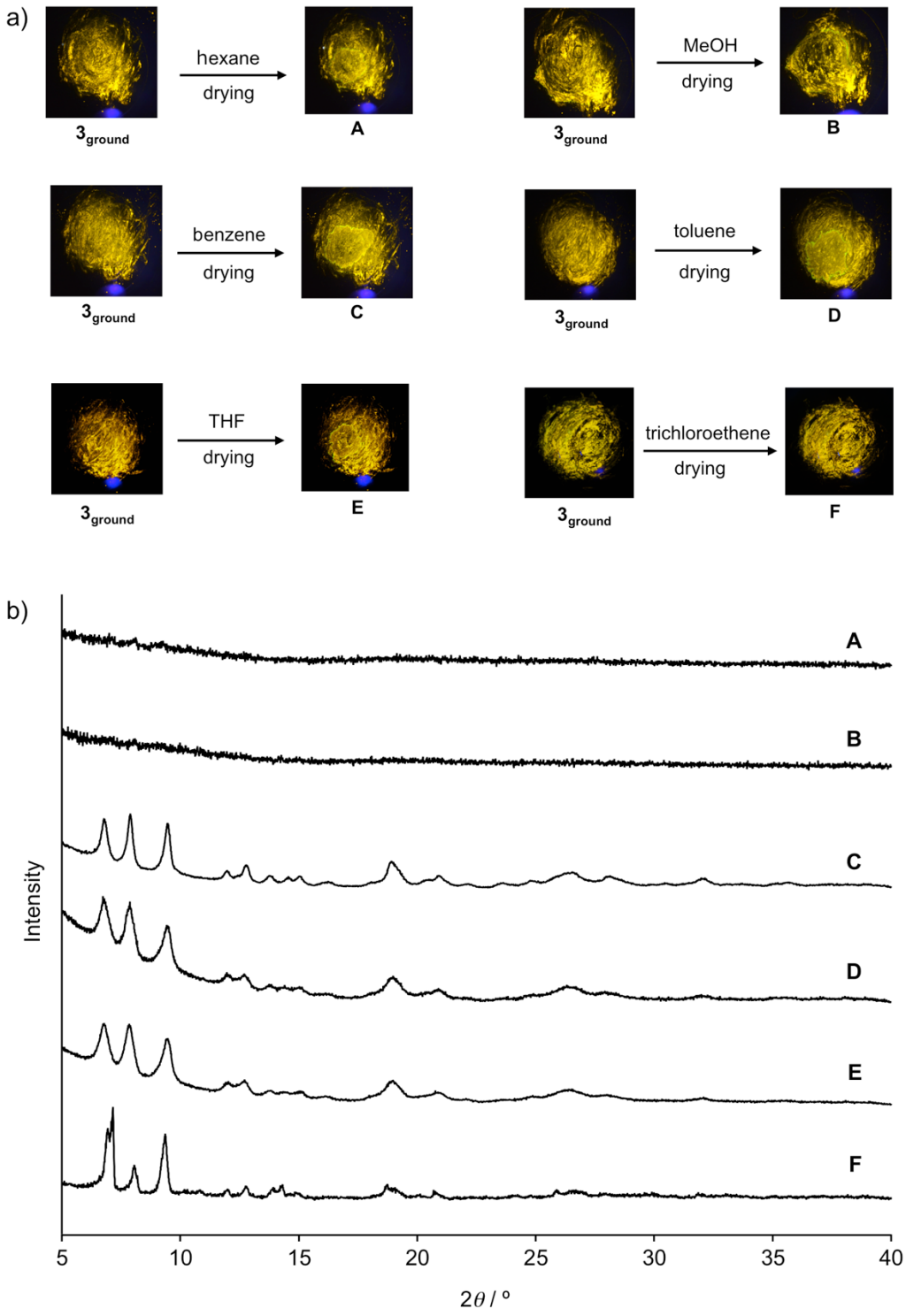

Figure S6. a) Photographs of $\mathbf{3_{ground}}$ obtained before and after the treatment of (**A**) hexane, (**B**) MeOH, (**C**) benzene, (**D**) toluene, (**E**) THF, and (**F**) trichloroethene taken under UV light (λ_{ex} = 365 nm). b) Powder XRD patterns of the powder samples obtained after treatment of $\mathbf{3_{ground}}$ with (**A**) hexane, (**B**) MeOH, (**C**) benzene, (**D**) toluene, (**E**) THF, and (**F**) trichloroethene.

2.4.6. Changes of 3/*solvent* in Response to Mechanical Stimulation

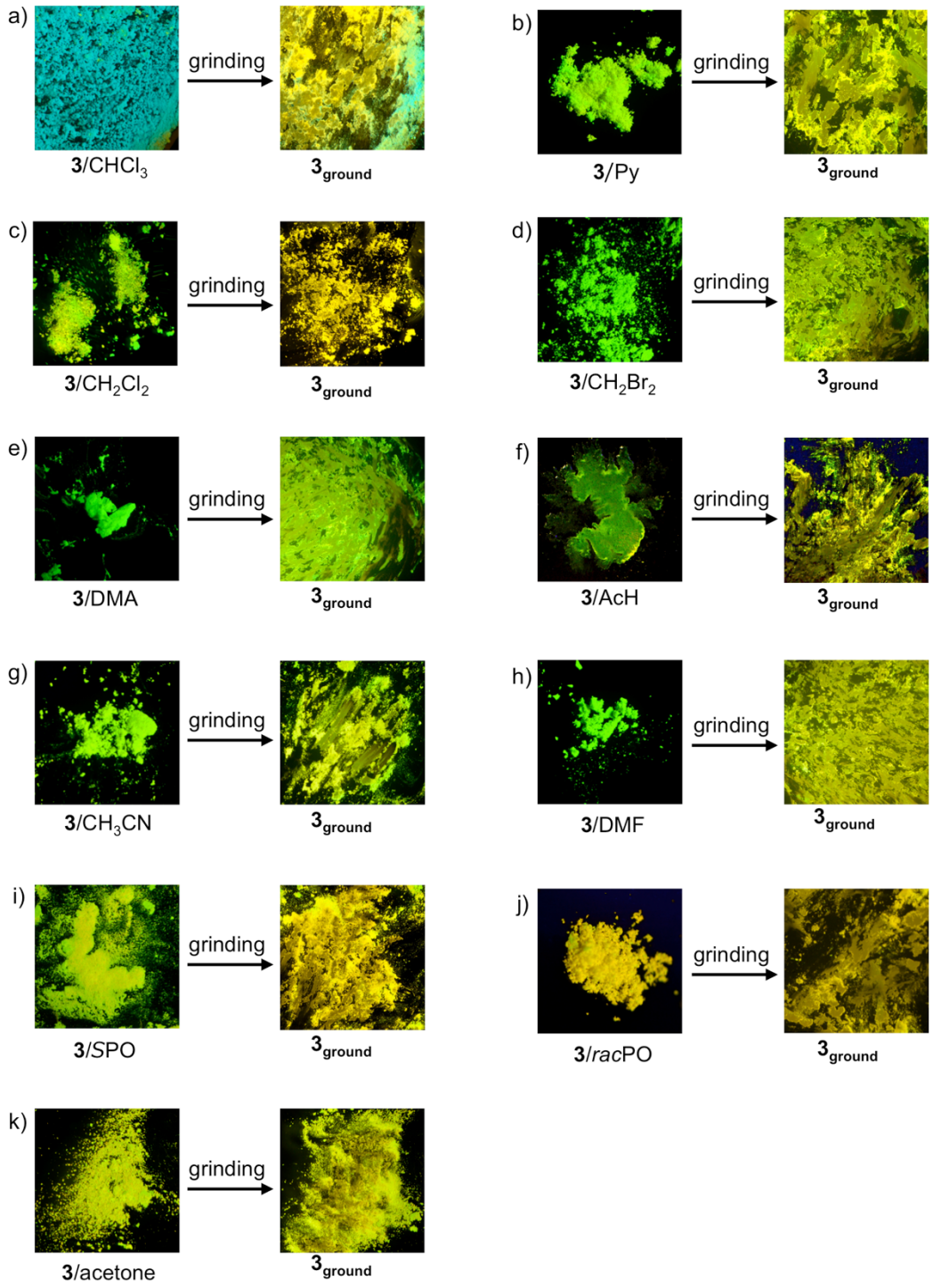

Figure S7. Photographs of eleven **3**/*solvent* (left-side panels) and their ground powder **3**$_{\mathbf{ground}}$ (left-side panels) taken under UV light (λ_{ex} = 365 nm), in which **3**/*solvent* corresponds to a) **3**/$CHCl_3$, b) **3**/Py, c) **3**/CH_2Cl_2, d) **3**/CH_2Br_2, e) **3**/DMA, f) **3**/AcH, g) **3**/CH_3CN, h) **3**/DMF, i) **3**/*S*PO, j) **3**/*rac*PO, and k) **3**/acetone. All **3**$_{\mathbf{ground}}$ are prepared by strong grinding of **3**/*solvent* using a pestle on glass substrates.

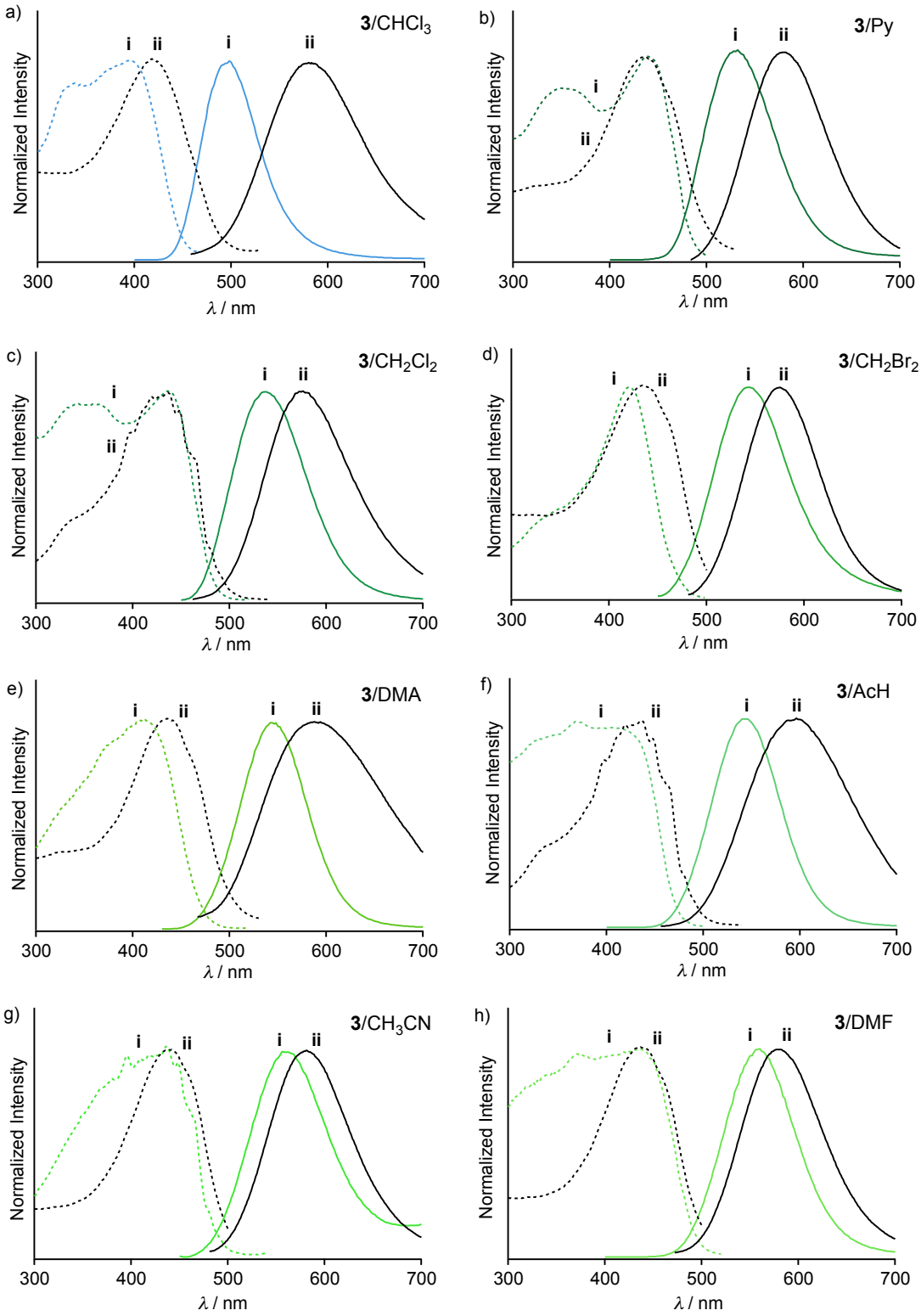
a)
3/CHCl3
b)
3/Py
c)
3/CH2Cl2
d)
3/CH2Br2
e)
3/DMA
f)
3/AcH
g)
3/CH3CN
h)
3/DMF
i
ii
Normalized Intensity
λ / nm
300
400
500
600
700

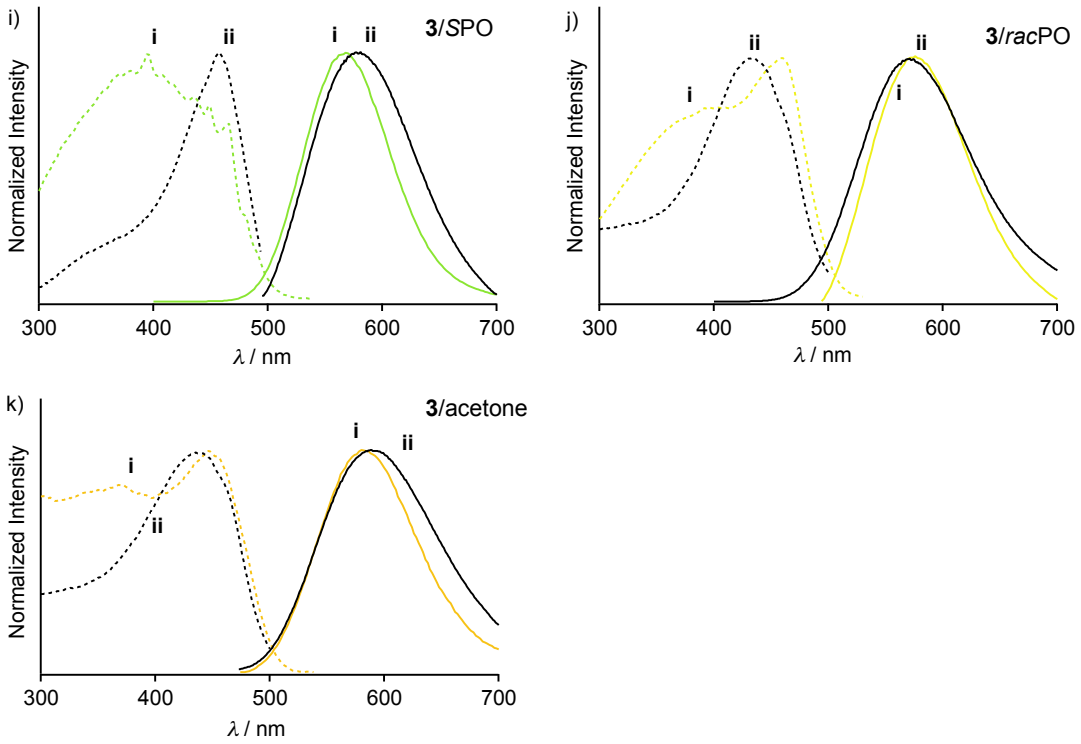

Figure S8. Excitation (dashed lines) and emission (solid lines) spectra of eleven **3**/*solvent* (denoted as "i") and their ground powder $\mathbf{3}_{\mathbf{ground}}$ (denoted as "ii"), in which **3**/*solvent* corresponds to a) **3**/$CHCl_3$, b) **3**/Py, c) **3**/CH_2Cl_2, d) **3**/CH_2Br_2, e) **3**/DMA, f) **3**/AcH, g) **3**/CH_3CN, h) **3**/DMF, i) **3**/*S*PO, j) **3**/*rac*PO, and k) **3**/acetone. The measurement conditions are summarized in Table S2.

Table S2. Summary of the measurement conditions for the excitation and emission spectra shown in Figure S8.

	3/*solvent*	Monitored emission wavelength of **3**/*solvent* / nm	Monitored emission wavelength of $\mathbf{3}_{\mathbf{ground}}$ / nm	Excitation wavelength of **3**/*solvent* / nm	Excitation wavelength of $\mathbf{3}_{\mathbf{ground}}$ / nm
Figure S8a	**3**/$CHCl_3$	494	580	393	418
Figure S8b	**3**/Py	530	579	439	435
Figure S8c	**3**/CH_2Cl_2	537	576	437	436
Figure S8d	**3**/CH_2Br_2	544	574	421	432
Figure S8e	**3**/DMA	546	584	412	437
Figure S8f	**3**/AcH	552	586	413	436
Figure S8g	**3**/CH_3CN	556	576	394	435
Figure S8h	**3**/DMF	560	579	371	433
Figure S8i	**3**/*S*PO	566	576	394	437
Figure S8j	**3**/*rac*PO	576	574	466	434
Figure S8k	**3**/acetone	580	589	447	435

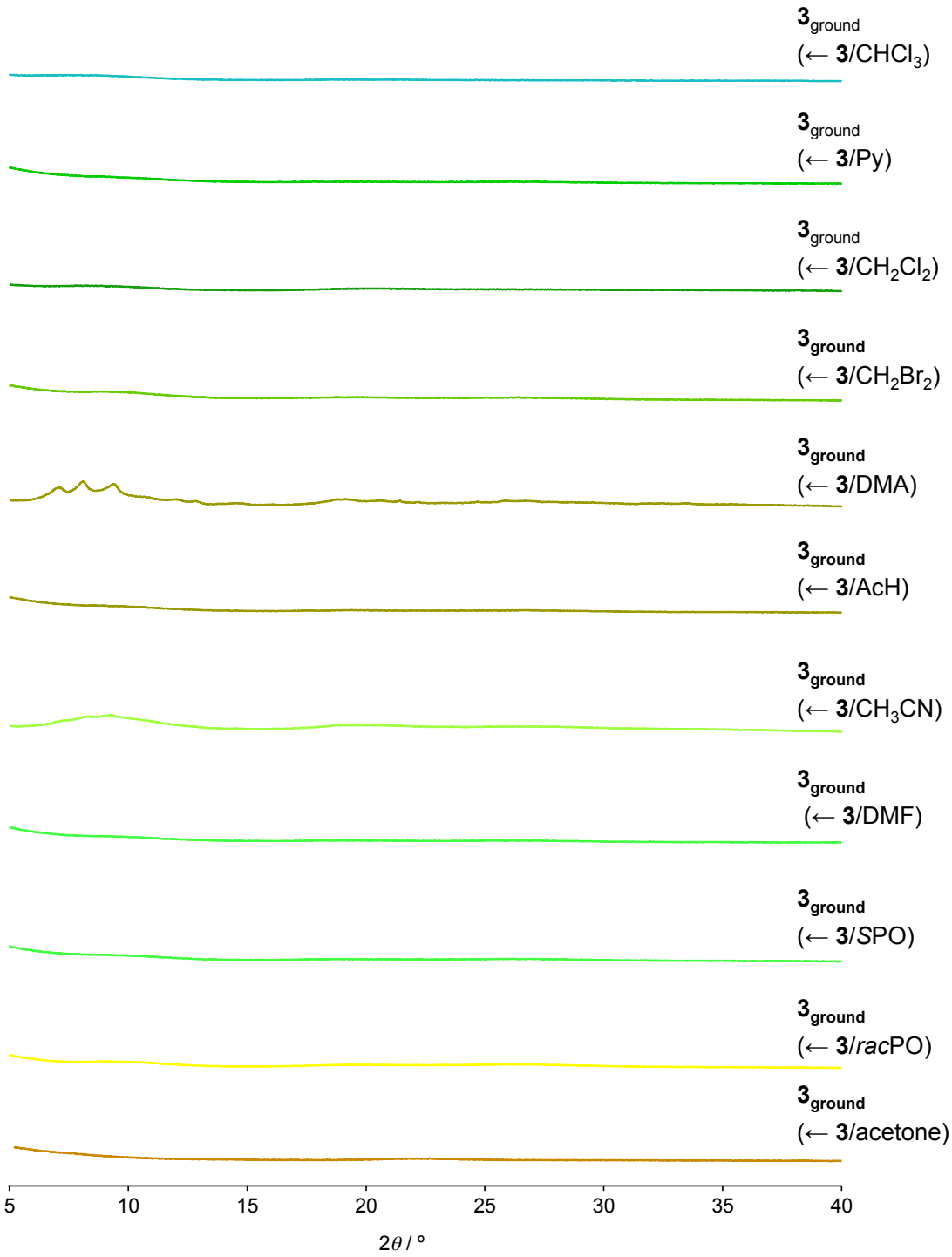

Figure S9. Powder XRD patterns of $\mathbf{3}_{\mathbf{ground}}$ obtained by grinding of **3**/$CHCl_3$, **3**/Py, **3**/CH_2Cl_2, **3**/CH_2Br_2, **3**/DMA, **3**/AcH, **3**/CH_3CN, **3**/DMF, **3**/*S*PO, **3**/*rac*PO, and **3**/acetone.

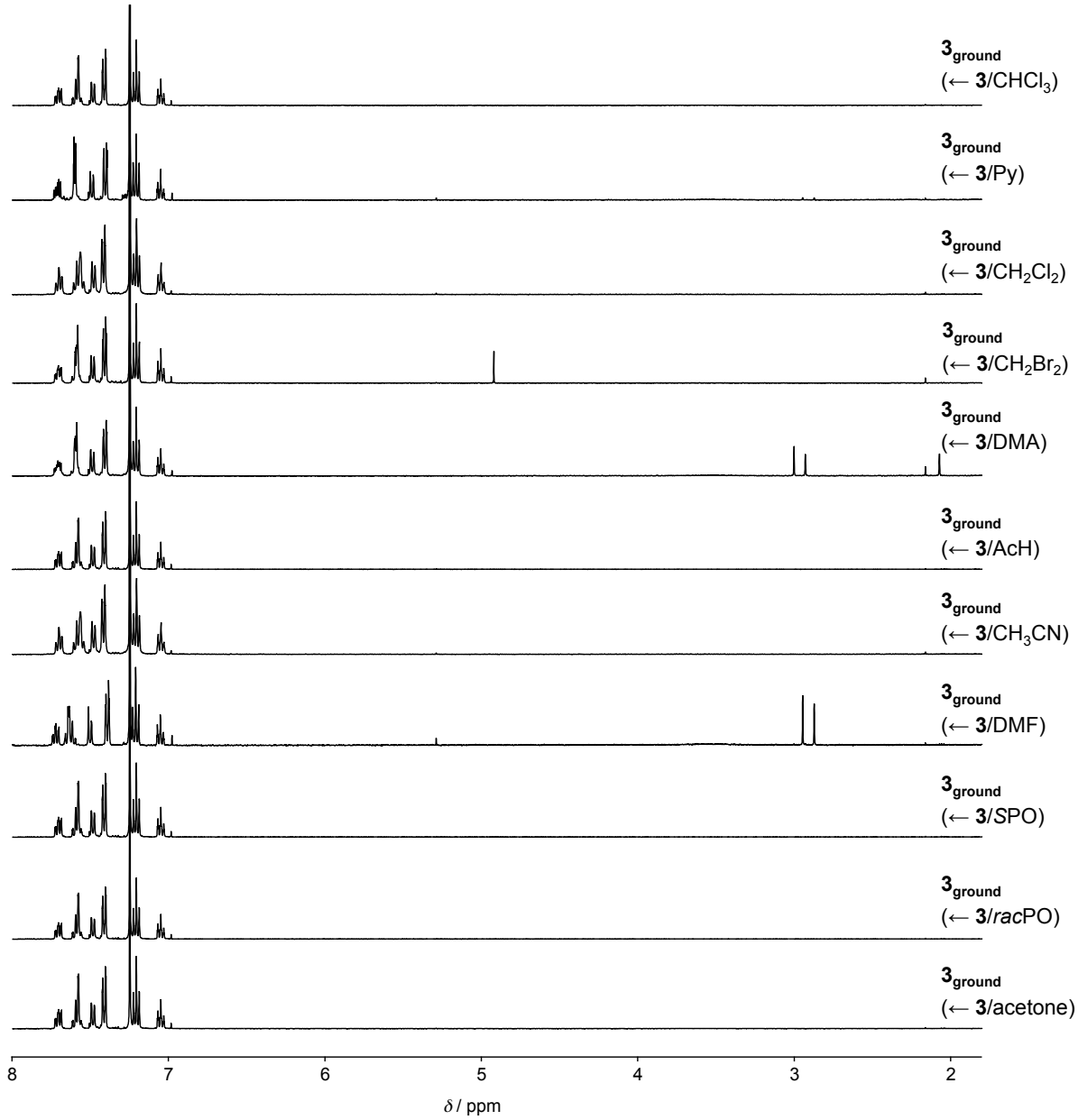

Figure S10 ^{1}H NMR spectra of eleven $\mathbf{3}_{\mathbf{ground}}$ obtained by grinding of **3**/$CHCl_3$, **3**/Py, **3**/CH_2Cl_2, **3**/CH_2Br_2, **3**/DMA, **3**/AcH, **3**/CH_3CN, **3**/DMF, **3**/*S*PO, **3**/*rac*PO, and **3**/acetone in $CDCl_3$.

Note: For $\mathbf{3}_{\mathbf{ground}}$ powders obtained from **3**/CH_2Br_2, **3**/DMA, and **3**/DMF by mechanical stimulation, the proton signals of residual solvents are observed in their ^{1}H NMR spectra. Considering high boiling point of these solvents, this result indicates that slight amount of released solvents from the crystal lattices remains around the $\mathbf{3}_{\mathbf{ground}}$ phases.

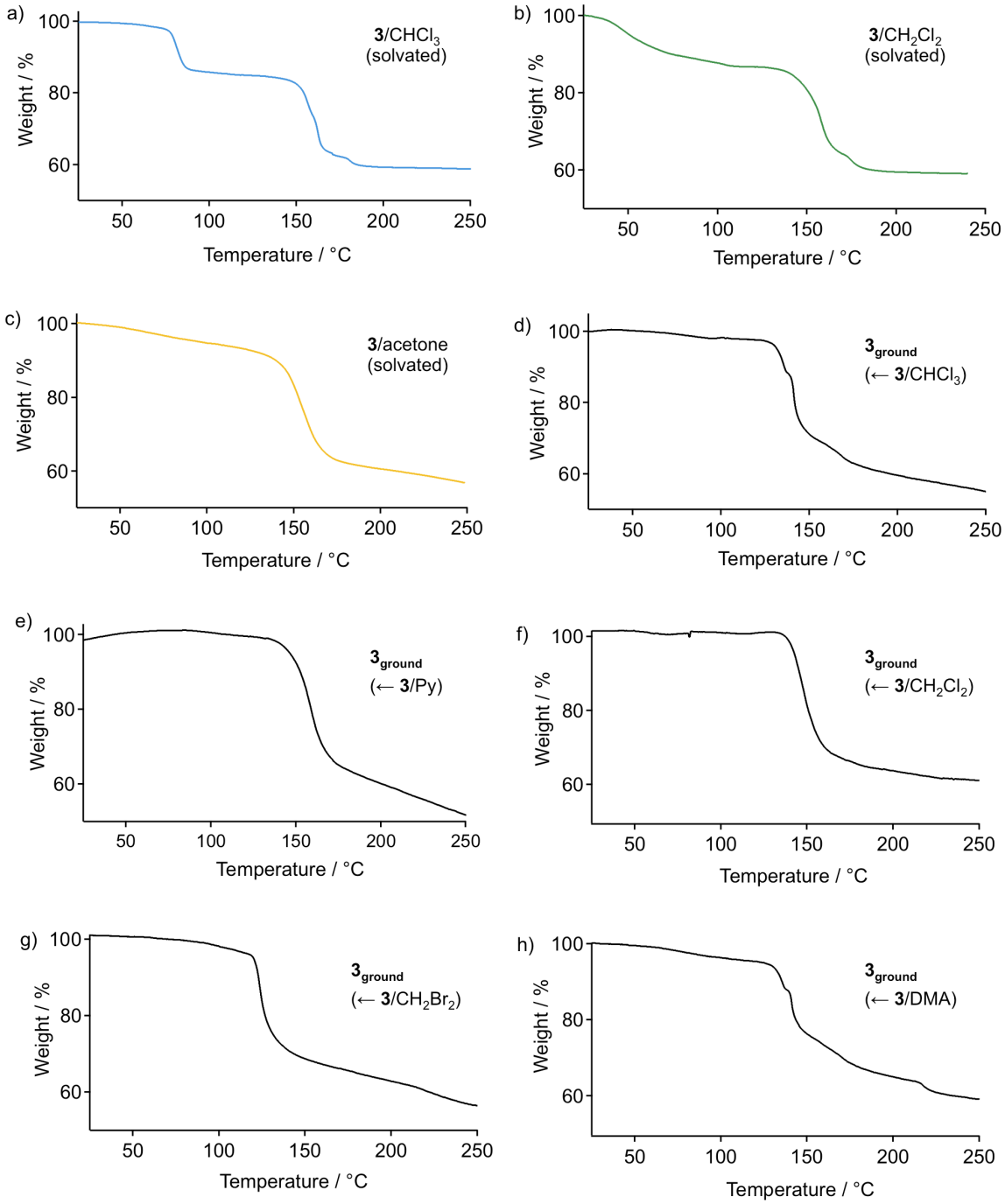
a)
100
80
60
Weight / %
3/CHCl3
(solvated)
50
100
150
200
250
Temperature / °C
b)
100
80
60
Weight / %
3/CH2Cl2
(solvated)
50
100
150
200
250
Temperature / °C
c)
100
80
60
Weight / %
3/acetone
(solvated)
50
100
150
200
250
Temperature / °C
d)
100
80
60
Weight / %
3ground
(← 3/CHCl3)
50
100
150
200
250
Temperature / °C
e)
100
80
60
Weight / %
3ground
(← 3/Py)
50
100
150
200
250
Temperature / °C
f)
100
80
60
Weight / %
3ground
(← 3/CH2Cl2)
50
100
150
200
250
Temperature / °C
g)
100
80
60
Weight / %
3ground
(← 3/CH2Br2)
50
100
150
200
250
Temperature / °C
h)
100
80
60
Weight / %
3ground
(← 3/DMA)
50
100
150
200
250
Temperature / °C

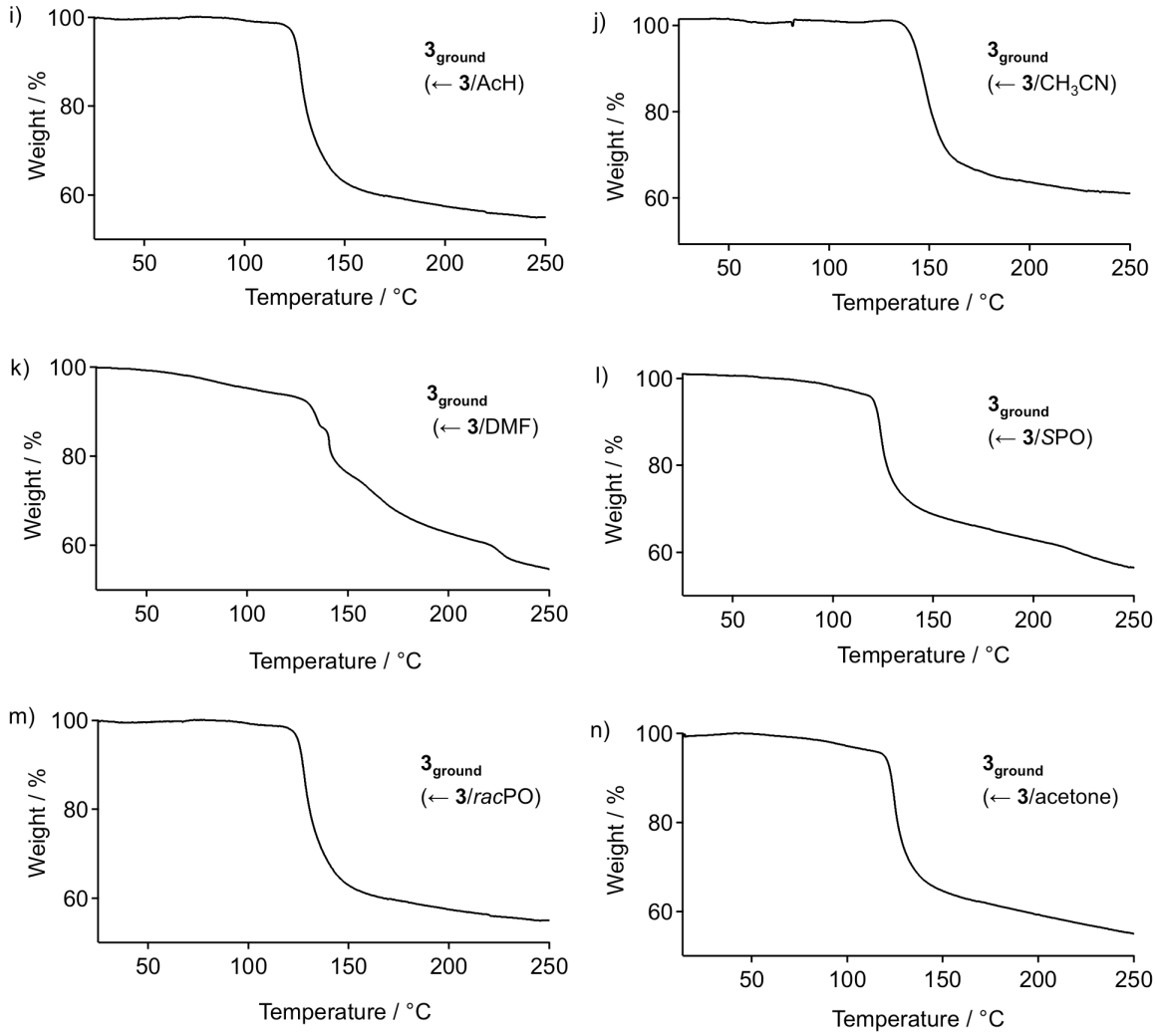

Figure S11. TGA profiles of powder samples of a) **3**/$CHCl_3$, b) **3**/CH_2Cl_2, c) **3**/acetone (***solvated forms***) and $\mathbf{3}_{ground}$ (***solvent-free forms***) which are obtained from eleven **3**/*solvent* by mechanical stimulation, in which **3**/*solvent* corresponds to $\mathbf{3}_{ground}$ obtained from d) **3**/$CHCl_3$, e) **3**/Py, f) **3**/CH_2Cl_2, g) **3**/CH_2Br_2, h) **3**/DMA, i) **3**/AcH, j) **3**/CH_3CN, k) **3**/DMF, l) **3**/*S*PO, m) **3**/*rac*PO, and n) **3**/acetone. A heating rate is 2 °C/min.

2.4.7. Changes of 3/*solvent* upon Heating under Reduced Pressure

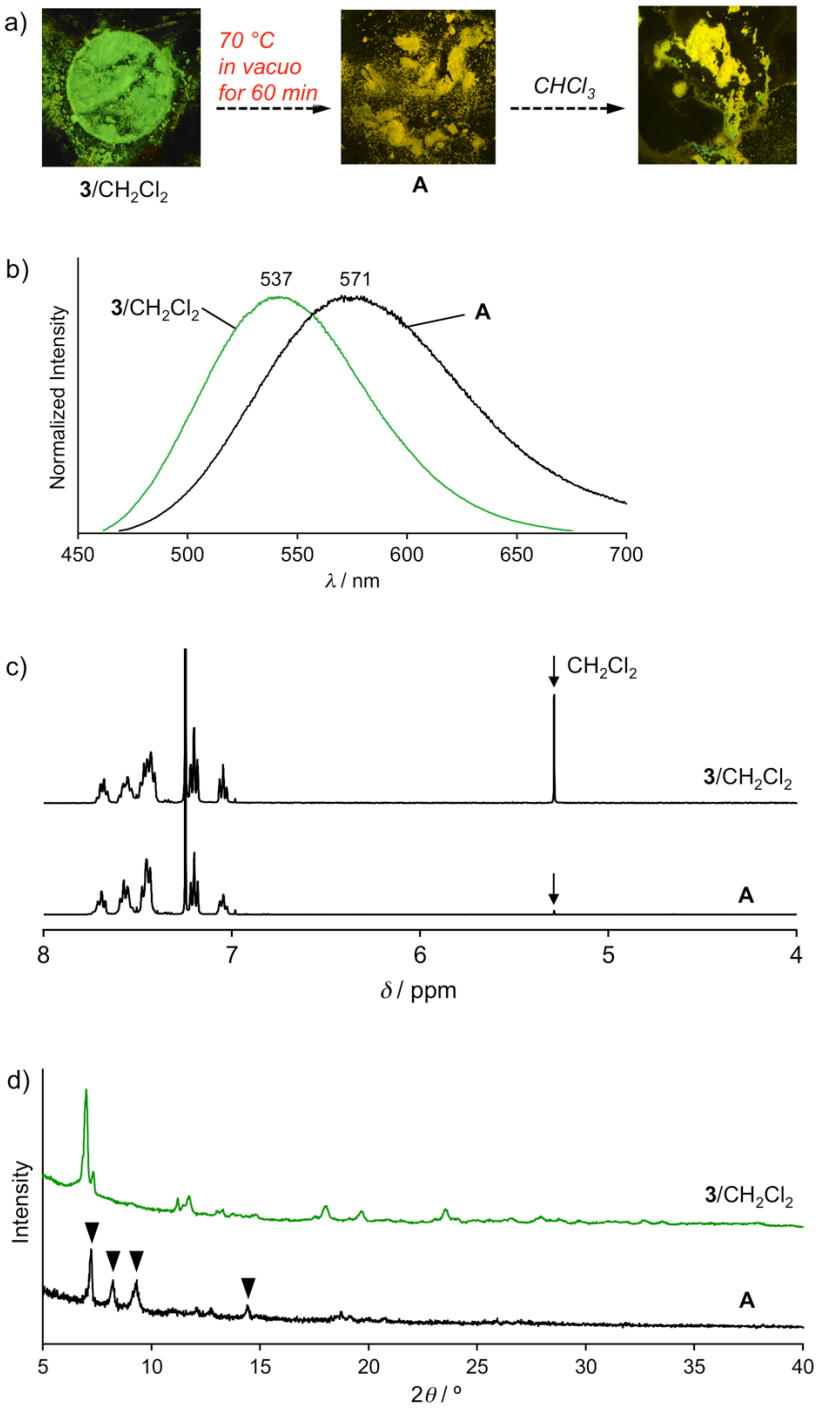

Figure S12. a) Photographs of **3**/CH_2Cl_2 before and after heating under reduced pressure taken under UV light, in which the resulting powder is denoted as **A**. The addition of $CHCl_3$ to **A** does not change emission color. b) Emission spectra (λ_{ex} = 365 nm), c) ^{1}H NMR spectra, and d) Powder XRD patterns of **3**/CH_2Cl_2 and **A**. Arrows in c) denoted as the proton signals of residual CH_2Cl_2 (boiling point is 40 °C). The peaks with low intensity denoted as triangles in d) indicate the partial crystallization.

2.4.8. Data for Single-Crystal X-Ray Structural Analyses

Single-crystal X-ray structural analyses were carried out on a Rigaku R-AXIS RAPID diffractometer using graphite monochromated Mo-K_α radiation. The structure was solved by direct methods and expanded using Fourier techniques. Non-hydrogen atoms were refined anisotropically. Hydrogen atoms were refined using the riding model. All calculations were performed using the CrystalStructure crystallographic software package except for refinement, which was performed using SHELXL-2013.[34]

Table S3 Summary of X-ray crystallographic data of **3**/*solvent*.

compound	**3**/$CHCl_3$	**3**/Py	**3**/CH_2Cl_2	**3**/CH_2Br_2
CCDC Number	1486479	1486482	1486477	1486476
Empirical Formula	$C_{27}H_{19}Au_2Cl_3N_2$	$C_{28.5}H_{20.5}Au_2N_{2.5}$	$C_{27}H_{20}Au_2Cl_2N_2$	$C_{27}H_{20}Au_2Br_2N_2$
Formula Weight	871.75	791.93	837.31	926.21
Crystal System	orthorhombic	monoclinic	monoclinic	monoclinic
Crystal Size / mm	0.577×0.079×0.037	0.098×0.074×0.070	0.103×0.097×0.078	0.194×0.123×0.086
a / Å	15.6589(7)	14.0428(11)	14.3824(8)	14.3746(13)
b / Å	21.6542(10)	22.6970(14)	22.3603(9)	22.3016(17)
c / Å	15.3795(6)	15.0676(12)	15.4312(7)	15.6172(16)
α / °	90	90	90	90
β / °	90	95.697(6)	94.258(3)	94.317(8)
γ / °	90	90	90	90
V / Å^3	5214.9(4)	4778.8(6)	4948.9(4)	4992.3(8)
Space Group	*Pbcn* (#60)	*I*2/*a* (#15)	*I*2/*a* (#15)	*I*2/*a* (#15)
Z value	8	8	8	8
D_{calc} / g cm^{-3}	2.221	2.201	2.242	2.464
Temperature / K	123	123	123	123
$2\theta_{max}$ / °	55.0	55.0	55.0	55.0
μ(Mo K_α) / cm^{-1}	116.053	123.291	121.191	149.720
No. of Reflections	Total: 77894 Unique: 5972 R_{int} = 0.0966	Total: 22305 Unique: 5479 R_{int} = 0.1726	Total: 23287 Unique: 5627 R_{int} = 0.1025	Total: 24242 Unique: 5721 R_{int} = 0.1839
R_1[a]	0.0362	0.0734	0.0518	0.0870
wR_2[b]	0.0972	0.2274	0.1345	0.1740
GOF[c]	1.011	1.051	1.083	0.994
Max./Mini. peak *I*[d] / Å^3	1.79 e$^-$/−1.36 e$^-$	2.36 e$^-$/−3.07 e$^-$	2.85 e$^-$/−3.67 e$^-$	3.95 e$^-$/−4.51 e$^-$

[a]:$I > 2.00\sigma(I)$. [b]:All reflections. [c]:Goodness of Fit Indicator. [d]: in Final Diff. Map.

compound	**3**/DMA	**3**/AcH	**3**/CH_3CN	**3**/DMF
CCDC Number	1486480	1486474	1486478	1486481
Empirical Formula	$C_{28}H_{22.5}Au_2N_{2.5}O_{0.5}$	$C_{27}H_{20}Au_2N_2O_{0.5}$	$C_{28}H_{21}Au_2N_3$	$C_{27.5}H_{21.5}Au_2N_{2.5}O_{0.5}$
Formula Weight	795.94	774.40	793.43	788.92
Crystal System	0.110×0.109×0.091	0.155×0.134×0.124	0.151×0.116×0.099	0.107×0.097×0.094
Crystal Size / mm	monoclinic	monoclinic	monoclinic	monoclinic
a / Å	14.126(2)	14.049(2)	14.5267(12)	13.946(3)
b / Å	22.8906(11)	23.107(3)	22.4381(19)	22.946(4)
c / Å	14.8860(6)	14.788(2)	14.9342(16)	14.767(3)
α / °	90	90	90	90
β / °	95.518(9)	95.085(4)	97.384(4)	94.872(9)
γ / °	90	90	90	90
V / Å^3	4791.0(9)	4781.6(12)	4827.5(8)	4708.6(16)
Space Group	*I*2/*a* (#15)	*I*2/*a* (#15)	*I*2/*a* (#15)	*I*2/*a* (#15)
Z value	8	4	8	8
D_{calc} / g cm^{-3}	2.207	2.192	2.183	2.226
Temperature / K	123	123	123	123
$2\theta_{max}$ / °	55.0	51.0	54.9	51.0
μ(Mo K$_\alpha$) / cm^{-1}	123.038	123.199	122.055	125.137
No. of Reflections	Total: 18503 Unique: 4359 R_{int} = 0.0767	Total: 9549 Unique: 2279 R_{int} = 0.0779	Total: 21404 Unique: 5502 R_{int} = 0.0905	Total: 16988 Unique: 4370 R_{int} = 0.1690
R_1[a]	0.0395	0.0427	0.0546	0.0798
wR_2[b]	0.0672	0.0625	0.1172	0.2505
GOF[c]	1.011	1.069	1.063	1.081
Max./Mini. peak *I*[d] / Å^3	1.32 e$^-$/−1.10 e$^-$	1.25 e$^-$/−1.07 e$^-$	2.36 e$^-$/−2.24 e$^-$	3.02 e$^-$/−2.90 e$^-$

[a]:$I > 2.00\sigma(I)$. [b]:All reflections. [c]:Goodness of Fit Indicator. [d]: in Final Diff. Map.

compound	**3**/*S*PO	**3**/*rac*PO	**3**/acetone	**3**/*none*
CCDC Number	1486484	1486483	1486475	1486485
Empirical Formula	$C_{29}H_{24}Au_2N_2O$	$C_{26.75}H_{19.5}Au_2N_2O_{0.25}$	$C_{26.75}H_{19.5}Au_2N_2O_{0.25}$	$C_{26}H_{18}Au_2N_2$
Formula Weight	810.45	766.89	766.89	752.27
Crystal System	triclinic	monoclinic	monoclinic	monoclinic
Crystal Size / mm	0.466×0.226×0.211	0.162×0.137×0.123	0.565×0.072×0.054	0.141×0.071×0.058
a / Å	13.9136(9)	14.2069(14)	13.6877(11)	14.0825(19)
b / Å	14.8769(9)	22.8755(17)	26.0965(17)	13.9789(14)
c / Å	15.0369(9)	14.8349(11)	26.9019(19)	21.934(2)
α / °	78.416(3)	90	90	90
β / °	65.9278(14)	95.445(4)	90.5498(19)	92.577(6)
γ / °	63.373(5)	90	90	90
V / Å^3	2539.8(3)	4799.4(7)	9608.9(12)	4313.5(9)
Space Group	*P*1 (#1)	*I*2/*a* (#15)	$P2_1/n$ (#14)	*I*2/*a* (#15)
Z value	4	2	2	8
D_{calc} / g cm^{-3}	2.119	2.123	2.140	2.317
Temperature / K	123	123	123	123
$2\theta_{max}$ / °	52.0	51.0	55.0	50.1
μ(Mo K$_\alpha$) / cm^{-1}	116.037	122.723	122.567	136.516
No. of Reflections	Total: 21049 Unique: 15961 R_{int} = 0.0830	Total: 17826 Unique: 4377 R_{int} = 0.1430	Total: 87827 Unique: 21691 R_{int} = 0.2838	Total: 16641 Unique: 3817 R_{int} = 0.2236
R_1[a]	0.0850	0.0860	0.0934	0.0925
wR_2[b]	0.2511	0.2474	0.2736	0.2856
GOF[c]	1.124	1.045	0.903	1.017
Max./Mini. peak I[d] / Å^3	6.69 e$^-$/−4.66 e$^-$	3.89 e$^-$/−2.53 e$^-$	1.94 e$^-$/−2.13 e$^-$	2.20 e$^-$/−1.78 e$^-$

[a]:$I > 2.00\sigma(I)$. [b]:All reflections. [c]:Goodness of Fit Indicator. [d]: in Final Diff. Map.

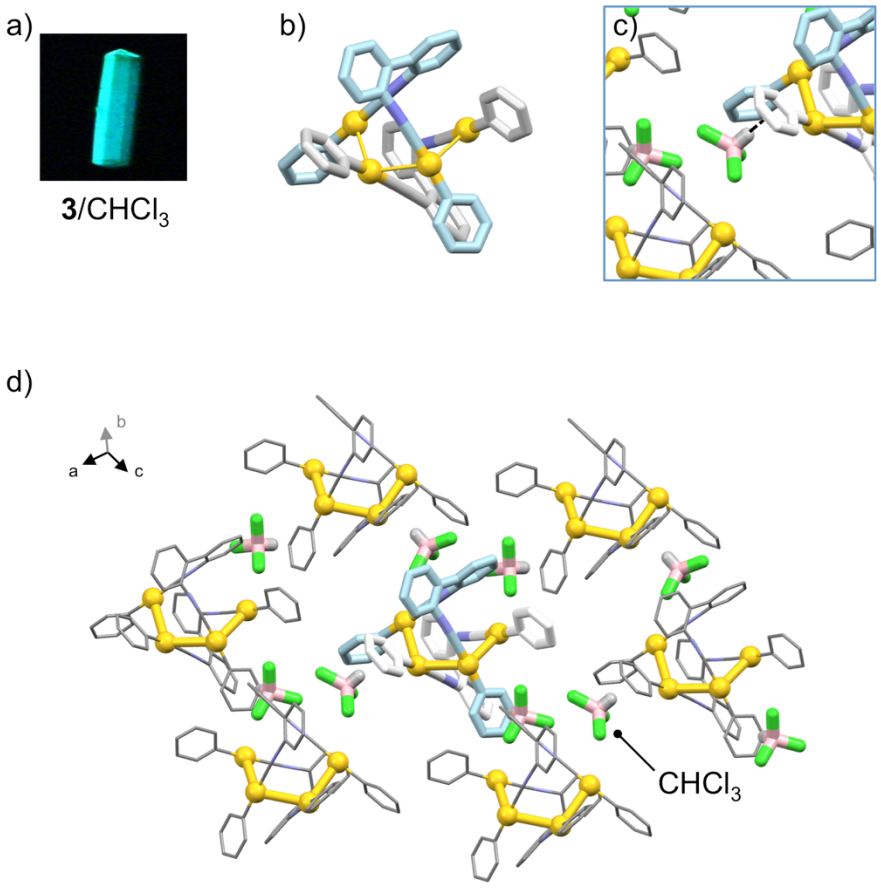

Figure S13. a) Photograph of the single crystal of **3**/$CHCl_3$ taken under UV light. b–d) Single-crystal structures of **3**/$CHCl_3$. All the H atoms are omitted for clarity.

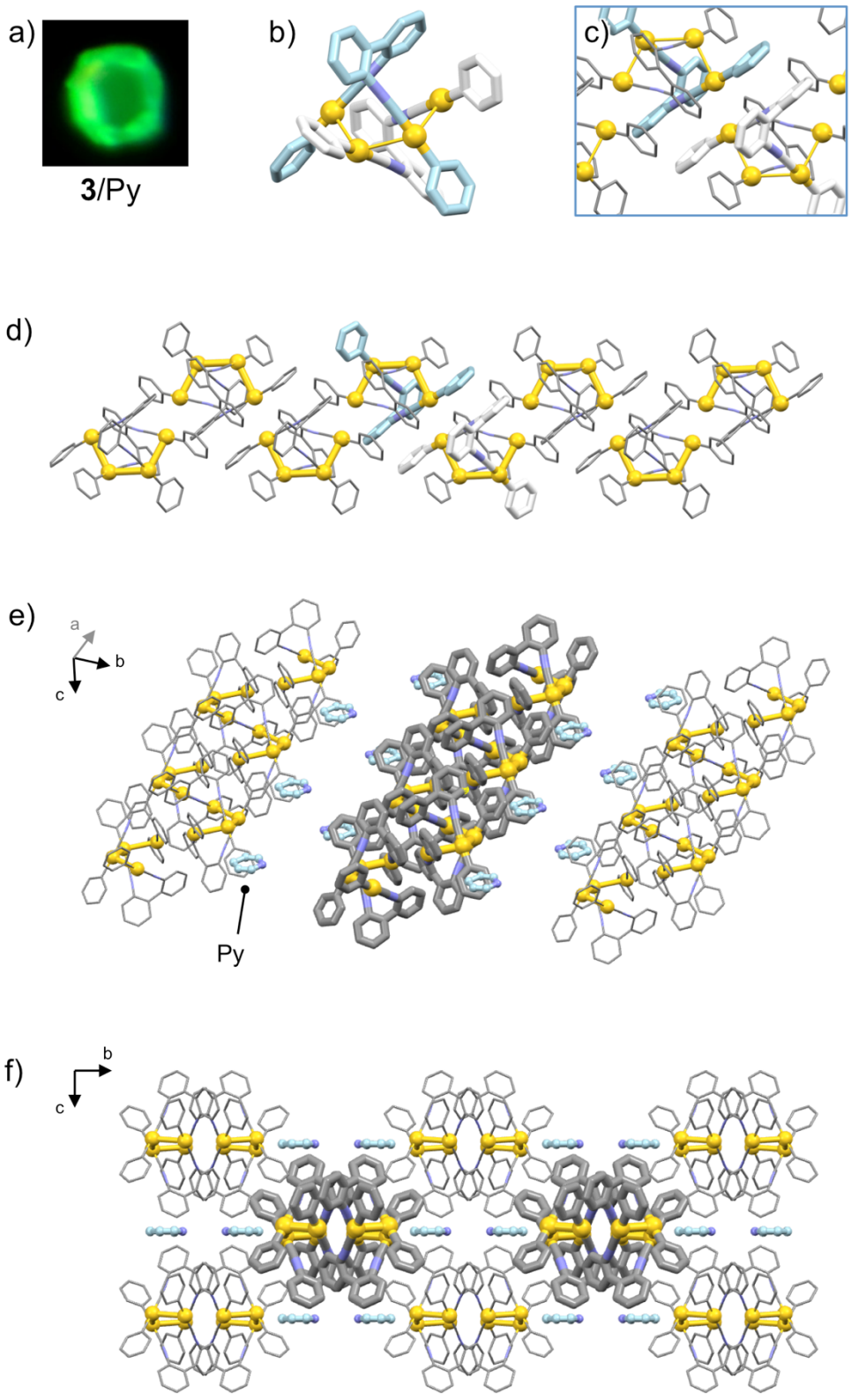

Figure S14. a) Photograph of the single crystal of **3**/Py taken under UV light. b–f) Single-crystal structures of **3**/Py. All the H atoms are omitted for clarity.

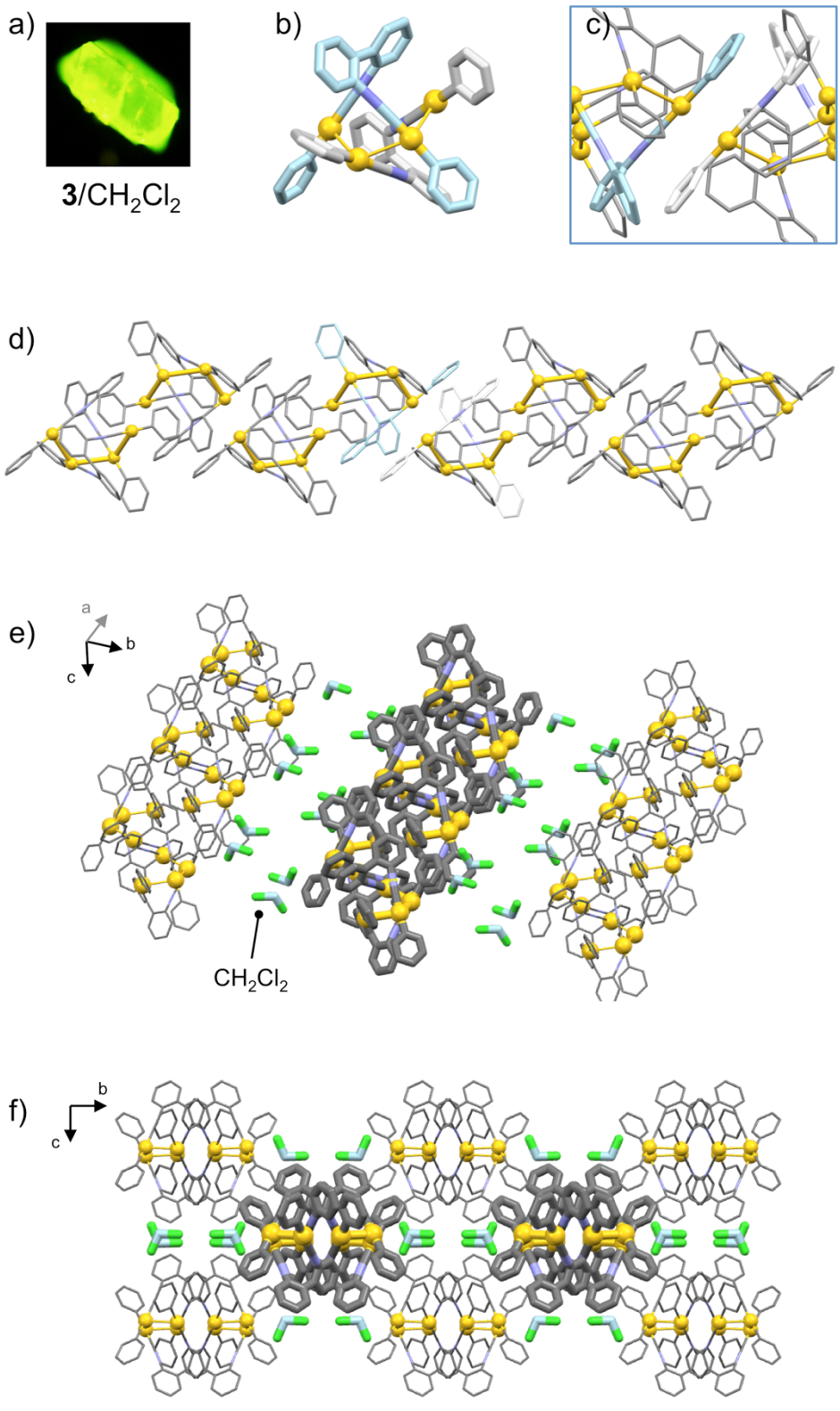

Figure S15. a) Photograph of the single crystal of **3**/CH_2Cl_2 taken under UV light. b–f) Single-crystal structures of **3**/CH_2Cl_2. All the H atoms are omitted for clarity.

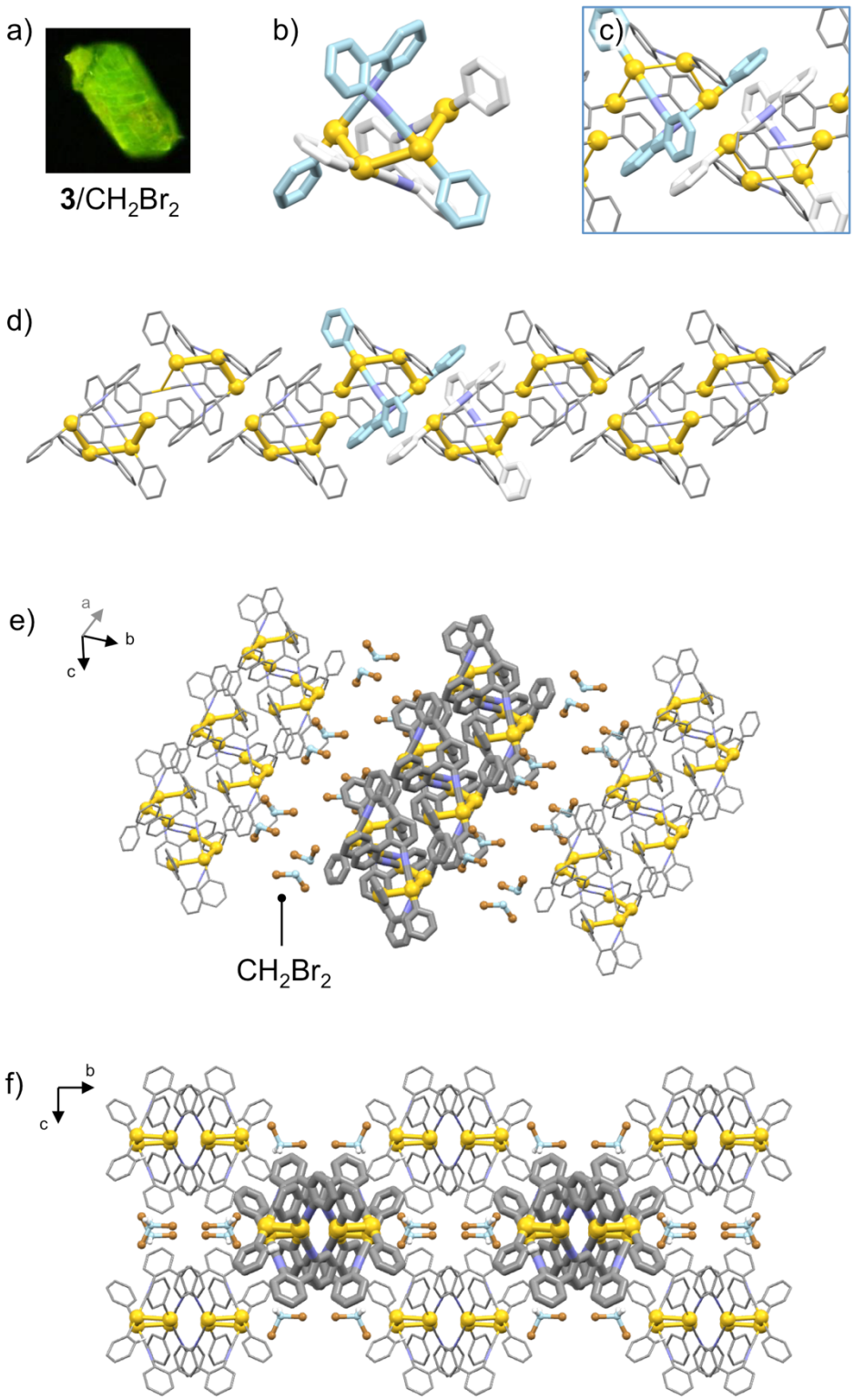

Figure S16. a) Photograph of the single crystal of **3**/CH_2Br_2 taken under UV light. b–f) Single-crystal structures of **3**/CH_2Br_2. All the H atoms are omitted for clarity.

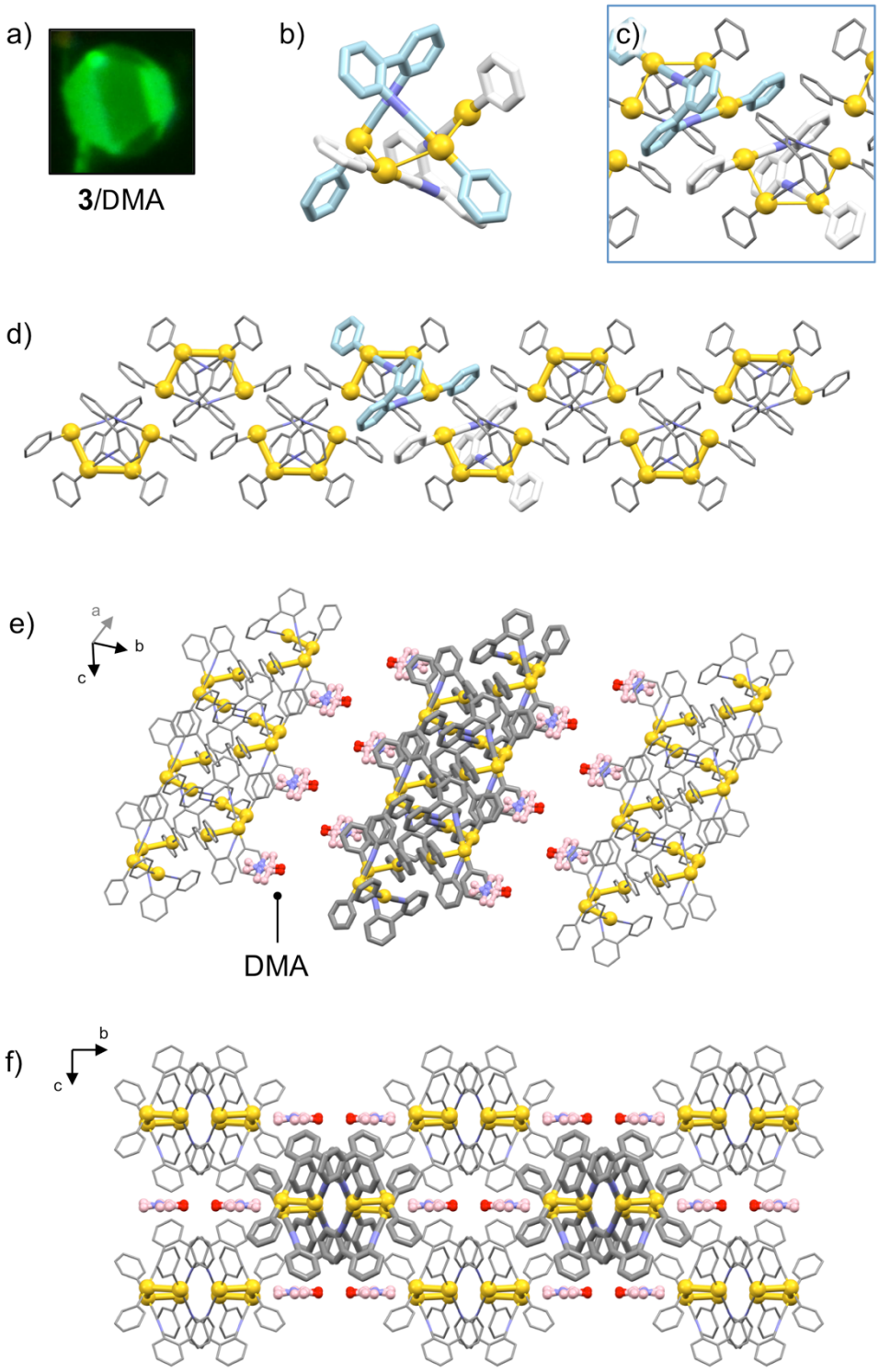

Figure S17. a) Photograph of the single crystal of **3**/DMA taken under UV light. b–f) Single-crystal structures of **3**/DMA. DMA molecules are disordered. All the H atoms are omitted for clarity.

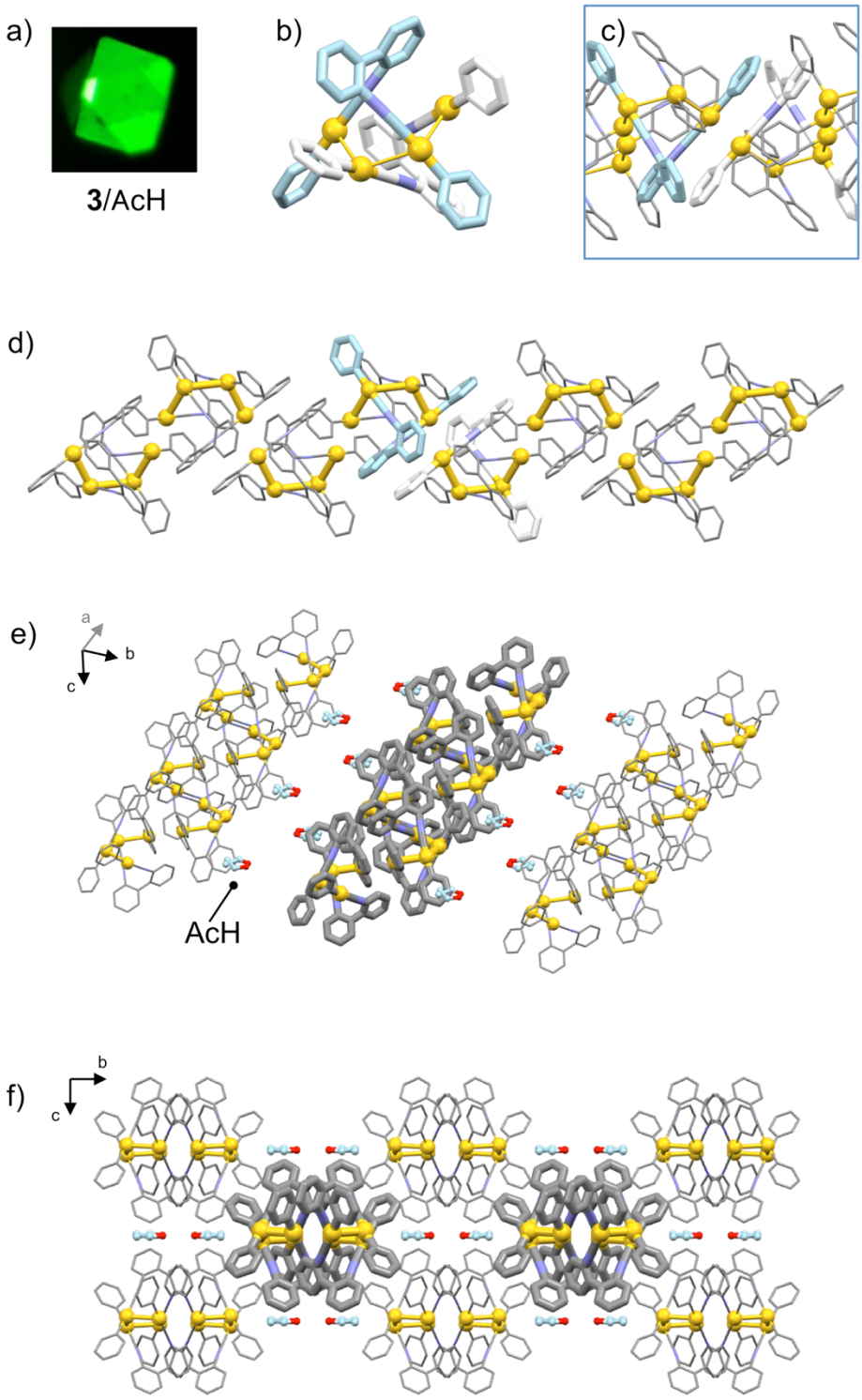

Figure S18. a) Photograph of the single crystal of **3**/AcH taken under UV light. b–f) Single-crystal structures of **3**/AcH. AcH molecules are disordered. All the H atoms are omitted for clarity.

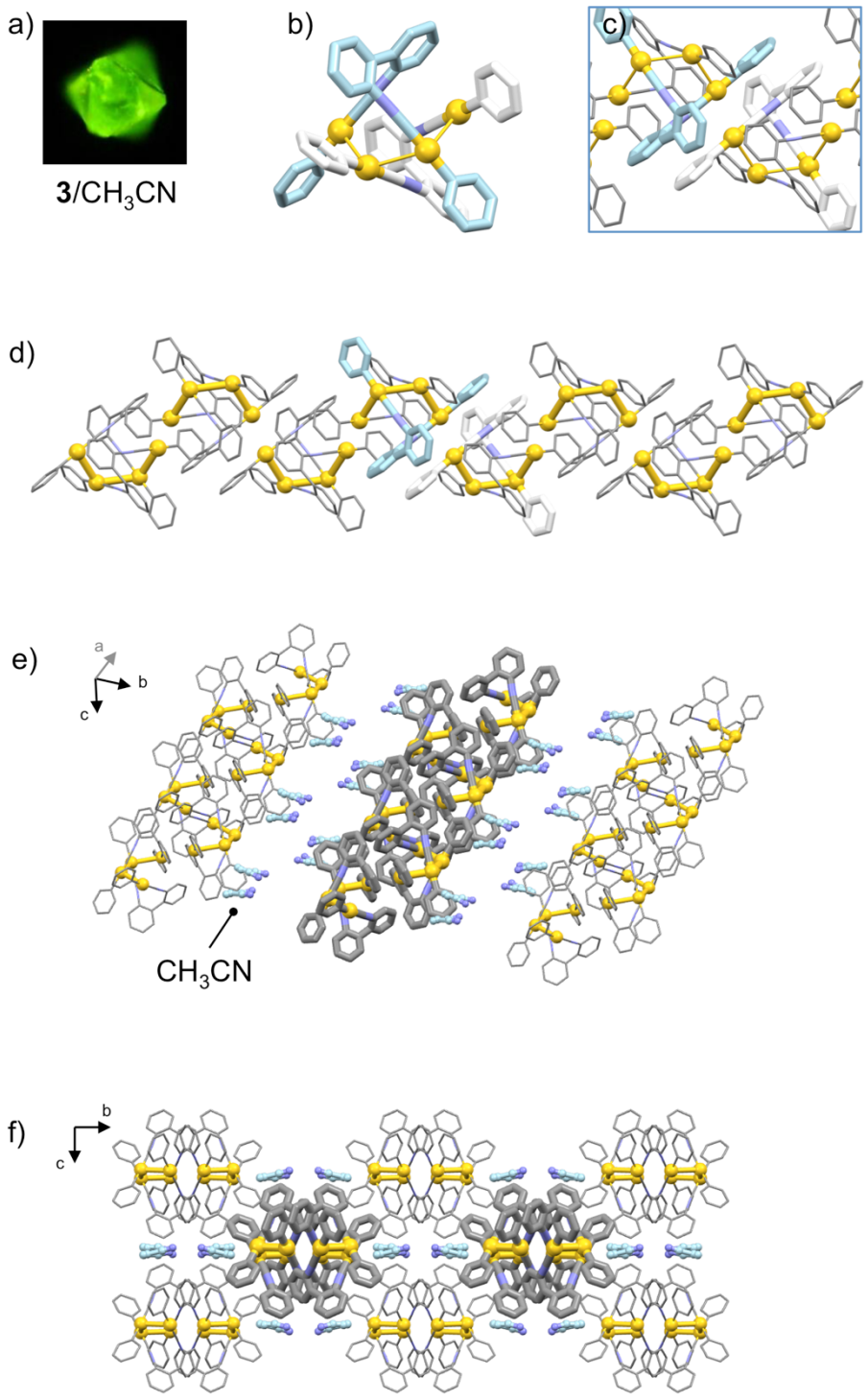

Figure S19. a) Photograph of the single crystal of **3**/CH_3CN taken under UV light. b–f) Single crystal-structures of **3**/CH_3CN. CH_3CN molecules are disordered. All the H atoms are omitted for clarity.

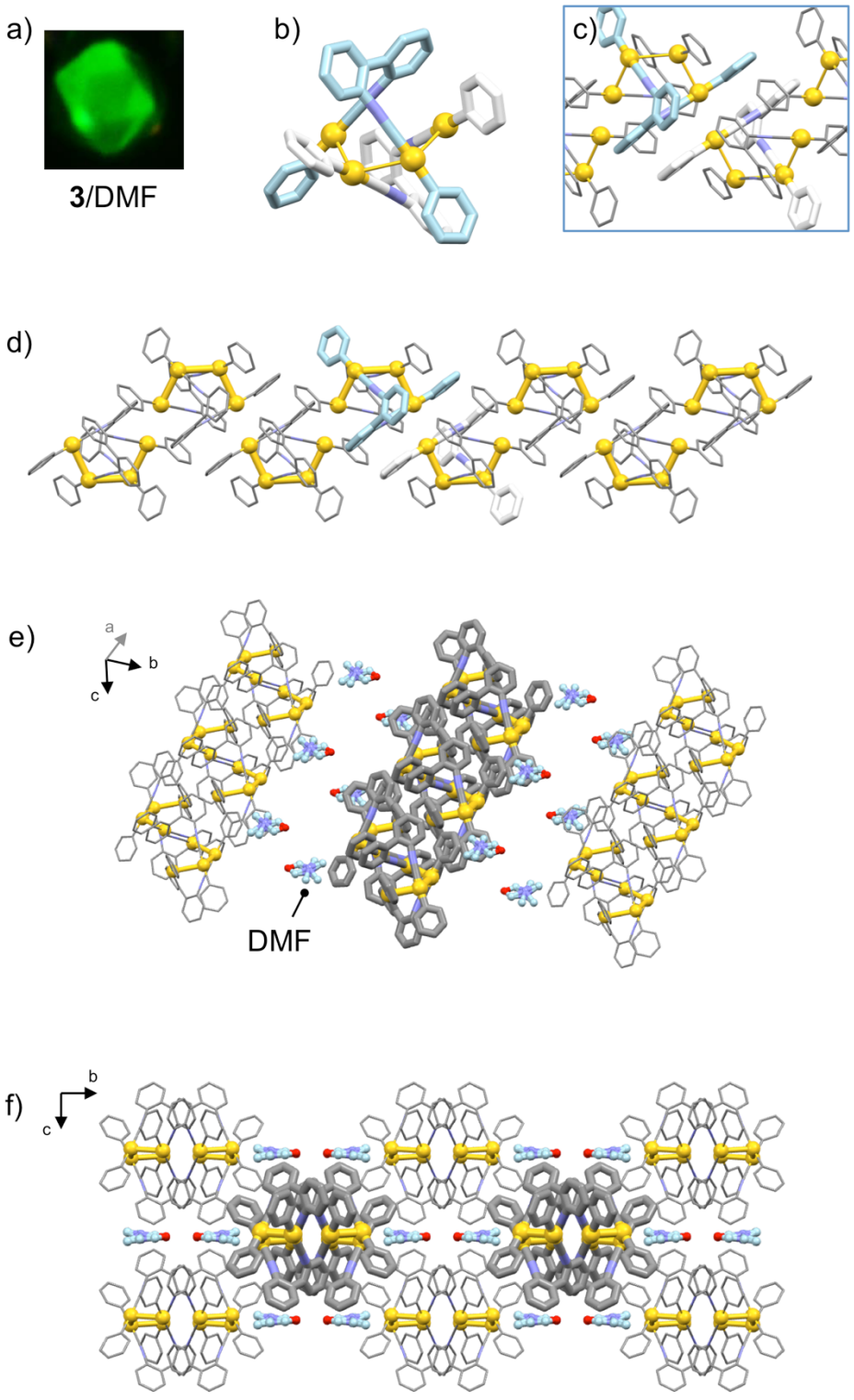

Figure S20. a) Photograph of the single crystal of **3**/DMF taken under UV light. b–f) Single-crystal structures of **3**/DMF. DMF molecules are disordered. All the H atoms are omitted for clarity.

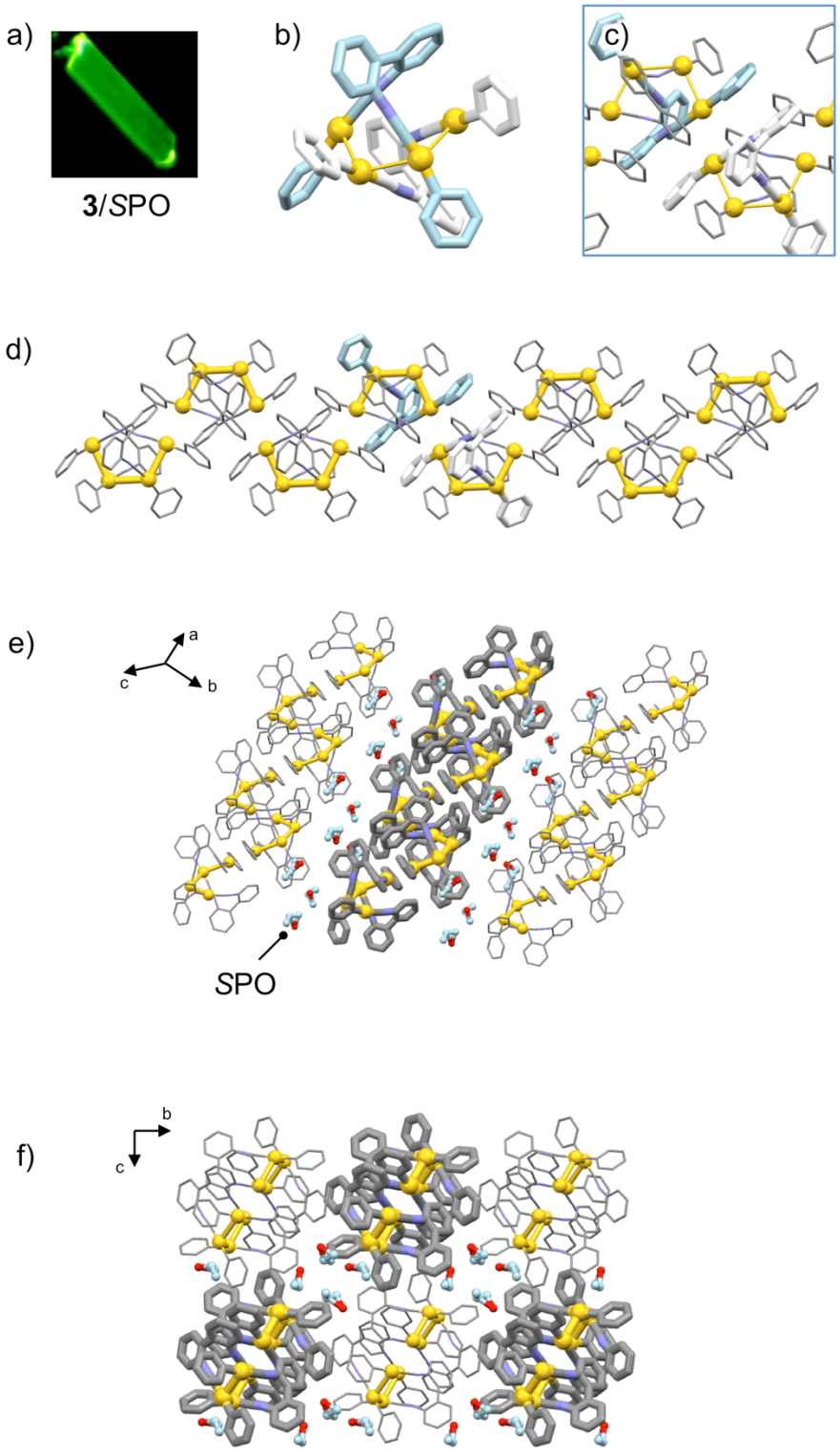

Figure S21. a) Photograph of the single crystal of **3**/*S*PO taken under UV light. b–f) Single-crystal structures of **3**/*S*PO. All the H atoms are omitted for clarity.

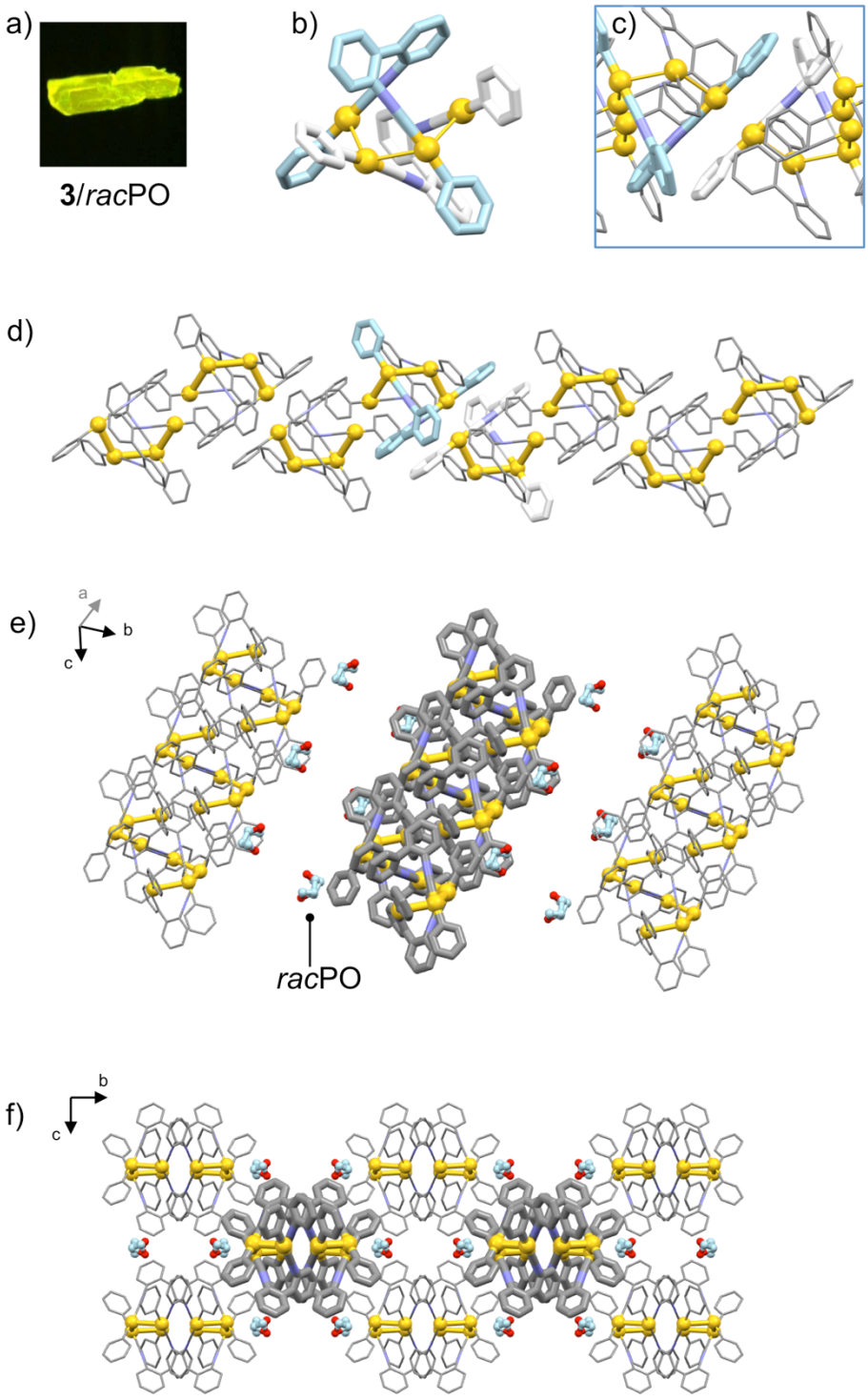

Figure S22. a) Photograph of the single crystal of **3**/*rac*PO taken under UV light. b–f) Single-crystal structures of **3**/*rac*PO. *rac*PO molecules are disordered. All the H atoms are omitted for clarity.

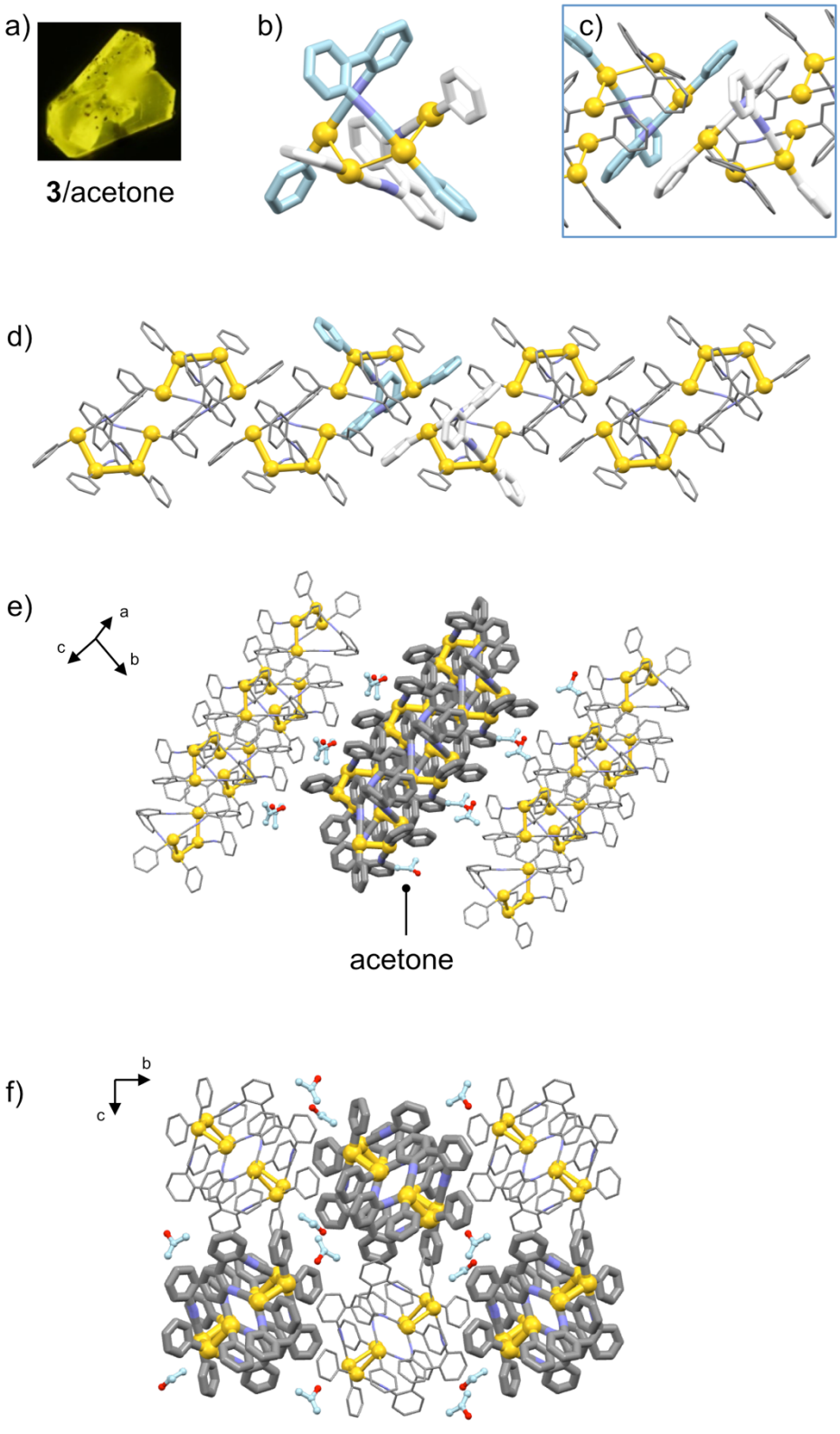

Figure S23. a) Photograph of the single crystal of **3**/acetone taken under UV light. b–f) Single-crystal structures of **3**/acetone. All the H atoms are omitted for clarity.

2.4.9. Comparison of the Powder Samples and the Single Crystals of 3/*solvent*

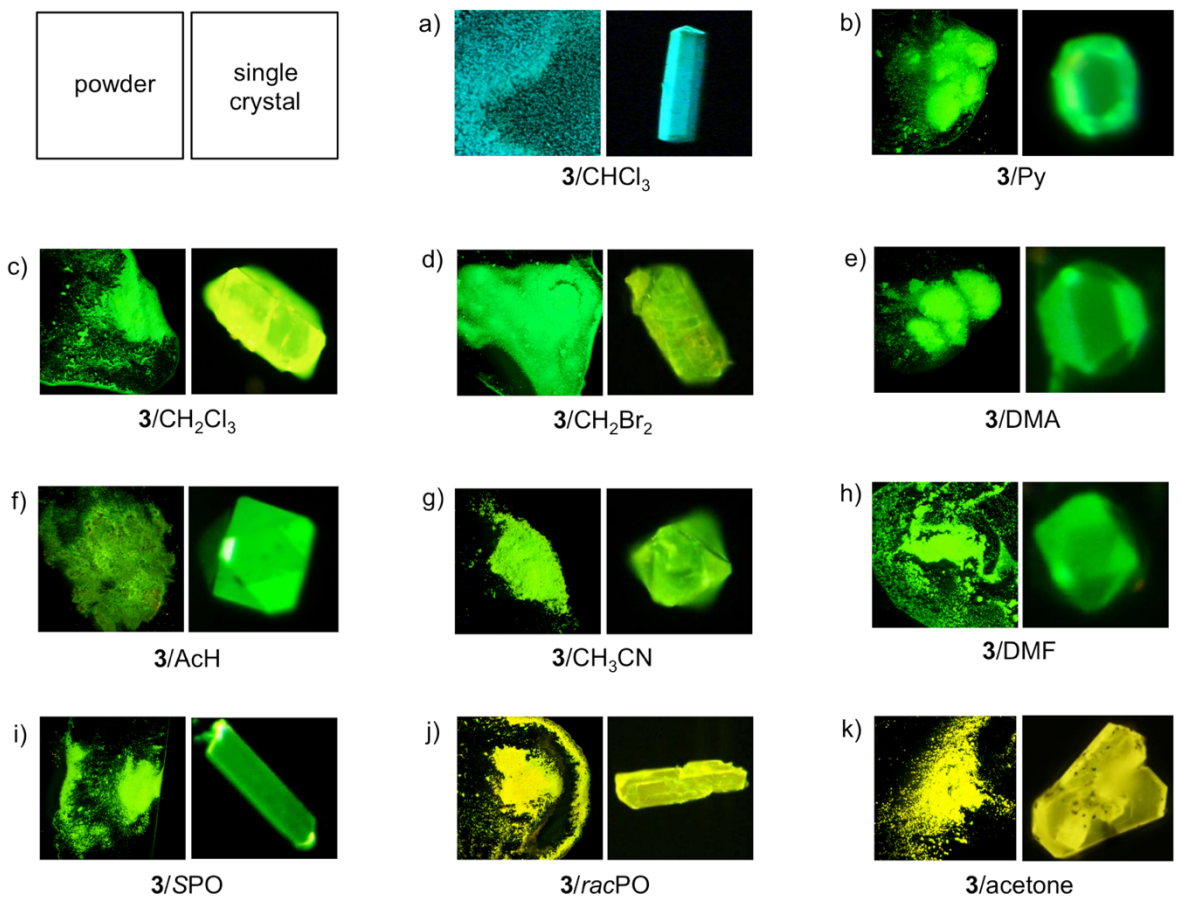

Figure S24. Photographs of the powders (left-side panels) and the single crystals (right-side panels) of eleven **3**/*solvent*, in which **3**/*solvent* to a) **3**/$CHCl_3$, b) **3**/Py, c) **3**/CH_2Cl_2, d) **3**/CH_2Br_2, e) **3**/DMA, f) **3**/AcH, g) **3**/CH_3CN, h) **3**/DMF, i) **3**/*S*PO, j) **3**/*rac*PO, and k) **3**/acetone taken under UV light.

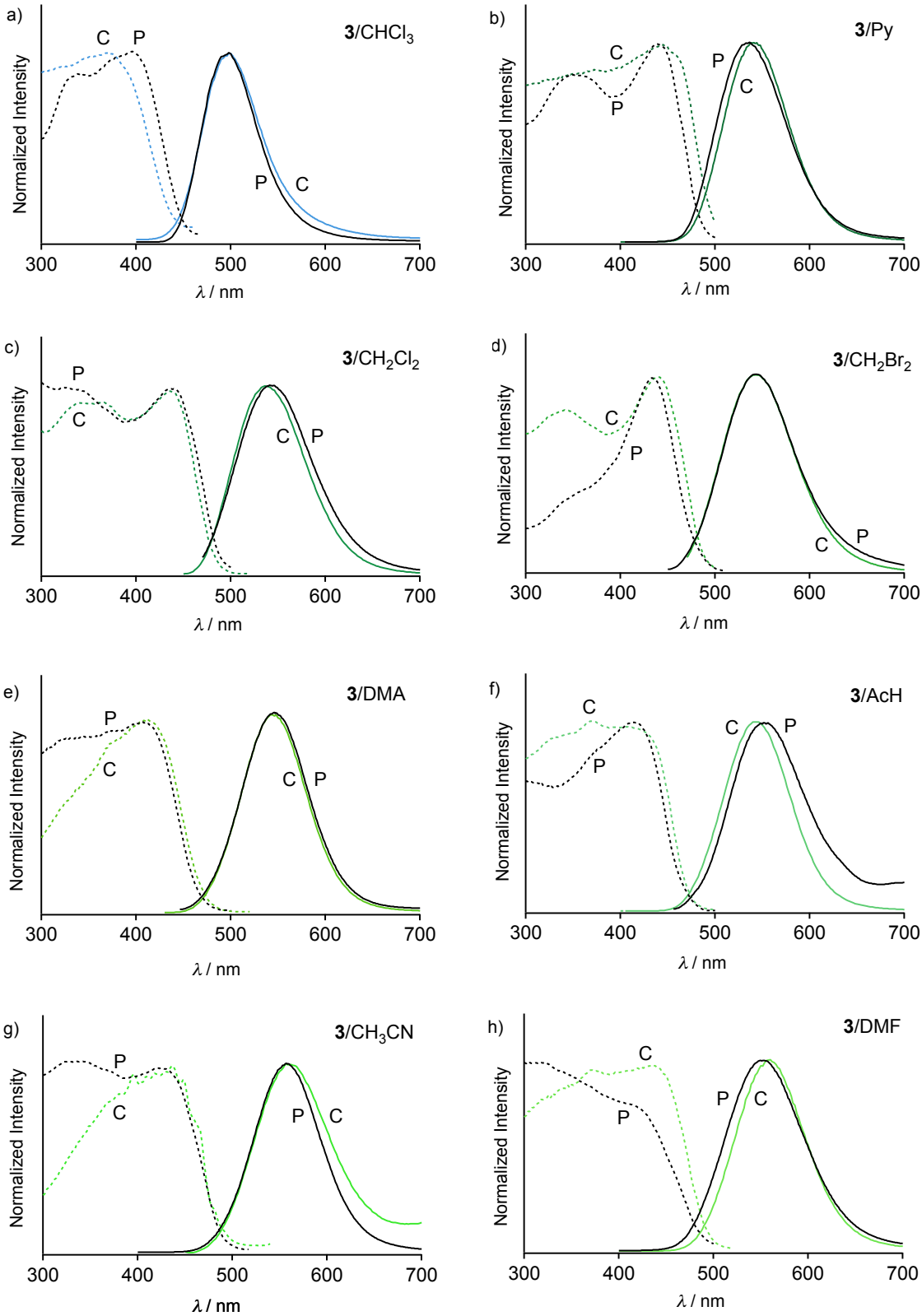
a)
3/CHCl3
C
P
P
C
Normalized Intensity
300
400
500
600
700
λ / nm
b)
3/Py
C
P
P
C
Normalized Intensity
300
400
500
600
700
λ / nm
c)
3/CH2Cl2
P
C
C
P
Normalized Intensity
300
400
500
600
700
λ / nm
d)
3/CH2Br2
C
P
C
P
Normalized Intensity
300
400
500
600
700
λ / nm
e)
3/DMA
P
C
C
P
Normalized Intensity
300
400
500
600
700
λ / nm
f)
3/AcH
C
P
C
P
Normalized Intensity
300
400
500
600
700
λ / nm
g)
3/CH3CN
P
C
P
C
Normalized Intensity
300
400
500
600
700
λ / nm
h)
3/DMF
C
P
P
C
Normalized Intensity
300
400
500
600
700
λ / nm

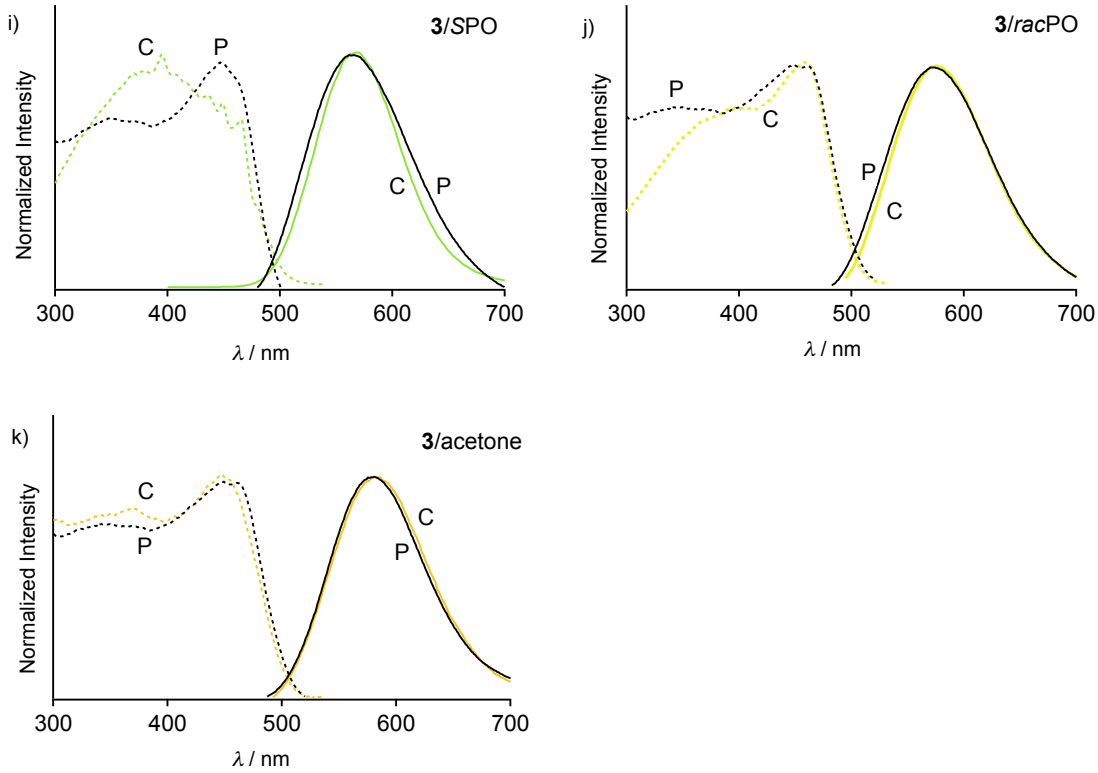

Figure S25. Excitation (dashed lines) and emission (solid lines) spectra of eleven powder forms (denoted as "P") and single crystals (denoted as "C") of **3**/*solvent*, in which **3**/*solvent* corresponds to a) **3**/$CHCl_3$, b) **3**/Py, c) **3**/CH_2Cl_2, d) **3**/CH_2Br_2, e) **3**/DMA, f) **3**/AcH, g) **3**/CH_3CN, h) **3**/DMF, i) **3**/*S*PO, j) **3**/*rac*PO, and k) **3**/acetone. The measurement conditions are summarized in Table S4.

Table S4 Summary of the measurement conditions for the excitation and emission spectra shown in Figure S25.

Figure	**3**/*solvent*	Monitored emission wavelength of powder / nm	Monitored emission wavelength of single crystal / nm	Excitation wavelength of powder / nm	Excitation wavelength of single crystal / nm
Figure S25a	**3**/$CHCl_3$	494	494	365	365
Figure S25b	**3**/Py	530	539	365	365
Figure S25c	**3**/CH_2Cl_2	537	532	365	365
Figure S25d	**3**/CH_2Br_2	544	544	365	365
Figure S25e	**3**/DMA	546	545	365	365
Figure S25f	**3**/AcH	552	549	365	365
Figure S25g	**3**/CH_3CN	556	558	365	365
Figure S25h	**3**/DMF	560	571	365	365
Figure S25i	**3**/*S*PO	566	568	365	365
Figure S25j	**3**/*rac*PO	576	577	365	365
Figure S25k	**3**/acetone	580	580	365	365

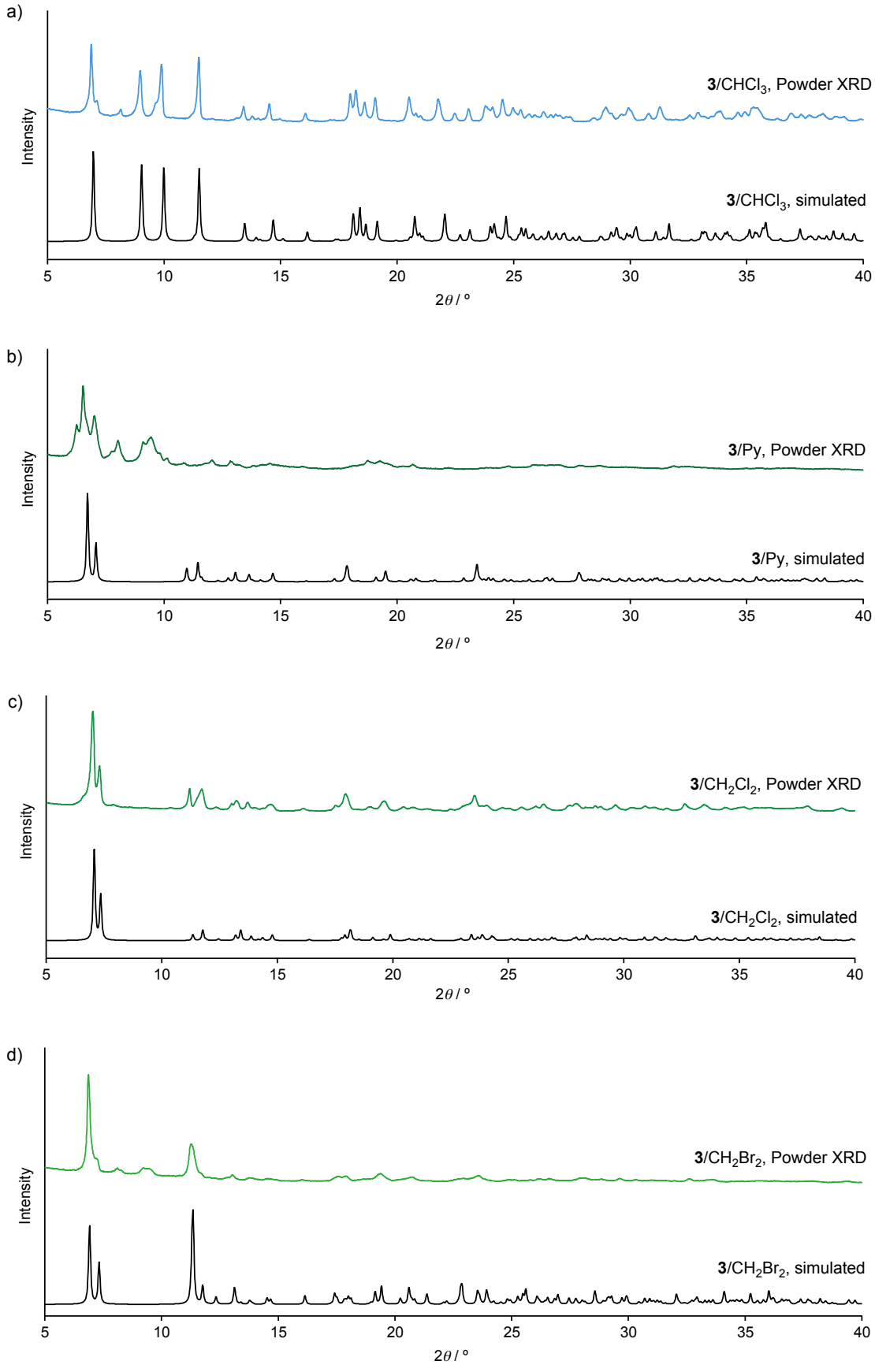
a)
Intensity
3/CHCl3, Powder XRD
3/CHCl3, simulated
5
10
15
20
25
30
35
40
2θ / °
b)
Intensity
3/Py, Powder XRD
3/Py, simulated
5
10
15
20
25
30
35
40
2θ / °
c)
Intensity
3/CH2Cl2, Powder XRD
3/CH2Cl2, simulated
5
10
15
20
25
30
35
40
2θ / °
d)
Intensity
3/CH2Br2, Powder XRD
3/CH2Br2, simulated
5
10
15
20
25
30
35
40
2θ / °

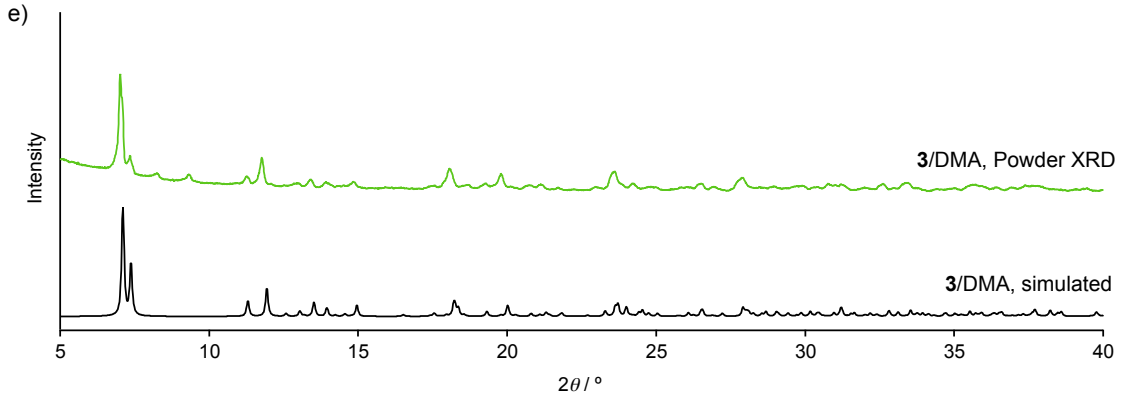
e)
Intensity
3/DMA, Powder XRD
3/DMA, simulated
5
10
15
20
25
30
35
40
2θ / °

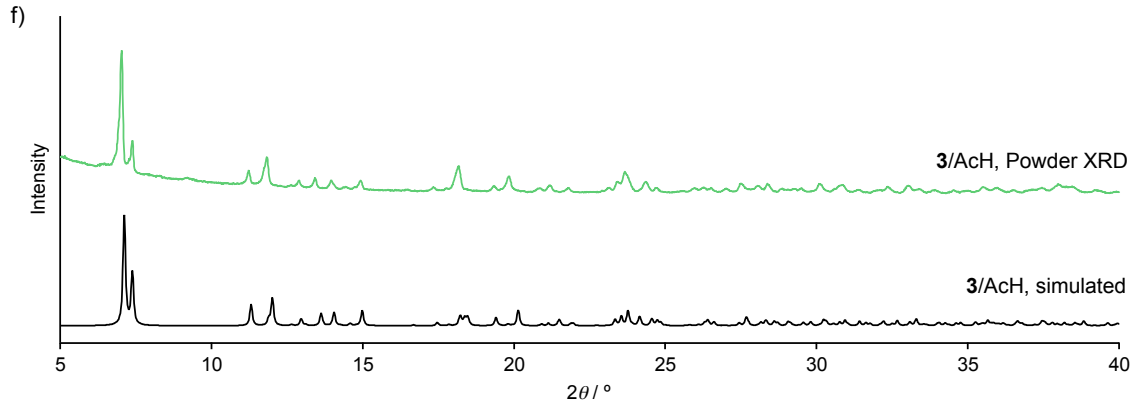
f)
Intensity
3/AcH, Powder XRD
3/AcH, simulated
5
10
15
20
25
30
35
40
2θ / °

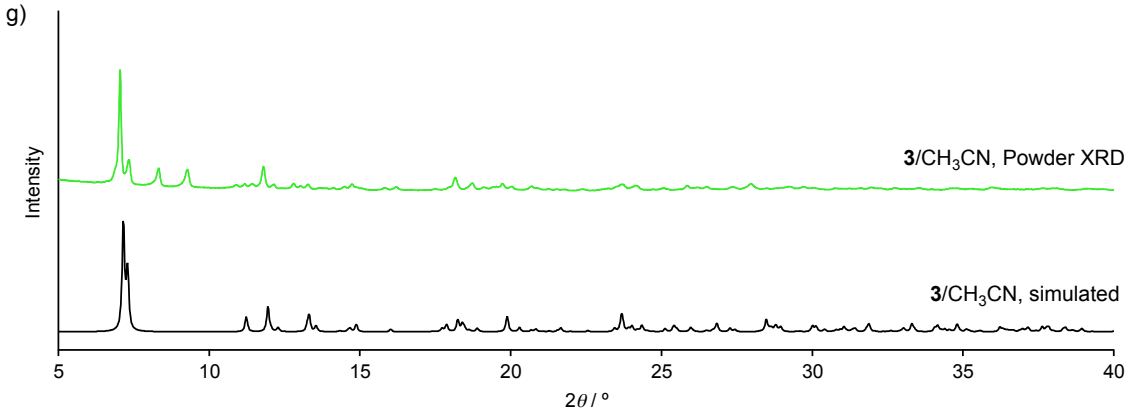
g)
Intensity
3/CH3CN, Powder XRD
3/CH3CN, simulated
5
10
15
20
25
30
35
40
2θ / °

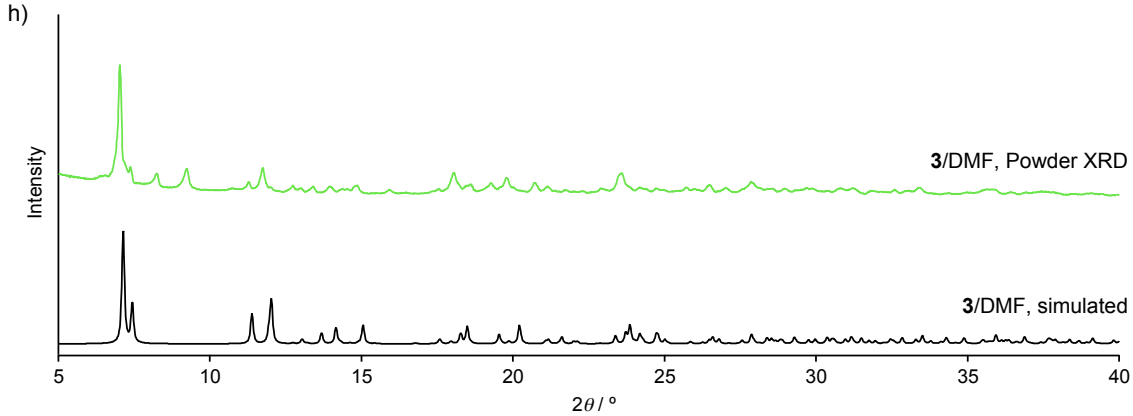
h)
Intensity
3/DMF, Powder XRD
3/DMF, simulated
5
10
15
20
25
30
35
40
2θ / °

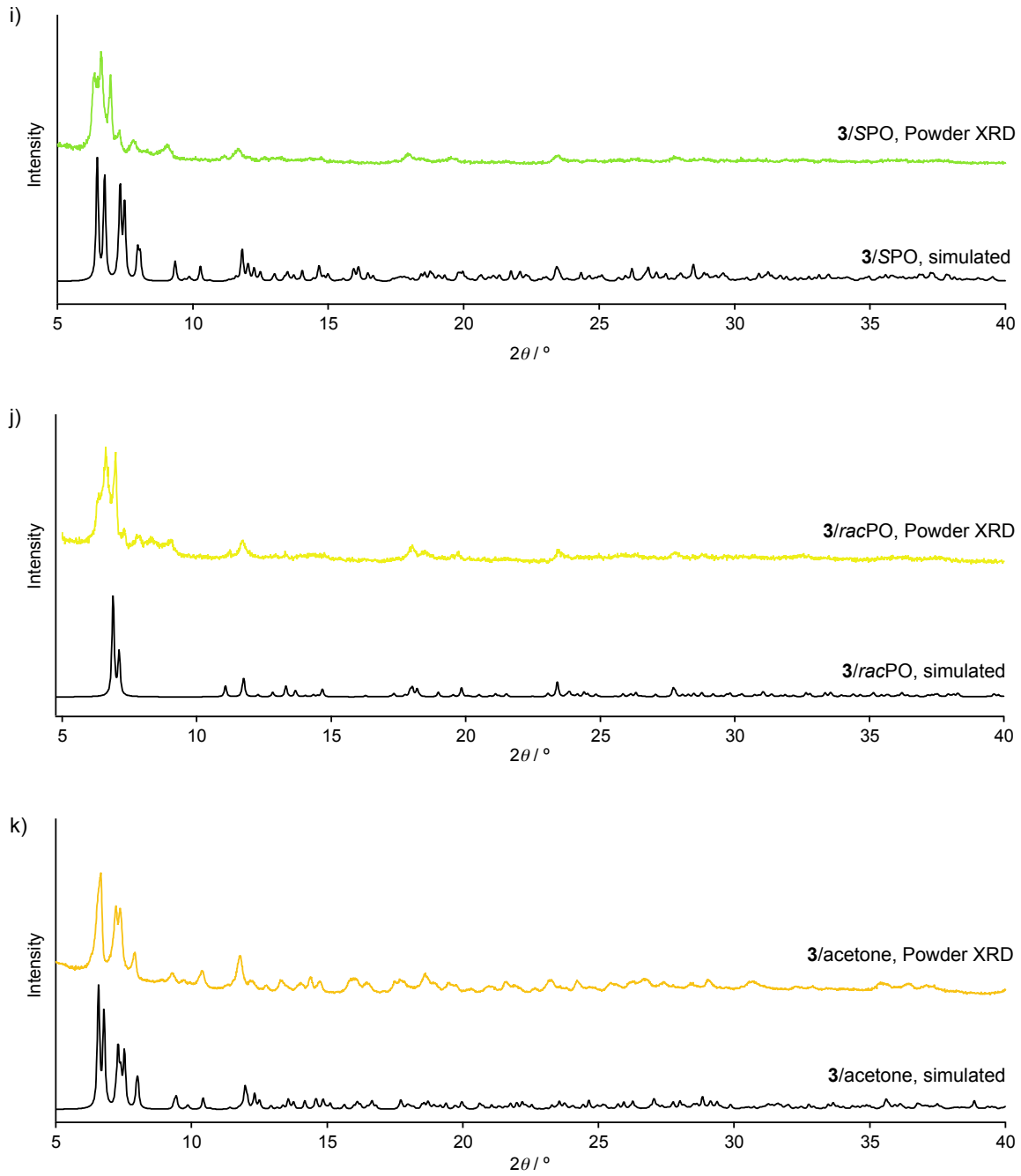

Figure S26. Experimental powder XRD patterns of eleven **3**/*solvent* obtained by solvent addition to $\mathbf{3}_{\mathbf{ground}}$ (colored solid lines) and simulated powder patterns of **3**/*solvent* derived form the single crystal structures (black solid lines), in which **3**/*solvent* corresponds to a) **3**/$CHCl_3$, b) **3**/Py, c) **3**/CH_2Cl_2, d) **3**/CH_2Br_2, e) **3**/DMA, f) **3**/AcH, g) **3**/CH_3CN, h) **3**/DMF, i) **3**/*S*PO, j) **3**/*rac*PO, and k) **3**/acetone.

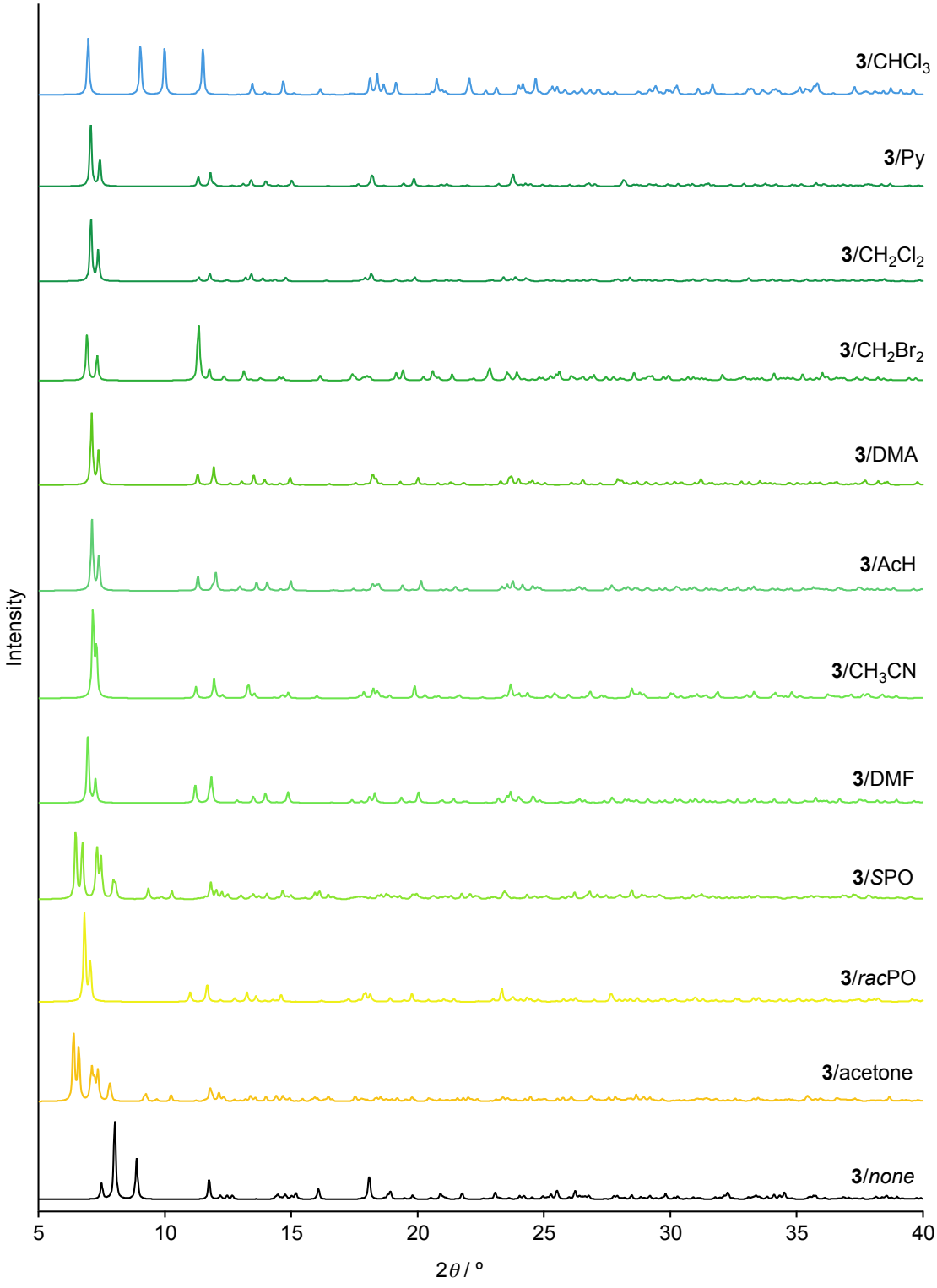

Figure S27. Simulated powder patterns derived from the single crystals of **3**/*solvent* and **3**/*none*, in which **3**/*solvent* corresponds to **3**/$CHCl_3$, **3**/Py, **3**/CH_2Cl_2, **3**/CH_2Br_2, **3**/DMA, **3**/AcH, **3**/CH_3CN, **3**/DMF, **3**/*S*PO, **3**/*rac*PO, and **3**/acetone.

2.4.10. The Single-Crystal Structure of 3/*none*

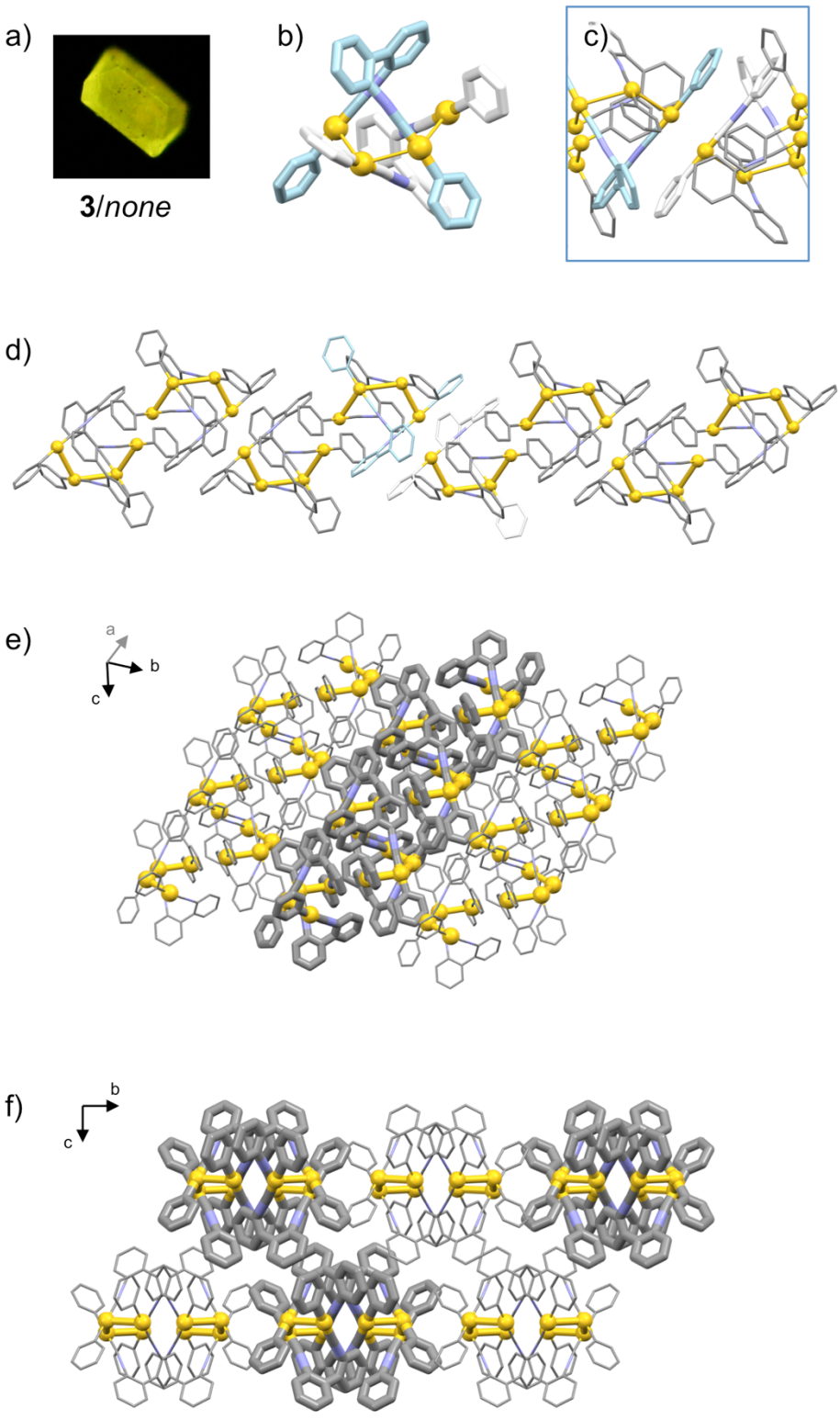

Figure S28. a) Photograph of the single crystal of **3**/*none* taken under UV light. b–f) Single-crystal structures of **3**/*none*. All the H atoms are omitted for clarity.

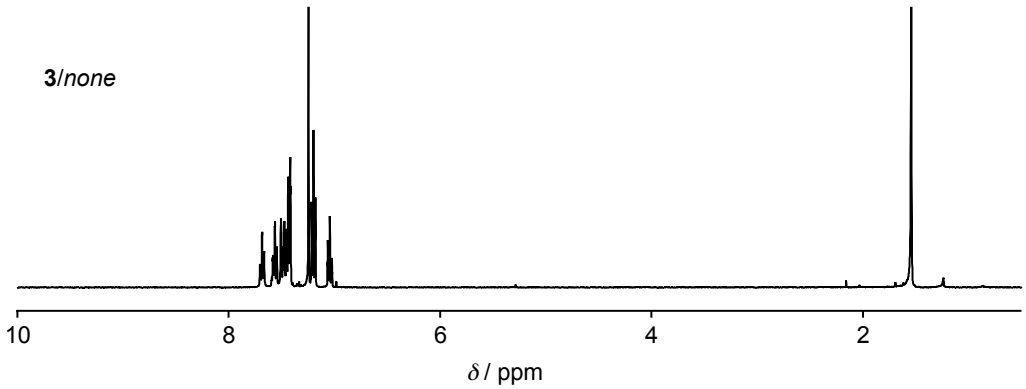

Figure S29. ^{1}H NMR spectrum of **3**/*none* in $CDCl_3$.

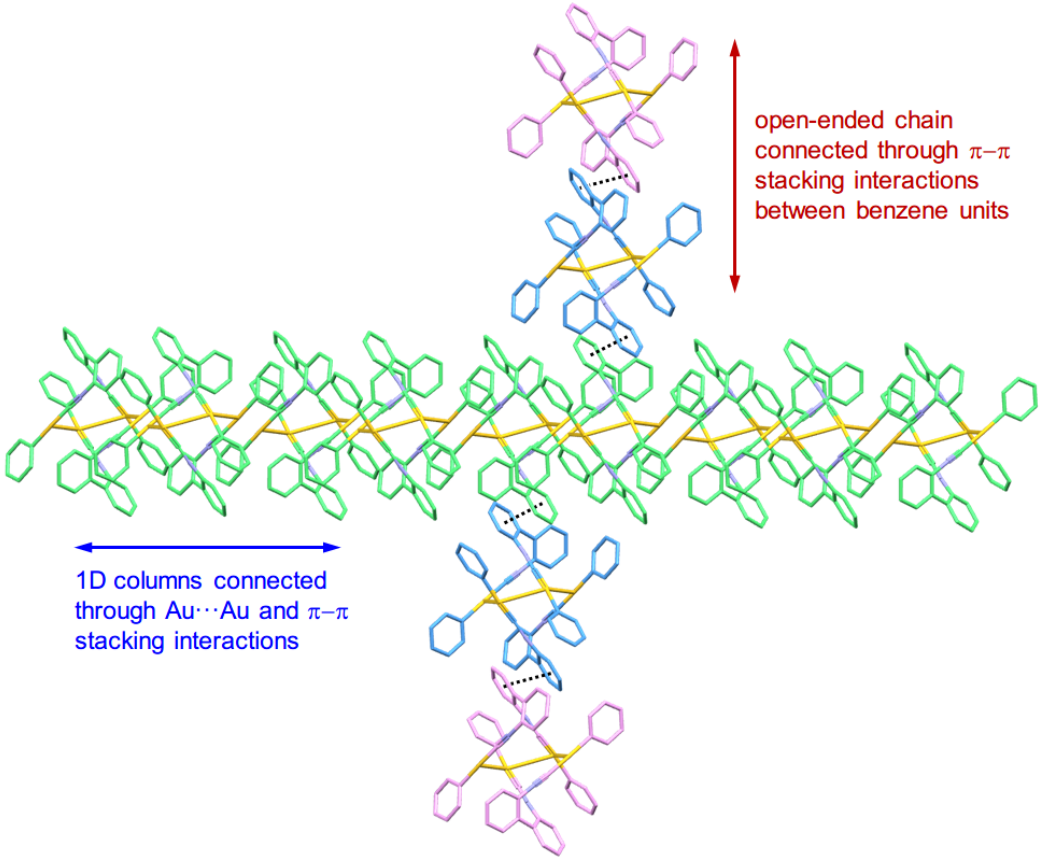

Figure S30. Single-crystal structures of **3**/*none* in which dotted lines denote intermolecular interactions between 1D columnar structures. The molecules with green colored carbon atoms form a 1D columnar structure through inter-dimer interactions as mentioned in the text (both Au···Au and π–π stacking interactions, see also Figure S28c). Orthogonal to this 1D column, molecules are connected through π–π stacking interactions (dotted lines). All the H atoms are omitted for clarity.

2.4.11. TD-DFT Calculations of 3/$CHCl_3$, 3/CH_2Cl_2, and 3/acetone.

All calculations were performed using the Gaussian 09W (revision C.01) and Gaussian 09 program package.[35] In the calculations, the SDD basis set with an effective core potential was used for Au and other atoms. The tetramer of **3**/$CHCl_3$, **3**/CH_2Cl_2, and **3**/acetone were calculated for understanding three types of emission colors of **3**/*solvent*. Comparison of experimental and theoretical studies of optical properties of **3**/*solvent* showed very good matching. Especially, simulated excitation spectra and those from the experiments exhibited the similar traces (Figure S31).

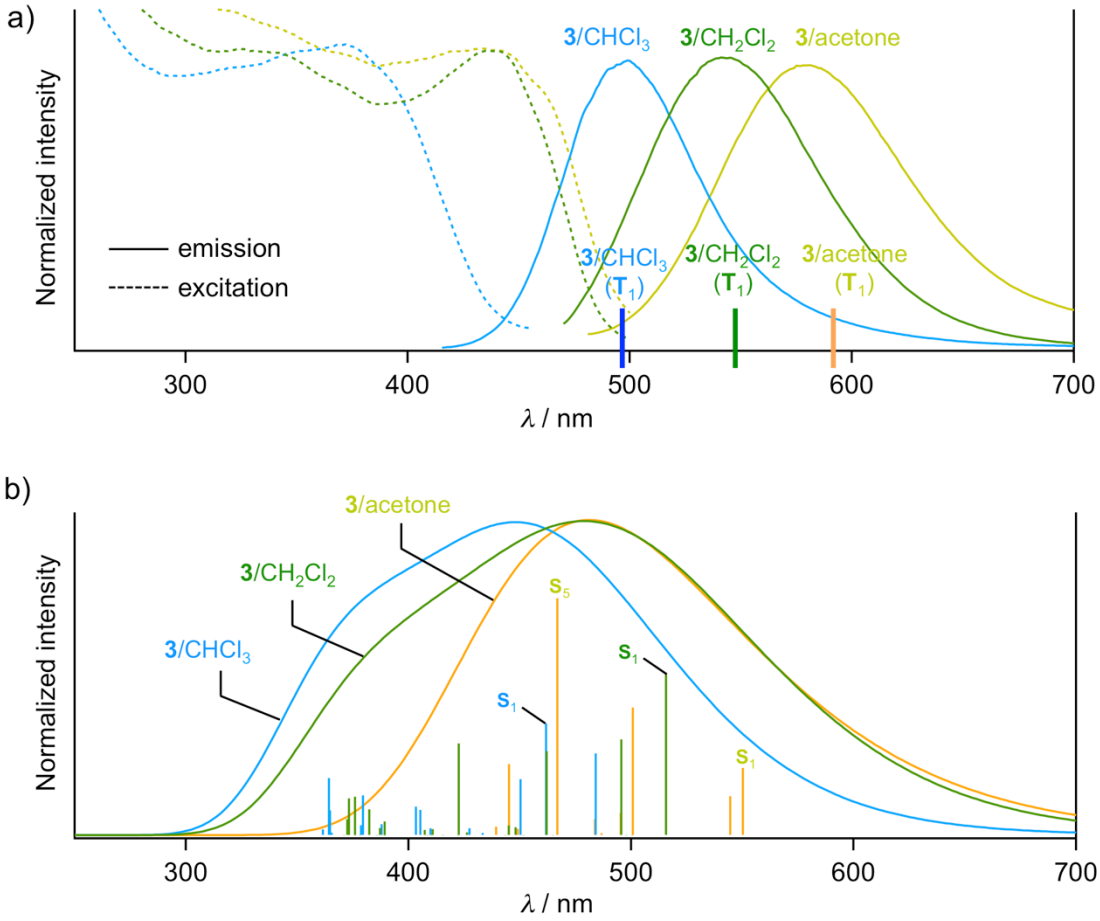

Figure S31. Comparison of experimental and theoretical studies on optical properties of **3**·*solvent*. a) Blue lines: normalized excitation (dashed line, detected at 498 nm) and emission (solid line, λ_{ex} = 365 nm) spectra of **3**/$CHCl_3$. Greenish lines: normalized excitation (dashed line, detected at 534 nm) and emission (solid line, λ_{ex} = 365 nm) spectra of **3**/CH_2Cl_2. Orange lines: normalized excitation (dashed line, detected at 580 nm) and emission (solid line, λ_{ex} = 365 nm) spectra of **3**/acetone. b) Simulated UV/vis absorption spectra of **3**/$CHCl_3$ (blue line), **3**/CH_2Cl_2 (green line), and **3**/acetone (Orange line) based on the TD-DFT calculations of the tetramers derived from the corresponding single crystalline structures (B3LYP/SDD).

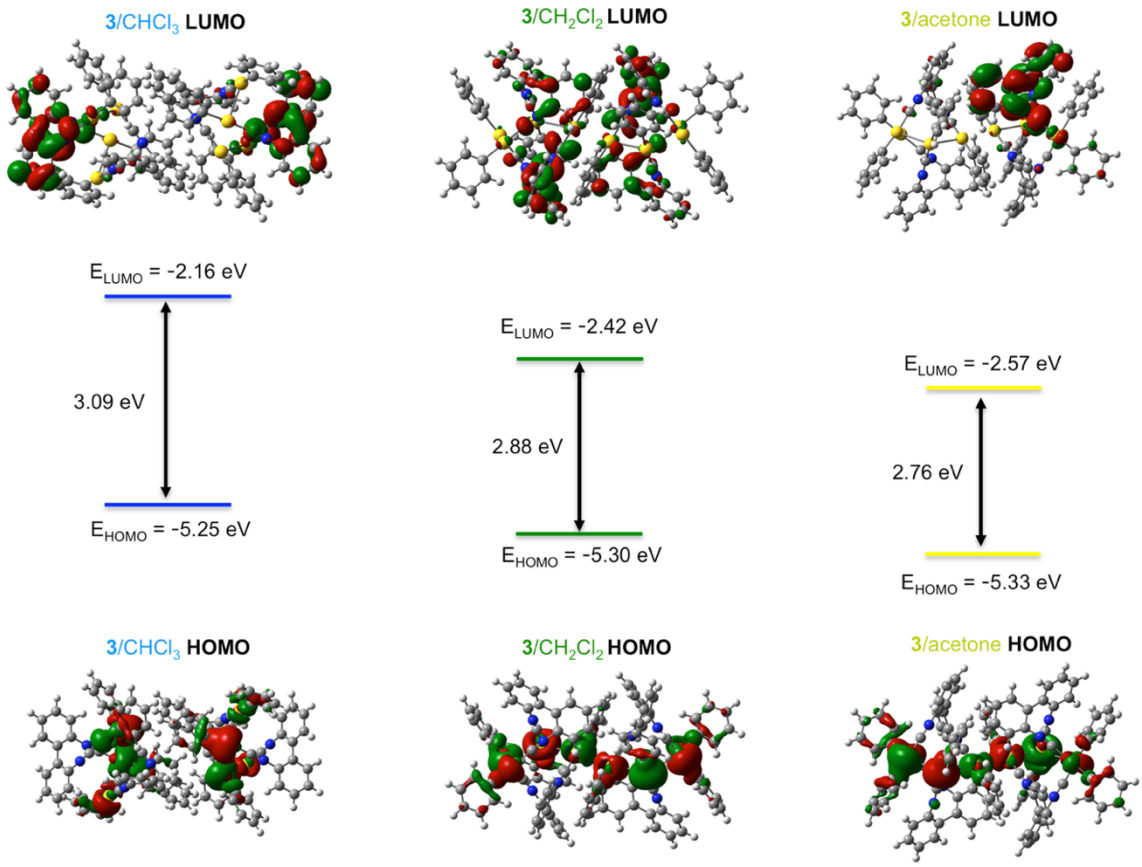

Figure S32. Frontier molecular orbitals and corresponding energy levels obtained by TD-DFT calculations of the tetramers derived from the single-crystal structures of **3**/$CHCl_3$, **3**/CH_2Cl_2, and **3**/acetone (B3LYP/SDD).

2.5. References

23. (a) Yan, X.; Wang, F.; Zheng, B.; Huang, F. *Chem. Soc. Rev.* **2012**, *41*, 6042; (b) Jobbágy, C.; Deák, A. *Eur. J. Inorg. Chem.* **2014**, *2014*, 4434.
24. (a) Shimizu, M.; Hiyama, T. *Chem. Asi. J.* **2010**, *5*, 1516; (b) Gierschner, J.; Park, S. Y. *J. Mater. Chem. C* **2013**, *1*, 5818; (c) Varughese, S. *J. Mater. Chem. C* **2014**, *2*, 3499; (d) Yan, D.; Evans, D. G. *Mater. Horiz.* **2014**, *1*, 46.
25. (a) Wadas, T. J.; Wang, Q. M.; Kim, Y. J.; Flaschenreim, C.; Blanton, T. N.; Eisenberg, R. *J. Am. Chem. Soc.* **2004**, *126*, 16841; (b) Grove, L. J.; Rennekamp, J. M.; Jude, H.; Connick, W. B. *J. Am. Chem. Soc.* **2004**, *126*, 1594; (c) Dou, C.; Chen, D.; Iqbal, J.; Yuan, Y.; Zhang, H.; Wang, Y. *Langmuir* **2011**, *27*, 6323; (d) Malwitz, M. A.; Lim, S. H.; White–Morris, R. L.; Pham, D. M.; Olmstead, M. M.; Balch, A. L. *J. Am. Chem. Soc.* **2012**, *134*, 10885; (e) Kobayashi, A.; Hara, H.; Yonemura, T.; Chang, H. C.; Kato, M. *Dalton Trans.* **2012**, *41*, 1878; (f) Koshevoy, I. O.; Chang, Y. C.; Karttunen, A. J.; Haukka, M.; Pakkanen, T.; Chou, P. T. *J. Am. Chem. Soc.* **2012**, *134*, 6564; (g) Kobayashi, A.; Komatsu, K.; Ohara, H.; Kamada, W.; Chishina, Y.; Tsuge, K.; Chang, H. C.; Kato, M. M. *Inorg. Chem.* **2013**, *52*, 13188; (h) Sun, H.; Liu, S.; Lin, W.; Zhang, K. Y.; Lv, W.; Huang, X.; Huo, F.; Yang, H.; Jenkins, G.; Zhao, Q.; Huang, W. *Nat. Commun.* **2014**, *5*, 3601; (i) Deak, A.; Jobbagy, C.; Marsi, G.; Molnar, M.; Szakacs, Z.; Baranyai, P. *Chem. Eur. J.* **2015**, *21*, 11495; (j) Jiang, B.; Zhang, J.; Ma, J. Q.; Zheng, W.; Chen, L. J.; Sun, B.; Li, C.; Hu, B. W.; Tan, H.; Li, X.; Yang, H. B. *J. Am. Chem. Soc.* **2016**, *138*, 738.
26. For selected reviews of luminescent solid-state compounds that change their emission properties in response to volatile organic solvents, see: (a) Kato, M. *Bull. Chem. Soc. Jpn.* **2007**, *80*, 287; (b) Zhang, X.; Li, B.; Chen, Z.-H.; Chen, Z.-N. *J. Mater. Chem.* **2012**, *22*, 11427; (c) Kreno, L. E.; Leong, K.; Farha, O. K.; Allendorf, M.; Van Duyne, R. P.; Hupp, J. T. *Chem. Rev.* **2012**, *112*, 1105; (d) Wenger, O. S. *Chem. Rev.* **2013**, *113*, 3686; (e) Zhou, X.; Lee, S.; Xu, Z.; Yoon, J. *Chem. Rev.* **2015**, *115*, 7944.
27. For selected solid-state luminescent compounds that can change their emission properties to discriminate five or fewer volatile organic compounds, see reference 3. For rare examples of solid-state luminescent compounds that can discriminate more than ten volatile organic compounds, see: (a) Fernandez, E. J.; Lopez-De-Luzuriaga, J. M.; Monge, M.; Olmos, M. E.; Perez, J.; Laguna, A.; Mohamed A. A.; Fackler, Jr. J. P. *J. Am. Chem. Soc.* **2003**, *125*, 2022; (b) Kato, M.; Kishi, S.; Wakamatsu, Y.; Sugi,

Y.; Osamura, Y.; Koshiyama, T.; Hasegawa, M. *Chem. Lett.* **2005**, *34*, 1368; (c) Ni, J.; Zhang, L. Y.; Wen, H. M.; Chen, Z. N. *Chem. Commun.* **2009**, 3801; (d) Takashima, Y.; Martinez, V. M.; Furukawa, S.; Kondo, M.; Shimomura, S.; Uehara, H.; Nakahama, M.; Sugimoto, K.; Kitagawa, S. *Nat. Commun.* **2011**, *2*, 168; (e) Ito, S.; Hirose, A.; Yamaguchi, M.; Tanaka, K.; Chujo, Y. *J. Mater. Chem. C* **2016**, *4*, 5564.

28. (a) White-Morris, R. L.; Olmstead, M. M.; Balch, A. L.; Elbjeirami, O.; Omary, M. A. *Inorg. Chem.* **2003**, *42*, 6741; (b) Cauteruccio, S.; Loos, A.; Bossi, A.; Blanco Jaimes, M. C.; Dova, D.; Rominger, F.; Prager, S.; Dreuw, A.; Licandro, E.; Hashmi, A. S. *Inorg. Chem.* **2013**, *52*, 7995; (c) Fujisawa, K.; Okuda, Y.; Izumi, Y.; Nagamatsu, A.; Rokusha, Y.; Sadaike, Y.; Tsutsumi, O. *J. Mater. Chem. C* **2014**, *2*, 3549.
29. (a) Hau, F. K.; He, X.; Lam, W. H.; Yam, V. W. *Chem. Commun.* **2011**, *47*, 8778; (b) Hau, F. K.; Yam, V. W. *Dalton Trans.* **2015**, *45*, 300.
30. (a) Bayon, R.; Coco, S.; Espinet, P.; Fernandez-Mayordomo, C.; Martin-Alvarez, J. M. *Inorg. Chem.* **1997**, *36*, 2329; (b) Coco, S.; Cordovilla, C.; Espinet, P.; Martin-Alvarez, J.; Munoz, P. *Inorg. Chem.* **2006**, *45*, 10180.
31. Ito, H.; Saito, T.; Oshima, N.; Kitamura, N.; Ishizaka, S.; Hinatsu, Y.; Wakeshima, M.; Kato, M.; Tsuge, K.; Sawamura, M. *J. Am. Chem. Soc.* **2008**, *130*, 10044.
32. (a) Sagara, Y.; Mutai, T.; Yoshikawa, I.; Araki, K. *J. Am. Chem. Soc.* **2007**, *129*, 1520; (b) Ooyama, Y.; Kagawa, Y.; Fukuoka, H.; Ito, G.; Harima, Y. *Eur. J. Org. Chem.* **2009**, *2009*, 5321; (c) Yoon, S.-J.; Chung, J. W.; Gierschner, J.; Kim, K. S.; Choi, M.-G.; Kim, D.; Park, S. Y. *J. Am. Chem. Soc.* **2010**, *132*, 13675; (d) Zhang, G.; Lu, J.; Sabat, M.; Fraser, C. L. *J. Am. Chem. Soc.* **2010**, *132*, 2160; (e) Sagara, Y.; Kato, T. *Angew. Chem. Int. Ed.* **2011**, *50*, 9128; (f) Mizoshita, N.; Tani, T.; Inagaki, S. *Adv. Mater.* **2012**, *24*, 3350; (g) Nagura, K.; Saito, S.; Yusa, H.; Yamawaki, H.; Fujihisa, H.; Sato, H.; Shimoikeda, Y.; Yamaguchi, S. *J. Am. Chem. Soc.* **2013**, *135*, 10322; (h) Yagai, S.; Okamura, S.; Nakano, Y.; Yamauchi, M.; Kishikawa, K.; Karatsu, T.; Kitamura, A.; Ueno, A.; Kuzuhara, D.; Yamada, H.; Seki, T.; Ito, H. *Nat. Commun.* **2014**, *5*, 4013; (i) Sagara, Y.; Lavrenova, A.; Crochet, A.; Simon, Y. C.; Fromm, K. M.; Weder, C. *Chem. Eur. J.* **2016**, *22*, 4374.
33. Seki, T.; Ozaki, T.; Okura, T.; Asakura, K.; Sakon, A.; Uekusa, H.; Ito, H. *Chem. Sci.* **2015**, *6*, 2187.
34. (a) Seki, T.; Sakurada, K.; Ito, H. *Angew. Chem. Int. Ed.* **2013**, *52*, 12828; (b) Ito, H.; Muromoto, M.; Kurenuma, S.; Ishizaka, S.; Kitamura, N.; Sato, H.; Seki, T. *Nat.*

Commun. **2013**, *4*, 2009; (c) Seki, T.; Sakurada, K.; Ito, H. *Chem. Commun.* **2015**, *51*, 13933; (d) Yagai, S.; Seki, T.; Aonuma, H.; Kawaguchi, K.; Karatsu, T.; Okura, T.; Sakon, A.; Uekusa, H.; Ito, H. *Chem. Mater.* **2016**, *28*, 234; (e) Seki, T.; Ito, H. *Chem. Eur. J.* **2016**, *22*, 4322; (f) Seki, T.; Sakurada, K.; Muromoto, M.; Seki, S.; Ito, H. *Chem. Eur. J.* **2016**, *22*, 1968; (g) Seki, T.; Takamatsu, Y.; Ito, H. *J. Am. Chem. Soc.* **2016**, *138*, 6252.

35. Seki, T.; Sakurada, K.; Muromoto, M.; Ito, H. *Chem. Sci.* **2015**, *6*, 1491.
36. For reports of mechano-induced solvent release from solvated crystalline materials of organic and organometallic compounds, see: (a) Shan, X.-C.; Jiang, F.-L.; Chen, L.; Wu, M.-Y.; Pan, J.; Wan, X.-Y.; Hong, M.-C. *J. Mater. Chem. C* **2013**, *1*, 4339; (b) Ohba, T.; Kobayashi, A.; Chang, H. C.; Kato, M. *Dalton Trans.* **2013**, *42*, 5514; (c) Choi, S. J.; Kuwabara, J.; Nishimura, Y.; Arai, T.; Kanbara, T. *Chem. Lett.* **2012**, *41*, 65; (d) Zhang, X.; Wang, J. Y.; Ni, J.; Zhang, L. Y.; Chen, Z. N. *Inorg. Chem.* **2012**, *51*, 5569.
37. (a) Grein, F. *J. Phys. Chem. A* **2002**, *106*, 3823; (b) Grein, F. *Theor. Chem. Acc.* **2003**, *109*, 274.
38. (a) MacNeil, D. D.; Decken, A. 2,2'-Dibromobiphenyl.*Acta Cryst. Sect. C* **1999**, *55*, 628–630; (b) Leroux, F.; Maurin, M.; Nicod, N.; Scopelliti, R. *Tetrahedron Lett.* **2004**, *45*, 1899.
39. (a) Bhardwaj, R. M.; Price, L. S.; Price, S. L.; Reutzel-Edens, S. M.; Miller, G. J.; Oswald, I. D. H.; Johnston, B. F.; Florence, A. J. *Cryst. Growth Des.* **2013**, *13*, 1602; (b) Sekiya, R.; Yamasaki, Y.; Tada, W.; Shio, H.; Haino, T. *CrystEngComm* **2014**, *16*, 6023; (c) Bērziņš, A.; Skarbulis, E.; Actiņš, A. *Cryst. Growth Des.* **2015**, *15*, 2337.
40. Six solved crystal structures (three non-solvated and three solvated crystals) of one compound with distinct emission properties have been reported, see: Fan, Y.; Zhao, Y.; Ye, L.; Li, B.; Yang, G.; Wang, Y. *Cryst. Growth Des.* **2009**, *9*, 1421.
41. Optical properties of the monomeric state of **3** in $CHCl_3$ are quite different from those in crystalline phases (Figure S1 and S2). This indicates that the solid-state optical properties of **3** are strongly affected by intermolecular interactions.
42. Emission spectra of $\mathbf{3}_{\mathbf{ground}}$ prepared from eleven **3**/*solvent* display emission maxima slightly different from each other, ranging from 570 to 584 nm. This is likely because of the formation of slightly different degrees of amorphous phases.
43. Photophysical property data for **3**/*solvent* are summarized in Figure S3 and Table S1.

44. Solvents in this study were hexamethyldisilane, methoxytrimethylsilane, bromochloromethane, propargyl chloride, THF, 1-chloro-2-methylpropane, 1-chloro-2,2-dimethylpropane, 1-chloropropane, 2-chloropropane, 2,2-dibromopropane, 2-bromopropane, (*S*)-2-amino-1-propanol, (*R*)-2-amino-1-propanol, 2-amino-1-propanol, MeOH, (2*S*,3*S*)-2,3-dimethyloxirane, 2,2-dimethyloxirane, 2,3-dimethyl-2-butene, 2-methyl-2-butene, methyl (*R*)-2-hydroxypropanoate, methyl 2-hydroxypropanoate, methyl (*S*)-2-hydroxypropanoate, hexane, benzene, toluene, (1*R*,2*R*)-1,2-dibromocyclohexane, and trichloroethene.
45. We suppose that these differences in the powder XRD patterns are caused by the different solubility of **3** in these solvents: the solubility of **3** in hexane or MeOH is too low to recover a crystalline phase. In contrast, **3** partially dissolves in other solvents (benzene, toluene, THF, or trichloroethene) to recover partial crystalline phases.
46. For $\mathbf{3}_{\mathbf{ground}}$ powders obtained from **3**/CH_2Br_2, **3**/DMA, and **3**/DMF by mechanical stimulation, the proton signals of residual solvents are observed in their ^{1}H NMR spectra (Figure S10). Considering the high boiling points of these solvents, this result indicates that small amounts of solvents released from the crystal lattices remain around the $\mathbf{3}_{\mathbf{ground}}$ phases.
47. For the three powder samples of **3**/CH_2Cl_2, heating–evacuation experiments (70 °C under vacuum for 30 min) were carried out. ^{1}H NMR spectra of the resulting powders in $CDCl_3$ confirmed the proton signals of the residual CH_2Cl_2 molecules (boiling point is 40 °C) had a ratio of 2.5 mol% with respect to **3** (average value for three samples).
48. The powder pattern simulated from the single crystal of **3**/*none* did not match the XRD pattern of the powder of **3** obtained by the addition of trichloroethene. This indicates that, different from the solvents used in **3**/*solvent*, trichloroethene cannot effectively induce crystal formation of **3** when trichloroethene is simply added to $\mathbf{3}_{\mathbf{ground}}$.
49. As shown in Figure S30, through these π–π stacking interactions between benzene units, molecules are connected to form an open-ended chain in the direction orthogonal to the 1D columns connected through Au···Au and π–π stacking interactions.
50. (a) Bernstein, J.; Davey, R. J.; Henck, J. O. *Angew. Chem. Int. Ed.* **1999**, *38*, 3440; (b) Braga, D.; Grepioni, F. *Chem. Soc. Rev.* **2000**, *29*, 229; (c) Bernstein, J. *Polymorphism in Molecular Crystals*; Clarendon Press/International Union of Crystallography, 2002;

Vol. 14; (d) Blagden, N.; Davey, R. J. *Cryst. Growth Des.* **2003**, *3*, 873; (e) Herbstein, F. H. *Acta Cryst. Sect. B* **2006**, *62*, 341.

51. (a) Balch, A. L. *Gold Bull.* **2004**, *37*, 45; (b) Pyykkö, P. *Angew. Chem. Int. Ed.* **2004**, *43*, 4412; (c) Katz, M. J.; Sakai, K.; Leznoff, D. B. *Chem. Soc. Rev.* **2008**, *37*, 1884; (d) Schmidbaur, H.; Schier, A. A Briefing on Aurophilicity. *Chem. Soc. Rev.* **2008**, *37*, 1931; (e) Laguna, A. *Modern Supramolecular Gold Chemistry: Gold-Metal Interactions and Applications*, Wiley-VCH; John Wiley distributor, Weinheim Chichester, 2008; (f) Balch, A. L. *Angew. Chem. Int. Ed.* **2009**, *48*, 2641. (g) Chen, Y.; Cheng, G.; Li, K.; Shelar, D. P.; Lu, W.; Che, C.-M. *Chem. Sci.* **2014**, *5*, 1348.
52. Seki, T.; Kurenuma, S.; Ito, H. *Chem. Eur. J.* **2013**, *19*, 16214.
53. We performed time-dependent density functional theory calculations of **3**/$CHCl_3$, **3**/CH_2Cl_2, and **3**/acetone, as representative **3**/*solvent*, based on coordination of the single-crystal structures (B3LYP/SDD). The results indicate that electron delocalization of LUMO energy levels differed slightly (Figure S31 and S32), but clear factors that explain the luminescent properties of **3**/*solvent* could not be elucidated.
54. Jong, J. D.; Boyer, J. H. *J. Org. Chem.* **1972**, *37*, 3571–3577.
55. Krasovskiy, A.; Malakhov, V.; Gavryushin, A.; Knochel, P. *Angew. Chem. Int. Ed.* **2006**, *45*, 6040.
56. Sheldrick, G. M. SHELXL-2013, Program for the Refinement of Crystal Structures; University of Göttingen, Göttingen, Germany, 2013.
57. Gaussian 09, Revision C.01, Frisch, M. J.; Trucks, G. W.; Schlegel, H. B.; Scuseria, G. E.; Robb, M. A.; Cheeseman, J. R.; Scalmani, G.; Barone, V.; Mennucci, B.; Petersson, G. A.; Nakatsuji, H.; Caricato, M.; Li, X.; Hratchian, H. P.; Izmaylov, A. F.; Bloino, J.; Zheng, G.; Sonnenberg, J. L.; Hada, M.; Ehara, M.; Toyota, K.; Fukuda, R.; Hasegawa, J.; Ishida, M.; Nakajima, T.; Honda, Y.; Kitao, O.; Nakai, H.; Vreven, T.; Montgomery, J., J. A.; Peralta, J. E.; Ogliaro, F.; Bearpark, M.; Heyd, J. J.; Brothers, E.; Kudin, K. N.; Staroverov, V. N.; Kobayashi, R.; Normand, J.; Raghavachari, K.; Rendell, A.; Burant, J. C.; Iyengar, S. S.; Tomasi, J.; Cossi, M.; Rega, N.; Millam, N. J.; Klene, M.; Knox, J. E.; Cross, J. B.; Bakken, V.; Adamo, C.; Jaramillo, J.; Gomperts, R.; Stratmann, R. E.; Yazyev, O.; Austin, A. J.; Cammi, R.; Pomelli, C.; Ochterski, J. W.; Martin, R. L.; Morokuma, K.; Zakrzewski, V. G.; Voth, G. A.; Salvador, P.; Dannenberg, J. J.; Dapprich, S.; Daniels, A. D.; Farkas, Ö.;

Foresman, J. B.; Ortiz, J. V.; Cioslowski, J.; Fox, D. J.; Gaussian, Inc., Wallingford CT, 2009.

Chapter 3.

Luminescent Mechanochromism of a Chiral Complex: Distinct Crystal Structures and Color Changes of Racemic and Homochiral Gold(I) Isocyanide Complexes with a Binaphthyl Moiety

3.1. Introduction

The luminescence properties of mechanochromic solid-state materials are strongly correlated with their molecular packing arrangements in the solid state.[1,2] Thus, controlling the molecular arrangements of mechanochromic compounds is important to tune their emission properties. Taking advantage of polymorphism have been one of method for revealing mechanochromism.[2] However, it is still difficult to predict, design, and control the polymorphism.

Racemic and homochiral compounds often crystallize into different structures that show different physical properties even though they have the same chemical composition. Wallach's rule states that racemic crystals tend to be denser than their homochiral equivalents.[3] Based on this viewpoint, crystals of racemic and homochiral compounds have been investigated with the aim of controlling the molecular packing arrangement in the solid phase and the resulting physical properties.[4]

In 1982, Roitman *et al*.[5a] reported that racemic and homochiral 1-phenylpropyl 9-anthroate crystals display obviously different emission properties. Numerous crystals with different enantiomer compositions that afford distinct emission properties have been reported.[5] However, the different mechanochromic properties of racemic and homochiral crystalline luminescent materials have not been investigated.[6]

Through the studies of mechanochromism by Ito, H. *et al.*, it was suggested that the aryl gold(I) isocyanide moiety is an excellent basic structure to produce new mechanochromic materials.[2a,7] The author anticipates that aryl gold(I) isocyanides could be modified with chiral structures to afford new mechanochromic complexes. In this chapter, binaphthyl gold(I) isocyanide complex **1** which possesses an axially chiral moiety will be described. Crystals prepared from racemic [(*rac*)-**1**] and homochiral [(*S*)-**1**] complexes display distinct emission colors. These two different crystals exhibit luminescent mechanochromism, showing similar red-shifted emission after grinding (Figure 1a and b).

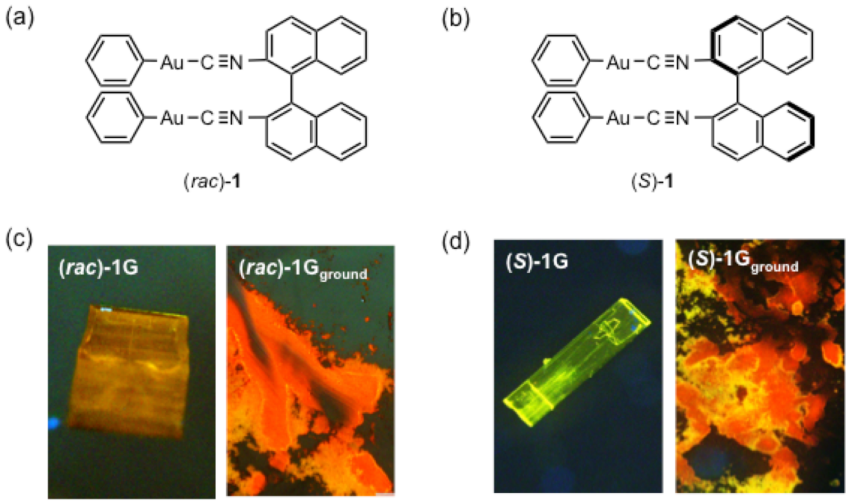

Figure 1. Chemical structure of (a) (*rac*)-**1** and (b) (*S*)-**1**. Photographs of (c) (*rac*)-**1G** and (*rac*)-**1G**$_{ground}$ and (d) (*S*)-**1G** and (*S*)-**1G**$_{ground}$ taken under ultraviolet irradiation (λ_{ex} = 365 nm).

3.2. Results and discussion

3.2.1. Synthesis and Preparation

Gold(I) isocyanide complexes (*rac*)-**1** and (*S*)-**1** were synthesized from the corresponding chiral isocyanide gold(I) complex precursors, (*rac*)-2,2'-[NC-Au(I)-Cl]$_2$-binaphthyl and (*S*)-2,2'-[NC-Au(I)-Cl]$_2$-binaphthyl, respectively,[8] through modification of our reported procedures (see detail in the experimental section).[7] Crystallization of (*rac*)-**1** from CH_2Cl_2/hexane for 6 h afforded cubic crystals of (*rac*)-**1G** that displayed yellowish green emission under ultraviolet irradiation (Figure 1c, λ_{ex} = 365 nm). The same crystallization process of (*S*)-**1** afforded hexagonal crystals of (*S*)-**1G** showing green emission (Figure 1d), which is clearly different from that of (*rac*)-**1G** crystals. Both (*rac*)-**1G** and (*S*)-**1G** displayed luminescent mechanochromism (Figure 1c and d). When the yellowish green-emitting crystals of (*rac*)-**1G** were ground by a mortar and pestle or ball mill at room temperature, a powder of (*rac*)-**1G$_{ground}$** exhibiting red emission was formed. Similar mechanical stimulation of the green-emitting crystals of (*S*)-**1G** gave the powder (*S*)-**1G$_{ground}$**, which has a similar emission color to that of (*rac*)-**1G** crystals.

3.2.2. Single Crystal X-ray Diffraction (XRD) Analyses

To investigate the crystal structures, single-crystal X-ray diffraction (XRD) analyses of (*rac*)-**1G** and (*S*)-**1G** crystals were performed. Single-crystal XRD analysis revealed that (*rac*)-**1G** crystallized in the *Pbcn* space group. In the (*rac*)-**1G** crystal, two molecules of the same enantiomer formed a dimer unit, denoted as an *S*-*S* or *R*-*R* dimer, where each molecule was connected through aurophilic interactions with Au–Au distances of 3.06, 3.34, and 3.06 Å and CH–π interactions (Figure 2a). Both the *S*-*S* and *R*-*R* dimers contained an inversion center (red dots in Figure 2b and c). The *S*-*S* dimers adopted a layer structure, denoted as an *S*-type layer. Adjacent to the *S*-type layer, an *R*-type layer formed through the interactions of *R*-*R* dimers (Figure 2c). The crystalline lattice contained CH_2Cl_2, which was used for recrystallization.

The crystal structure of (*S*)-**1G** was quite different from that of (*rac*)-**1G**. (*S*)-**1G** crystallized in the chiral space group $P2_12_12_1$. In the crystal, two (*S*)-**1** molecules formed a dimer unit, similar to those found in (*rac*)-**1G**. Each dimer was held together by three aurophilic bonds with Au–Au distances of 3.07, 3.14, and 3.16 Å and CH– π interactions (Figure 2d). The relative arrangement of dimers in (*S*)-**1G** was markedly different from that in (*rac*)-**1G**. In the case of (*S*)-**1G**, two adjacent *S*-*S* dimers were packed as shown in Fig. 2e and S11 and there were no inversion centers. This difference of dimer arrangement reflects how the layer structure of (*S*)-**1G** is distinct from that of (*rac*)-**1G** (Figure 2c and f). Disordered CH_2Cl_2 molecules were located between the two adjacent dimers (Figure 2f).

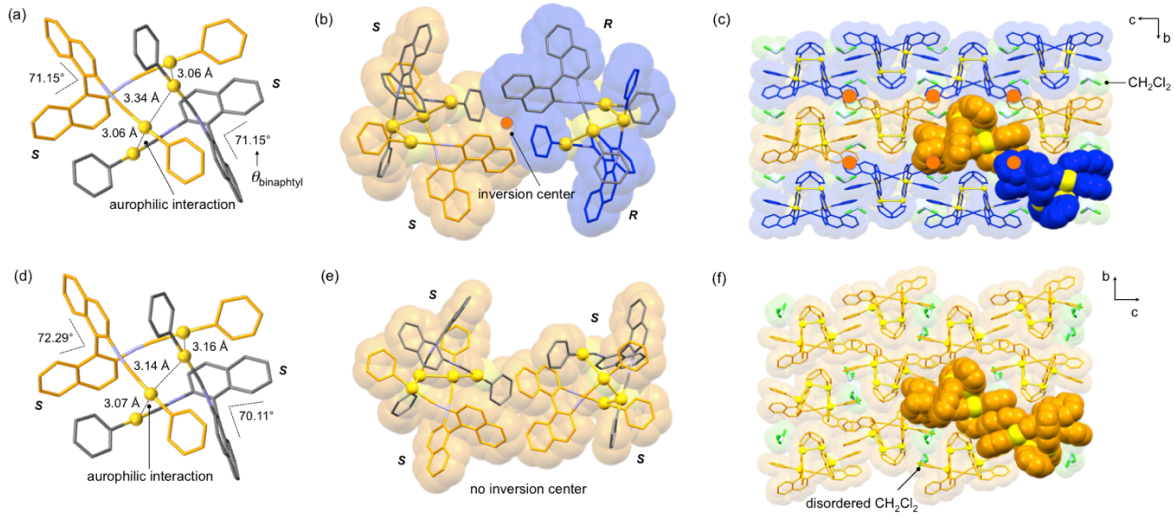

Figure 2. Single-crystal structures of (a–c) (*rac*)-**1G**, and (d–f) (*S*)-**1G**. (a) Dimer, (b) tetramer, and (c) layer structures of (*rac*)-**1G**. (d) Dimer, (b) tetramer, and (c) layer structures of (*S*)-**1G**. All H atoms were omitted for clarity.

3.2.3. Studies of Crystal Structure Alterations by Mechanical Stimulation

The structural changes of (*rac*)-**1G** and (*S*)-**1G** induced by mechanical stimulation were observed by powder XRD measurements. Ground powders (*rac*)-**1G**$_{\mathbf{ground}}$ and (*S*)-**1G**$_{\mathbf{ground}}$ were prepared by ball milling (*rac*)-**1G** and (*S*)-**1G** for 30 min at 4600 rpm, respectively. The lack of features in the powder XRD patterns of (*rac*)-**1G**$_{\mathbf{ground}}$ and (*S*)-**1G**$_{\mathbf{ground}}$ reveals that both powders are amorphous (orange lines in Figure 3a and b). As already mentioned above, crystals of (*rac*)-**1G** and (*S*)-**1G** included 0.25 and 0.5 equiv. of CH_2Cl_2 molecules in each crystalline lattice, respectively [thermogravimetric analysis (TGA) (Figure S1), ^{1}H NMR spectral data (Figure S2), and single-crystal XRD analysis (Figure S3 and S4) are presented in the experimental section]. In contrast, elemental analyses, TGA and ^{1}H NMR spectroscopy of (*rac*)-**1G**$_{\mathbf{ground}}$ and (*S*)-**1G**$_{\mathbf{ground}}$ revealed that both the ground powders do not include CH_2Cl_2 molecules (Table S1, Figure S1 and S2). The CH_2Cl_2 molecules in both (*rac*)-**1G** and (*S*)-**1G** can be removed by holding the samples under vacuum at 65 °C for 1 h (Figure S5). Both (*rac*)-**1G** and (*S*)-**1G** remained crystalline after removal of CH_2Cl_2, and their emission colors did not change (Figure S6–S8). These results indicate that inclusion/desorption of CH_2Cl_2 do not correspond to the alterations of the crystal structures and the mechanochromic properties.

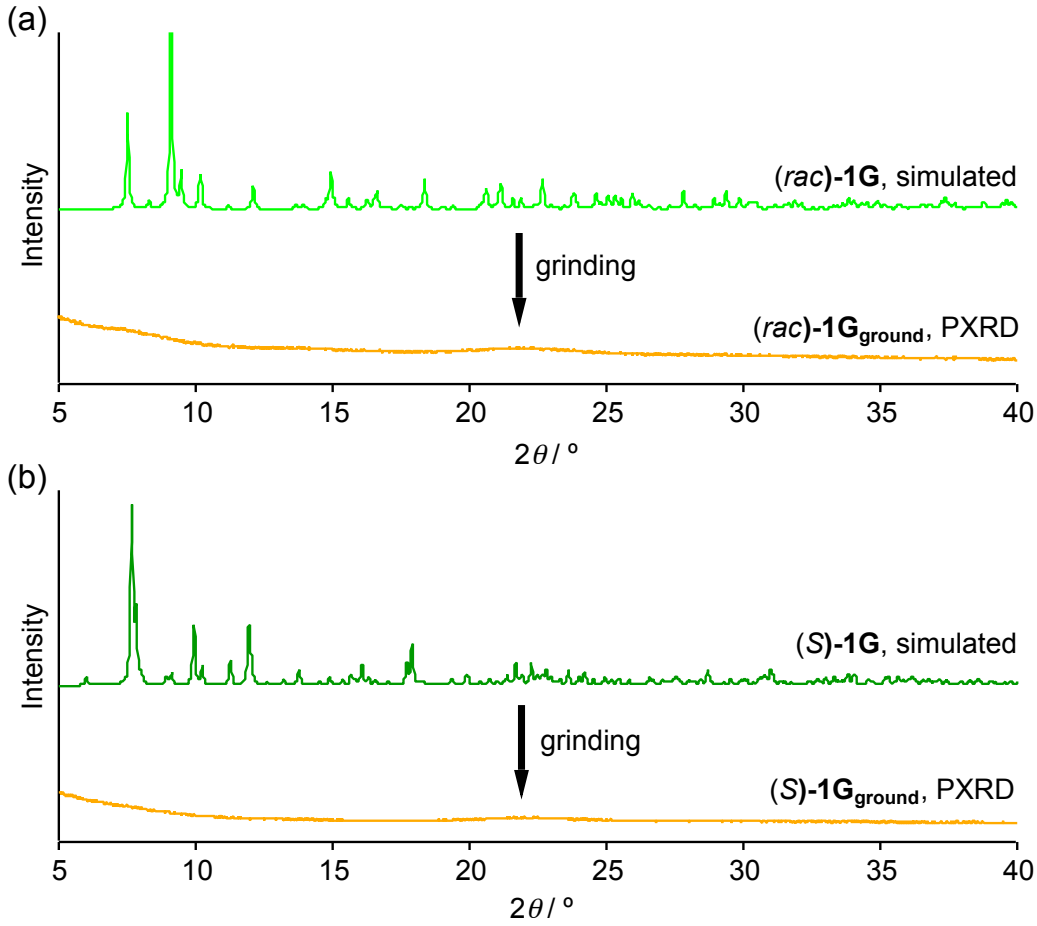

Figure 3. PXRD pattern changes from (a) (*rac*)-**1G** (light green line, simulated pattern) to (*rac*)-**1G**$_{ground}$ (orange line) and (b) (*S*)-**1G** (green line, simulated pattern) to (*S*)-**1G**$_{ground}$ (orange line).

3.2.4. Luminescent Mechanochromism of (*rac*)-1G and (*S*)-1G

Emission spectroscopy measurements of pristine (*rac*)-**1G** and (*S*)-**1G** and their ground phases were performed. The emission spectrum of (*rac*)-**1G** is broad with a maximum emission wavelength $\lambda_{em,max}$ of 546 nm upon excitation at 365 nm (light green solid line in Figure 4a). Upon grinding, the emission of (*rac*)-**1G** shows a clear red shift. The ground powder (*rac*)-**1G$_{ground}$** exhibited a broad emission spectrum with $\lambda_{em,max}$ at 664 nm (orange solid line in Figure 4a). The emission spectrum of (*S*)-**1G** (green solid line in Figure 2a) is different from that of (*rac*)-**1G**. For example, $\lambda_{em,max}$ of (*S*)-**1G** is 517 nm, which is shorter than that of (*rac*)-**1G**. In contrast, the emission spectrum of (*S*)-**1G$_{ground}$** ($\lambda_{em,max}$ = 664 nm) (red solid line in Figure 4a) is almost the same as that of (*rac*)-**1G$_{ground}$**.

Excitation spectra of the samples were measured. The excitation spectrum of (*rac*)-**1G** contained a broad band ranging from 350 to 480 nm with a maximum excitation wavelength $\lambda_{ex,max}$ of 454 nm (λ_{em} = 546 nm, light green solid line in Figure 4b). The excitation spectrum of (*rac*)-**1G$_{ground}$** also possessed a similar broad band with $\lambda_{ex,max}$ = 449 nm (λ_{em} = 546 nm, orange solid line in Figure 4b). In the case of (*S*)-**1G**, similar excitation spectral changes were observed. The excitation spectrum of (*S*)-**1G** obtained at 517 nm contained a broad band spanning 350–500 nm with $\lambda_{ex,max}$ = 458 nm (green solid line in Figure 4b). Excitation of (*S*)-**1G$_{ground}$** at 664 nm produced a similar broad excitation band with $\lambda_{ex,max}$ = 445 nm. This result indicates that the excitation spectra of this system are not strongly influenced by distinct molecular packing arrangements.

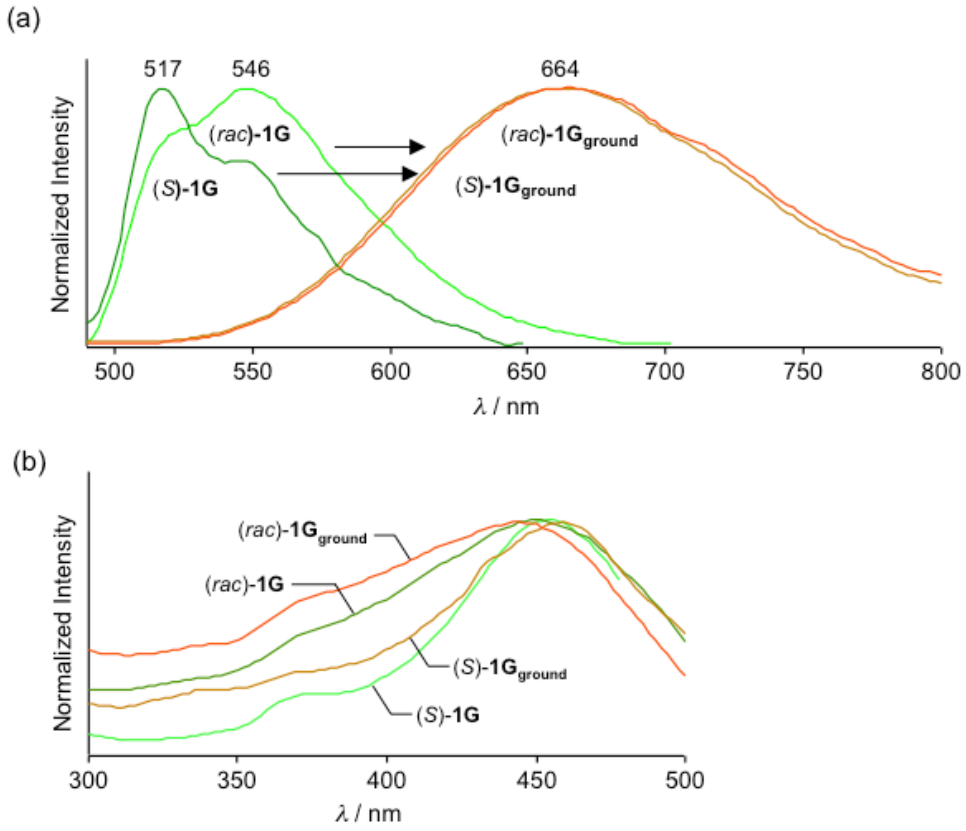

Figure 4. (a) Emission spectra changes from (*rac*)-**1G** to (*rac*)-**1G$_{ground}$**, and from (*S*)-**1G** to (*S*)-**1G$_{ground}$** (λ_{ex}=365 nm). (b) Excitation spectra of (*rac*)-**1G**, (*S*)-**1G**, (*rac*)-**1G$_{ground}$**, and (*rac*)-**1G$_{ground}$** obtained at each $\lambda_{em,max}$.

Emission lifetimes and quantum yields Φ_{em} of both crystals and their ground powders were measured. (*rac*)-**1G** showed a low Φ_{em} of 0.08 with an average emission lifetime τ_{av} of 5.34 μs, while the ground powder (*rac*)-**1G$_{ground}$** displayed an increased Φ_{em} of 0.21. τ_{av} of (*rac*)-**1G$_{ground}$** is 5.10 μs, which is slightly shorter than that of (*rac*)-**1G** (Table 1, Figure S3). In the case of (*S*)-**1G**, Φ_{em} was also low (0.02). After grinding, Φ_{em} of (*S*)-**1G$_{ground}$** increased to 0.13. Meanwhile, τ_{av} of (*S*)-**1G** and (*S*)-**1G$_{ground}$** were almost the same at 5.34 and 5.36 μs, respectively. The photoluminescent intensities of (*rac*)-**1** and (*S*)-**1** in CH_2Cl_2 were very weak, so we could not measure their emission properties. This indicates that the high emission intensities of solid-state (*rac*)-**1** and (*S*)-**1** strongly depend on their aggregated structures.[9]

Table 1. Photophysical properties of (*rac*)-**1G**, (*S*)-**1G**, (*rac*)-**1G$_{ground}$**, and (*S*)-**1G$_{ground}$**

1.	$\lambda_{em,max}$[a] / nm	Φ_{em} (λ_{ex} / nm) / %	τ_{av}[b] / μs
(*rac*)-**1G**	546	0.08 (454)	5.34
(*S*)-**1G**	517	0.02 (458)	5.34
(*rac*)-**1G$_{ground}$**	664	0.21 (449)	5.10
(*S*)-**1G$_{ground}$**	664	0.13 (445)	5.36

[a]: maximum emission wavelength (λ_{ex} = 365 nm), [b]: $\tau_{av} = \Sigma \tau_n A_n^2 / \Sigma \tau_n A_n$, obtained by tail fitting (λ_{ex} = 370 nm).

The relationships between the emission properties and crystal structures of each phase are now discussed. Dimer units constructed from two molecules of the same enantiomer, such as *S*-*S* dimers, are observed in both (*rac*)-**1G** and (*S*)-**1G**. The fundamental structures of dimers found in (*rac*)-**1G** and (*S*)-**1G** crystals are very similar. For example, three aurophilic bonds are present in both crystals, and the average Au–Au distances of (*rac*)-**1G** and (*S*)-**1G** are 3.15 and 3.12 Å, respectively, which is a difference of only 0.03 Å. The minimum dihedral angle between the naphthyl groups of the binaphthyl moiety ($\theta_{binaphthyl}$) of (*rac*)-**1G** was 71.15°, and that of (*S*)-**1G** was 70.11°. The average $\theta_{binaphthyl}$ of dimers in (*rac*)-**1G** and (*S*)-**1G** were 71.15° and 71.20°, respectively. Therefore, the considerable structural difference between crystalline (*rac*)-**1G** and (*S*)-**1G** probably lies in the relative arrangements of the dimer units rather than the structure of the dimer unit itself. The powder XRD patterns suggest that both (*rac*)-**1G$_{ground}$** and (*S*)-**1G$_{ground}$** adopt random molecular arrangements, indicating collapse of the dimer packing upon mechanical stimulation (Figure 5). Both ground powders show similar red-shifted emission with higher Φ_{em} than those of their parent crystals. Because a red shift of emission and increase of Φ_{em} are typically observed for mechanochromic gold(I) isocyanide complexes, these experimental results suggest that the aurophilic interactions strengthen after mechanical stimulation.[7] The elaborated crystal structure and photophysical property differences between (*rac*)-**1** and (*S*)-**1** crystals, which originated from different enantiomer compositions, were amalgamated into uniform amorphous structures with similar emission colors by grinding. It should be noted that only mechanical stimulation promoted this amorphization with the disappearance of the individuality of racemic and homochiral crystals.

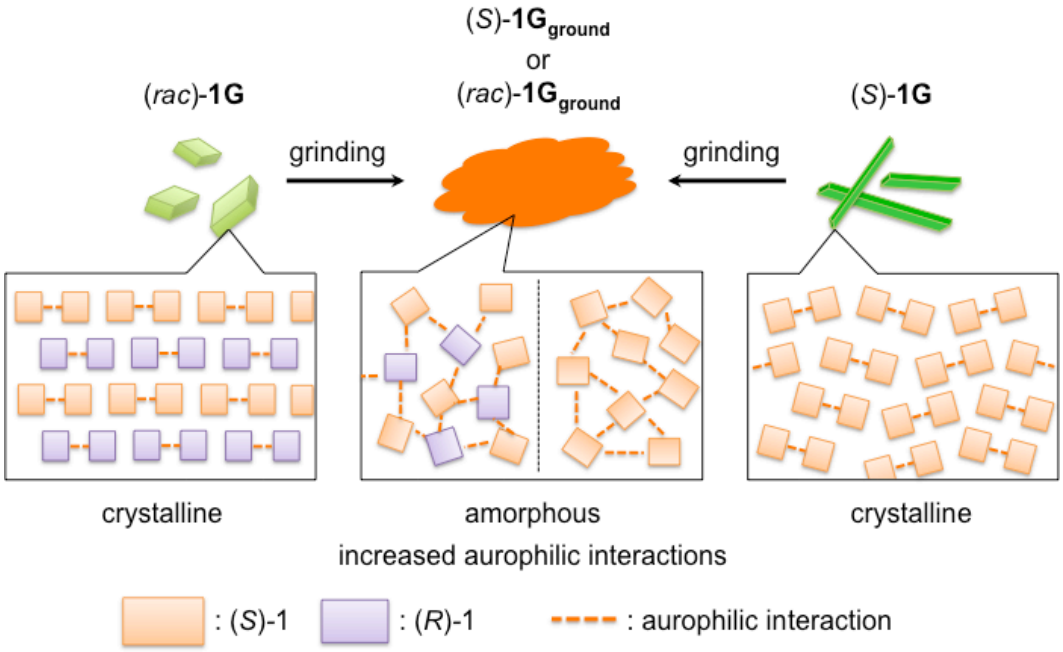

Figure 5. Top: schematics of mechanochromism of (*rac*)-**1G** converting to (*rac*)-**1G** $_{\text{ground}}$ (from left to center) and (*S*)-**1G** converting to (*S*)-**1G** $_{\text{ground}}$ (from right to center). Bottom: schematics of the corresponding molecular arrangements in which orange and purple rectangles represent (*S*)-**1** and (*R*)-**1** molecules, respectively.

3.3. Summary

Racemic and homochiral forms of gold(I) isocyanide complex **1** possessing a binaphthyl moiety with distinct luminescent crystals that exhibit mechanochromism. Crystals of (*rac*)-**1G** and (*S*)-**1G** showed distinct emission colors and different crystal packing structures. The powders obtained by grinding both crystals were amorphous and displayed similar emission colors. This is the first example of luminescent mechanochromism of racemic and homochiral compounds that display distinct emission colors. These results indicate that the introduction of chirality can be a promising structure modification to fine tune the properties of mechanochromic materials.

3.4. Experimental Section

3.4.1. General

All commercially available reagents and solvents are of reagent grade and were used without further purification unless otherwise noted. Solvents for the synthesis were purchased from commercial suppliers, degassed by three freeze-pump-thaw cycles and further dried over molecular sieves (4 Å). NMR spectra were recorded on a JEOL JNM-ECX400P or JNM-ECS400 spectrometer (^{1}H: 400 MHz; ^{13}C: 99.5 MHz) using tetramethylsilane and $CDCl_3$ as internal standards, respectively. Emission spectra were recorded on a Hitachi F-7000 spectrometer. The emission quantum yields of the solid samples were recorded on a Hamamatsu Quantaurus-QY spectrometer with an integrating sphere. Emission lifetime measurements were recorded on a Hamamatsu Quantaurus-Tau spectrometer. Elemental analyses and low- and high-resolution mass spectra were recorded at Global Facility Center, Creative Research Institution, Hokkaido University. Photographs were obtained using Olympus BX51 or SZX7 microscopes with Olympus DP72, Nikon D5100 or RICOH CX1 digital cameras. Thermal gravimetric analysis profiles were recorded on Bruker TG-DTA2010SAT.

3.4.2. Synthesis of (*rac*)-1 and (*S*)-1

*Synthesis of (rac)-**1**.*

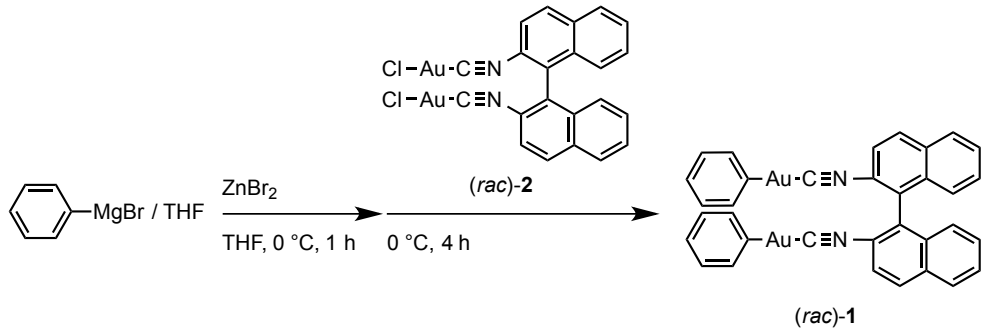

A powder of zinc bromide (0.067 g, 0.30 mol) was placed in an oven-dried two-neck flask. The flask was connected to a vacuum/nitrogen manifold through a rubber tube. It was evacuated and then backfilled with nitrogen. This cycle was repeated three times. THF (1.0 mL) was then added in the flask through the rubber septum using a syringe and stirred at 0 °C. A phenylmagnesium bromide reagent in THF (0.400 ml, 0.30 mmol, 0.75 M) was then added to the reaction mixture using a syringe and stirred at 0 °C for 1 h. Then, a solid of (*rac*)-**2** [10](0.072 g, 0.10 mmol) was added and the mixture was stirred at 0 °C. After the reaction completion was monitored by TLC analysis, the reaction mixture was quenched by the addition of a phosphate buffer solution and then extracted with CH_2Cl_2 three times and washed with H_2O and brine. The organic layers were collected and dried over $MgSO_4$. After filtration, the solvent was removed in vacuo. Further purification by flash column chromatography (SiO_2, CH_2Cl_2/hexane = 1:1) gave an analytically pure orange solid of (*rac*)-**1** (0.060 g, 0.070 mmol, 70 %). ^{1}H NMR (400 MHz, $CDCl_3$, δ): 7.01–7.06 (m, 2H), 7.16–7.20 (m, 6H), 7.29 (dd, *J* = 1.6, 8.0 Hz, 4H), 7.52 (t, *J* = 7.8 Hz, 2H), 7.71–7.75 (m, 4H) 8.09 (d, *J* = 8.4 Hz, 2H), 8.20 (d, *J* = 8.2 Hz, 2H). ^{13}C NMR (100 MHz, $CDCl_3$, δ): 122.7 (C), 123.2 (CH), 126.0 (CH), 126.2 (CH), 127.5 (CH), 129.2 (CH), 129.3 (CH), 131.0 (C), 131.6 (C), 132.1 (CH), 133.8 (C), 140.6 (CH), 162.5 (C), 164.6 (CH). MS-ESI (m/z): $[M+Na]^+$ calculated for $C_{34}H_{22}Au_2N_2Na^+$, 875.10; found, 875.10. Anal. Calcd for $C_{34}H_{22}Au_2N_2$: C, 47.90; H, 2.60; N, 3.29. Found: C, 48.48; H, 2.74; N, 3.10.

*Synthesis of (S)-**1**.*

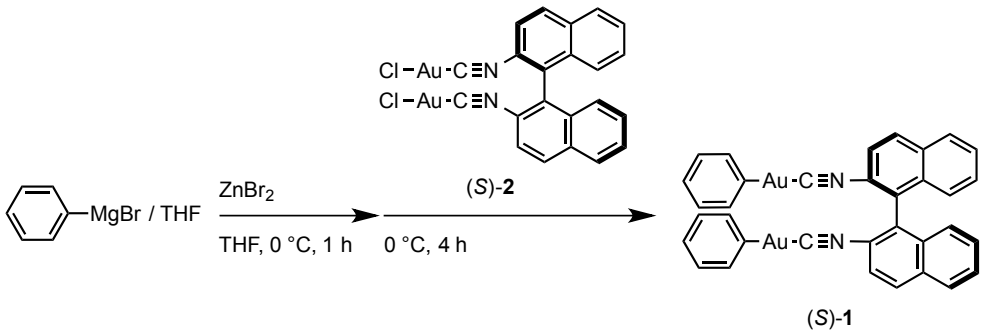

(*S*)-**1** was prepared from (*S*)-**2** [10](0.145, 0.20 mmol) according to the procedure similar to that described for the preparation of (*rac*)-**1**. Yield: 74 % (0.127g, 0.149 mmol, orange solid). ^{1}H NMR (400 MHz, $CDCl_3$, δ): 7.01–7.06 (m, 2H), 7.16–7.20 (m, 6H), 7.30 (dd, *J* = 1.6, 8.0 Hz, 4H), 7.52 (t, *J* = 7.8 Hz, 2H), 7.71–7.75 (m, 4H) 8.09 (d, *J* = 8.0 Hz, 2H), 8.19 (d, *J* = 8.8 Hz, 2H). ^{13}C NMR (100 MHz, $CDCl_3$, δ): 122.7 (C), 123.3 (CH), 126.0 (CH), 126.1 (CH), 127.5 (CH), 129.2 (CH), 129.3 (CH), 131.0 (C), 131.6 (C), 132.0 (CH), 133.8 (C), 140.6 (CH), 162.5 (C), 164.4 (C). MS-ESI (m/z): $[M+Na]^+$ calculated for $C_{34}H_{22}Au_2N_2Na^+$, 875.10; found, 875.10. Anal. Calcd. For $C_{34}H_{22}Au_2N_2$: C, 47.90; H, 2.60; N, 3.29. Found: C, 48.23; H, 2.75; N, 3.09.

Preparation of the single crystals of (*rac*)-**1G** and (*S*)-**1G**: The resulting solid was dissolved in CH_2Cl_2 in a vial and hexane was carefully layered for crystallization and allowed to stand at room temperature to give CH_2Cl_2 included crystals (*rac*)-**1G** and (*S*)-**1G**.

3.4.3. Optical properties of solution phase

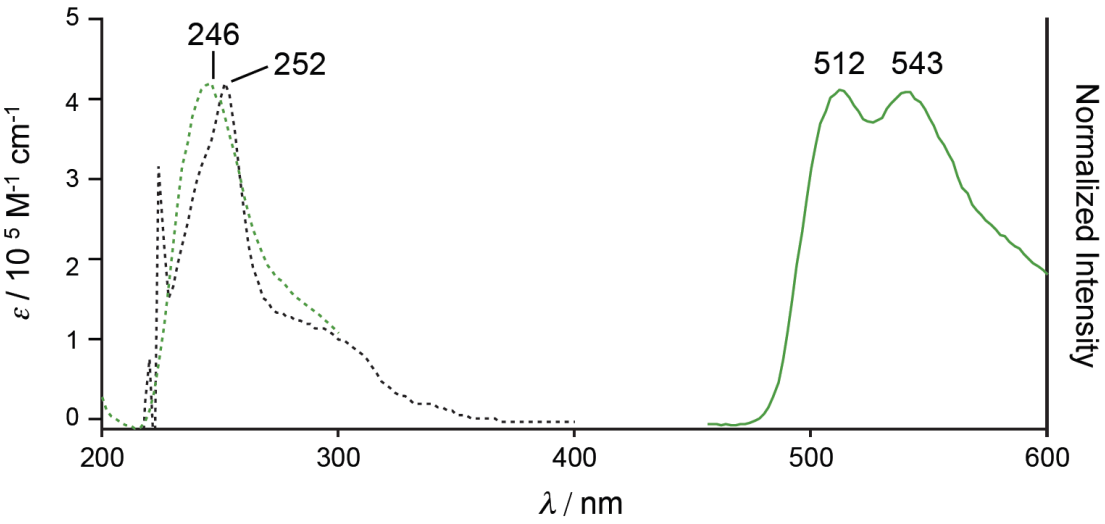

Figure S1. UV/vis absorption (black dashed line), excitation (green dashed line, λ_{em} = 512 nm), and emission spectra (green solid line, λ_{ex} = 246 nm) of (*rac*)-**1** in CH_2Cl_2 (*c* = 2.8 Å~ 10^{-5} M) at room temperature.

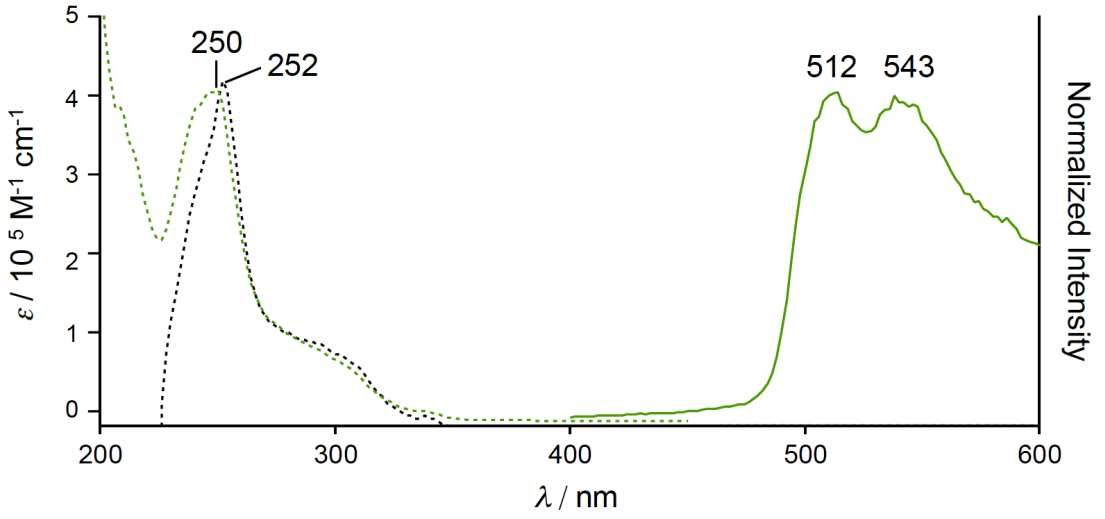

Figure S2. UV/vis absorption (black dashed line), excitation (green dashed line, λ_{em} = 512 nm), and emission spectra (green solid line, λ_{ex} = 250 nm) of (*S*)-**1** in CH_2Cl_2 (c = 3.2 Å~ 10^{-5} M) at room temperature.

3.4.4. Photophysical properties of each solid phase

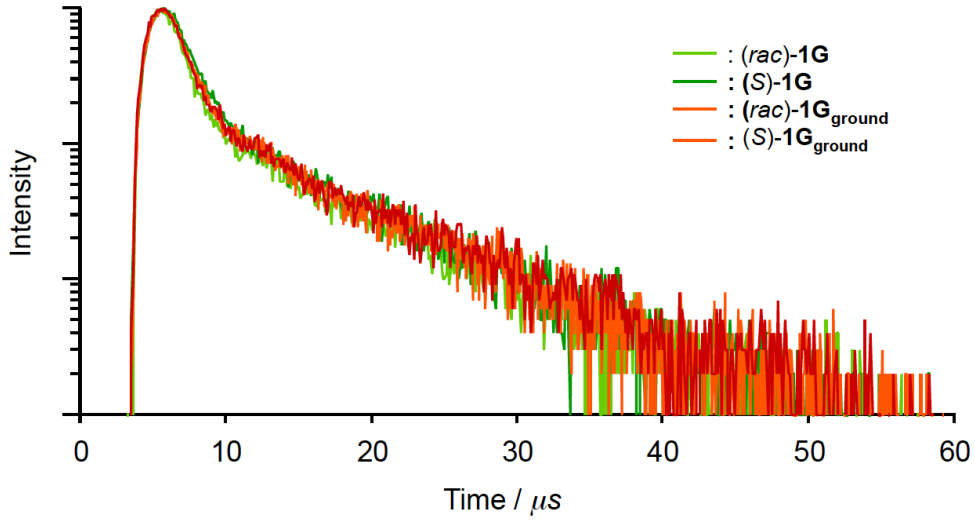

Figure S3. Emission decay profiles of (*rac*)-**1G** (λ_{em} = 546 nm), (*S*)-**1G** (λ_{em} = 517 nm), (*rac*)-**1G**$_{ground}$ (λ_{em} = 664 nm), and (*S*)-**1G**$_{ground}$ (λ_{em} = 664 nm). Excitation wavelength is 370 nm.

Table S1. Photophysical properties of (*rac*)-**1G**, (*S*)-**1G**, (*rac*)-**1G**$_{ground}$, and (*S*)-**1G**$_{ground}$

	Φ_{em} / -	τ_{av} / μs[e,f] (λ_{em} / nm)	τ_1 / μs[e] (A / -)	τ_2 / μs[e] (A / -)
(*rac*)-**1G**	0.081[a]	5.34 (546)	1.40 (0.90)	10.11 (0.10)
(*S*)-**1G**	0.023[b]	5.34 (517)	1.60 (0.87)	9.60 (0.13)
(*rac*)-**1G**$_{ground}$	0.21[c]	5.10 (664)	1.41 (0.87)	8.86 (0.14)
(*S*)-**1G**$_{ground}$	0.13[d]	5.36 (664)	1.38 (0.87)	9.37 (0.13)

[a]λ_{ex} = 454 nm. [b]λ_{ex} = 458 nm. [c]λ_{ex} = 449 nm. [d]λ_{ex} = 445 nm. [e]λ_{ex} = 370 nm. [f]$\tau_{av} = (A_1\tau_1^2 + A_2\tau_2^2 + \cdots) / (A_1\tau_1 + A_2\tau_2 + \cdots)$. Emission decay were fitted by tail fitting.

3.4.5. TGA profiles

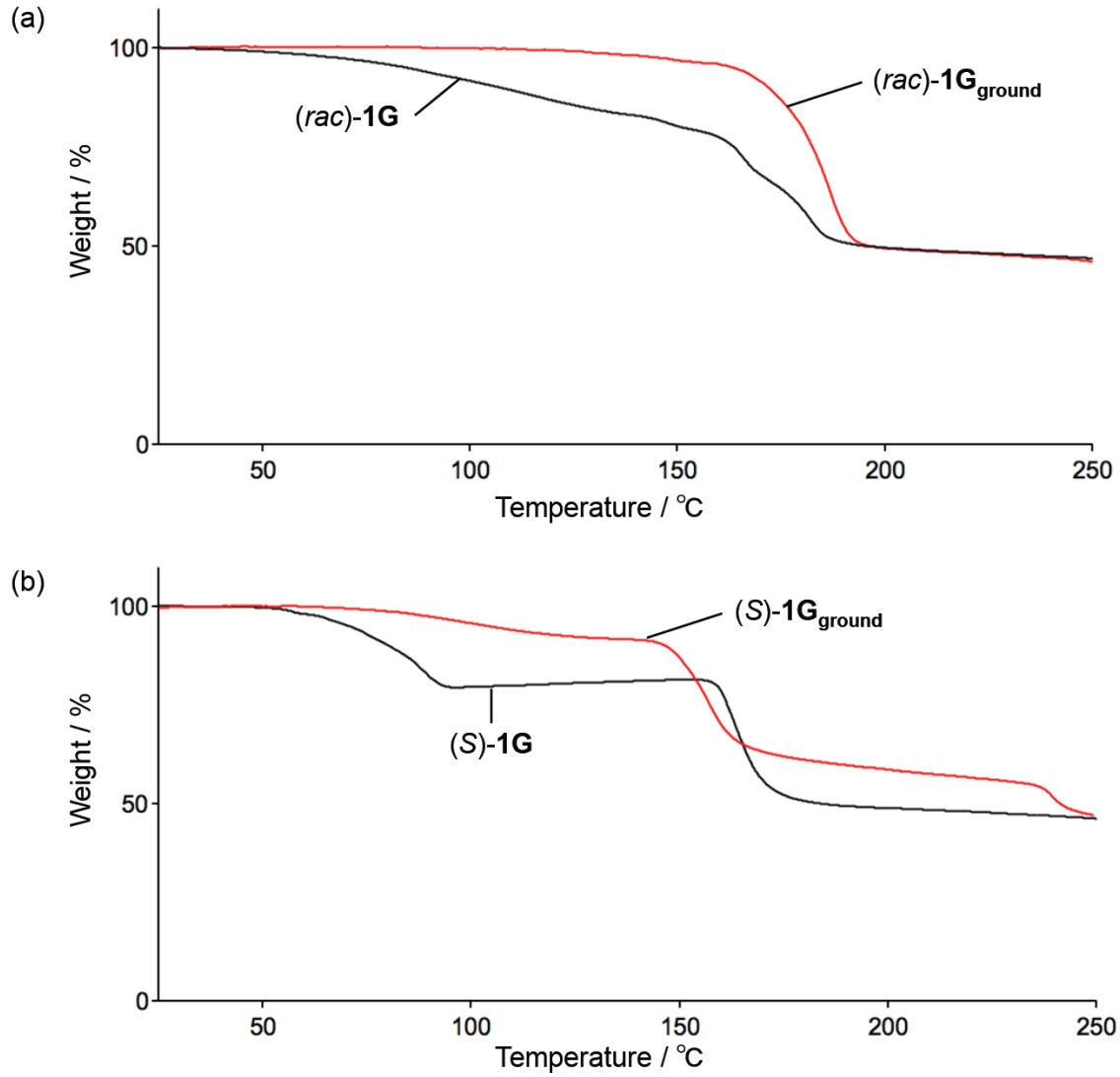

Figure S4. TGA profiles of (*rac*)-**1G** [black line in (a)], (*rac*)-**1G**$_{ground}$ [red line in (a)], (*S*)-**1G** [black line in (b)], and (*S*)-**1G**$_{ground}$ [red line in (b)] at heating rates of 5 °C min^{-1}.

3.4.6. NMR spectra and elemental analysis

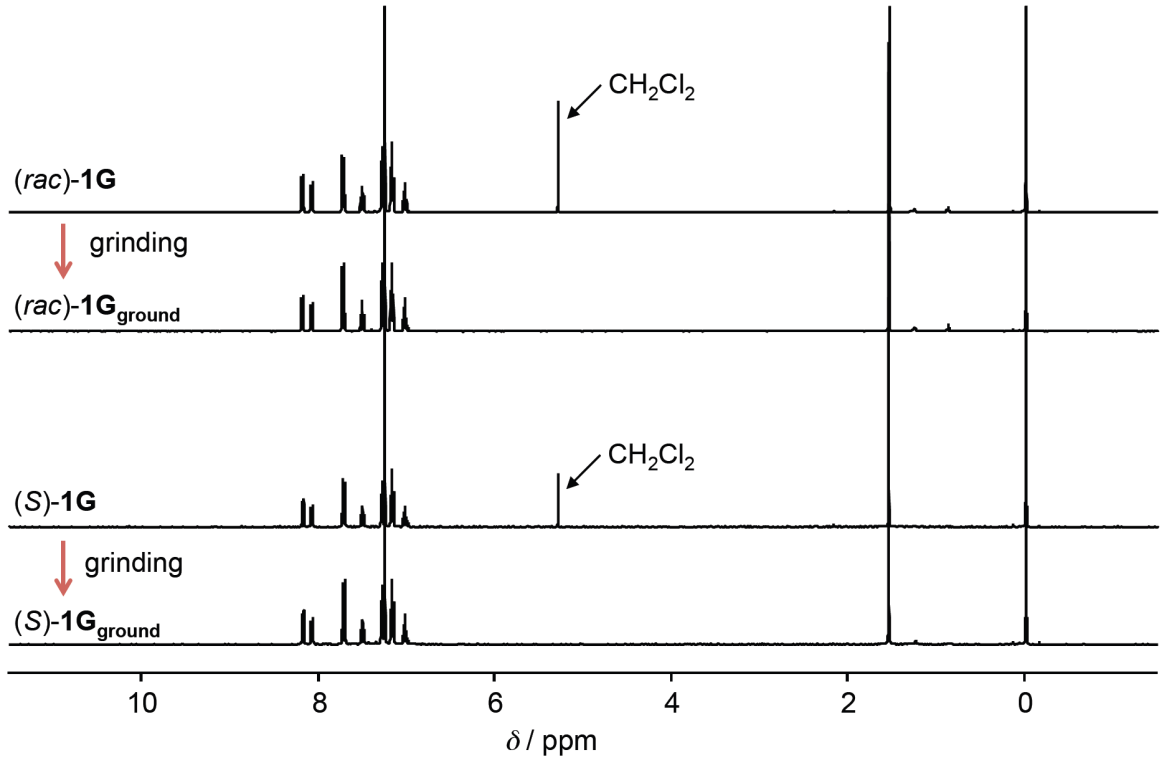

Figure S5. ^{1}H NMR spectra of (*rac*)-**1G**, (*rac*)-**1G**$_{ground}$, (*S*)-**1G**, and (*S*)-**1G**$_{ground}$ dissolved in $CDCl_3$.

Table S2. Elemental analyses of the ground powders (*rac*)-**1G**$_{ground}$ and (*S*)-**1G**$_{ground}$.

	C	H	N
Calculated for **1** ($C_{34}H_{22}Au_2N_2$)	47.90	2.60	3.29
(*rac*)-**1G**$_{ground}$	48.23	2.73	3.08
(*S*)-**1G**$_{ground}$	47.46	2.55	3.21

3.4.7. The CH_2Cl_2 release by heating under vacuum from (*rac*)-1G and (*S*)-1G

No emission color change takes place when CH_2Cl_2 was released from (*rac*)-**1G** and (*S*)-**1G** by heating under vacuum, rather than mechanical stimulation. The CH_2Cl_2 molecules included in both crystals of (*rac*)-**1G** and (*S*)-**1G** (Figure S6) can be released under vacuum at 65 ºC for 1 h which is confirmed by ^{1}H-NMR studies (Figure S7). The emission spectra of (*rac*)-**1G** and (*S*)-**1G** after releasing CH_2Cl_2 by above procedure were almost identical to those containing CH_2Cl_2 (Figure S8). During this procedure for releasing CH_2Cl_2, molecular arrangements of both complexes are unchanged, which are confirmed by intact PXRD patterns (Figure S9). These results indicate that mechano-induced emission color changes of these complexes are caused by the phase transition into amorphous phase rather than just by the release of included CH_2Cl_2 molecules.

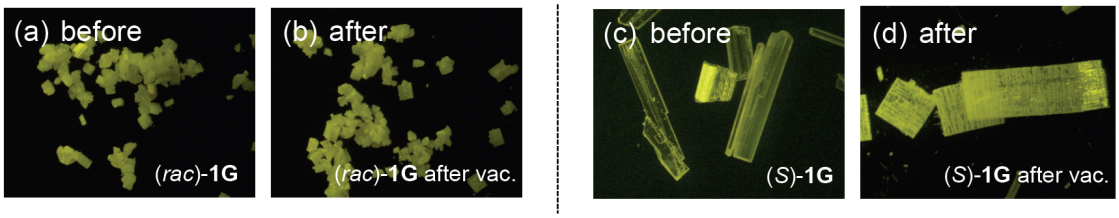

Figure S6. Photographs of (a) (*rac*)-**1G** and (c) (*S*)-**1G** crystals and the corresponding crystals of (b) (*rac*)-**1G** and (d) (*S*)-**1G** obtained after heated at 65 ºC for 1h under vacuum. These photographs were taken under UV irradiation at 367 nm at room temperature under air.

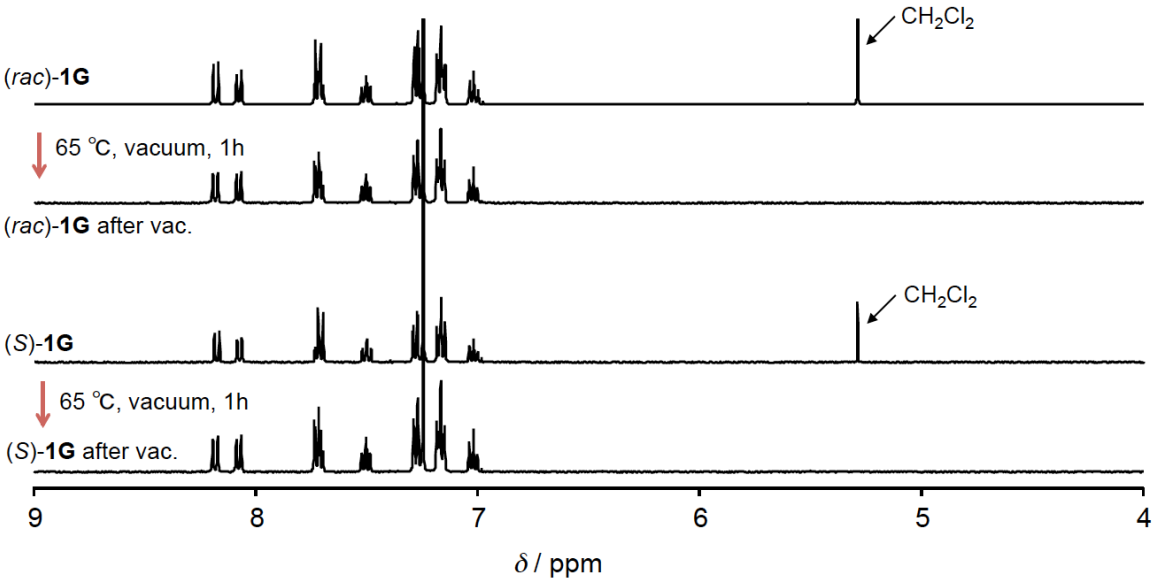

Figure S7. ^{1}H-NMR spectra of (a) (*rac*)-**1G** obtained before and after heating at 65 ºC for 1h and (b) (*S*)-**1G** obtained before and after heating at 65 ºC for 1h dissolved in $CDCl_3$.

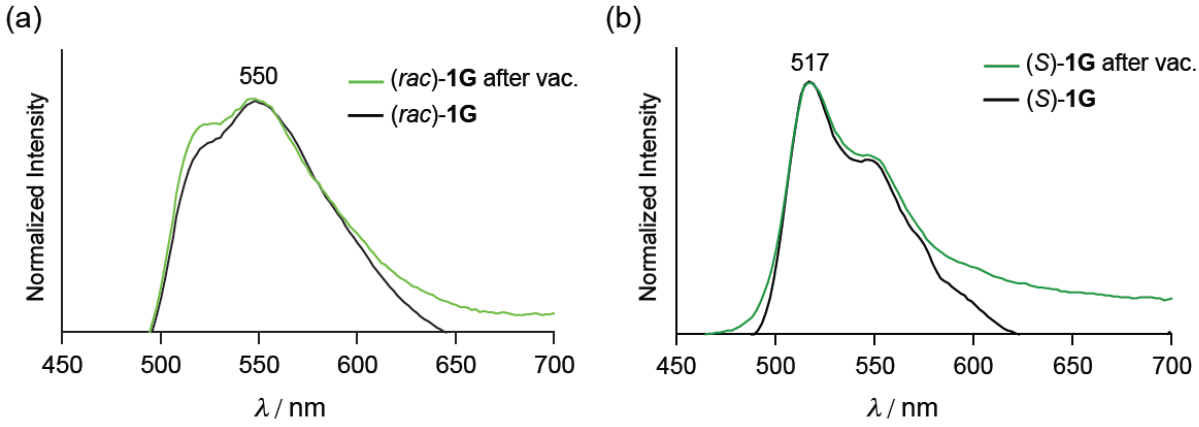

Figure S8. Emission spectra of a (a) (*rac*)-**1G** before (black line) and after heating at 65 ºC for 1h (light green line) and (b) (*S*)-**1G** before (black line) and after heating at 65 ºC for 1h (green line). Excitation wavelength is 365 nm.

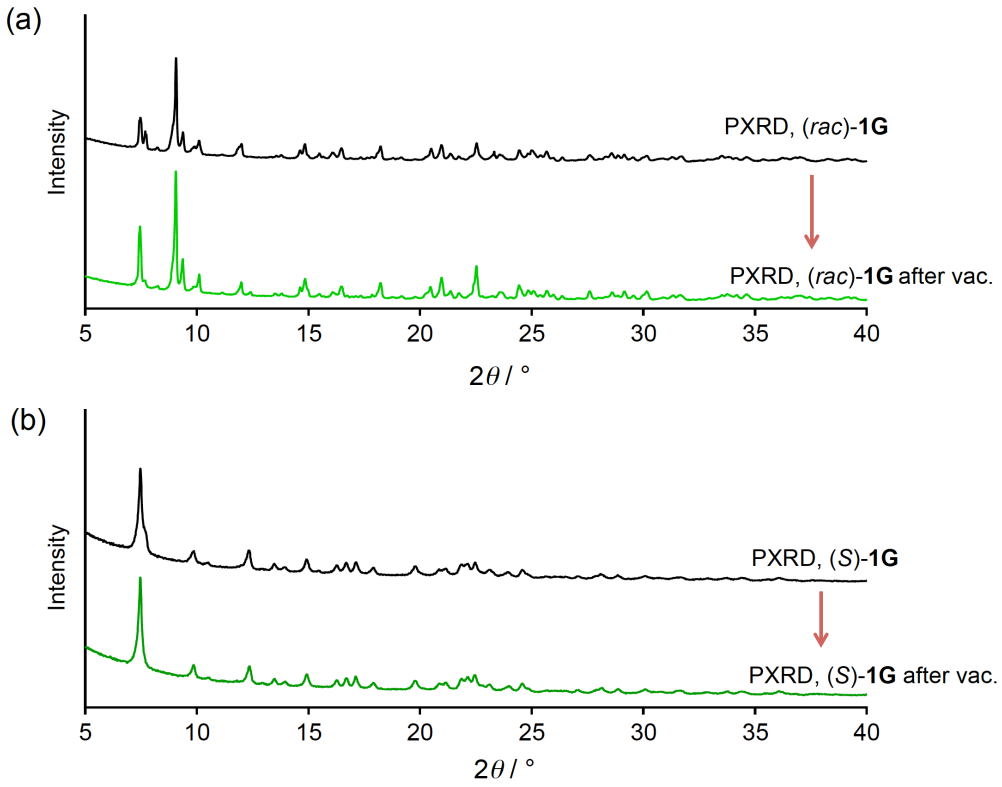

Figure S9. PXRD patterns of (a) (*rac*)-**1G** before (black line) and after heating at 65 ºC for 1h (yellowish green line) and (b) (*S*)-**1G** before (black line) and after heating at 65 ºC for 1h (green line).

3.4.8. Crystal structures of (*rac*)-1G and (*S*)-1G

Single crystal X-ray structural analyses were carried out on a Rigaku R-AXIS RAPID diffractometer using graphite monochromated Mo-K_α radiation. The structure was solved by direct methods and expanded using Fourier techniques. Non-hydrogen atoms were refined anisotropically. Hydrogen atoms were refined using the riding model. All calculations were performed using the CrystalStructure crystallographic software package except for refinement, which was performed using SHELXL-2013.[12]

Table S3. Summary of X-ray crystallographic data for (*rac*)-**1G** and (*S*)-**1G**.

Crystal	(*rac*)-**1G**	(*S*)-**1G**
CCDC Name	1472283	1472333
Empirical Formula	$C_{34.25}H_{22.5}Au_2Cl_{0.5}N_2$	$C_{34.5}H_{23}Au_2ClN_2$
Formula Weight	873.73	894.96
Crystal System	orthorhombic	orthorhombic
Crystal Size / mm	0.165 × 0.131 × 0.072	0.362 × 0.091 × 0.036
a / Å	13.0435(4)	13.3962(12)
b / Å	18.7272(7)	19.3637(16)
c / Å	23.6159(9)	22.587(2)
α / °	90	90
β / °	90	90
γ / °	90	90
V / Å^3	5768.6(4)	5859.0(9)
Space Group	*Pbcn* (#60)	$P2_12_12_1$ (#19)
Z value	8	8
D_{calc} / g·cm^{-3}	2.012	2.029
Temperature / K	123	123
$2\theta_{max}$ / °	52.0	52.0
μ (MoK$_\alpha$) / cm^{-1}	102.685	101.568
No. of Reflections Measured	Total : 46284 Unique : 5667 (R_{int} = 0.0887)	Total : 5525 Unique : 2516 (R_{int} = 0.0574)
Residuals: R_1 (I > 2.00σ (I)) / %	3.80	6.43
Residuals: wR_2 (All reflections) / %	7.49	13.83
Goodness of Fit (GOF)	1.061	1.052
Maximum peak in Final Diff. Map / Å^3	0.85 e$^-$	1.67 e$^-$
Minimum peak in Final Diff. Map / Å^3	–1.19 e$^-$	–1.75 e$^-$
Flack Parameter	-	0.004 (15)

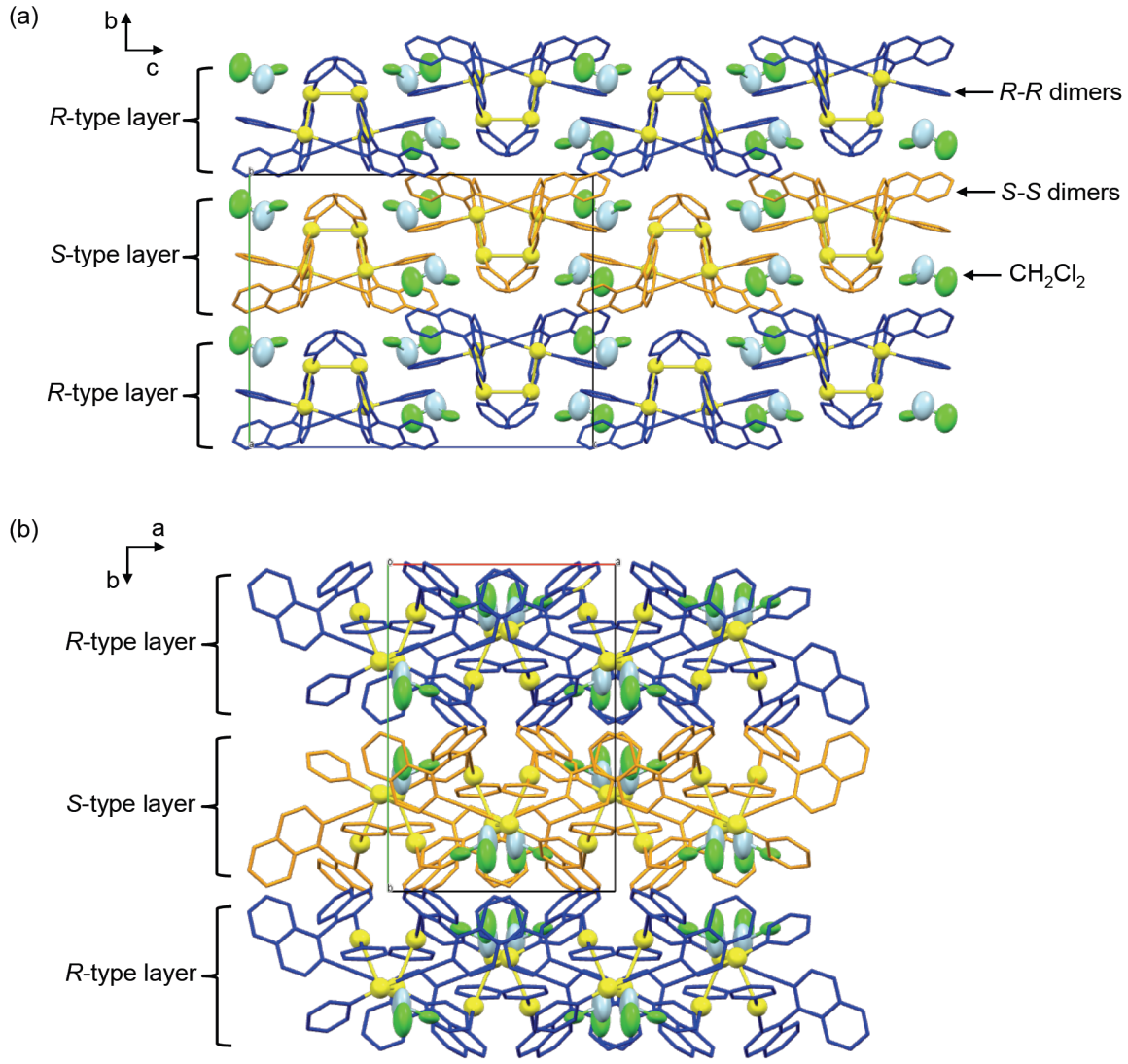

Figure S10. Single crystal structure of (*rac*)-**1G**. Packing structure of (*rac*)-**1G** viewed along a axis (a) and *c* axis (b). All the H atoms were omitted for clarity.

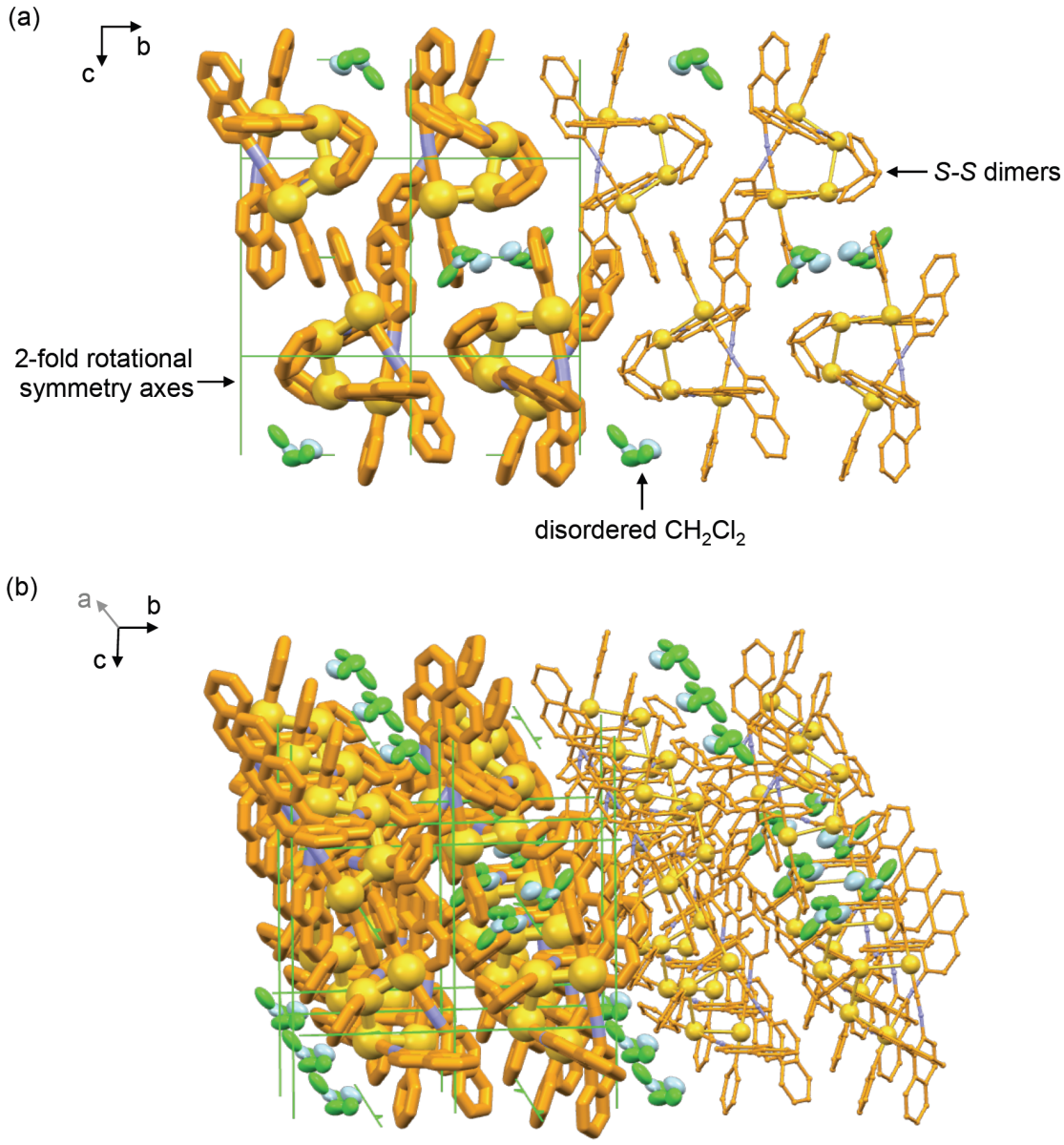

Figure S11. Single crystal structure of (*S*)-**1G**. (a) Packing structure of (*S*)-**1G** viewed along *a* axis. (b) Packing structure of (*S*)-**1G**. Light green lines denote 2-fold rotational symmetry axes. All the H atoms were omitted for clarity.

3.5. References

2. (a) Z. Chi, X. Zhang, B. Xu, X. Zhou, C. Ma, Y. Zhang, S. Liu and J. Xu, *Chem. Soc. Rev.*, 2012, **41**, 3878–3896; (b) X. Zhang, Z. Chi, Y. Zhang, S. Liu and J. Xu, *J. Mater. Chem. C*, 2013, **1**, 3376–3390; (c) Y. Sagara and T. Kato, *Nat. Chem.*, 2009, **1**, 605–610; (d) A. L. Balch, *Angew. Chem. Int. Ed.*, 2009, **48**, 2641–2644; (e) C. Jobbágy and A. Deák, *Eur. J. Inorg. Chem.*, 2014, **2014**, 4434–4449. (f) Y. Sagara, S. Yamane, M. Mitani, C. Weder and T. Kato, *Adv. Mater.*, 2016, **28**, 977–1326.
3. (a) H. Ito, T. Saito, N. Oshima, N. Kitamura, S. Ishizaka, Y. Hinatsu, M. Wakeshima, M. Kato, K. Tsuge and M. Sawamura, *J. Am. Chem. Soc.*, 2008, **130**, 10044–10045; (b) M. Osawa, I. Kawata, S. Igawa, M. Hoshino, T. Fukunaga and D. Hashizume, *Chem. Eur. J.*, 2010, **16**, 12114–12126; (c) S. Varughese, *J. Mater. Chem. C*, 2014, **2**, 3499–3516; (d) Y. Hong, J. W. Lam and B. Z. Tang, *Chem. Soc. Rev.*, 2011, **40**, 5361–5388; (e) M. Shimizu and T. Hiyama, *Chem. Asi. J.*, 2010, **5**, 1516–1531; (f) J. Gierschner and S. Y. Park, *J. Mater. Chem. C*, 2013, **1**, 5818–5832; (g) Y. Sagara, T. Mutai, I. Yoshikawa and K. Araki, *J. Am. Chem. Soc.*, 2007, **129**, 1520–1521; (h) G. Zhang, J. Lu, M. Sabat and C. L. Fraser, *J. Am. Chem. Soc.*, 2010, **132**, 2160–2162.
4. (a) O. Wallach, *Liebigs Ann. Chem.*, 1895, **286**, 90-143; (b) C. P. Brock, W. B. Schweizer and J. D. Dunitz, *J. Am. Chem. Soc.*, 1991, **113**, 9811–9820.
5. (a) K. J. Stine, J. Y. J. Uang and S. D. Dingman, *Langmuir*, 1993, **9**, 2112–2118; (b) L. Brammer, *Chem. Soc. Rev.*, 2004, **33**, 476–489; (c) J. Zhang, Y. G. Yao and X. Bu, *Chem. Mater.*, 2007, **19**, 5083–5089; (d) A. J. Bailey, C. Lee, R. K. Feller, J. B. Orton, C. Mellot-Draznieks, B. Slater, W. T. A. Harrison, P. Simoncic, A. Navrotsky, M. C. Grossel and A. K. Cheetham, *Angew. Chem. Int. Ed.*, 2008, **47**, 8634–8637.
6. (a) Z. Ludmer, M. Lahav, L. Leiserowitz and L. Roitman, *J. Chem. Soc., Chem. Commun.*, 1982, **6**, 326–328; (b) C. D. Delfs, H. J. Kitto, R. Stranger, G. F. Swiegers, S. B. Wild, A. C. Willis and G. J. Wilson, *Inorg. Chem.*, 2003, **42**, 4469–4478; (c) E. C. Yang, H. K. Zhao, B. Ding, X. G. Wang and X. J. Zhao, *Crystal Growth & Design*, 2007, **7**, 2009–2015; (d) K. A. McGee and K. R. Mann, *J. Am. Chem. Soc.*, 2009, **131**, 1896–1902; (e) T. F. Mastropietro, Y. J. Yadav, E. I. Szerb, A. M. Talarico, M. Ghedini and A. Crispini, *Dalton Trans.*, 2012, **41**, 8899–8907.

7. For chiral Pt(II) complexes: the two enantiomers of Pt(II) complexes show chiroptical property switching upon mechanical stimulation; X. P. Zhang, J. F. Mei, J. C. Lai, C. H. Li and X. Z. You, *J. Mater. Chem. C*, 2015, **3**, 2350–2357.
8. (a) S. Yagai, T. Seki, H. Aonuma, K. Kawaguchi, T. Karatsu, T. Okura, A. Sakon, H. Uekusa and H. Ito, *Chem. Mater.*, 2016, **28**, 234–241; (b) T. Seki, T. Ozaki, T. Okura, K. Asakura, A. Sakon, H. Uekusa and H. Ito, *Chem. Sci.*, 2015, **6**, 2187–2195; (c) H. Ito, M. Muromoto, S. Kurenuma, S. Ishizaka, N. Kitamura, H. Sato and T. Seki, *Nat. Commun.*, 2013, **4**, 2009; (d) T. Seki, K. Sakurada and H. Ito, *Angew. Chem. Int. Ed.*, 2013, **52**, 12828–12832.
9. C. Bartolome, D. Garcia-Cuadrado, Z. Ramiro and P. Espinet, *Inorg. Chem.*, 2010, **49**, 9758–9764.
10. (a) Y. Hong, J. W. Y. Lam and B. Z. Tang, *Chem. Soc. Rev.*, 2011, **40**, 5361–5388. (b) N. B. Shustova, B. D. McCarthy and M. Dinca, *J. Am. Chem. Soc.*, 2011, **133**, 20126–20129.
11. Bartolome, C.; Garcia-Cuadrado, D.; Ramiro, Z.; Espinet, P. *Inorg. Chem*. **2010**, *49*, 9758.
12. http://www.ccdc.cam.ac.uk/free_services/mercury/downloads/Mercury_3.0/
13. Sheldrick, G. M. SHELXL-2013, Program for the Refinement of Crystal Structures; University of Göttingen, Göttingen, Germany, 2013.

Chapter 4.

Mechano-Responsive Luminescence via Crystal-to-Crystal Phase Transitions between Chiral and Non-Chiral Space Groups

4.1. Introduction

Research on mechano-responsive luminescent (MRL) materials has rapidly grown over the past decade due to the strong interest in the underlying fundamental mechanisms, and on account of the potential applications.[1] In many cases, the changes to the chemical bonding or structure on the molecular level, which are caused by a macroscopic mechanical stimulus, are responsible for the alternation of the properties of such MRL compounds.[1,2] Several basic design concepts for mechano-responsive luminescent materials have been proposed.[1] For example, Moore and co-workers have developed mechano-responsive polymers by introducing segments called mechanophores, whose chemical structures are very sensitive to the force that is applied.[1a] Introducing flexible substituents in a rigid luminescent core represents another design strategy to achieve MRL properties, which has been reported by Sagara and Kato for liquid crystalline materials.[1c] Focusing on crystalline MRL solids, Eisenberg *et al.* have reported seminal mechano-responsive luminescent crystals that exhibit increasing emission intensity upon grinding, due to changes of the molecular arrangement, which release acid vapors.[2a] Generally, the luminescence changes of crystalline MRL solids occur due to changes of the crystal structure following mechanical stimulation.[3]

The difference in lattice energy between the polymorphic solid structures that are interconverted upon mechanical stimulation are considered crucial for the design for mechano-responsive solid materials.[1] However, predicting the crystal structures of polymorphs and the associated energy differences is usually difficult. Nevertheless, Wallach's rule can serve as an empirical guide for the understanding of polymorph stability: the density of crystal phases with chiral space groups (hereafter denoted "chiral crystals") is lower than that of crystals with centrosymmetric space groups (henceforth denoted "achiral crystals").[7] In general, the thermodynamic stability of polymorphs increases with their density.[8] Transforming chiral crystals by mechanical stimulation into achiral crystals under concomitant changes of the luminescent or optical properties, represents an unprecedented design concept for mechano-responsive functional materials. Previously, thermally induced phase transitions from chiral crystals to achiral crystals have been reported.[9] However, reports of mechano-responsive "*chiral-crystal-to-achiral-crystal phase transitions"* accompanied by emission changes remain, to the best of our knowledge, elusive, and could be used for a new, rational design of MRL materials.

We have previously revealed that many aryl gold(I)-isocyanide compounds exhibit MRL properties in the solid state under simultaneous prominent changes of the molecular

arrangement.[2e-f,5e-g,6] Very recently, we have designed an aryl gold(I)-isocyanide complex with a binaphthyl moiety, which exhibits a stable axially chiral structure and distinct mechano-responsive behavior between racemic and homochiral crystals.[2f] However, it was not designed for the interconversion between chiral and achiral crystals. To implement the aforementioned concept into MRL materials, a molecule that can form chiral and achiral crystals is required. Therefore, we have designed a new aryl gold(I)-isocyanide complex with a biphenyl unit (**1**) that is able to adopt *M*- (*M*-**1**) or *P*-conformations (*P*-**1**) (Figure 1a). **1** is achiral in solution, as the C_{ipso}–C_{ipso} bond in the biphenyl moiety can rotate freely. In the solid state, however, the free rotation is inhibited by intermolecular interactions with other molecules, which results in the formation of either *M*-**1** or *P*-**1**. We anticipated that **1** should be able to form both chiral and achiral crystals, and that mechanical stress should be able to interconvert these crystals through the change of molecular chirality (Figure 1b). Herein, we report the first MRL material that exhibits a *chiral-crystal-to-achiral-crystal* phase transition (Figure 1c).[10]

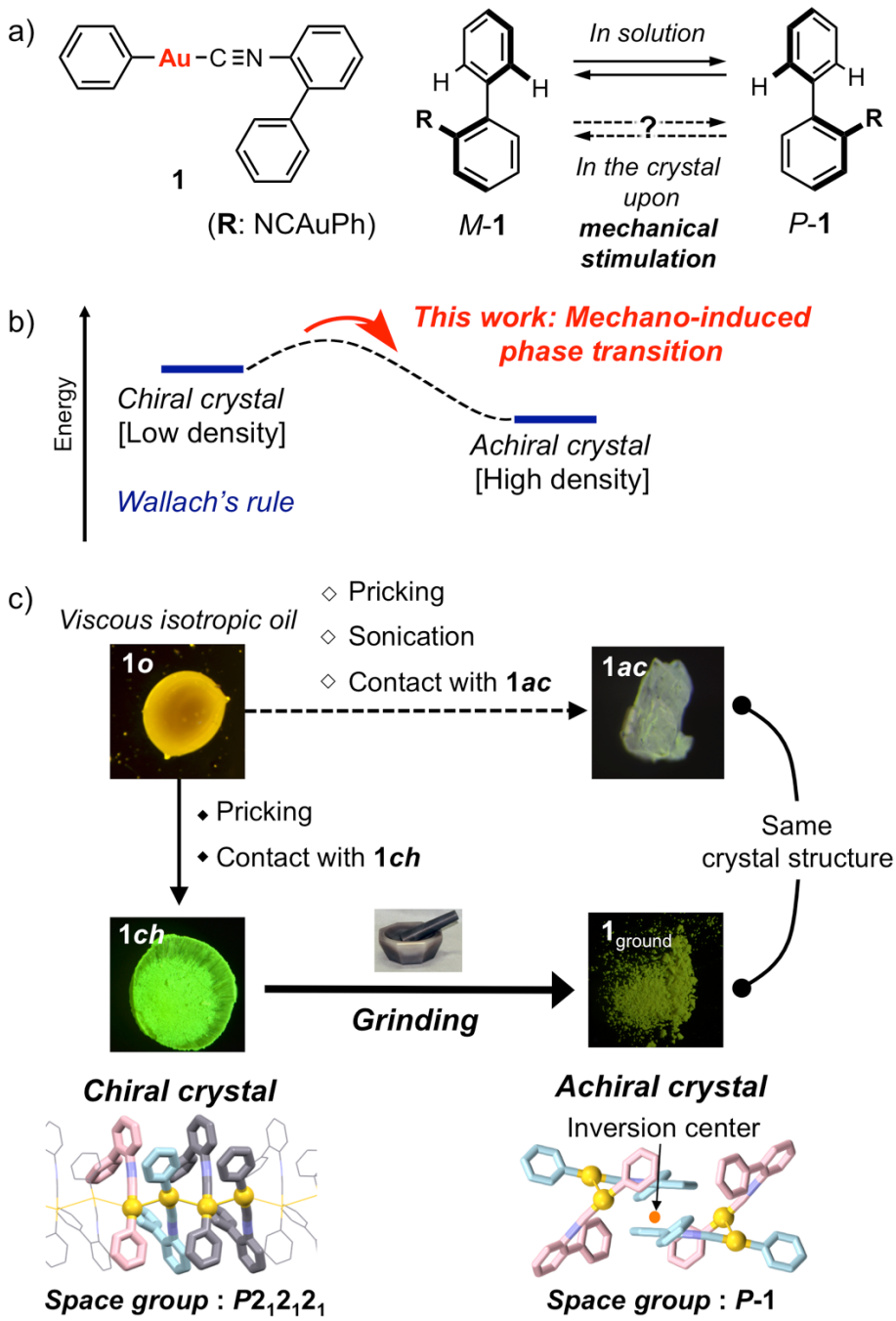

Figure 1. a) Molecular design concept. b) Schematic diagram of Wallach's rule and phase transition of the present study. c) Photographs of **1*o***, **1*ch***, $\mathbf{1}_{\text{ground}}$, and **1*ac*** recorded under illumination with UV light, as well as a representation of the phase transitions with crystal structures.

4.2. Results and Discussion

4.2.1. Synthesis and Preparation

Gold(I) isocyanide complex **1** was prepared according to a slightly modified, previously described procedure.[4g] After chromatographic purification of **1** and removal of the solvent, a viscous oil (**1*o***) was obtained (Figure 1b and the experimental section). **1*o*** showed orange emission under illumination with UV light. Interestingly, pricking **1*o*** using a needle randomly afforded either **1*ch***, i.e., a yellow crystal with green emission, or **1*ac***, which consists of whitish gray crystals with blueish green emission (Figure 1b, S1, and S3). On the other hand, **1*o*** selectively transformed into crystalline **1*ch*** or **1*ac*** upon getting in contact with a small piece of **1*ch*** or **1*ac***, respectively. Remarkably, several parts of the resulting solid phases of **1*ch*** and **1*ac*** exhibit sufficiently high quality for single-crystal X-ray diffraction (XRD) measurements.[11] Furthermore, sonicating **1*o*** for 20 min always afforded a whitish gray powder of **1*ac***, while **1*ch*** was not obtained (Figure 1b and S5). ^{1}H NMR spectroscopic, elemental, and thermogravimetric (TGA) analyses of **1*ch*** and **1*ac*** indicated that solvent was not included in the crystal lattice (Figures S6 and S7 and Table S1).

4.2.2. Single Crystal XRD Analyses of 1*ch* and 1*ac*

To investigate the crystal structure of **1*ch*** and **1*ac***, single crystal XRD of both the single crystal samples were performed. Interestingly, green **1*ch*** crystallized in the chiral space group $P2_12_12_1$ (Figures 2c and S8, Table S2).[12] The axial chirality of the biphenyl moiety, resulted in the formation of molecules with *M*- and *P*-conformations, which dimerized. As these molecules adopt dihedral angels of 50.82° (*M*-conformer) and 76.42° (*P*-conformer) between the phenyl rings of the biphenyl group ($\theta_{biphenyl}$), the *M*- and *P*-conformers are not enantiomers, and were thus denoted as M_1 and P_2, respectively. In the asymmetric unit, dimers were formed between M_1 and P_2 (Figure 2a), which are connected via aurophilic interactions with gold-gold distances of 3.1089(9) Å and CH-π interactions with carbon atom-phenyl ring distance of 3.684 Å (Figure 2a). As illustrated in Figure 2b, the dimer in **1*ch*** also interacts with adjacent dimers through aurophilic [Au-Au: 3.2310(9) Å] and CH-π (carbon atom-phenyl ring: 3.479 Å) interactions. It should be noted that the packing arrangement of these asymmetric dimers with no inversion center renders **1*ch*** chiral. The dimers form columnar structures through aurophilic interactions and CH-π interactions (Figure 2b).

Contrary to **1*ch***, the bluish-green-emitting crystal **1*ac*** crystallizes in the centrosymmetric (achiral) space group *P*-1, which possesses inversion centers. The dimer unit in **1*ac*** contains two crystallographically independent *M*-conformers, i.e., the $\theta_{biphenyl}$ of the two molecules is 43.43° and 44.49°, respectively. These molecules were denoted as M_3 and M_4 (Figure 2d). In the dimer, M_3 and M_4 engage in the intermolecular aurophilic interactions [Au-Au] 3.343(1) Å] and CH-p interactions (carbon atom-phenyl ring: 3.407 Å) (Figure 2d). Moreover, this dimer interacted with a dimer consisting of P_3 and P_4, i.e., the corresponding enantiomers of M_3 and M_4, via CH–π and π–π interactions (Figures 2e,f and S9). The inversion center is located between these dimers, which renders **1*ac*** centrosymmetric and thus achiral.

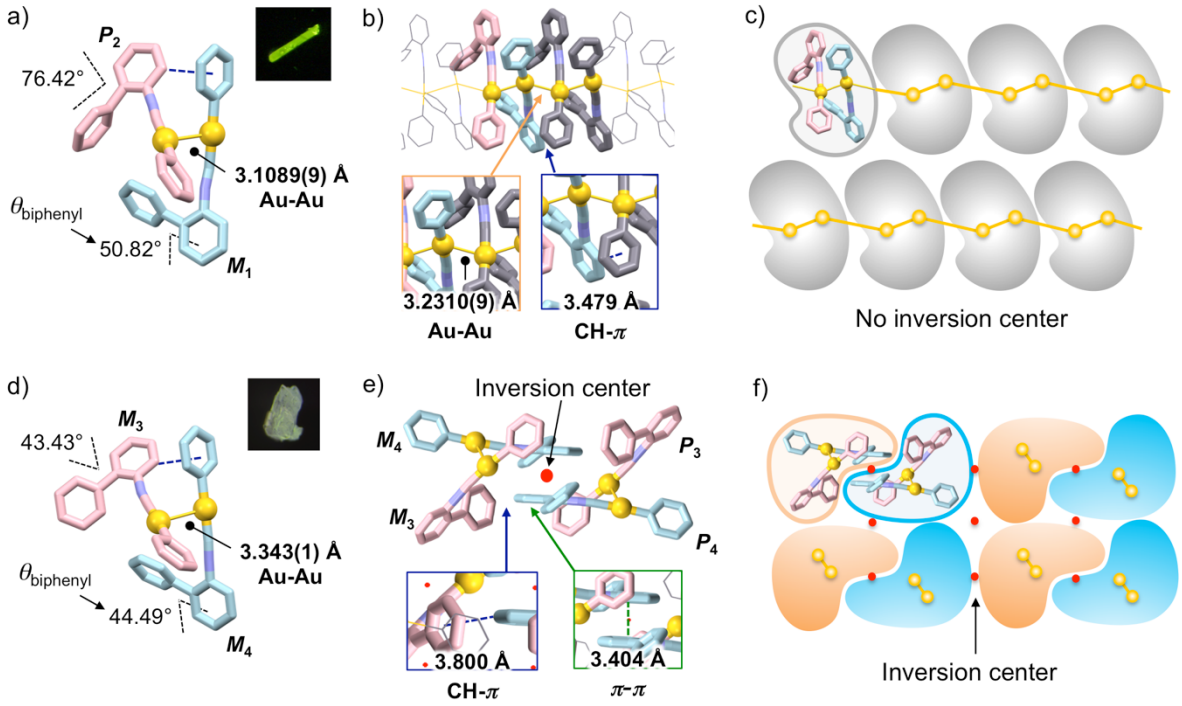

Figure 2. Crystal structures of **1*ch*** and **1*ac***. a) Dimer of M_1 and P_2, b) columnar structure, and c) packing structure of **1*ch*** with no inversion center. d) Dimer of M_3 and M_4, e) tetramer with inversion center, and f) packing structure of **1*ac***.

4.2.3. Studies on Mechano-Induced Crystal Structure Alterations

Studies on mechano-induced structure changes indicate that **1** exhibits *chiral-crystal-to-achiral-crystal* phase transitions, which are associated with concomitantly decreasing emission intensity. The sample of **1*ch*** obtained from pricking **1*o*** exhibited intense powder XRD (PXRD) peaks. The peak positions were in accordance with those of the simulated PXRD patterns of the single-crystal XRD measurements of **1*ch*** (Figure 3). Ball-milling of **1*ch*** for 30 min afforded a whitish gray powder of $\mathbf{1}_{ground}$, which exhibited weak green emission under illumination with UV light, implying the occurrence of mechano-induced phase transitions (Figure 1b). ^{1}H NMR spectroscopic and elemental analyses of $\mathbf{1}_{ground}$ provided no evidence for any potential chemical changes upon grinding (Figure S6 and Table S1). Indeed, the PXRD pattern of $\mathbf{1}_{ground}$ is different from that of the unground phase. $\mathbf{1}_{ground}$ exhibited intense peaks and the peak positions matched those of the simulated PXRD pattern of the single crystal of **1*ac*** (Figure 3). This result indicates that the mechano-induced phase transition of **1** (**1*ch*** → $\mathbf{1}_{ground}$) proceeds from chiral crystals ($P2_12_12_1$) to achiral crystals (P-1).

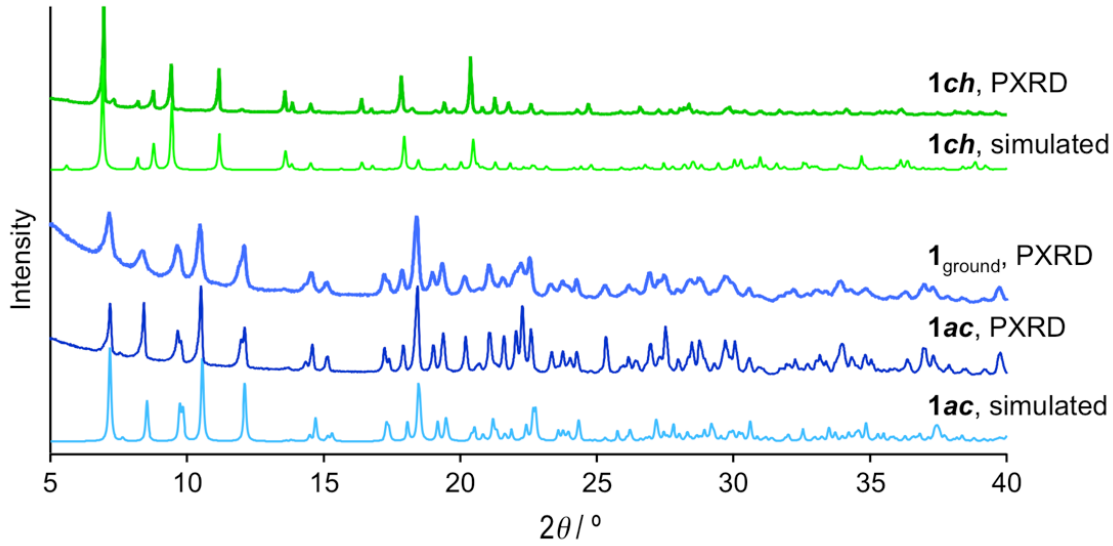

Figure 3. PXRD patterns of **1*ch*** (dark green), **1*ac*** (dark blue) and $\mathbf{1}_{ground}$ (blue), and simulated patterns from the single crystals of **1*ch*** and **1*ac*** (light green and light blue, respectively).

4.2.4. Thermal Analyses

A thermal analysis of **1*ch*** and **1*ac*** revealed that **1*ch*** and **1*ac*** melt at 73 °C and 105 °C, respectively (Figure S11). At these temperatures, both samples exhibited only endothermic peaks in their DSC profiles (Figure S12). As thermodynamically stable phases usually exhibit higher melting temperatures, **1*ch*** should be a metastable phase, while **1*ac*** should be thermodynamically more stable. Furthermore, the crystalline lattice densities of **1*ch*** and **1*ac*** were 1.925 and 2.001 g/cm^3, respectively. These results indicate that the behavior of **1** may be rationalized using Wallach's rule under consideration of the chiral and achiral space groups of **1*ch*** and **1*ac***.[6] It should be noted that **1*ch*** and **1*ac*** do not exhibit thermal phase transitions, which was confirmed by visual observation and DSC analyses. Only mechanical stress is able to transform **1*ch*** into **1*ac***.

4.2.5. Luminescent Properties and Mechano-Responsive Luminescence

The emission properties of **1*ch*** and **1*ac*** are clearly different: green-emitting crystals of **1*ch*** obtained from pricking exhibited a broad emission band ($\lambda_{em,max}$ = 542 nm) (Figure 4, solid green line),[13] and the excitation spectrum of **1*ch***, monitored at 542 nm, ranged between 300 and 500 nm with a maximum excitation wavelength of $\lambda_{ex,max}$ = 445 nm (Figure 4, green dashed line). Moreover, absolute emission quantum yield (Φ_{em}) and average emission lifetime (τ_{av}) values of 0.34 and 4.77 μs were recorded for **1*ch*** (Figure S13 and Table S3).[14] In contrast, **1*ac*** showed hypsochromically shifted excitation and emission spectra,[14] i.e., **1*ac*** exhibits a broad emission spectrum with $\lambda_{em,max}$ = 515 nm (Figure 4, black solid line), while the excitation spectrum showed a broad peak with $\lambda_{ex,max}$ = 319 nm (Figure 4, black dashed line). Compared to **1*ch***, the Φ_{em} (0.03) and τ_{av} (18.2 μs) values of **1*ac*** are lower and longer, respectively (Figure S13 and Table S3). In order to obtain mechanistic insight into the emission properties of **1*ch*** and **1*ac***, we carried out time-dependent (TD) DFT calculations based on the single-crystal structures. The results of these calculations indicated that the aurophilic interactions should be responsible for the destabilization of the HOMO energy level of **1*ch*** relative to that of **1*ac***. (Figures S15 and S16).[15]

As shown in Figure 4, $\mathbf{1}_{ground}$ exhibited an emission spectrum with weak intensity (Φ_{em} = 0.28) and an emission maximum at $\lambda_{em,max}$ = 539 nm (Figure 3b, blue solid line), which is similar to that of **1*ch*** ($\lambda_{em,max}$ = 542 nm). Moreover, the emission decay of $\mathbf{1}_{ground}$ (τ_{av} = 5.30 μs) is comparable to that of **1*ch*** (Figure S13 and Table S3). These similarities in the photophysical properties of **1*ch*** and $\mathbf{1}_{ground}$ are inconsistent with the fact that the PXRD pattern of $\mathbf{1}_{ground}$ is reasonably matched to the simulated pattern of **1*ac*** rather than **1*ch***. This may indicate that $\mathbf{1}_{ground}$ contains a small amount of the original **1*ch*** phase within a major crystalline domain consisting of **1*ac***.[16] This contamination of a small amount of **1*ch*** could be responsible for the overall green emission of $\mathbf{1}_{ground}$, followed by energy transfer from the main **1*ac*** domain.[5e]

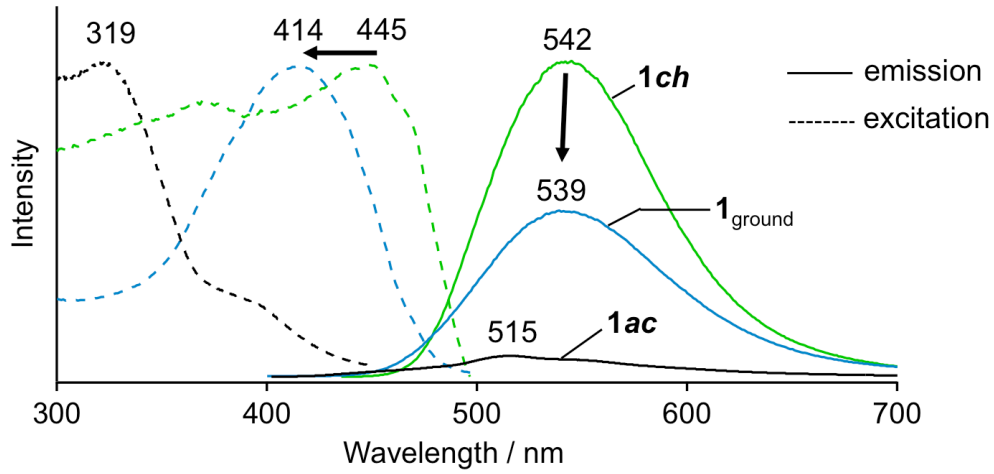

Figure 4. Excitation (dashed lines) spectra of **1*ch*** (green), $\mathbf{1}_{ground}$ (blue), and **1*ac*** (black) normalized relative to their maximum intensities recorded at 542, 539, and 515 nm, respectively. Emission spectra (solid lines, λ_{irr} = 365 nm) normalized relative to the corresponding absorption intensities at 365 nm. Arrows indicate changes upon grinding.

4.3. Summary

Gold complex **1**, which contains a biphenyl moiety, afforded chiral crystals of **1*ch*** and centrosymmetric (achiral) crystals of **1*ac***, both of which exhibit distinct emission properties. The single-crystal and powder XRD analyses revealed that chiral crystals of **1*ch*** transformed into achiral crystals similar to **1*ac*** upon grinding. The change of emission and optical properties of **1*ch*** upon grinding is correlated to the crystalline structural changes. This is the first example of mechano-induced *chiral-crystal-to-achiral-crystal* (CCAC) transition under concomitantly changing luminescent properties. These results indicate that the dynamic alternation of chirality of crystalline phases may be a promising key strategy to design universal mechano-responsive functional materials.

4.4. Experimental Section

4.4.1. General

All commercially available reagents and solvents are of reagent grade and were used without further purification unless otherwise noted. Solvents for the synthesis were purchased from commercial suppliers, degassed by three freeze-pump-thaw cycles and further dried over molecular sieves (4 Å). NMR spectra were recorded on a JEOL JNM-ECX400P or JNM-ECS400 spectrometer (^{1}H: 400 MHz; ^{13}C: 99.5 MHz) using tetramethylsilane and $CDCl_3$ as internal standards, respectively. Emission spectra were recorded on a Hitachi F-7000 spectrometer. Absorption spectra were recorded on the basis of synchronous fluorescence spectroscopy using a Hitachi F-7000 spectrometer equipped with an integrating sphere. Fluorescence microscopic spectra were recorded on a Photonic Hamamatsu PMA-12 Multichannel Analyzer. The emission quantum yields of the solid samples were recorded on a Hamamatsu Quantaurus-QY spectrometer with an integrating sphere. Emission lifetime measurements were recorded on a Hamamatsu Quantaurus-Tau spectrometer. Elemental analyses and low- and high resolution mass spectra were recorded at the Global Facility Center at Hokkaido University. Photographs were obtained using Olympus BX51 or SZX7 microscopes with Olympus DP72, Nikon D5100 digital cameras. Thermal gravimetric analysis profiles were recorded on Bruker TG-DTA2010SAT.

4.4.2. Synthesis

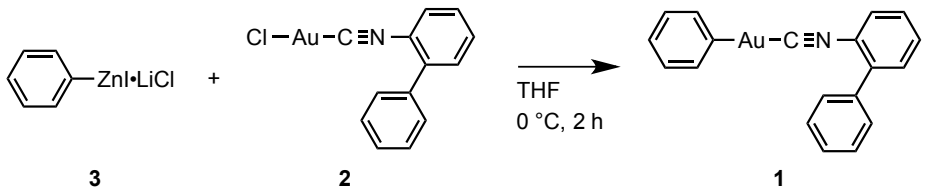

3 **2** **1**

A powder of chlorogold(I) isocyanide complex **2** (0.206 g, 0.50 mmol) was placed in an oven-dried two neck flask. The flask was connected to vacuum/nitrogen manifold through a rubber tube. It was evacuated and then backfilled with nitrogen. This process was repeated three times. Dry THF (1.0 ml) was then added to the flask under nitrogen atmosphere. After cooling to 0 °C, organozinc iodide reagent **3** in THF (0.58 ml, 0.60 mmol, 1.03 M) was added to the mixture dropwise and stirred for 2 h.[17] The reaction was quenched by addition of a phosphate buffer solution and then extracted with CH_2Cl_2 three times and washed with H_2O and brine. The organic layers were collected and dried over $MgSO_4$. After filtration, the solvent was removed *in vacuo*. Further purification by flash column chromatography (SiO_2, volume ratio of CH_2Cl_2/hexane=1) gave an analytically pure yellowish orange oil **1*o*** with yellow emission under UV light. (0.186 g, 0.4 mmol, 82 %). ^{1}H NMR (400 MHz, $CDCl_3$, δ): 7.05–7.09 (m, 1H), 7.23 (t, *J* = 7.6 Hz, 2H), 7.40 (dd, *J* = 1.6 Hz, 8.0 Hz, 2H), 7.45–7.57 (m, 7H), 7.62 (t, *J* = 7.6 Hz, 2H). ^{13}C NMR (100 MHz, $CDCl_3$, □): 123.1 (*C*), 126.2 (*C*H), 127.3 (*C*), 127.5 (*C*H), 128.3 (*C*H), 128.7 (*C*H), 128.9 (*C*H), 129.2 (*C*H), 131.1 (*C*H), 131.4 (*C*H), 136.1 (*C*), 139.9 (*C*), 140.4 (*C*H), 162.9 (*C*H), 163.5 (*C*). MS-ESI (*m*/*z*): $[M+Na]^+$ calculated for $C_{19}H_{14}AuNNa$, 476.06840; found, 476.06894. Anal. Calcd for $C_{19}H_{14}AuN$: C, 50.34; H, 3.11; N, 3.09. Found: C, 50.08; H, 3.00; N, 2.98.

4.4.3. Preparation of 1*ch* and 1*ac* from 1*o*

Pricking **1*o*** to obtain **1*ch*** or **1*ac***: We perturbed the viscous oil of **1*o*** in a glass vial using a needle like the following figure, and two or three spots were made through the procedure. After around 1 h under ambient temperature, small size of crystalline domain, either **1*ch*** or **1*ac***, was appeared from the spots and spontaneously developed to the entire region.

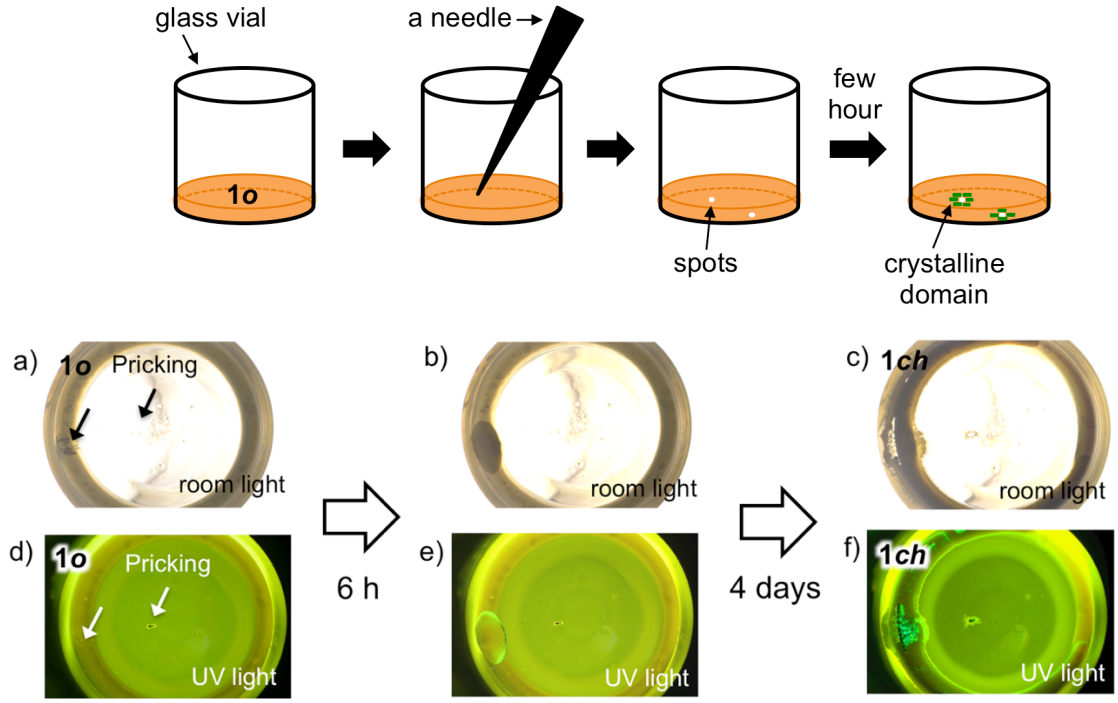

Figure S1. Photographs of the spontaneous phase transition from **1*o*** to **1*ch*** which is triggered by pricking. Photographs are taken a–c) under room light, and d–f) under UV light.

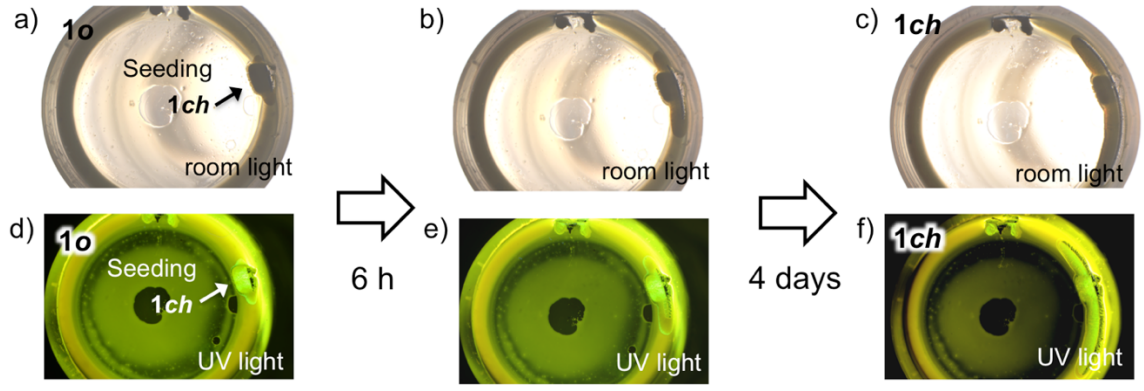

Figure S2. Photographs of crystal seeding of **1*ch*** from **1*o*** by crystal contact. Photographs are taken a), b) and c) under room light, d), e) and f) under UV light.

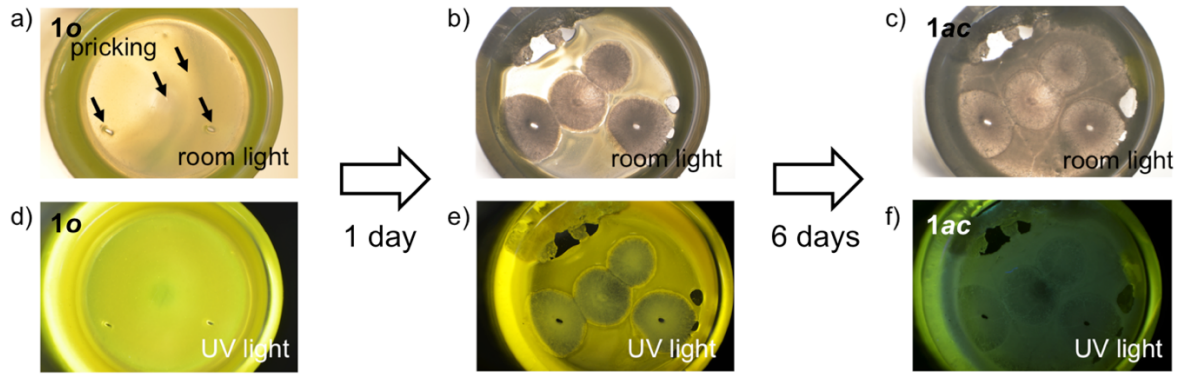

Figure S3. Photographs of the spontaneous phase transition from **1*o*** to **1*ac*** which is triggered by pricking. Photographs are taken a–c) under room light, and d–f) under UV light.

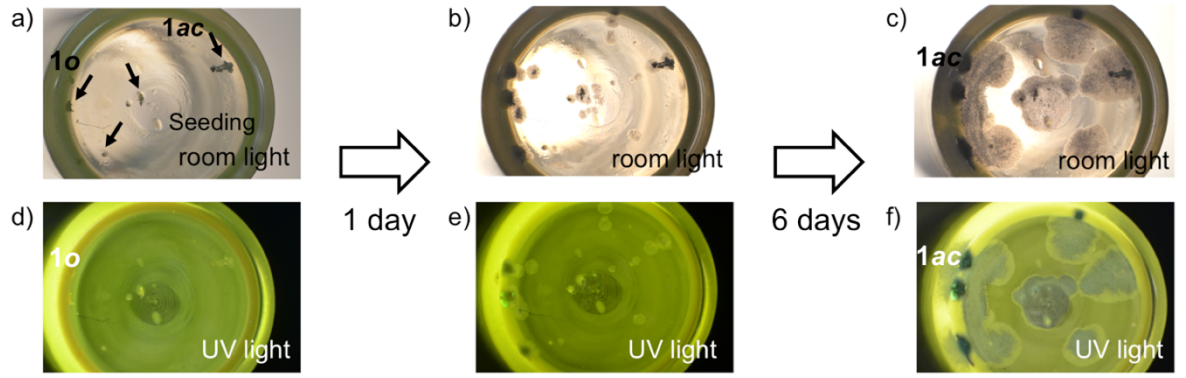

Figure S4. Photographs of crystal seeding of **1*ac*** from **1*o*** by crystal contact. Photographs are taken a), b) and c) under room light, d), e) and f) under UV light.

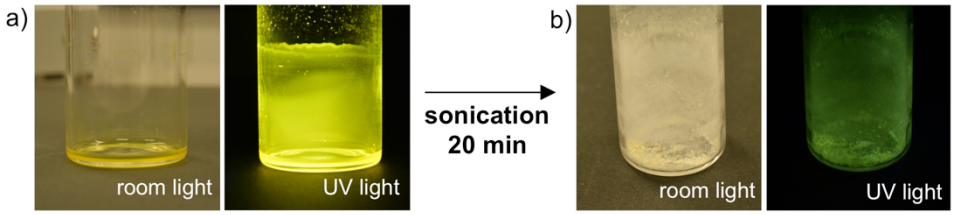

Figure S5. Photographs of a) **1*o*** and b) **1*ac*** under room light (left) and UV light (right). **1*ac*** was obtained by sonication of **1*o*** for 20 min.

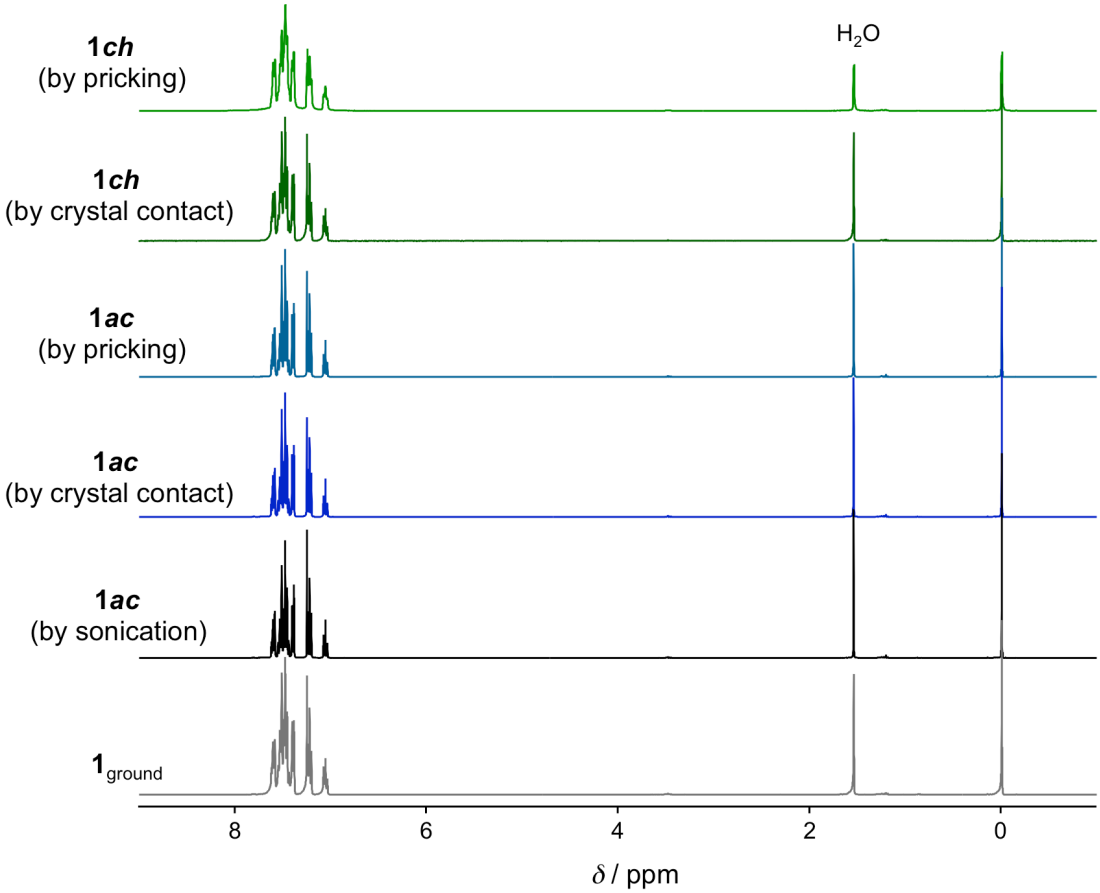

Figure S6. ^{1}H NMR spectra of **1*ch*** and **1*ac*** obtained by several procedures dissolved in $CDCl_3$. Light green line: **1*ch*** was obtained by pricking, dark green line: **1*ch*** by crystal contact, blueish-green line: **1*ac*** by pricking, blue line: **1*ac*** by crystal contact, black line: **1*ac*** by sonication, and gray line: $\mathbf{1}_{ground}$.

Table S1 Elemental analyses of the **1*ch*, 1*ac*,** and $\mathbf{1}_{ground}$

	C	H	N
Calculated for 1 ($C_{19}H_{14}AuN$)	50.34	3.11	3.09
1*ch*[a]	49.90	3.30	3.07
1*ac*[a]	49.98	3.33	3.12
1_{ground}	50.12	3.02	3.04

[a]Samples were obtained by pricking **1*o***.

4.4.4. TGA of 1*ch* and 1*ac*

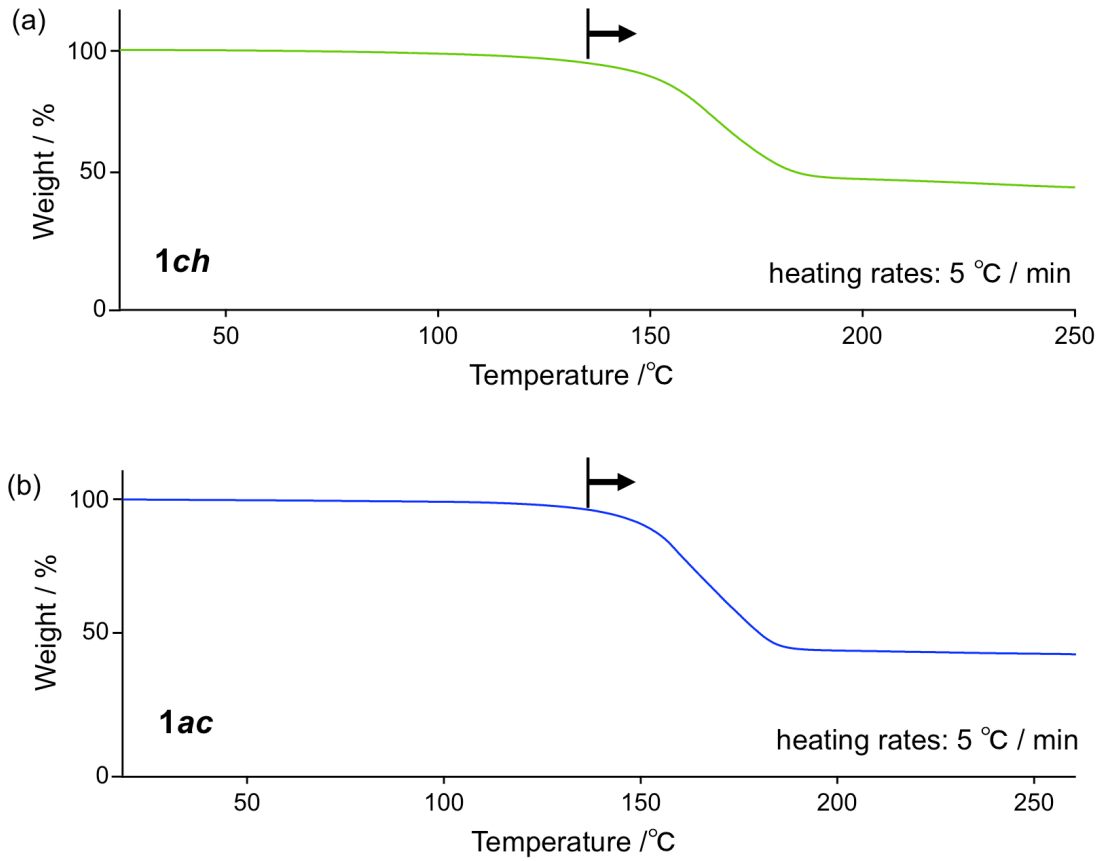

Figure S7. TGA profiles of a) **1*ch*** and b) **1*ac***. The both samples were obtained by pricking **1*o***. A heating rate is 5 °C/min. There was no decrease of weight percent of the samples until decomposition. Arrows indicate the starting decomposition. These results indicate that both samples do not include solvent molecules in the crystals.

4.4.5. Data for Single-Crystal X-Ray Structural Analyses

Single-crystal X-ray structural analyses were carried out on a Rigaku R-AXIS RAPID diffractometer using graphite monochromated Mo-K_α radiation. The structure was solved by direct methods and expanded using Fourier techniques. Non-hydrogen atoms were refined anisotoropically. Hydrogen atoms were refined using the riding model. All calculations were performed using the CrystalStructure crystallographic software package except for refinement, which was performed using SHELXL-2013.[18]

Table S2 Summary of X-ray crystallographic data of **1*ch*** and **1*ac***.

compound	**1*ch*** by pricking	**1*ch*** by crystal contact	**1*ac*** by pricking
CCDC Number	1537799	1537800	1537801
Empirical Formula	$C_{19}H_{14}AuN$	$C_{19}H_{14}AuN$	$C_{19}H_{14}AuN$
Formula Weight	453.29	453.29	453.29
Crystal System	orthorhombic	orthorhombic	triclinic
Crystal Size / mm	0.339×0.092×0.042	0.227×0.030×0.021	0.214×0.151×0.115
a / Å	6.0647(3)	6.0437(6)	9.9203(7)
b / Å	20.1459(9)	20.048(2)	13.1108(7)
c / Å	25.5946(12)	25.411(2)	13.2410(11)
α / °	90	90	105.287(3)
β / °	90	90	98.379(2)
γ / °	90	90	110.223(4)
V / Å^3	3127.1(2)	3078.9(5)	1504.50(19)
Space Group	$P2_12_12_1$ (#19)	$P2_12_12_1$ (#19)	P-1 (#2)
Z value	8	8	4
D_{calc} / g cm^{-3}	1.925	1.956	2.001
Temperature / K	123	123	123
$2\theta_{max}$ / °	55.0	51.0	55.0
μ(Mo K_α) / cm^{-1}	94.338	95.815	98.041
No. of Reflections	Total: 44933 Unique: 7143 R_{int} = 0.1176	Total: 39813 Unique: 5732 R_{int} = 0.5022	Total: 14812 Unique: 6830 R_{int} = 0.1053
R_1[a]	0.0506	0.0859	0.0743
wR_2[b]	0.1264	0.2139	0.1464
GOF[c]	1.085	0.839	1.131
Max./Mini. peak I[d] / Å^3	2.26 e$^-$/−2.35 e$^-$	2.14 e$^-$/−2.14 e$^-$	3.32 e$^-$/−4.73 e$^-$
Flack parameter	−0.004(12)	−0.03(4)	-

[a]:$I > 2.00\sigma(I)$. [b]:All reflections. [c]:Goodness of Fit Indicator. [d]: in Final Diff. Map.

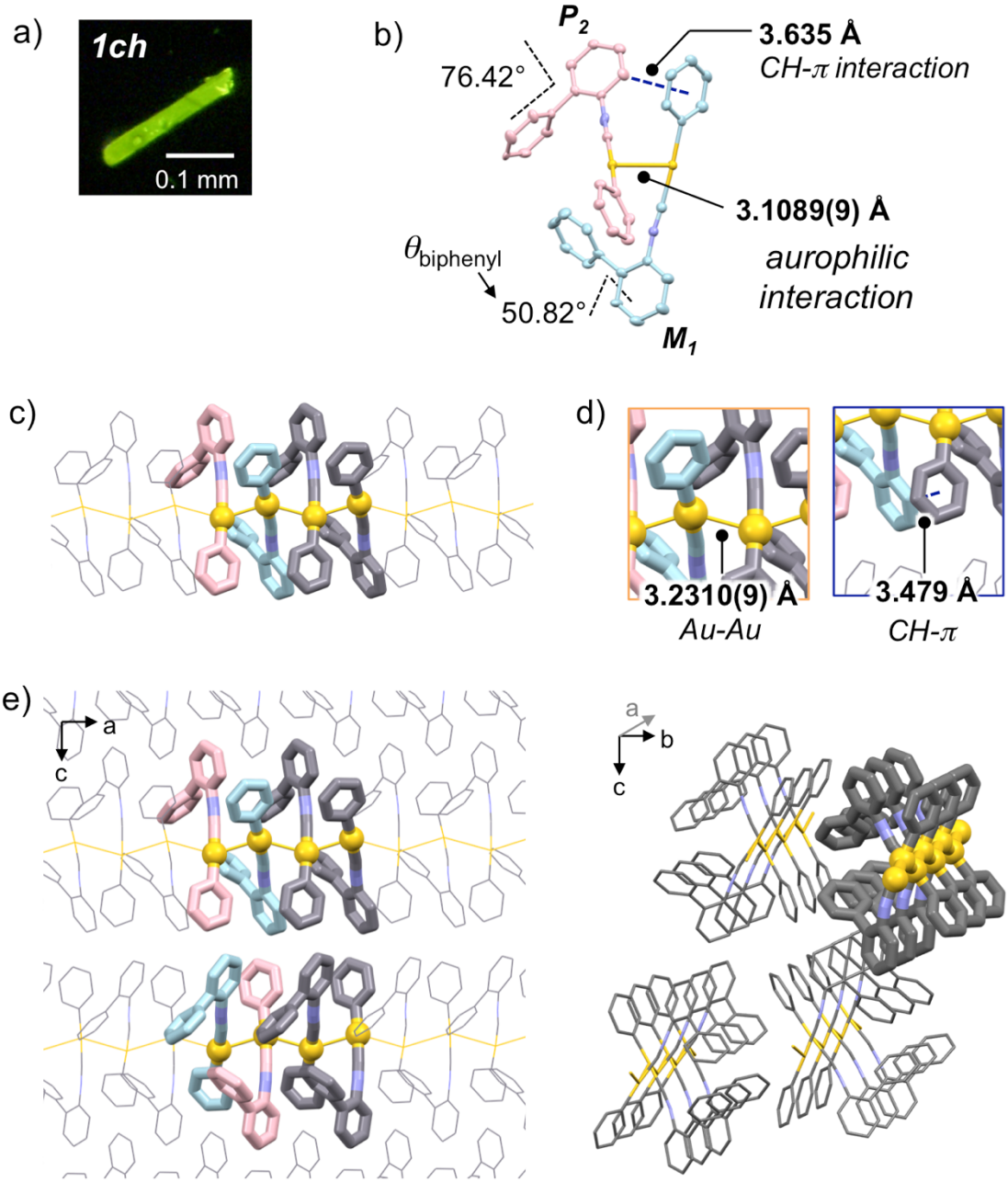

Figure S8. a) Photograph of the single crystal of **1*ch*** taken under UV light. b-e) Single crystal structure of **1*ch***. All the H atoms are omitted for clarity.

Note: The crystal structure of **1*ch*** obtained by crystal contact was the same with that of **1*ch*** obtained by pricking.

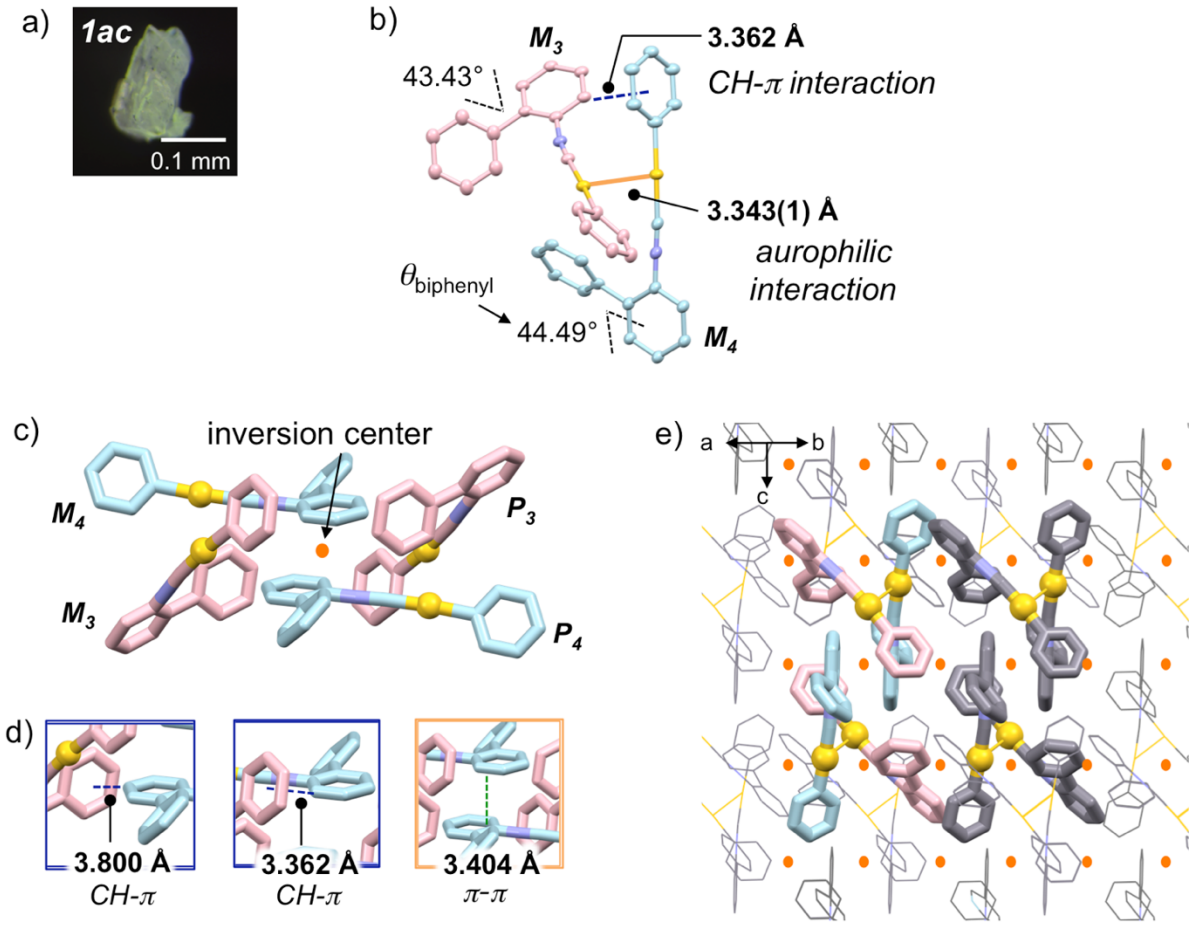

Figure S9. a) Photograph of the single crystal of **1*ac*** obtained by pricking taken under UV light. b) Dimer formed by ***M*₃** and ***M*₄** molecule through the CH-π and aurophilic interactions in the single crystal **1*ac***. c) Tetramer formed by the dimers ***M*₃-*M*₄** and ***P*₃-*P*₄** through d) CH-π and π-π interactions with forming inversion center. e) Packing structures of single crystal **1*ac***. All the H atoms are omitted for clarity.

4.4.6. PXRD Patterns and Simulated Powder Patterns of 1*ch* and 1*ac*

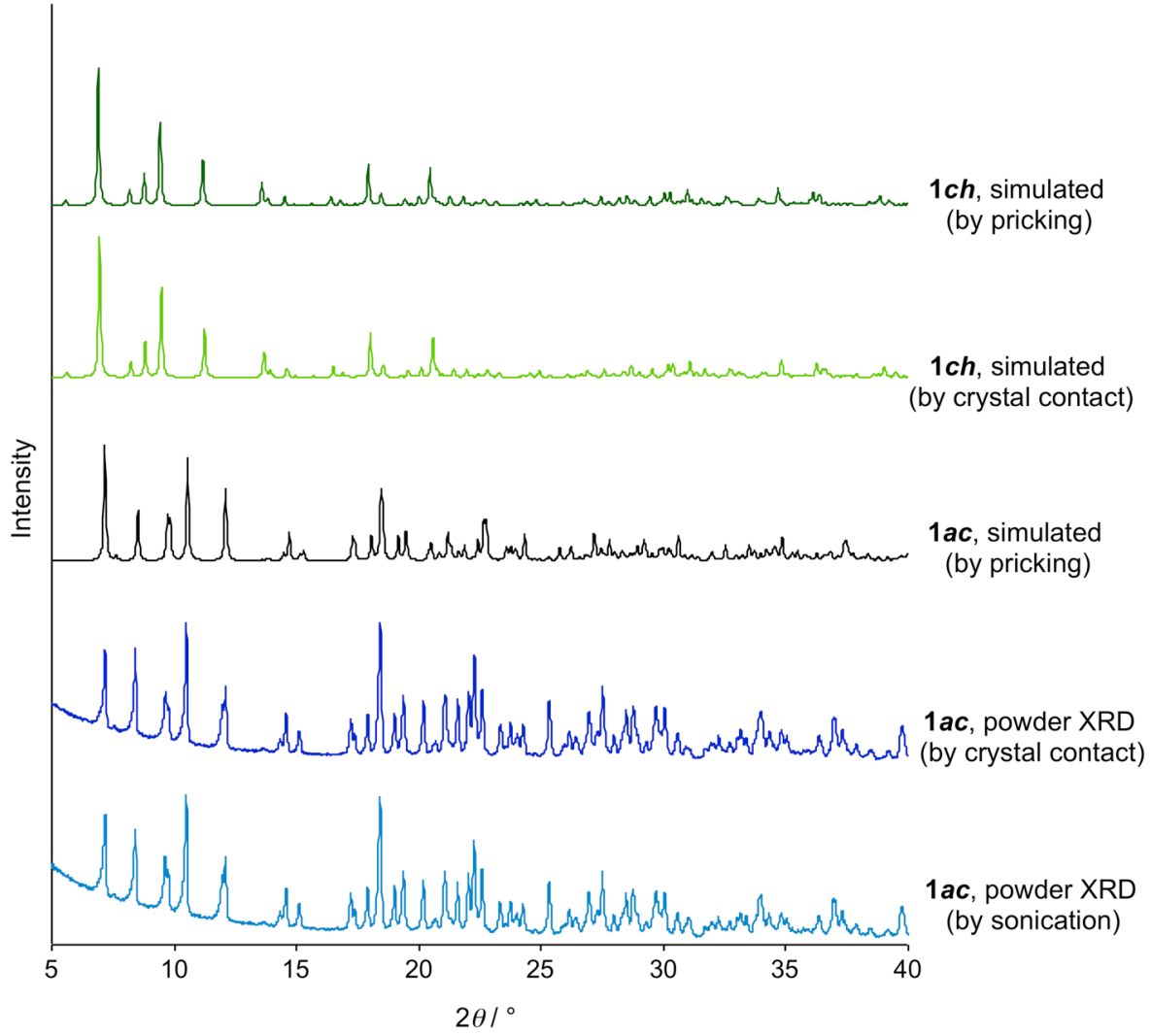

Figure S10. Simulated powder patterns derived from the single crystals of **1*ch*** obtained by pricking (green line) and crystal contact (light green line), and **1*ac*** obtained by pricking (black line). Powder diffraction patterns of **1*ac*** samples obtained by crystal contact (blue line) and sonication (light blue line).

4.4.7. Observation of Crystal Melting and DSC of 1*ch* and 1*ac*

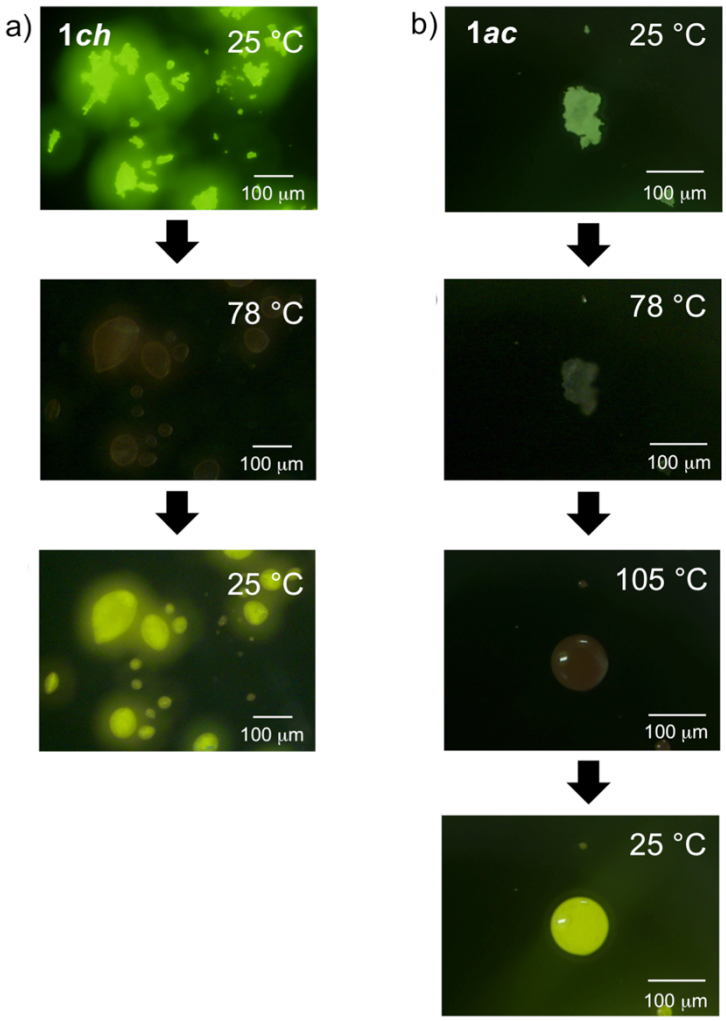

Figure S11. Photographs of a) **1*ch*** and b) **1*ac*** taken under UV irradiation at various temperatures. Heating and cooling rates were 5 and 10 °C/min, respectively.

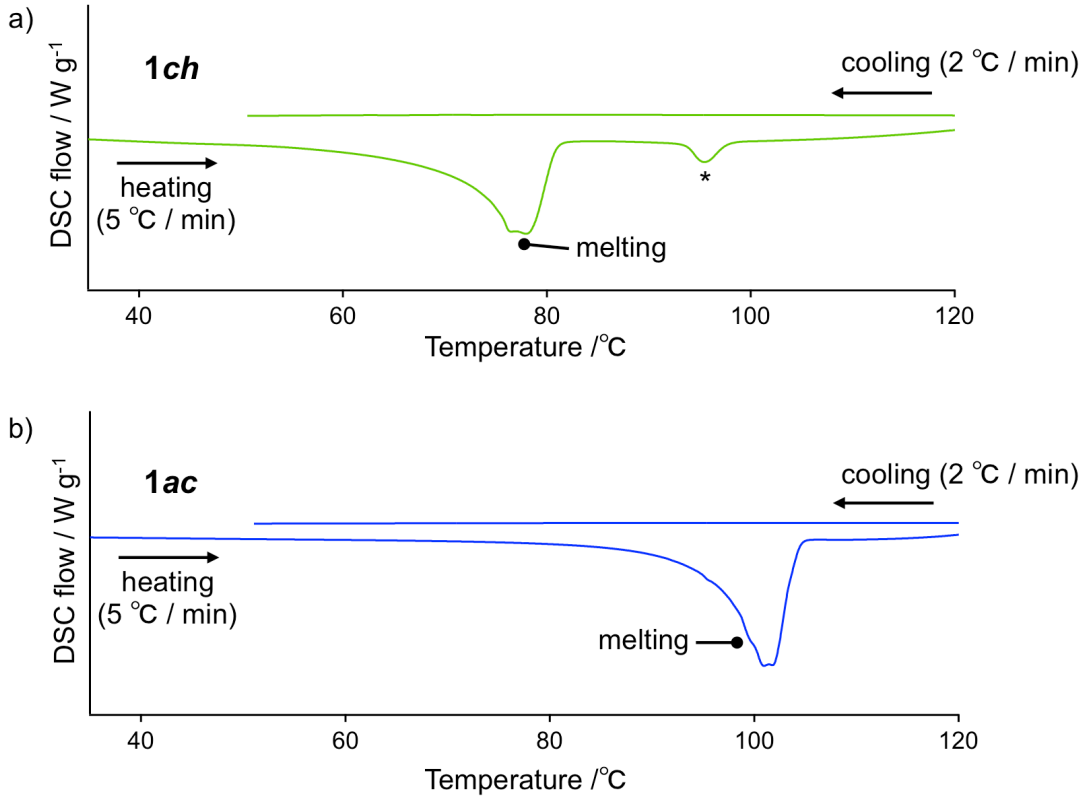

Figure S12. DSC profiles of a) **1*ch*** and b) **1*ac***. Heating and cooling rates were 5 and 2 °C / min, respectively. *: An unassignable peak. From the observation of **1*ch*** melting, the crystal **1*ch*** was melted from 78 °C. Therefore, the peak at 95 °C is not important to understand the crystal-to-crystal phase transition of **1*ch***.

4.4.8. Photophysical Properties

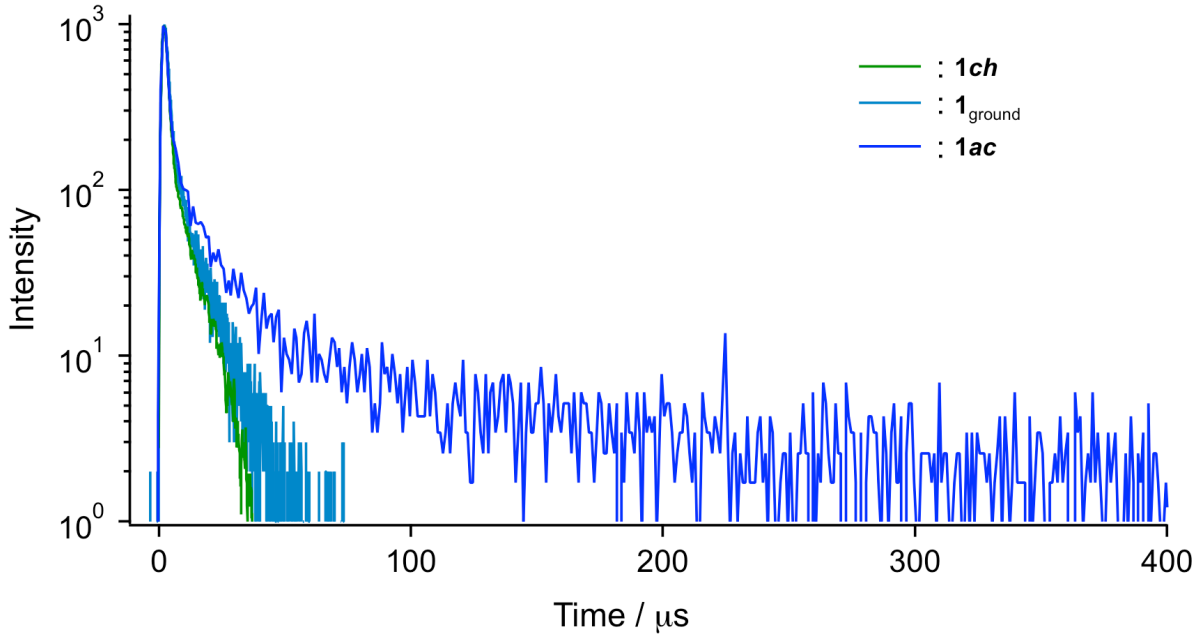

Figure S13. Emission decay profiles of **1*ch*** (green line), $\mathbf{1}_{ground}$ (blueish green line), and **1*ac*** (blue line). **1*ch*** and **1*ac*** were prepared by pricking **1*o***.

Table S3 Photophysical properties of **1*ch***, $\mathbf{1}_{ground}$, and **1*ac***.

	Φ_{em} / - (λ_{ex} / nm)	τ_{av} / μs[a,b] (λ_{em} / nm)	τ_1 / μs[a] (A / -)	τ_2 / μs[a] (A / -)	τ_3 / μs[a] (A / -)
1*ch*[c]	0.34 (445)	4.77 (542)	1.48 (0.86)	8.44 (0.14)	-
$\mathbf{1}_{ground}$	0.29 (414)	5.30 (539)	1.67 (0.87)	9.65 (0.13)	-
1*ac*[c]	0.03 (319)	18.18 (515)	1.19 (0.89)	9.69 (0.10)	56.68 (0.01)

[a]: λ_{ex} = 370 nm. [b]: $\tau_{av} = \Sigma \tau_n A_n^2 / \Sigma \tau_n A_n$. All emission decay was fitted by tail fitting. [c]: Obtained by pricking **1*o***.

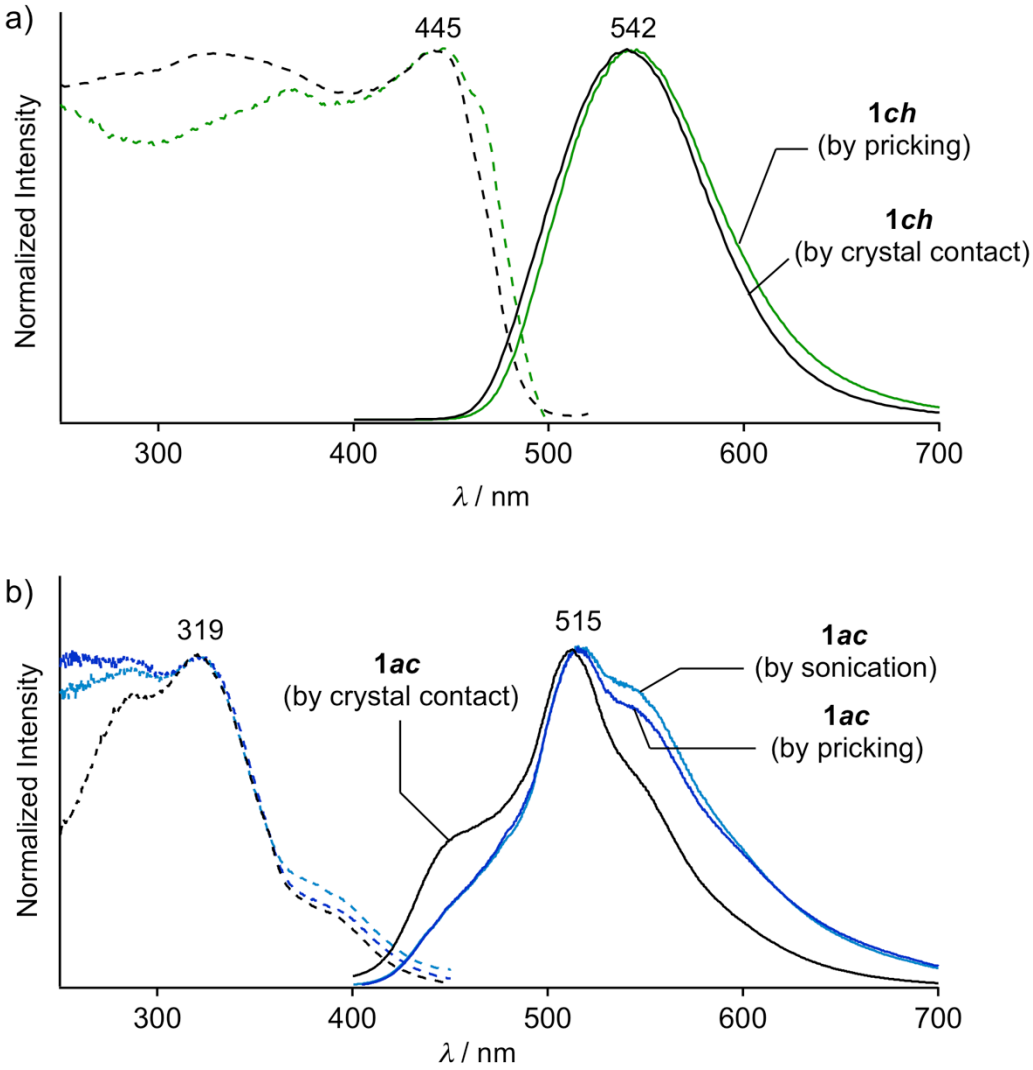

Figure S14. Emission (solid lines) and excitation (dashed lines) spectra of a) **1*ch*** obtained by pricking (green lines) and crystal contact (black lines) and b) **1*ac*** obtained by pricking (blue lines), crystal contact (black lines), and sonication (light blue lines). The emission and excitation spectra were normalized with their maximum intensities.

4.4.9. TD-DFT Calculations of 1*ch* and 1*ac*

All calculations were performed using the Gaussian 09W (revision C.01 and E.01) and Gaussian 09 (revision C.01 and E.01) program package.[19] The singlet state TD-DFT calculations of the tetramer of **1*ch*** and **1*ac*** were performed for understanding origin of the emission properties. In the calculations, the B3LYP functional and the SDD basis set with an effective core potential was used. The geometries of the tetramers were taken from the crystal structure of **1*ch*** and **1*ac***. The positions of heavy atoms were fixed and only the positions of H atoms were optimized using the Spartan'10 MMFF force-field calculations before TD-DFT calculations.[20] The simulated UV/vis absorption spectra and the excitation spectra from the experiments exhibited the similar traces (Figure S15). Thus, the results of TD-DFT calculations give us reasonable mechanistic insight for studying the emission properties of **1*ch*** and **1*ac***. The frontier molecular orbitals and corresponding energy levels of **1*ch*** and **1*ac*** indicated that the HOMO of **1*ch*** is higher than that of **1*ac*** (Figure S16). Furthermore, the HOMO is distributed to near the gold atoms. Therefore, the difference of aurophilic interactions in tetramer of **1*ch*** and **1*ac*** should influence in the emission/excitation properties of both crystals.

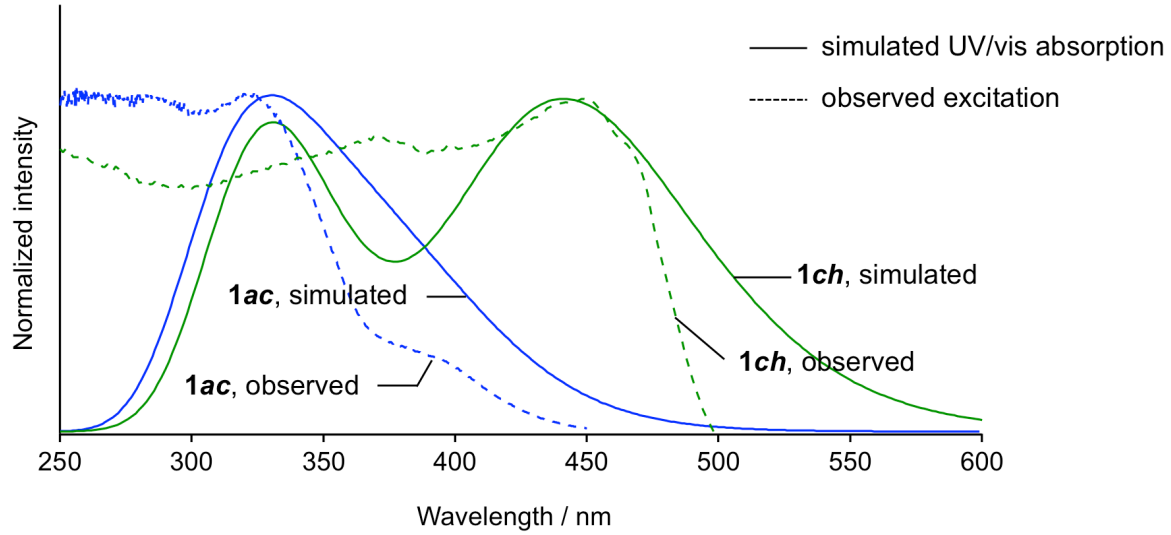

Figure S15. Comparison of experimental and theoretical studies on emission properties of **1*ch*** and **1*ac***. Excitation spectra of **1*ac*** (blue dashed line) and **1*ch*** (green dashed line). Simulated UV/vis absorption spectra of **1*ac*** (blue solid line) and **1*ch*** (green solid line) based on the singlet state TD-DFT calculations of the tetramers derived from the corresponding single crystalline structures (B3LYP/SDD).

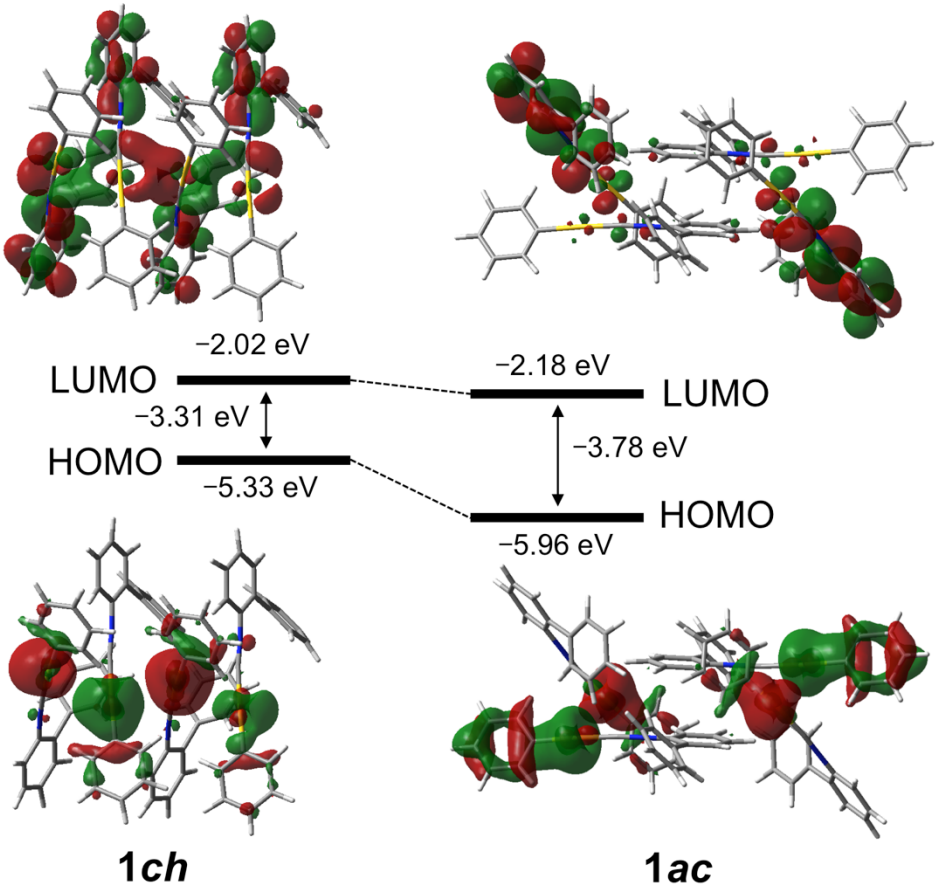

Figure S16. Frontier molecular orbitals and corresponding energy levels obtained by TD-DFT calculations of the tetramers derived from the single-crystal structures of **1*ch*** and **1*ac*** (B3LYP/SDD).

4.4.10. Optical Properties of Solution Phase

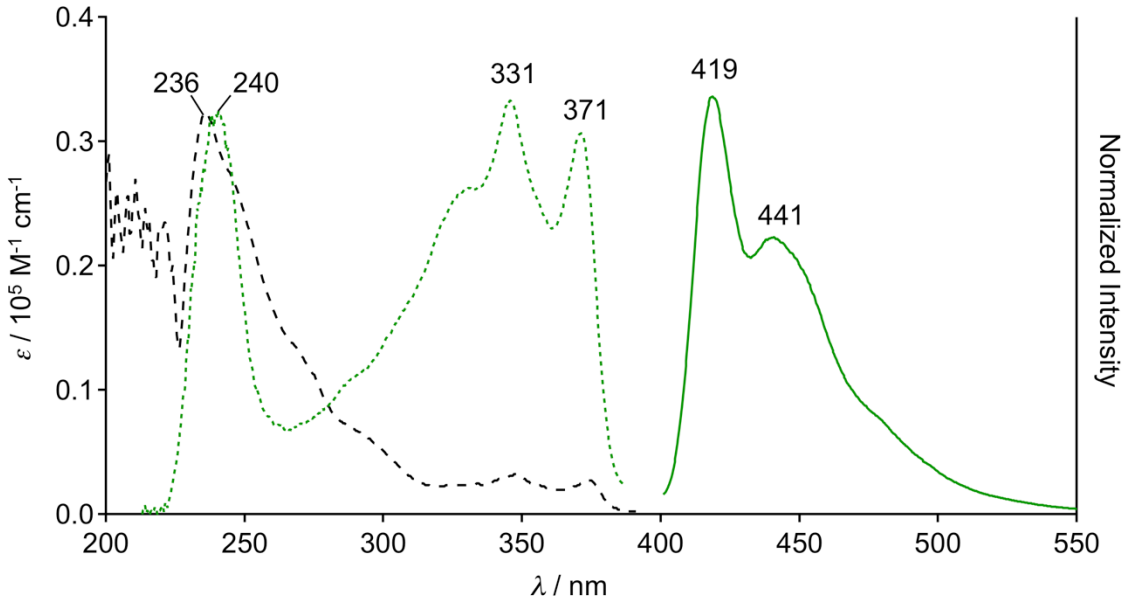

Figure S17. UV/vis absorption (black dashed line), excitation (green dotted line, λ_{em} = 419 nm), and emission spectra (green solid line, λ_{ex} = 240 nm) of **1** in CH_2Cl_2 (c = 8.0 × 10^{-6} M) at room temperature.

4.4.11. Evaluation of Changes of $\mathbf{1}_{gournd}$ after Ceased Grinding

We measured the emission and excitation spectra of $\mathbf{1}_{ground}$ just after ceased grinding (black solid and black dashed lines, respectively in Figure below). Then, after 30 min under ambient conditions, we again measured the emission and excitation spectra of $\mathbf{1}_{ground}$ (red solid and red dashed lines, respectively in Figure S18). As shown below, no changes in emission and excitation spectra were observed. The results indicate that there is no change of $\mathbf{1}_{ground}$ once the grinding is ceased.

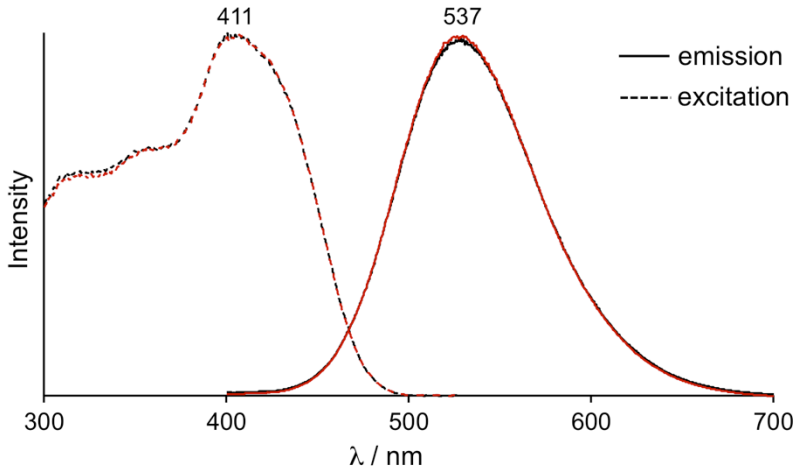

Figure S18. Emission (solid line) and excitation (dashed line) spectra of the $\mathbf{1}_{ground}$ (black line) and the $\mathbf{1}_{ground}$ after 30 min at ambient temperature (red line). Emission spectra measured at λ_{ex} = 365 nm. Excitation spectra monitored at 537 nm.

4.5. References

14. (a) Caruso, M. M.; Davis, D. A.; Shen, Q.; Odom, S. A.; Sottos, N. R.; White, S. R.; Moore, J. S. *Chem. Rev.* **2009**, *109*, 5755. (b) Chi, Z.; Zhang, X.; Xu, B.; Zhou, X.; Ma, C.; Zhang, Y.; Liu, S.; Xu, J. *Chem. Soc. Rev.* **2012**, *41*, 3878. (c) Sagara, Y.; Yamane, S.; Mitani, M.; Weder, C.; Kato, T. *Adv. Mater.* **2016**, *28*, 977.
15. (a) Lee, A. Y.; Eisenberg, R. *J. Am. Chem. Soc.* **2003**, *125*, 7778. (b) Sagara, Y.; Mutai, T.; Yoshikawa, I.; Araki, K. *J. Am. Chem. Soc.* **2007**, *129*, 1520. (c) Gierschner, J.; Park, S. Y. *J. Mater. Chem. C* **2013**, *1*, 5818. (d) Zhang, G.; Lu, J.; Sabat, M.; Fraser, C. L. *J. Am. Chem. Soc.* **2010**, *132*, 2160. (e) Ito, H.; Saito, T.; Oshima, N.; Kitamura, N.; Ishizaka, S.; Hinatsu, Y.; Wakeshima, M.; Kato, M.; Tsuge K.; Sawamura, M. *J. Am. Chem. Soc.* **2008**, *130*, 10044. (f) Jin, M.; Seki, T.; Ito, H. *Chem. Commun.* **2016**, *52*, 8083.
16. Several phase transition patterns of MRL solid materials have already been reported. For *crystal-to-amorphous* (CA) transitions, see: ref. 2g-i; for *amorphous-to-crystal* (AC) transitions, see: ref. 4; for *crystal-to-crystal* (CC) transitions, see: ref. 5; for *single-crystal-to-single-crystal* (SCSC) transformations, see: ref. 6.
17. Lv, Y.; Liu, Y.; Ye, X.; Liu, G.; Tao, X. *CrystEngComm.* **2015**, *17*, 526.
18. (a) Yoon, S.-J.; Chung, J. W.; Gierschner, J.; Kim, K. S.; Choi, M.-G.; Kim, D.; Park, S. Y. *J. Am. Chem. Soc.* **2010**, *132*, 13675. (b) Harada, N.; Abe, Y.; Karasawa, S.; Koga, N. *Org. Lett.* **2012**, *14*, 6282. (c) Abe, Y.; Karasawa, S.; Koga, N. *Chem.–Eur. J.* **2012**, *18*, 15038. (d) Yagai, S.; Okamura, S.; Nakano, Y.; Yamauchi, M.; Kishikawa, K.; Karatsu, T.; Kitamura, A.; Ueno, A.; Kuzuhara, D.; Yamada, H.; Seki, T.; Ito, H. *Nat. Commun.* **2014**, *5*, 4013. (e) Seki, T.; Sakurada, K.; Ito, H. *Chem. Commun.* **2015**, *51*, 13933. (f) Seki, T.; Ozaki, T.; Okura, T.; Asakura, K.; Sakon, A.; Uekusa, H.; Ito, H. *Chem. Sci.* **2015**, *6*, 2187. (g) Seki, T.; Takamatsu, Y.; Ito, H. *J. Am. Chem. Soc.* **2016**, *138*, 6252.
19. (a) Ito, H.; Muromoto, M.; Kurenuma, S.; Ishizaka, S.; Kitamura, N.; Sato, H.; Seki, T. *Nat. Commun.* **2013**, *4*, 2009. (b) Seki, T.; Sakurada, K.; Ito, H. *Angew. Chem., Int. Ed.* **2013**, *52*, 12828. (c) Seki, T.; Sakurada, K.; Muromoto, M.; Seki, S.; Ito, H. *Chem.–Eur. J.* **2016**, *22*, 1968.
20. (a) Wallach, O. *Liebigs Ann. Chem.* **1895**, *286*, 90. (b) Brock, C. P.; Schweizer, W. B.; Dunitz, J. D. *J. Am. Chem. Soc.* **1991**, *113*, 9811.
21. *Polymorphism in Molecular Crystals,* Bernstein, J.; Oxford Univ. Press, 2002.

22. (a) Mercier, N.; Barres, A. -L.; Giffard, M.; Rau, I.; Kajzar, F.; Sahraoui, B. *Angew. Chem. Int. Ed.* **2006**, *45*, 2100. (b) van Eupen, J. Th. H.; Elffrink, W. W. J.; Keltjens, R.; Bennema, P.; De Gelder, R.; Smits, J. M. M.; van Eck, E. R. H.; Kentgens, A. P. M.; Deij, M. A. ; Meekes, H.; Vlieg, E. *Crystal Growth Des.* **2008**, *8*, 71.
23. All the reported CC mechanochromic compounds exhibited phase transitions from one achiral crystal to another achiral crystal; for details, see: ref. 5.
24. The PXRD patterns of the powder samples of **1ac** and **1ch** were matched with those of the simulation patterns. See: Figure 3 and S10.
25. Several single-crystal XRD measurements were carried out on crystals of **1*ch*** obtained from pricking or crystal contact in order to examine the potential occurance of different enantiomorphs. However, just one type of enantiomorph was observed.
26. As the emission intensity of **1** in CH_2Cl_2 was very weak, we could not analyze the photophysical properties. This indicates that the emission properties of solid-state **1** are determined by their aggregation structures (cf. Figure S17); for details, see: Hong, Y.; Lam, J. W. Y.; Tang, B. Z. *Chem. Soc. Rev.* **2011**, *40*, 5361.
27. **1*ch*** obtained from crystal contact exhibited the same emission properties than **1*ch*** obtained from pricking **1*o***. **1*ac*** obtained from sonication or crystal contact also exhibited similar emission properties to samples of **1*ac*** obtained from pricking **1*o*** (cf. Figure S14).
28. The HOMO-LUMO energy gap in **1*ac*** is by 0.47 eV larger than that in **1*ch***. The HOMO in both crystals in located on the gold atoms (cf. Figure S15).
29. The $\mathbf{1}_{ground}$ showed no further changes over time, after ceasing the grinding. See: Figure S18.
30. Krasovskiy, A.; Malakhov, V.; Gavryushin, A.; Knochel, P. *Angew. Chem. Int. Ed.* **2006**, *45*, 6040–6044.
31. Sheldrick, G. M. SHELXL-2013, Program for the Refinement of Crystal Structures; University of Göttingen, Göttingen, Germany, **2013**.
32. Gaussian 09, Revision C.01, Frisch, M. J.; Trucks, G. W.; Schlegel, H. B.; Scuseria, G. E.; Robb, M. A.; Cheeseman, J. R.; Scalmani, G.; Barone, V.; Mennucci, B.; Petersson, G. A.; Nakatsuji, H.; Caricato, M.; Li, X.; Hratchian, H. P.; Izmaylov, A. F.; Bloino, J.; Zheng, G.; Sonnenberg, J. L.; Hada, M.; Ehara, M.; Toyota, K.; Fukuda, R.; Hasegawa, J.; Ishida, M.; Nakajima, T.; Honda, Y.; Kitao, O.; Nakai, H.; Vreven, T.; Montgomery, J., J. A.; Peralta, J. E.; Ogliaro, F.; Bearpark, M.; Heyd, J. J.;

Brothers, E.; Kudin, K. N.; Staroverov, V. N.; Kobayashi, R.; Normand, J.; Raghavachari, K.; Rendell, A.; Burant, J. C.; Iyengar, S. S.; Tomasi, J.; Cossi, M.; Rega, N.; Millam, N. J.; Klene, M.; Knox, J. E.; Cross, J. B.; Bakken, V.; Adamo, C.; Jaramillo, J.; Gomperts, R.; Stratmann, R. E.; Yazyev, O.; Austin, A. J.; Cammi, R.; Pomelli, C.; Ochterski, J. W.; Martin, R. L.; Morokuma, K.; Zakrzewski, V. G.; Voth, G. A.; Salvador, P.; Dannenberg, J. J.; Dapprich, S.; Daniels, A. D.; Farkas, Ö.; Foresman, J. B.; Ortiz, J. V.; Cioslowski, J.; Fox, D. J.; Gaussian, Inc., Wallingford CT, 2009.

33. Spartan ’10; Wavefunction, Inc.: Irvine, CA.

Chapter 5.

Mechanical-Stimulation-Triggered and Solvent-Vapor-Induced Reverse Single-Crystal-to-Single-Crystal Phase Transitions with Alterations of the Luminescence Color

5.1. Introduction

Luminescent solids that undergo solid-state structural changes upon external stimuli under subsequent modification of their emission properties constitute an attractive research subject owing to their potential applications for highly functional devices or sensors.[1] Reversible emission change is also an important property for the development of further compound functionalities.[1g,2] In rare cases, certain luminescent crystalline compounds undergo single-crystal-to-single-crystal (SCSC) phase transitions upon temperature changes, irradiation with light, or exposure to small-molecule vapors.[3] Although SCSC transitions are generally difficult, they can provide detailed information on the molecular level pertaining to changes of the structure and/or the emission properties.[1g,3-5] One intriguing example of such structural transitions in molecular crystals are mechanical-stimulation-triggered SCSC transitions.[1d-g,5] We have recently reported the first example for two "molecular domino" phenomena using arylgold(I) isocyanide complexes **1**[5a] and **2**:[5b] upon gentle mechanical pricking on the surface of thermally metastable polymorph crystals of **1** and **2**, the entire crystals spontaneously transform into their thermally stable polymorphs (Figure 1a).[5] These phase changes proceeded in an SCSC manner under a concomitant drastic change of the emission color that arises from changes in the crystal structure. A comparison of the crystal structures of the mother and daughter phases revealed changes in the aurophilic interactions and dihedral angles between the aryl groups, both of which are key features that determine the luminescence properties of these compounds.[5] These mechanical-stimulation-triggered SCSC phase transitions are only able to drive the transformation of a metastable polymorph into a thermodynamically more stable polymorph.[5] In these cases, reversed phase changes were not observed, and recrystallization was the only way to recover the original polymorph.[5a-d] Some mechanically responsive crystalline materials exhibit a self-healing behavior through SCSC phase transitions.[5e,6] However, the phenomenon is still rare and unknown in the fields of mechano-responsive luminescent crystalline materials.

Herein, we report the first example of a mechanical-stimulation-triggered SCSC transition under a concomitant change of the emission color and reversion through exposure to solvent vapors. Gold(I) complex **3** crystallizes under the inclusion of MeOH solvate molecules, and exhibits a molecular domino-type SCSC phase transition upon mechanical stimulation (cutting) that is accompanied by a drastic color change of the luminescence from green to orange under concomitant release of MeOH from the crystal (Figure 1b). Remarkably, the resulting daughter

phase can be reversed into the original phase in an SCSC manner upon exposure to a saturated MeOH vapor environment (Figure 1b).

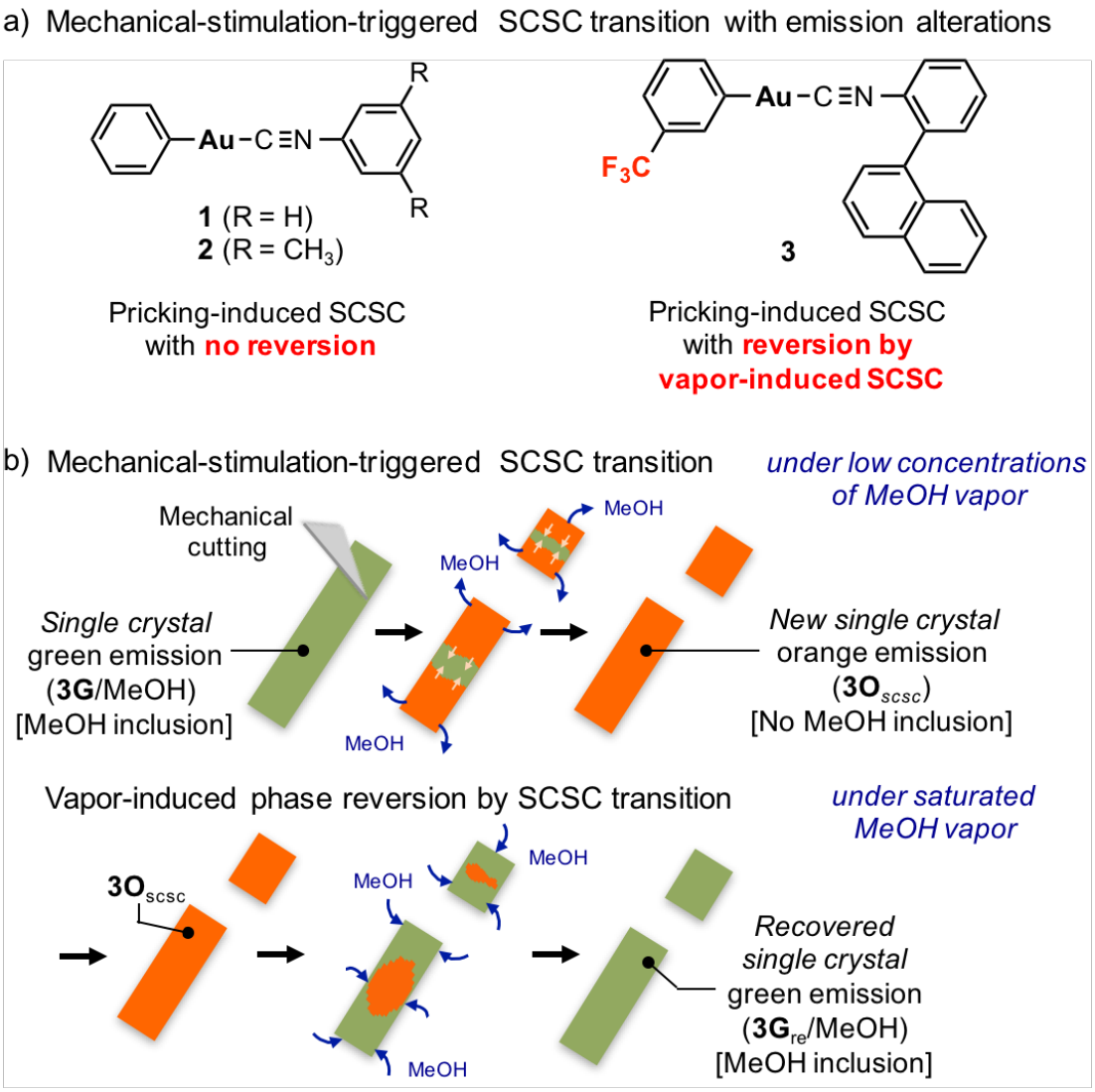

Figure 1. a) Molecular structure of the aryl gold(I) isocyanide complexes of **1**, **2**, and **3**. b) Schematic representation of the present work.

5.2. Results and discussion

5.2.1. Synthesis and Preparation

Gold(I) isocyanide complex **3** was prepared according to a previously described procedure.[7] A recrystallization from CH_2Cl_2 and MeOH afforded needle-shaped crystals of **3G**/MeOH (Figure 2a). The green emission of the **3G**/MeOH crystals did not change in a vial or a petri dish saturated with MeOH vapor (*cf.* the experimental section and Figure S1). However, an orange emission was observed when the **3G**/MeOH crystals were transferred to a glass plate under ambient atmosphere at room temperature (Figure S1). The resulting orange-emitting crystal showed no further emission change upon mechanical stress such as cutting or grinding.

However, even under MeOH vapor, a change of the emission color from green to orange was triggered by mechanical stimulation. As shown in Figure 2a, a single thin crystal of **3G**/MeOH was placed on a glass plate at 22 °C in an open petri dish that contained MeOH vapor (for details, see Figures S2 and S3). The crystal was then cut using a small knife (Figure 2b,c), after which the emission color changed to orange at the affected cross-sections (Figure 2d and Supporting Movie 1). Subsequently, the domain of the crystal exhibiting orange emission gradually expanded. After ca. 40 min, the entire crystal exhibited orange emission, denoted here as $\mathbf{3O}_{scsc}$ (Figure 2d,e and Supporting Movie 1).[8] Interestingly, a reversion of the emission of $\mathbf{3O}_{scsc}$ to the original green color, similar to that of **3G**/MeOH, was observed upon exposing $\mathbf{3O}_{scsc}$ to saturated MeOH vapor by putting a lid on the petri dish (Figure 2j). After ca. 15 min, the crystals had reverted entirely to the original phase, denoted as $\mathbf{3G}_{re}$/MeOH (Figure 2f–i). The recovered crystal fragments moreover displayed the same emission change to orange after cutting them under low concentrations of MeOH vapor.

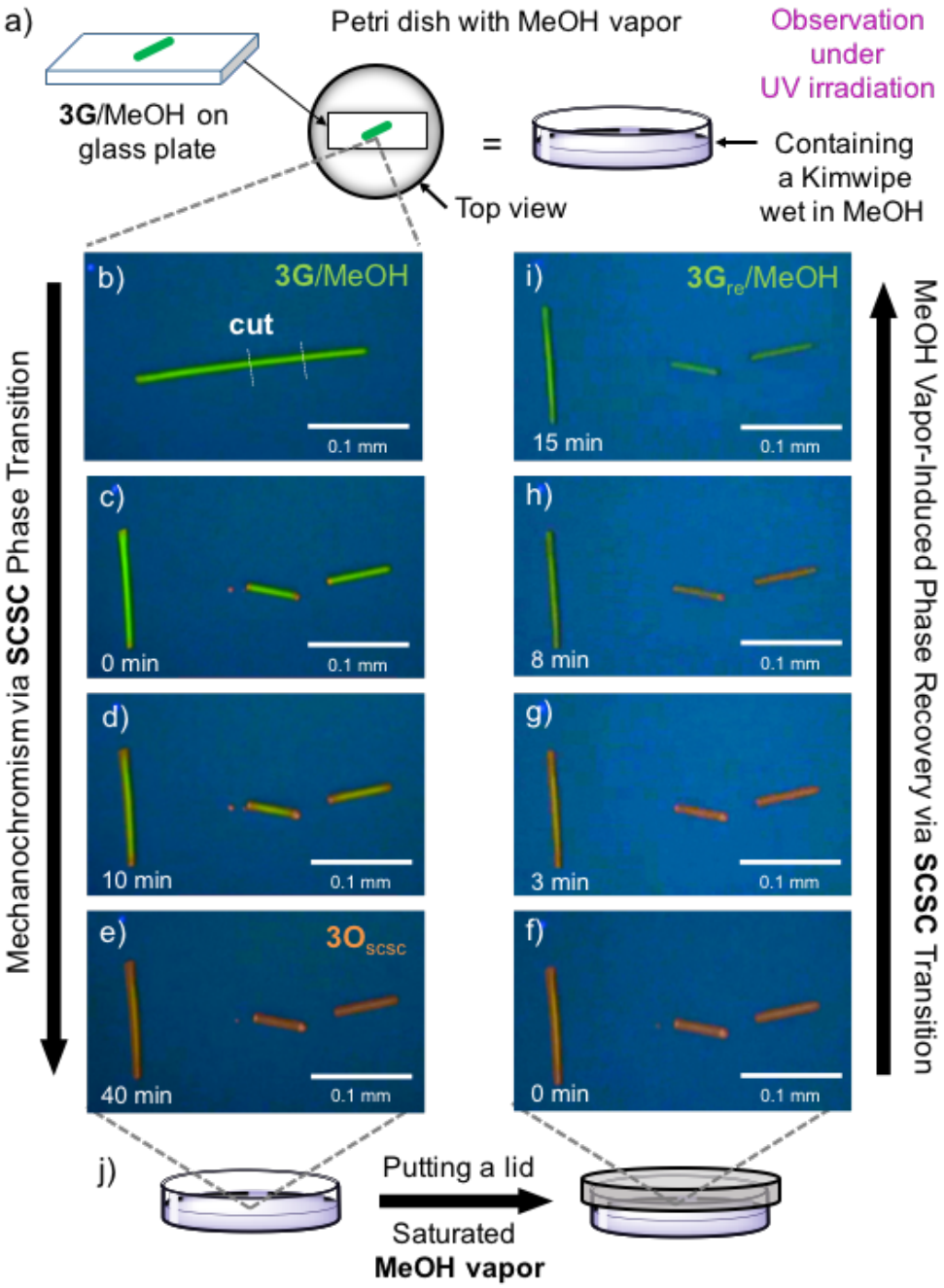

Figure 2. a) Schematic representation of **3G**/MeOH in a petri dish with MeOH vapor. b–e) Photographs of the mechanical-stimulation-triggered SCSC transition under UV irradiation (365 nm) accompanied by a color change of the luminescence; f–i) MeOH vapor-induced phase reversion in an SCSC manner; j) schematic representation of the procedure performed to saturate the petri dish with MeOH vapor.

5.2.2. Single Crystal X-Ray Diffraction Analyses

Subsequently, we performed single-crystal XRD measurements on the crystalline samples (Figure S4). **3G**/MeOH crystallizes in the acentric polar space group $Pna2_1$, and molecules of the recrystallization solvent MeOH were included in the crystal structure (Figures 3 and S5 as well as Table 1 and S1).[9] The axial chirality of the biaryl moiety in **3** results in the formation of (*R*)-**3** and (*S*)-**3** conformers. These molecules adopt the same dihedral angels between the phenyl and naphthyl rings of the biaryl moiety ($\theta_{ph\text{-}naph}$) of 60.0(3)° [(*S*)-**3**] and –60.0(3)° [(*R*)-**3**]. The dihedral angle between the phenyl ring on the gold atom and that in the isocyanide ligand ($\theta_{ph\text{-}ph}$) is 83.1(4)° in both conformers (Figure S5). The (*R*)-**3** and (*S*)-**3** conformers form a dimer with no inversion center, connected via an aurophilic interaction [Au···Au: 3.3096(5) Å] and two CH-π interactions (H···phenyl ring: 2.794(12) and 2.771(12) Å) (Figure 3a). As illustrated in Figure 3b, the dimer in **3G**/MeOH also interacts with adjacent dimers of the same conformation through aurophilic [Au ··· Au: 3.3096(5) Å] and CH-π (H ··· phenyl ring: 2.771(12) Å) interactions, forming a column. It should be noted that the dimers in the column are oriented in the same direction (Figure 3b). The column itself does not contain an inversion center, and neighboring columns (see light gray and orange columns in Figure 3c) are oriented in opposite directions, whereby the absence of inversion centers confirms the aforementioned polar space group. The included MeOH molecules ([**3**]/[MeOH] = 0.5, see Table 1) are located between the columns, and neighboring MeOH molecules interact via hydrogen bonds (O···O: 2.64(2) and 2.634(18) Å). Clear interactions were not observed between molecules of **3** in the columns and MeOH (Figure 3c,d and S5), implying that MeOH should be easily released from this structure. Face index measurements revealed that the columns and MeOH molecules extend along the long axis of the **3G**/MeOH crystal (Figures 3c,d).

In contrast to **3G**/MeOH, the orange-emitting crystal $\mathbf{3O}_{scsc}$, which was obtained from cutting **3G**/MeOH, crystallizes in the centrosymmetric space group *P*-1 and does not include any solvent molecules.[9] The dimer unit in $\mathbf{3O}_{scsc}$ contains (*S*)-**3** and (*R*)-**3** conformers arranged in an antiparallel manner with an inversion center through aurophilic interactions [Au···Au: 3.2077(3) Å] (Figure 4a). The $\theta_{ph\text{-}naph}$ dihedral angle of the (*S*)-**3** conformer in $\mathbf{3O}_{scsc}$ is 67.86(7)°, while the $\theta_{ph\text{-}ph}$ angle in the conformers is 33.03°, which is smaller than that in the **3G**/MeOH crystal. Neighboring dimers are packed so as to form an inversion center through π–π interactions [naphthyl···naphthyl rings: 3.470(4) Å] (Figures 4b,c). The crystallographic data thus indicate that the polar solvated **3G**/MeOH crystal is transformed upon exposure to

mechanical stress into the centrosymmetric **3O**$_{scsc}$ crystal under concomitant release of the solvent molecules.

The **3G**$_{re}$/MeOH crystal, obtained from **3O**$_{scsc}$ by adding MeOH vapor, was of sufficient quality for a single-crystal XRD analysis. Remarkably, the crystal structure of **3G**$_{re}$/MeOH matched that of **3G**/MeOH (Figure S7 and Table 1, S1). This was further confirmed by the simulated powder XRD patterns for both crystals (Figure S8).

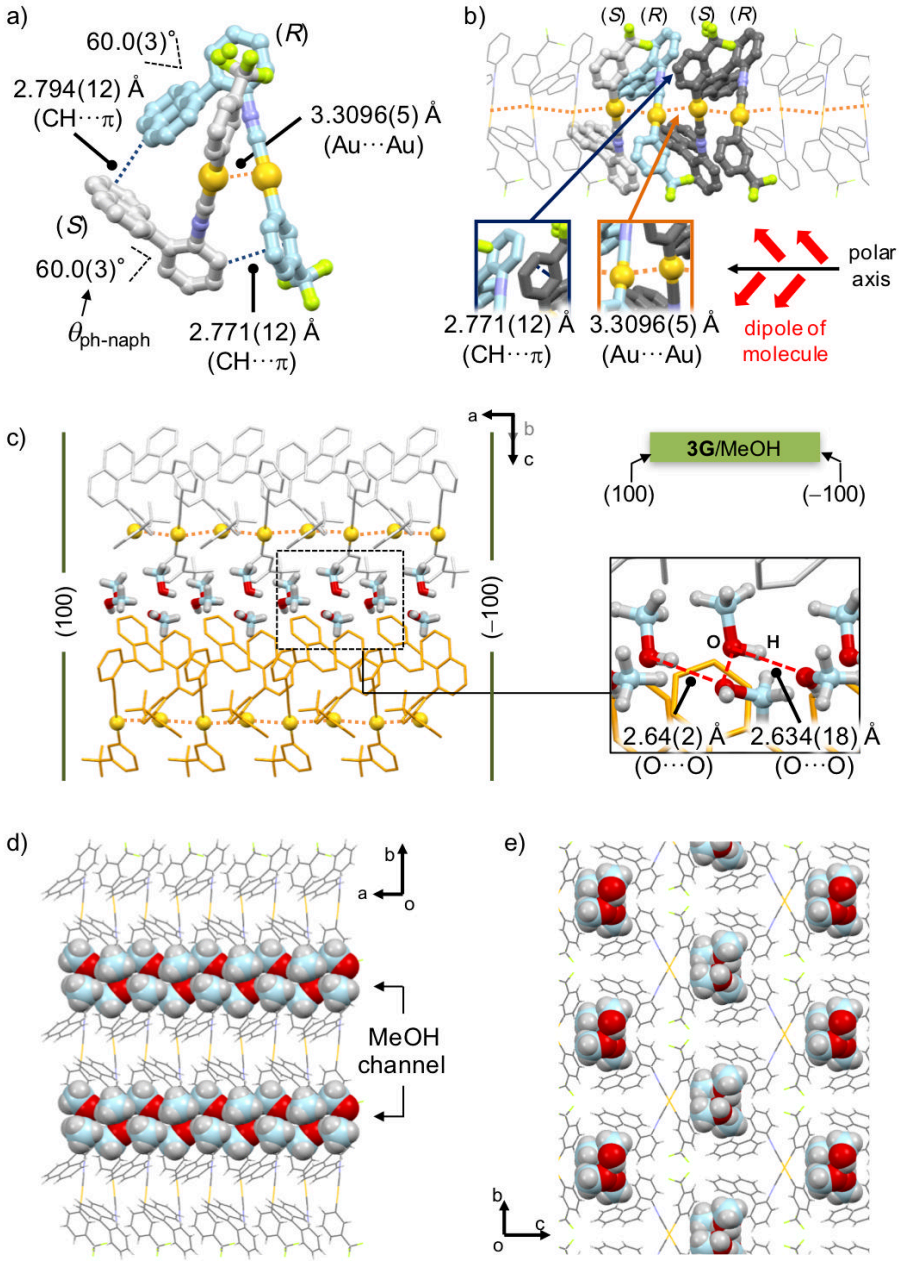

Figure 3. Crystal structures of **3G**/MeOH. a) Dimer of (*S*)- and (*R*)-**3**, b) columnar structure, and c) packing structure of **3G**/MeOH with MeOH inclusion in the absence of an inversion center. d) and e) MeOH channels illustrated in a space filling.

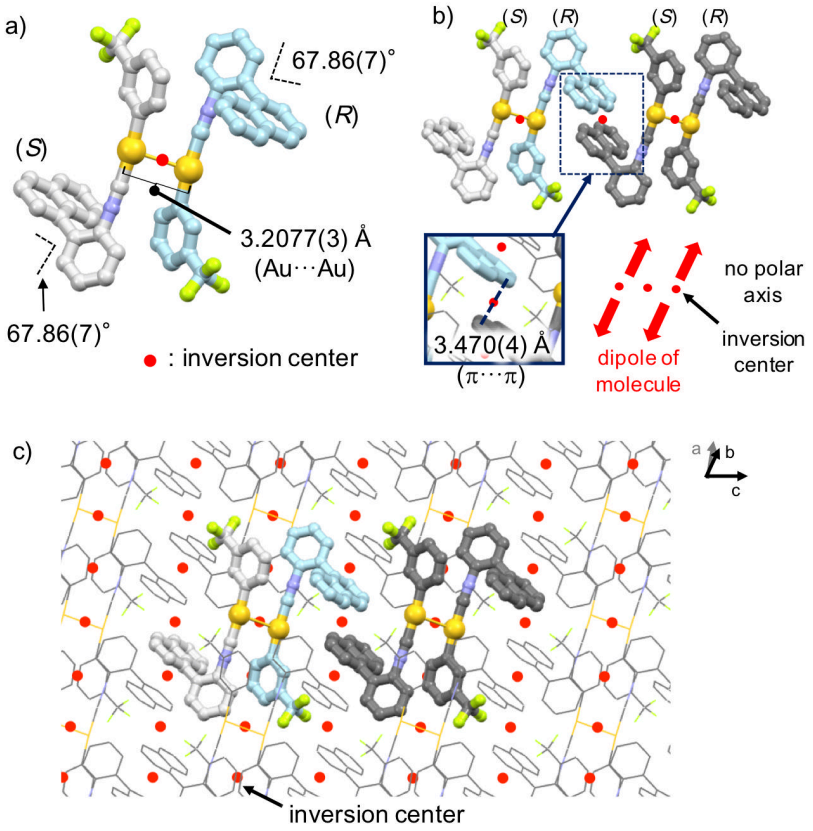

Figure 4. Crystal structures of **3O**$_{scsc}$. a) Dimer of (*S*)- and (*R*)-**3** with an inversion center, b) tetramer, and c) packing structure of **3O**$_{scsc}$.

Table 1. Selected X-ray crystallographic data of **3G**/MeOH, **3G**$_{re}$/MeOH, **3O**$_{scsc}$, and **3O**.

Polymorph	**3G**/MeOH	**3G**$_{re}$/MeOH	**3O**$_{scsc}$	**3O**
Space Group	*Pna*2$_1$ (#33)	*Pna*2$_1$ (#33)	*P*-1 (#2)	*P*-1 (#2)
Empirical Formula	$C_{24}H_{15}AuF_3N$, 2(CH_4O)	$C_{24}H_{15}AuF_3N$, 2(CH_4O)	$C_{24}H_{15}AuF_3N$	$C_{24}H_{15}AuF_3N$
Crystal System	orthorhombic	orthorhombic	triclinic	triclinic
Z value	4	4	2	2
a / Å	6.4976(3)	6.5333(2)	8.7329(2)	8.7264(6)
b / Å	14.3530(7)	14.3788(4)	9.2722(2)	9.3243(6)
c / Å	24.8911(12)	24.7773(12)	11.9521(3)	11.9764(9)
α / °	90	90	87.876(2)	87.967(2)
β / °	90	90	81.512(2)	81.741(2)
γ / °	90	90	82.835(2)	82.7141(19)
D_{calc} / g cm^{-3}	1.818	1.813	1.998	1.984
Residuals: R_1	0.0369	0.0331	0.0195	0.0746
Residuals: wR_2	0.0812	0.0754	0.0452	0.1899
Goodness of Fit	1.022	1.055	1.064	1.072

5.2.3. Studies on Luminescence Properties

The green-emitting crystal **3G**/MeOH exhibits an emission band with a maximum emission wavelength ($\lambda_{em,max}$) at 506 nm (Figure 5, green solid line). The green emission is described in Commission Internationale de l'Éclairage (CIE) 1931 chromaticity coordinates of (0.32, 0.57) as shown in Figure S11. The excitation spectrum of **3G**/MeOH monitored at 506 nm was recorded between 310 and 450 nm, whereby the maximum excitation wavelength $\lambda_{ex,max}$ was observed at 395 nm (Figure 4, green dashed line). The absolute emission quantum yield (Φ_{em}) and the average emission lifetime (τ_{av})[10] of **3G**/MeOH were determined to be 0.05 and 384.1 μs, respectively (Figure S12 and Table S3). In contrast, **3O**$_{scsc}$ presents a drastically red-shifted emission spectrum with CIE coordinates of (0.56, 0.43) and blue-shifted excitation band, i.e., **3O**$_{scsc}$ exhibits a broad emission spectrum with $\lambda_{em,max}$ = 612 nm (Figure 5, orange solid line, and S11), and the excitation spectrum is also broader with $\lambda_{ex,max}$ = 362 nm (Figure 5, orange dashed line). Compared to **3G**/MeOH, the Φ_{em} (0.19) and τ_{av} (14.6 μs) values for **3O**$_{scsc}$ are higher and shorter, respectively (Figure S12 and Table S3). The very weak emission intensity of **3** in CH_2Cl_2 suggests that the emission properties of the crystalline samples are determined by their aggregated structure (Figure S13).[11]

The recovered **3G**$_{re}$/MeOH phase exhibits emission ($\lambda_{em,max}$ = 506 nm) with CIE coordinates of (0.37, 0.54) and excitation ($\lambda_{ex,max}$ = 380 nm) bands almost identical to those of **3G**/MeOH (Figure 5, black solid and dashed lines, respectively). Moreover, the Φ_{em} (0.05) and τ_{av} (331.1 μs) values of **3G**$_{re}$/MeOH are also very similar to those of **3G**/MeOH (Figure S12 and Table S3). These results indicate that the emission properties of the mother phase are clearly recovered from the daughter phase after the MeOH-induced SCSC phase transition.

In order to obtain mechanistic insights into the emission properties of **3G**/MeOH and **3O**$_{scsc}$, we carried out time-dependent (TD) DFT calculations on the single-crystal structures. The tetramer geometry of **3G**/MeOH was thereby adopted from the crystal structure of **3O**$_{scsc}$. The simulated UV-vis absorption spectra were similar to the excitation spectra of both crystals, thus suggesting a reasonable excitation path for both samples (Figure S20). The HOMOs of both **3G**/MeOH and **3O**$_{scsc}$ are localized on the gold atoms, forming aurophilic interactions, and the LUMOs are mainly located on the isocyanide ligands (Figure S21 and Table S4–5). These results demonstrate the metal-metal-to-ligand charge transfer (MMLCT) character (from the gold atoms to the isocyanide ligands) of the excited states of **3G**/MeOH and **3O**$_{scsc}$. For many arylgold(I) isocyanide complexes, polymorphs with smaller $\theta_{ph\text{-}ph}$ values show a red-shifted emission compared to those with larger $\theta_{ph\text{-}ph}$ values.[13] The structures of **3G**/MeOH and

3O$_{scsc}$ obtained in this work are thus consistent with this trend (**3G**/MeOH: $\lambda_{em,max}$ = 506 nm, $\theta_{ph\text{-}ph}$ = 83.12°; **3O**$_{scsc}$: $\lambda_{em,max}$ = 612 nm, $\theta_{ph\text{-}ph}$ = 33.03°).[14]

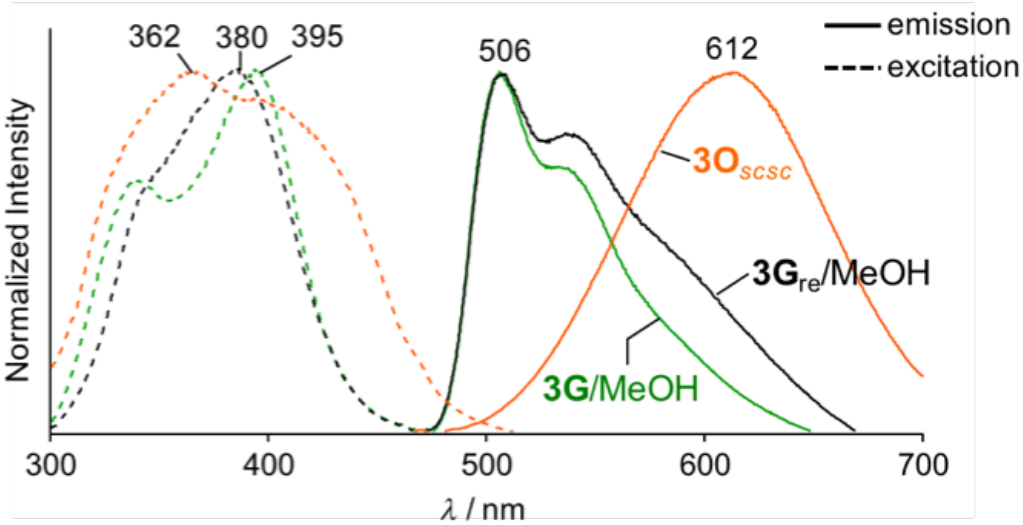

Figure 5. Emission spectra (λ_{ex} = 365 nm) of **3G**/MeOH (green solid line), **3G**$_{re}$/MeOH (black solid line), and **3O**$_{scsc}$ (orange solid line). Excitation spectra of **3G**/MeOH (green dashed line), **3G**$_{re}$/MeOH (black dashed line), and **3O**$_{scsc}$ (orange dashed line) recorded at emission maxima.

5.2.4. Control Experiment and Proposed Mechanism of the Reversible SCSC

The reversion of **3O** into **3G**/MeOH depends on the crystal preparation procedure. The phase transition from **3G**/MeOH to **3O**$_{scsc}$ was also observed when the crystal was gently heated at 30 °C under ambient atmosphere to release the MeOH molecules. The reversion of this heated sample was then confirmed by exposure to high concentrations of MeOH vapor at room temperature (Figure S14). The orange-emitting crystal **3O** was prepared by recrystallization from CH_2Cl_2 and hexane (instead of MeOH), and its crystal structure was confirmed to match that of **3O**$_{scsc}$ (Figures S6 and S8). In contrast to **3O**$_{scsc}$, the resulting crystal did not exhibit a phase transition into **3G**/MeOH upon exposure to saturated MeOH vapor or addition of liquid MeOH (Figure S15). An orange-emitting sample of a crystalline powder, which was obtained from ball-milling **3G**/MeOH (Figures S16–18), exhibited a crystal structure similar to that of **3O**$_{scsc}$, which was confirmed by powder XRD analysis (Figure S18). Changes of the emission color into the green were not observed for this powder sample upon exposure to saturated MeOH vapor (Figures S16–18).[12] SEM images of **3O**$_{scsc}$ and **3O** samples obtained from different procedures indicate their distinct surface characteristics (Figure S19). The crystal **3O**$_{scsc}$ had rough surface. Contrary to **3O**$_{scsc}$, **3O** obtained by recrystallization exhibited smooth surface (Figure S19). These results indicate that the crystal habit and surface conditions should be important for the reversion.

In the mechanical-stimulation-triggered SCSC transitions of **1** and **2**, the key factors are the phase transitions from metastable to stable phases. In this work, the key feature for the reversible phase changes in **3** is the release/inclusion of MeOH. In the presence of low concentrations of MeOH, the MeOH molecules remain in the **3G**/MeOH crystal through an adsorption/desorption equilibrium of MeOH on the crystal surface. By cutting the **3G**/MeOH crystal, this equilibrium is altered, and the molecular arrangement changed, which results in a release of MeOH from the crystal, which finally affords **3O**$_{scsc}$ under such a low concentration of MeOH vapor. The cut edge corresponds to the (100) or (−100) surface, which is oriented orthogonal to the channel of the MeOH molecules and the domain where phase changes would occur. We propose that the release of MeOH molecules from the cut crystal edge should affect the equilibrium on the very other side of the MeOH channels. This should be the reason why the emission-color changes start not only at the cut edge, but also at the other end of the crystalline needle (Figure 2). For the reversion, increasing the MeOH vapor concentration should shift the equilibrium toward the inclusion of MeOH and the SCSC phase changes from **3O**$_{scsc}$ to **3G**/MeOH.[15] It is reasonable to assume that **3G**/MeOH**,** which accommodates polar

MeOH molecules in the crystal structure, exhibits a “polar” molecular arrangement (Figure 3b) and that, after releasing the MeOH molecules, its crystal structure changes to a non-polar phase, where the molecular polarity is canceled in the centrosymmetric structure via the inversion center (Figure S22).[16]

5.3. Summary

We have discovered the first example for reversible mechanical-stimulation-triggered SCSC transitions under concomitant changes of the luminescence properties. Interestingly, these SCSC transitions occur between a polar crystal containing a polar solvent (MeOH) and a centrosymmetric crystal that does not contain solvent molecules. This solvent-related phase reversion represents a new design strategy for mechano-responsive SCSC materials.

5.4. Experimental Section

5.4.1. General

All commercially available reagents and solvents are of reagent grade and were used without further purification unless otherwise noted. Solvents for synthesis were purchased from commercial suppliers, degassed by three freeze-pump-thaw cycles and further dried over molecular sieves (4 Å). NMR spectra were recorded on a JEOL JNM-ECX400P or JNM-ECS400P spectrometer (^{1}H: 400 MHz; ^{13}C: 100 MHz) using tetramethylsilane and $CDCl_3$ as internal standards, respectively. Emission spectra were recorded on a Hitachi F-7000 spectrometer. Absorption spectra were recorded on the basis of synchronous fluorescence spectroscopy using a Hitachi F-7000 spectrometer equipped with an integrating sphere. The emission quantum yields of the solid samples were recorded on a Hamamatsu Quantaurus-QY spectrometer with an integrating sphere. Emission lifetime measurements were recorded on a Hamamatsu Quantaurus-Tau spectrometer. Elemental analyses and low- and high-resolution mass spectra were recorded at the Global Facility Center at Hokkaido University. Photographs were obtained using Olympus BX51 or SZX7 microscopes with Olympus DP72, Nikon D5100 digital cameras. Thermal gravimetric analysis profiles were recorded on Bruker TG-DTA2010SAT. Single crystal X-ray structural analyses were carried out on a Rigaku XtaLAB PRO MM007 diffractometers.

5.4.2. Synthesis

Complex **3** was prepared according to the previously published procedure with some modifications.[17]

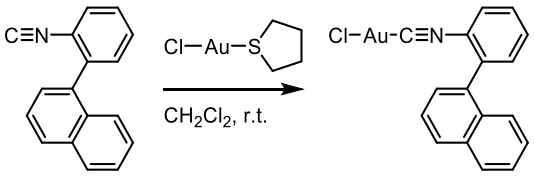

4 **5**

1-(2-Isocyanophenyl)naphthalene (**4**, 0.127 g, 0.55 mmol) and chloro(tetrahydrothiophene)gold(I) (0.160 g, 0.50 mmol) were dissolved in CH_2Cl_2 (16 mL) and stirred. After 2 h, the solvent was removed with a rotary evaporator under a reduced pressure. Washing with methanol of the residue gave an analytically pure white solid of **5** (0.166 g, 0.36 mmol, 72%). ^{1}H NMR (400 MHz, $CDCl_3$, δ): 7.40–7.50 (m, 3H), 7.54–7.62 (m, 4H), 7.68–7.74 (m, 2H), 7.97–8.00 (m, 2H). ^{13}C NMR (100 MHz, $CDCl_3$, δ): 124.4 (*C*), 124.7 (*C*H), 125.4 (*C*H), 126.6 (*C*H), 127.2 (*C*H), 127.5 (*C*H), 127.7 (*C*H), 129.0 (*C*H), 129.2 (*C*H), 129.9 (*C*H), 130.9 (*C*), 131.6 (*C*H), 132.3 (*C*H), 133.3 (*C*), 133.7 (*C*), 139.4 (*C*), 142.8 (*C*). Anal. MS-EI (*m*/*z*): $[M+H]^+$ calcd for $C_{17}H_{11}AuClN$, 461.02455; found, 461.01432. Calcd for $C_{17}H_{11}AuClN$: C, 44.23; H, 2.40; N, 3.03. Found: C, 44.12; H, 2.22; N, 2.92.

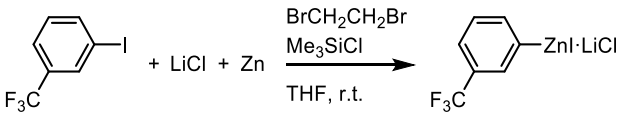

6

Anhydrous LiCl (0.806 g, 19 mmol) was placed in a flask and dried *in vacuo* for 30 min at 150 °C. Zinc powder (1.864 g, 19 mmol) was added under nitrogen atmosphere, and the resultant mixture of Zn and LiCl was dried *in vacuo* again for 30 min at 150 °C. The reaction flask was evacuated and refilled with nitrogen three times. After dry THF (20 mL) was added to the mixture, the Zn/LiCl powder was activated by addition of $BrCH_2CH_2Br$ (0.178 g, 5 mol%) and Me_3SiCl (1 drop). The powder of 1-iodo-3-(trifluoromethyl)benzene (5.168 g, 19 mmol) was then added at room temperature with stirring. The completion of the reaction was checked by GC analysis of the reaction aliquots. After 16 h, the solution of organozinc reagent was titrated with iodine. The organozinc solution in THF were carefully separated from the remaining zinc powder using a cannula, and transferred to another Schlenk flask under nitrogen.

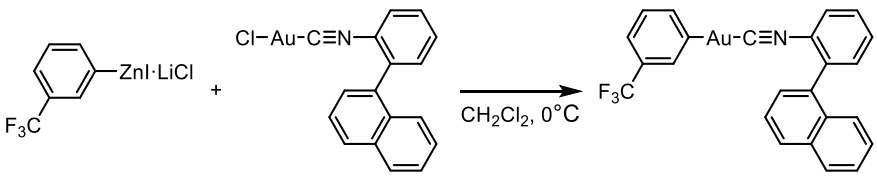

6 **5** **3**

To chloro(*o*-(1-naphthyl)phenylene isocyanide)gold(I) complex (**5**, 0.139 g, 0.3 mmol), dry THF (1 ml) was added under nitrogen atmosphere. After cooling to 0 °C, a THF solution of organozinc iodide reagent **6** (0.75 ml, 0.39 mmol, 0.52 M) was added dropwise with stirring. After stirring for 2 h, the reaction was quenched by the addition of a phosphate buffer solution and then extracted with CH_2Cl_2 three times and washed with H_2O. The organic layers were collected and dried over $MgSO_4$. After filtration, the solvent was removed *in vacuo*. Further purification by flash column chromatography (SiO_2, volume ratio of CH_2Cl_2/Hexane = 1:1) gave a yellow solid. The resulting solid was dried under reduced pressure to give **3** (0.129 g, 0.25 mmol, 80 %). ^{1}H NMR (400 MHz, $CDCl_3$, δ): 7.23–7.25 (m, 2H), 7.40–7.70 (m, 11H), 7.96–8.00 (m, 2H). ^{13}C NMR (400 MHz, $CDCl_3$, □): 121.0 (*C*), 122.3 (*C*H), 123.9 (*C*), 124.5 (*C*), 124.7 (*C*H), 125.3 (*C*H), 126.4 (*C*H), 127.5 (*C*H), 128.5 (*C*), 128.8 (*C*H), 128.9 (*C*H), 129.1 (*C*), 129.3 (*C*), 129.6 (*C*H), 130.1 (*C*H), 132.2 (*C*H), 133.6 (*C*), 133.8 (*C*H), 136.3 (*C*H), 138.8 (*C*H), 143.4 (*C*H), 162.1 (*C*), 163.2 (*C*). MS-EI (*m*/*z*): $[M+H]^+$ calcd for $C_{24}H_{15}AuNF_3$, 571.08221; found, 571.07198. Anal. Calcd for $C_{24}H_{15}AuNF_3$: C, 50.45; H, 2.65; N, 2.45. Found: C, 50.04; H, 2.45; N, 2.36.

5.4.3. Preparation of Crystals of 3G/MeOH and 3O

Preparation of **3G**/MeOH: The crystallization of **3G**/MeOH was accomplished by layering MeOH on a solution of **3** in CH_2Cl_2 at 2 °C for ~3 days (typically, such solutions contained 10 mg of the complex in 5 mL of CH_2Cl_2) which afforded **3G**/MeOH crystals that exhibited green emission under UV irradiation (365 nm; Figure S1a). Crystals of **3G**/MeOH did not show a change of emission when being placed in a petri dish (radius: 9 cm) that contained paper wipes (Kimwipes) impregnated with MeOH at 22 ºC (~75 mL; Figure S1c). b) Crystals of **3G**/MeOH showed an emission change from green to orange (**3O**$_{scsc}$; Figure S1b) when being exposed to ambient conditions.

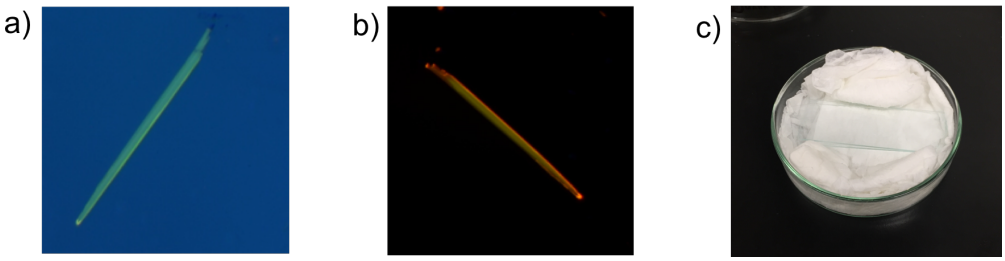

Figure S1. Photographs of a) a crystal of **3G**/MeOH in the petri dish containing MeOH vapor and b) an orange-emitting crystal obtained after exposing the **3G**/MeOH crystal to ambient conditions. c) A petri dish containing paper wipes (Kimwipes) impregnated with MeOH. Photographs in a) and b) were taken under irradiation with UV light (365 nm), while the photograph in c) was taken under illumination with ambient light.

Preparation of crystals of **3O**: The crystallization of **3O** was accomplished by a procedure similar to that used for the preparation of **3G**/MeOH, albeit that hexane was used instead of MeOH. Crystals of **3O** (size: ~1 mm) exhibit orange emission under irradiation with UV light (365 nm).

5.4.4. Procedures for Crystal Cutting and Changing MeOH Vapor Concentrations

Crystals of **3G**/MeOH in a petri dish under low concentrations of MeOH vapor at 22 ºC (without a lid; Figure S1) were cut with a small knife (Figure S2–3 and Supporting Movie 1). After ~5 min of cutting the crystal, the emission color of **3G**/MeOH spontaneously turned to orange. The entire crystal exhibited the orange emission after ~40 min (**3O**$_{SCSC}$). Remarkably, when the petri dish was covered with a lid, the orange emission color of **3O**$_{SCSC}$ changed to green, similar to that of **3G**/MeOH, and the entire crystal showed the green emission after ~15 min (Supporting Movie 1). The resulting crystal was denoted as **3G**$_{re}$/MeOH.

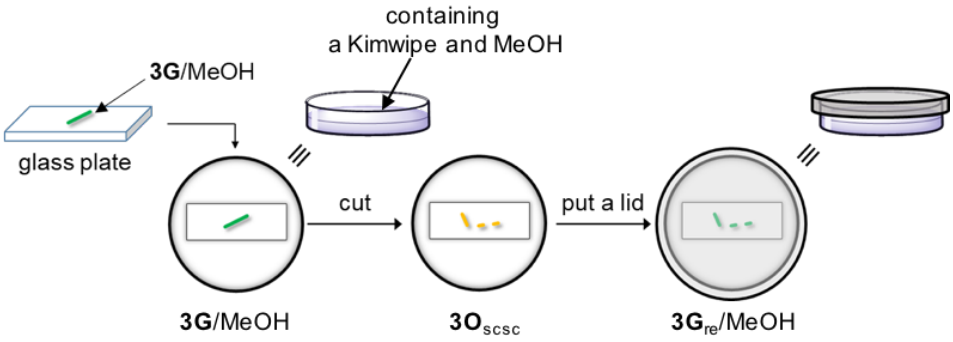

Figure S2. Schematic representation of the procedures for the mechano-induced SCSC phase transition of **3G**/MeOH in a petri dish under low concentrations of MeOH vapor (open petri dish) and the reverse SCSC phase transition of **3O**$_{scsc}$ under a high concentration of MeOH vapor (closed petri dish).

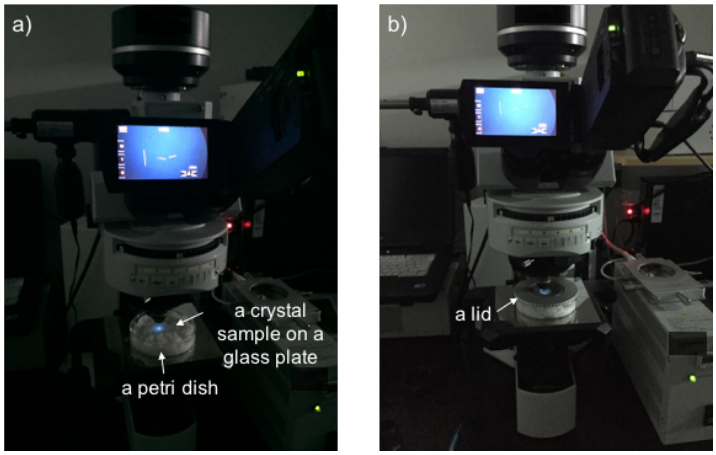

Figure S3. Photographs of the sample stage for a) cutting the crystals and b) increasing the concentration of MeOH vapor by putting a lid on the petri dish.

5.4.5. Data for Single Crystal X-ray Structural Analyses

Single-crystal X-ray diffraction (XRD) analyses were carried out on a Rigaku XtaLAB PRO MM007 diffractometer using graphite monochromated Mo-K_α radiation. Structures were solved by direct methods and expanded using Fourier techniques. All non-hydrogen atoms were refined anisotropically. Hydrogen atoms were refined using the riding model. All calculations were performed using the CrystalStructure crystallographic software package except for the refinements, which were performed using SHELXT.[18]

Single crystals of **3G**/MeOH were prepared by recrystallization (*cf.* page S5). After conducting the single-crystal diffraction measurements on a crystal of **3G**/MeOH (**A** in Figure S4), this crystal and another **3G**/MeOH crystal (**B**) were cut in the same petri dish containing a low concentration of MeOH vapor at 22 ºC (*cf.* Figures S2 and S3) to obtain crystals of **3O**$_{scsc}$ (**A'** and **B'**). For the single-crystal XRD measurements of **3O**$_{scsc}$, crystal **A'** (Figure S4) was used. Subsequently, the MeOH concentration was increased by putting a lid on the petri dish to induce the phase transition of the **3O**$_{scsc}$ crystals to the **3G**$_{re}$/MeOH crystals (*cf.* Figures S2 and S3). For the single-crystal XRD measurement of **3G**$_{re}$/MeOH, crystal **B"**, obtained from the sequential SCSC phase transitions **B** → **B'** → **B"**, was used.

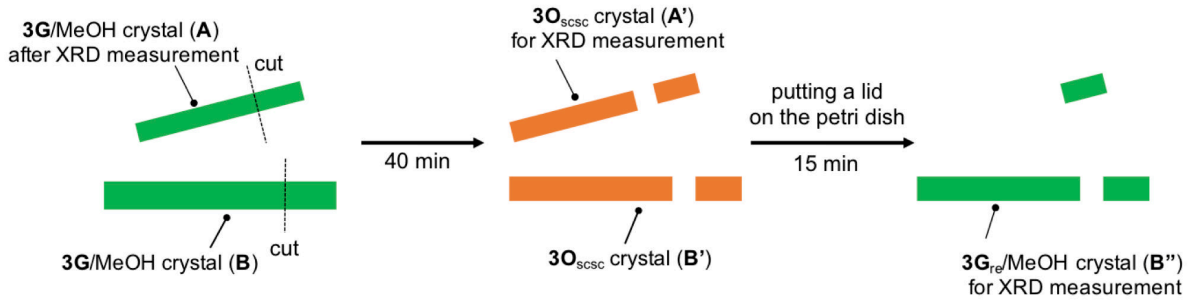

Figure S4. Schematic representation of the crystals of **3** that were used for the single-crystal XRD measurements upon mechanical-force-induced and MeOH-vapor-induced SCSC phase transitions.

Table S1. Summary of X-ray crystallographic data of **3G**/MeOH, **3G**$_{re}$/MeOH, **3O**$_{scsc}$, and **3O**.

Polymorph	**3G**/MeOH	**3G**$_{re}$/MeOH	**3O**$_{scsc}$	**3O**
CCDC Name	1582461	1582465	1582487	1582460
Empirical Formula	$C_{24}H_{15}AuF_3N$, $2(CH_4O)$	$C_{24}H_{15}AuF_3N$, $2(CH_4O)$	$C_{24}H_{15}AuF_3N$	$C_{24}H_{15}AuF_3N$
Formula Weight	635.44	635.44	571.35	571.35
Crystal System	orthorhombic	orthorhombic	triclinic	triclinic
Crystal Size / mm	0.236 × 0.028 × 0.016	0.508 × 0.049 × 0.043	0.125 × 0.028 × 0.016	0.674 × 0.473 × 0.100
a / Å	6.4976(3)	6.5333(2)	8.7329(2)	8.7264(6)
b / Å	14.3530(7)	14.3788(4)	9.2722(2)	9.3243(6)
c / Å	24.8911(12)	24.7773(12)	11.9521(3)	11.9764(9)
α / °	90.0000	90.0000	87.876(2)	87.967(2)
β / °	90.0000	90.0000	81.512(2)	81.741(2)
γ / °	90.0000	90.0000	82.835(2)	82.7141(19)
V / Å^3	2321.35(19)	2327.60(15)	949.55(4)	956.45(11)
Space Group	*Pna*2$_1$ (#33)	*Pna*2$_1$ (#33)	*P*-1 (#2)	*P*-1 (#2)
Z value	4	4	2	2
D_{calc} / g cm^{-3}	1.818	1.813	1.998	1.984
Temperature / K	93	93	93	123
$2\theta_{max}$ / °	0.0	50.7	0.0	55.0
μ (MoKα) / cm^{-1}	64.073	63.901	78.123	77.554
No. of Reflections Measured	Total : 5104 Unique : 4157 (R_{int} = 0.0429)	Total : 6087 Unique : 3415 (R_{int} = 0.0230)	Total : 13475 Unique : 4451 (R_{int} = 0.0264)	Total : 9332 Unique : 4347 (R_{int} = 0.1002)
No. of Observations (All reflections)	4157	3415	4451	4347
Residuals: R_1 ($I > 2.00\sigma(I)$)	0.0369	0.0331	0.0195	0.0746
Residuals: wR_2 (All reflections)	0.0812	0.0754	0.0452	0.1899
Goodness of Fit Indicator (*GOF*)	1.022	1.055	1.064	1.072
Maximum peak in Final Diff. Map / Å^3	1.63 e$^-$	1.35 e$^-$	1.16 e$^-$	4.80 e$^-$
Minimum peak in Final Diff. Map / Å^3	–2.03 e$^-$	–2.09 e$^-$	–1.00 e$^-$	–5.61 e$^-$

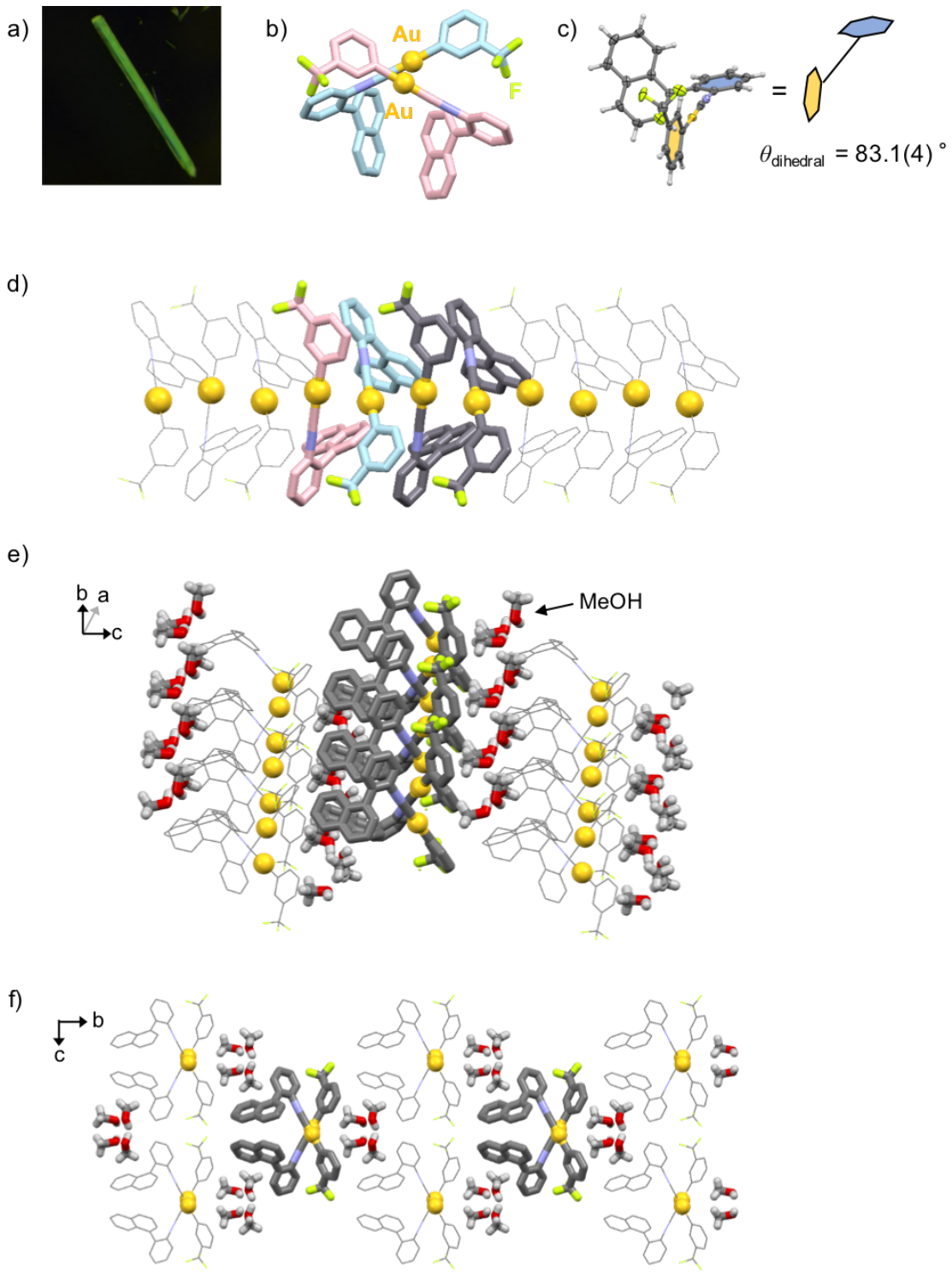

Figure S5. a) Photograph of the single crystal of **3G**/MeOH taken under UV light. b–f) Single crystal structures of **3G**/MeOH. All the H atoms of **3** except for those in c) are omitted for clarity.

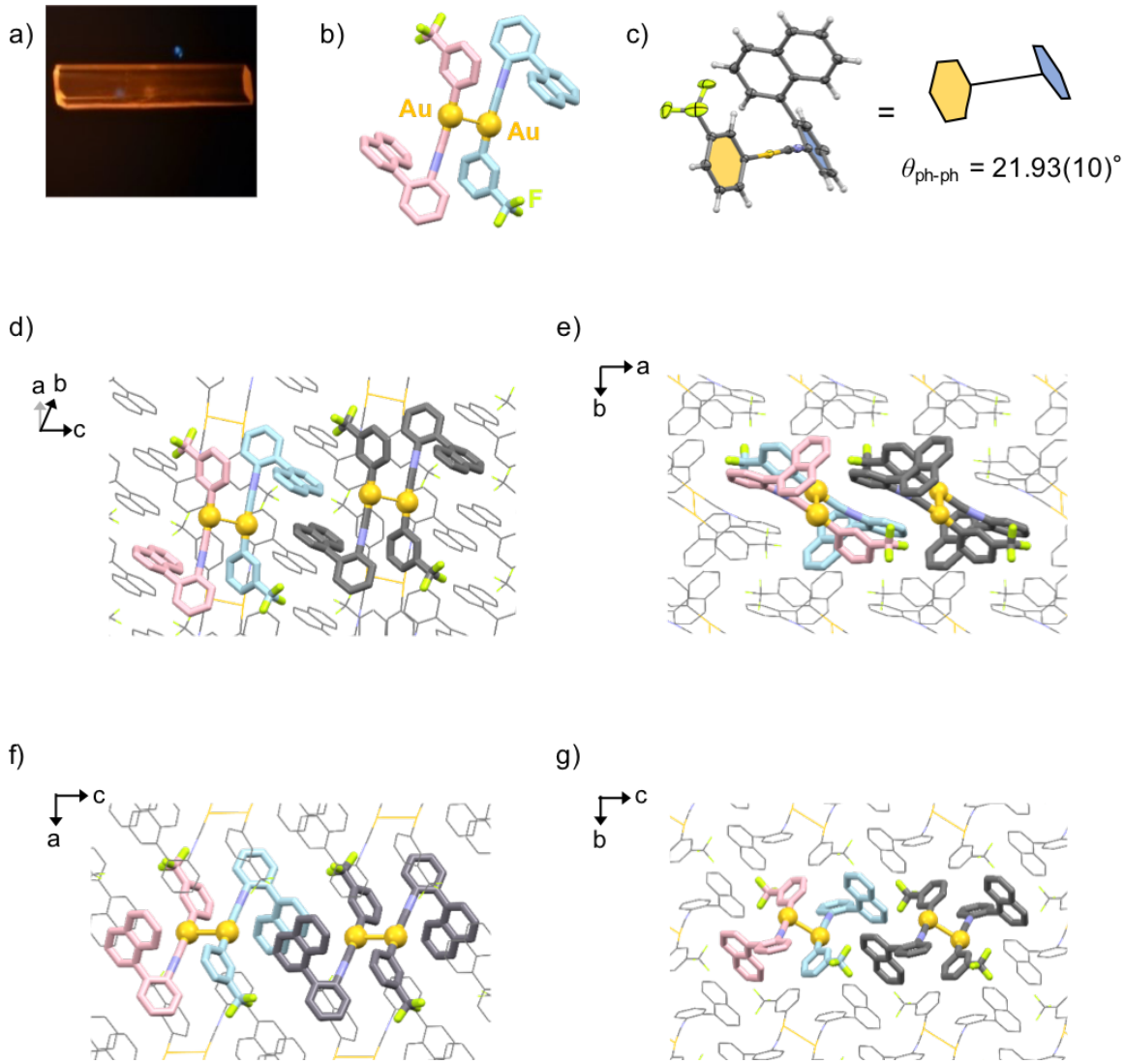

Figure S6. a) Photograph of the single crystal of **3O** obtained by recrystallization taken under UV light. b–f) Single crystal structures of **3O**. All the H atoms except for those in c) are omitted for clarity.

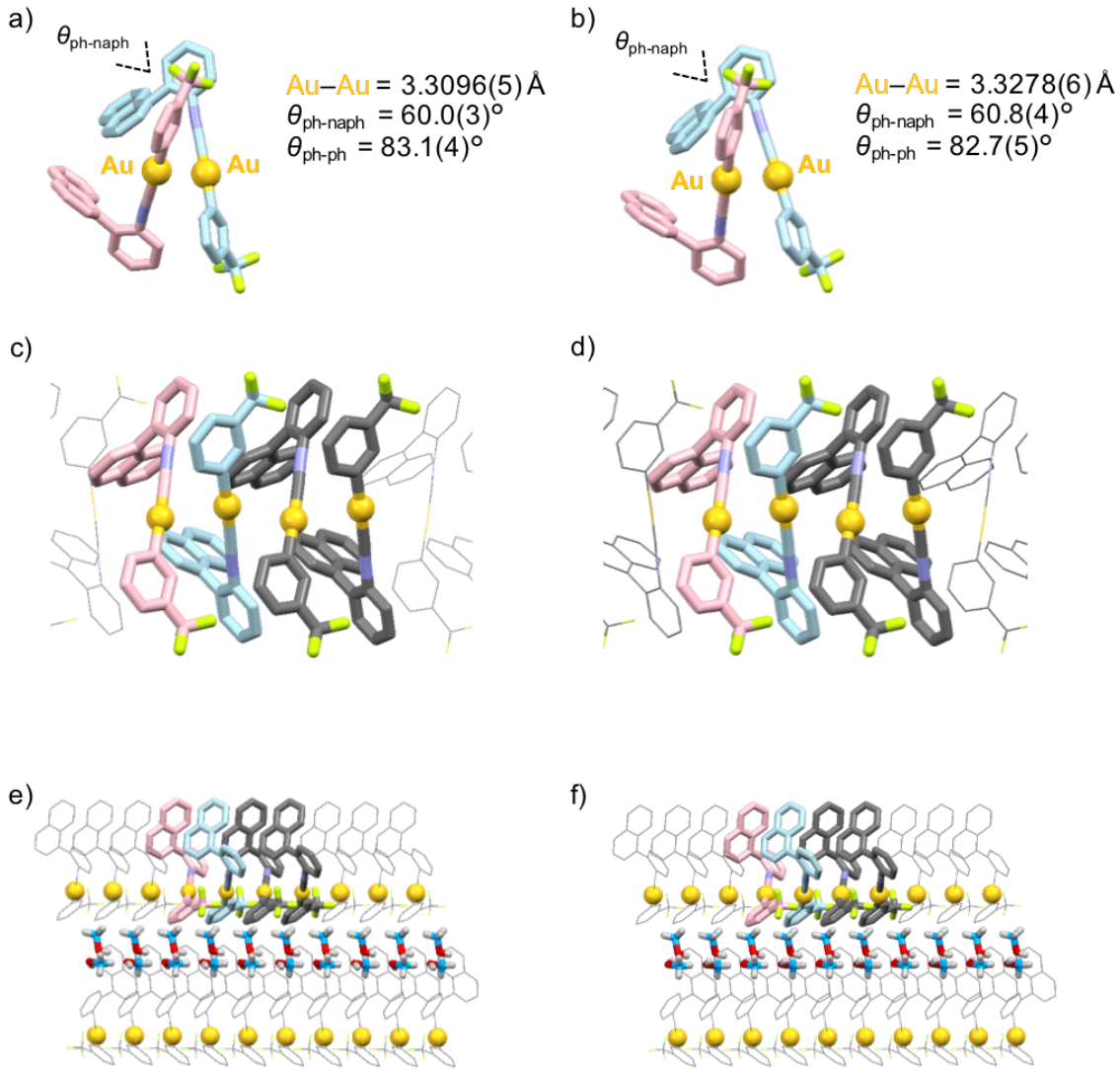

Figure S7. Comparison of the single crystal structures of **3G**/MeOH (a, c, and e) and **3G**$_{re}$/MeOH (b, d, and f). All the H atoms are omitted for clarity.

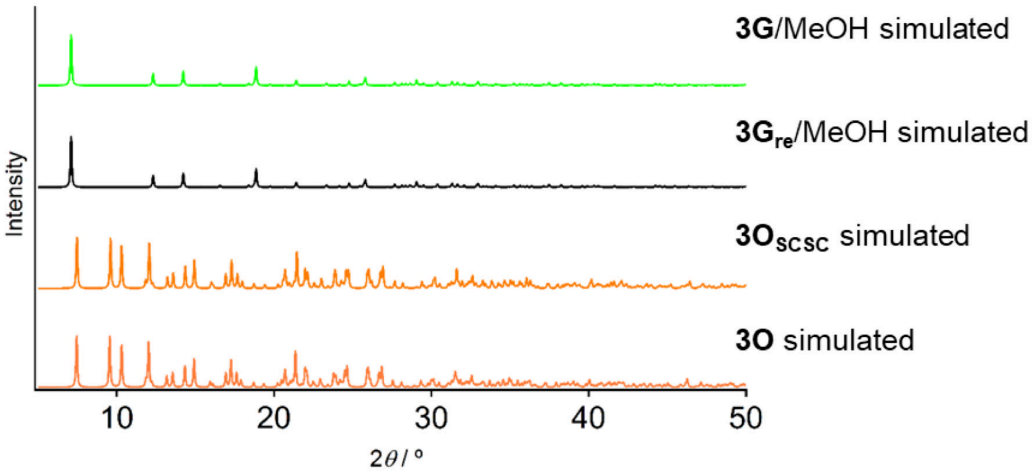

Figure S8. Simulated powder XRD patterns of **3G**/MeOH, **3G**$_{re}$/MeOH, **3O**$_{scsc}$, and **3O**.

5.4.6. ^{1}H NMR Spectra of 3G/MeOH and 3O

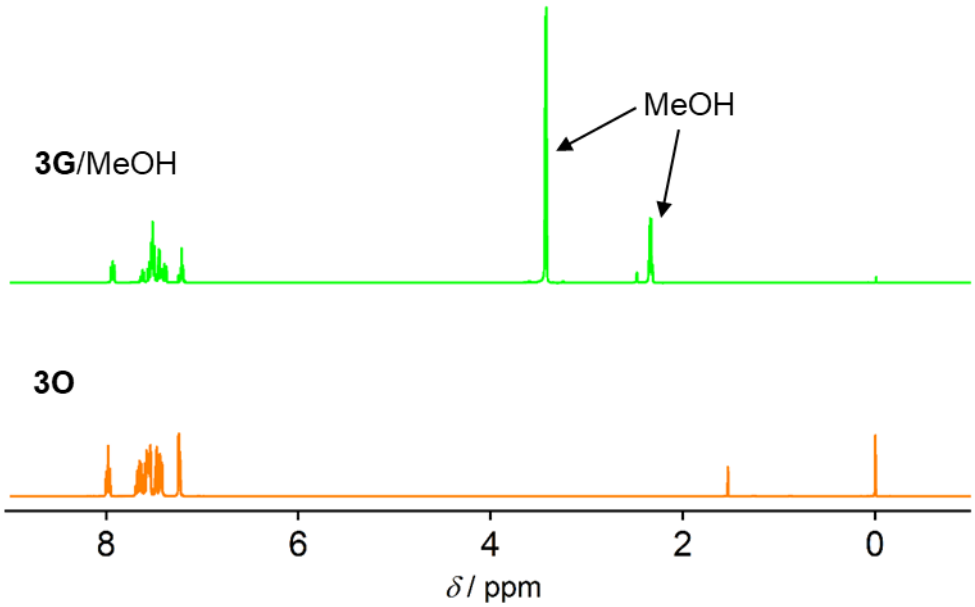

Figure S9. ^{1}H NMR spectra of **3G**/MeOH and **3O**, which are obtained by the recrystallization, dissolved in $CDCl_3$.

7. TGA and Elemental Analysis of 3O

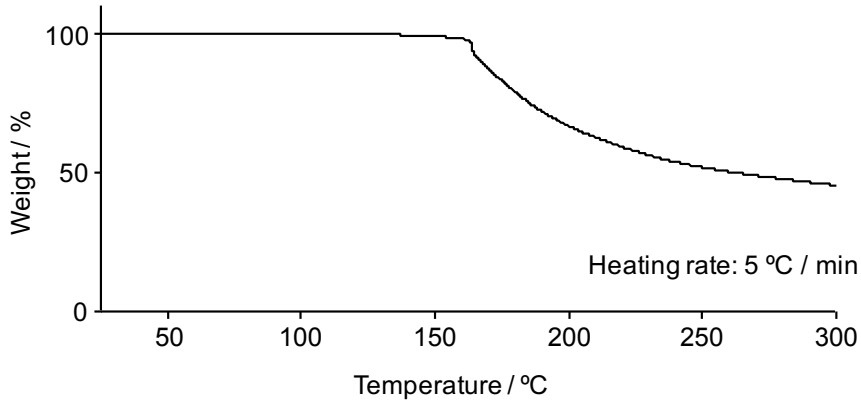

Figure S10. TGA profiles of **3O**. The heating rate is 5 ºC/min. There was no decrease in the weight percent of the sample until ca. 150 ºC. This result indicates that the **3O** crystal does not include solvent molecules.

Table S2. Elemental analysis of the **3O**.

	C	H	N
Calculated for **3** ($C_{24}H_{15}AuNF_3$)	50.45	2.65	2.45
3O[a]	50.00	2.46	2.36

[a]Sample was obtained by recrystallization.

8. Photophysical Properties

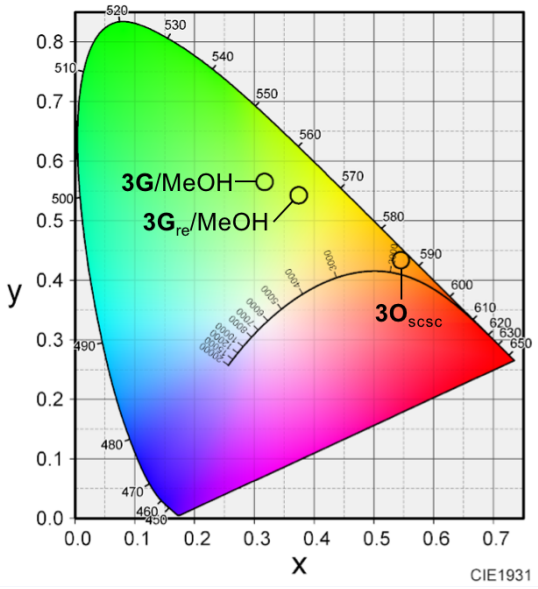

Figure S11. Emission colors of **3G**/MeOH, **3G**$_{re}$/MeOH, and **3O**$_{scsc}$ in a CIE 1931 chromaticity diagram.

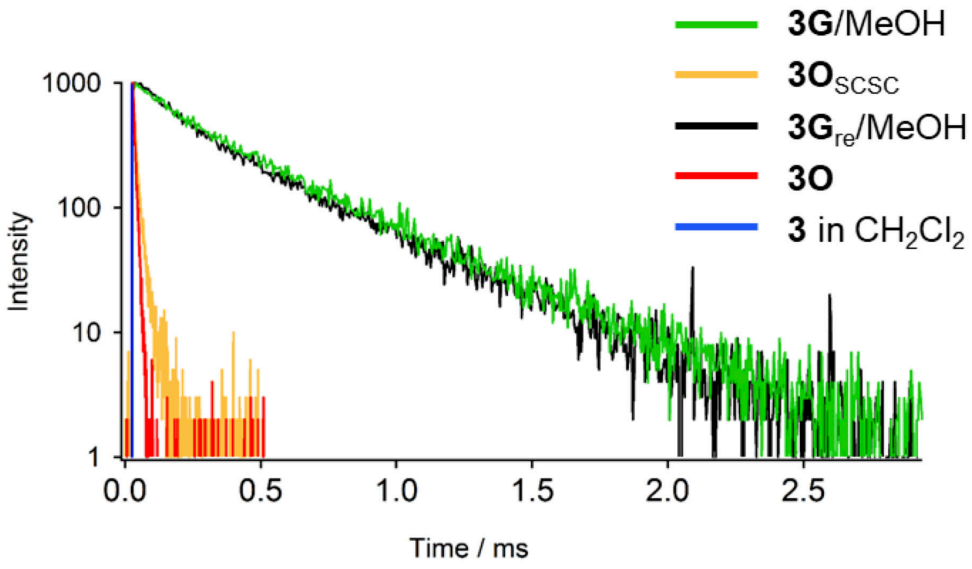

Figure S12. Emission decay profiles of **3G**/MeOH, **3O**$_{scsc}$, **3G**$_{re}$/MeOH , **3O**, and **3** in CH_2Cl_2 ($c = 1.79 \times 10^{-6}$ M).

Table S3. Photophysical properties of **3G**/MeOH, **3O**$_{scsc}$, **3G**$_{re}$/MeOH, **3O**, and **3** in CH_2Cl_2 (c = 1.79 × 10^{-6} M)

	Φ_{em} / - (λ_{ex} / nm)	τ_{av} / μs[a,b] (λ_{em} / nm)	τ_1 / μs[a] (A / -)	τ_2 / μs[a] (A / -)	τ_3 / μs[a] (A / -)
3G/MeOH	0.05 (395)	384 (506)	0.97 (0.51)	125 (0.14)	417 (0.35)
3O$_{scsc}$	0.19 (362)	14.6 (612)	0.16 (0.49)	6.84 (0.31)	19.2 (0.20)
3G$_{re}$/MeOH	0.05 (380)	331 (506)	2.78 (0.67)	115 (0.14)	384 (0.19)
3O	0.25 (381)	7.97 (603)	6.81 (0.89)	12.9 (0.11)	-
3 in CH_2Cl_2	0.07 (276)	6.01 × 10^{-3} (333)	2.38 × 10^{-3} (0.82)	9.86 × 10^{-3} (0.18)	-

[a] λ_{ex} = 370 nm. [b] $\tau_{av} = \Sigma \tau_n A_n^2 / \Sigma \tau_n A_n$.

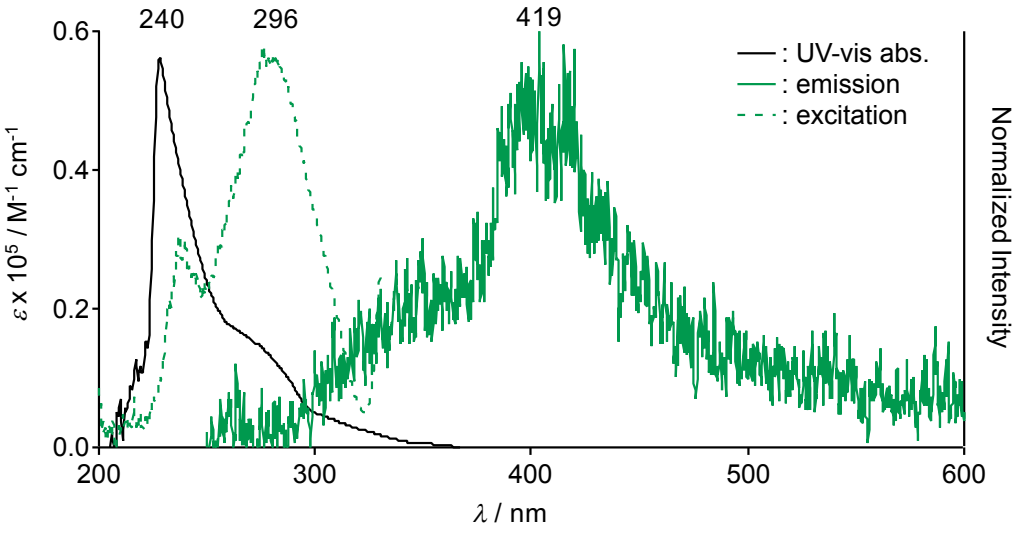

Figure S13. UV/vis absorption (black solid line), excitation (green dotted line, λ_{em} = 419 nm), and emission spectra (green solid line, λ_{ex} = 240 nm) of **3** in CH_2Cl_2 (c = 1.79 × 10^{-6} M) at room temperature.

5.4.9. Changes of the Luminescence after Exposure to External Stimuli

Crystals of **3** showed emission-color changes from green to orange upon gentle heating to 30 ºC for 10 min under ambient conditions (Figure S13a). The emission spectrum of the resulting orange-emitting crystal (**3O**$_{heat}$) matched that of **3O**$_{scsc}$ obtained from cutting crystals of **3G**/MeOH (Figure S13c). Furthermore, crystals of **3O**$_{heat}$ showed a recovery of their initial green emission upon increasing the concentration of the MeOH vapor (Figure S13b). Crystals of **3O**, obtained from recrystallization from CH_2Cl_2 and hexane (*cf.* page S5), did not show a change of their emission upon being exposed to high concentrations of MeOH vapor in a petri dish, or when liquid MeOH was added directly (Figure S14).

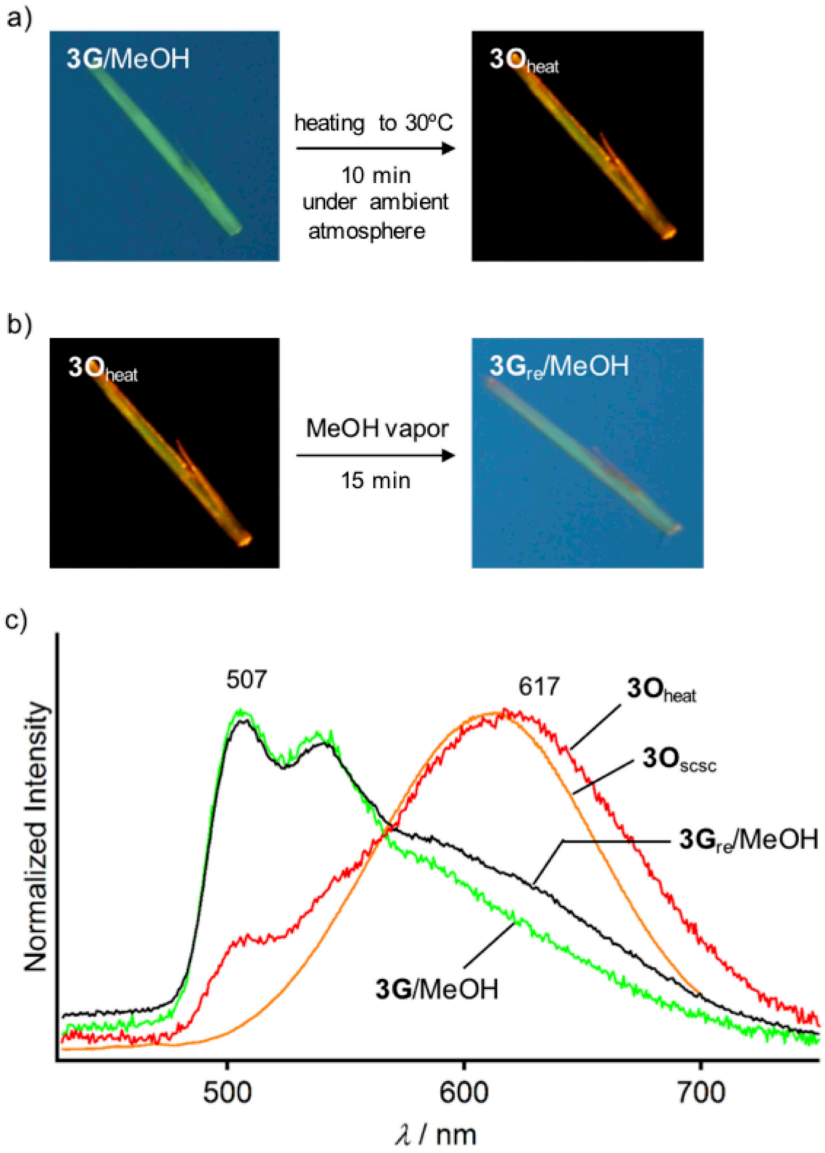

Figure S14. Photographs of a) a crystal of **3G**/MeOH upon heating to 30 ºC for 10 min and b) an orange-emitting crystal showing the recovery of the green emission upon exposure to high

concentrations of MeOH vapor. Photographs and emission spectra were taken under UV light (365 nm). c) Emission spectra of **3G**/MeOH (green line), $\mathbf{3O}_{heat}$ (red line), $\mathbf{3O}_{scsc}$ (orange line), and $\mathbf{3G}_{re}$/MeOH (black line).

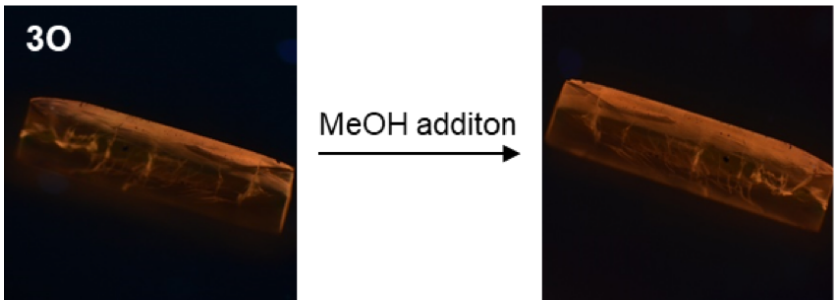

Figure S15. Photographs of the crystal **3O** obtained by recrystallization from CH_2Cl_2 with hexane. There is no emission color change upon liquid MeOH addition. The photographs were taken under UV light (365 nm).

5.4.10. Mechanochromic Luminescence of Powder Samples

Figure S16. Photographs of mechanochromism using semi-crystalline powder **3G**/MeOH. The grinding was performed by ball-milling for 20 min. The powder of **3O**$_{grinding}$ was obtained by grinding the powder sample of **3G**/MeOH. Upon adding MeOH solvent, **3O**$_{grinding}$ changed into yellow-emitting powder **3O′** The photographs were taken under UV light (365 nm).

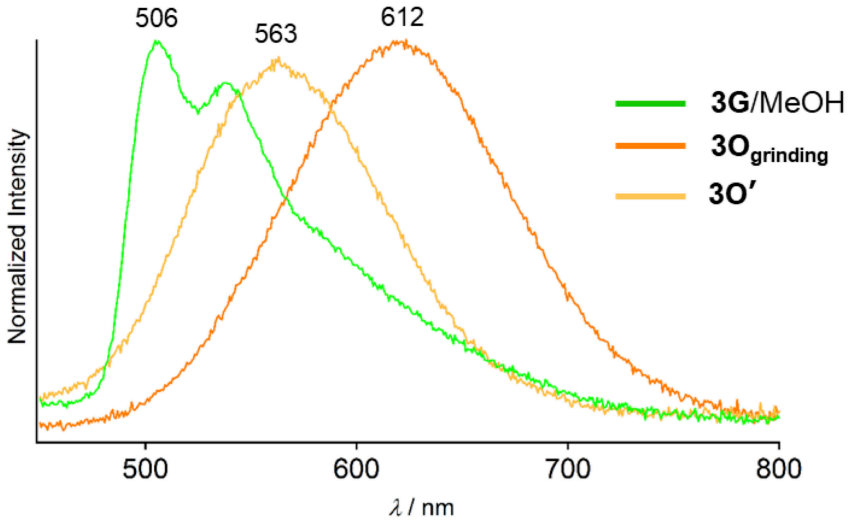

Figure S17. Emission spectra of **3G**/MeOH, **3O**$_{grinding}$, and **3O′** (λ_{ex} = 365 nm).

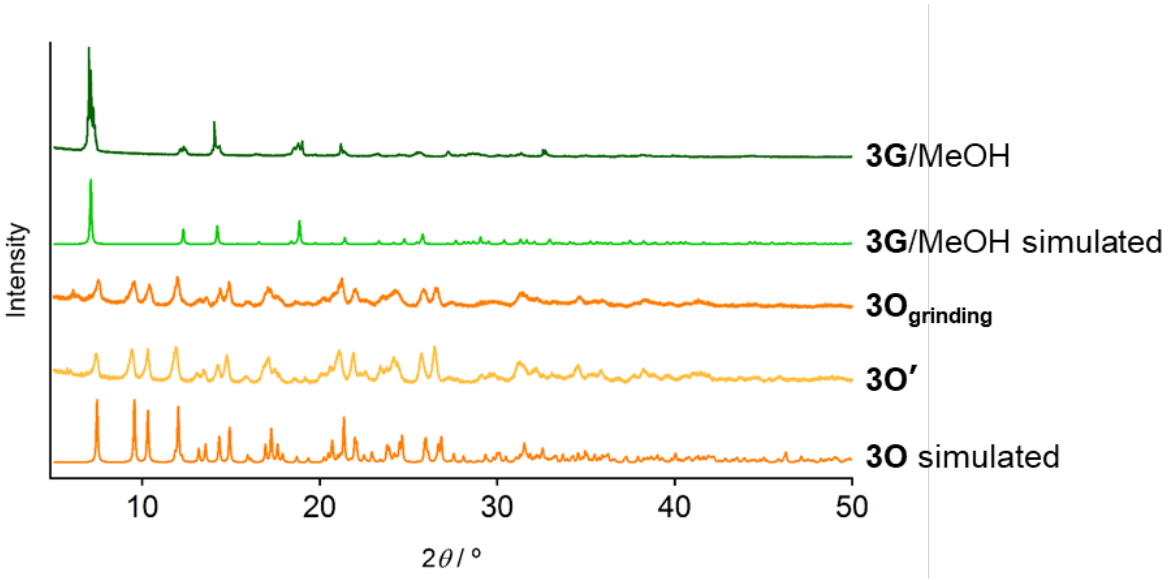

Figure S18. Powder XRD patterns of **3G**/MeOH, $\mathbf{3O}_{\text{grinding}}$, and **3O**′. Simulated powder XRD patterns derived from the single crystals of **3G**/MeOH and **3O**. Powder XRD pattern of **3O**′ was similar with that of $\mathbf{3O}_{\text{grinding}}$. It revealed that there was no molecular arrangement change upon the transformation from $\mathbf{3O}_{\text{grinding}}$ to **3O**′ by the MeOH addition.

11. SEM Images of the 3O Samples Prepared by Various Procedures

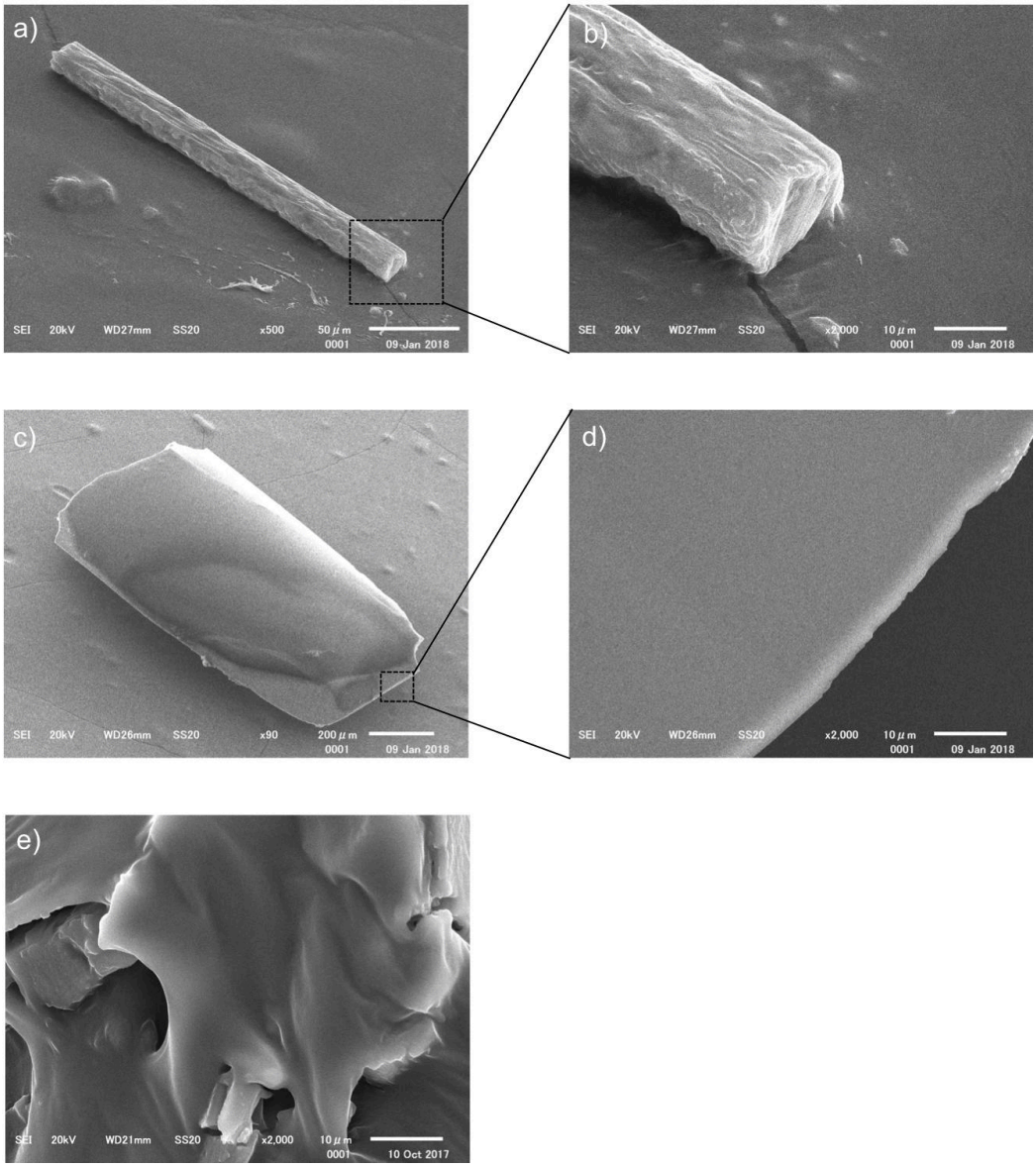

Figure S19. SEM images of orange-emitting **3O** samples prepared by a-b) cutting (**3O**$_{scsc}$), c-d) recrystallization (**3O**), and e) grinding (**3O**$_{grinding}$).

5.4.12. DFT Calculations of 3G/MeOH and $3O_{scsc}$

All calculations were performed using the Gaussian 09W (revision C.01 and E.01) and Gaussian 09 (revision C.01 and E.01) program package.[19] The singlet state TD-DFT calculations of a tetramer structure of the crystal **3G**/MeOH and $\mathbf{3O}_{scsc}$ were performed to understand the origin of their excitation and emission properties. In the calculations, the B3LYP functional and the SDD basis set with an effective core potential were used. The geometries of the tetramers were taken from the single crystal structures of **3G**/MeOH and $\mathbf{3O}_{scsc}$. The positions of the heavy atoms were fixed and only the positions of H atoms were optimized using the Spartan'10 MMFF force-field calculations before TD-DFT calculations.[20] The simulated UV/vis absorption spectra and the experimental excitation spectra exhibited the similar traces (Figure S19). Thus, the results of TD-DFT calculations give us a mechanistic insight for studying the correlation between the crystal structures and the emission properties.

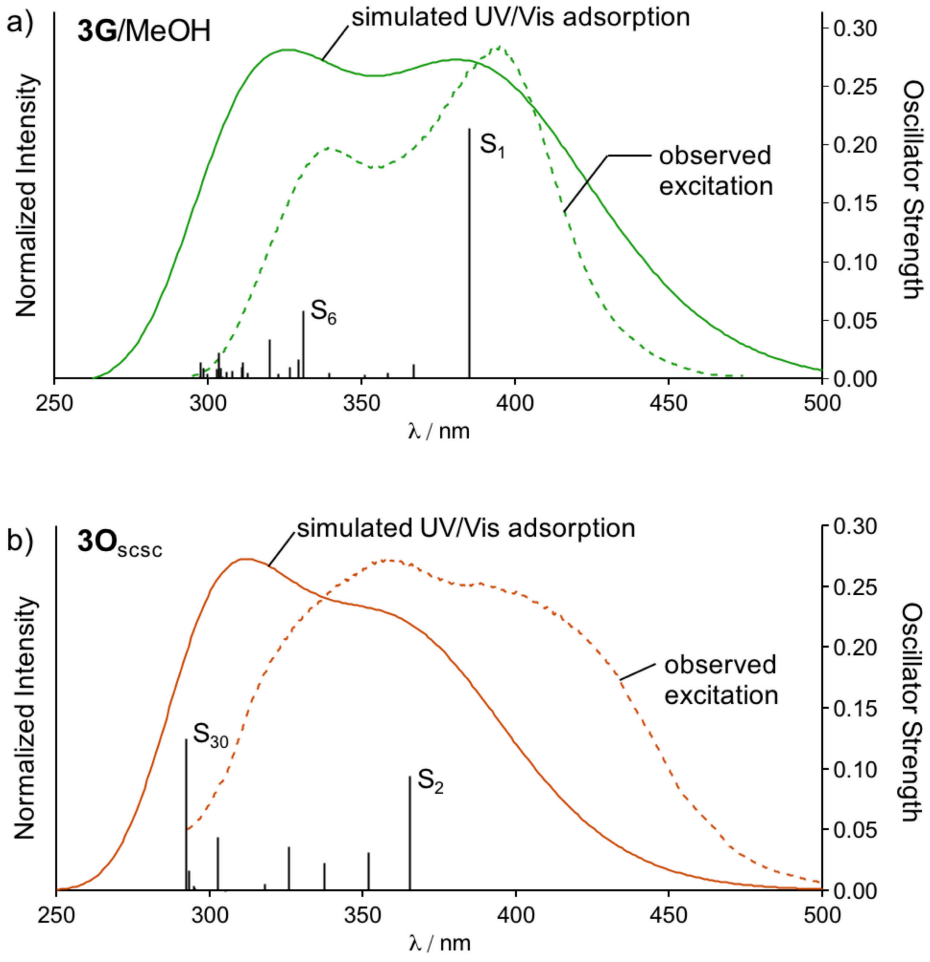

Figure S20. Comparison of experimental and theoretical results on the crystal **3G**/MeOH and $\mathbf{3O}_{scsc}$. a) Green dashed line shows excitation spectrum of **3G**/MeOH. Simulated UV/vis

absorption spectrum of the tetramer in the crystal **3G**/MeOH (green solid line) and the oscillator strengths (black bars) were derived from the singlet state TD-DFT calculations (B3LYP/SDD). b) Excitation spectrum (orange dashed line), simulated UV/vis absorption spectrum (orange solid line), and the oscillator strengths (black bars) of the tetramer taken from the single crystal structure of **3O**$_{scsc}$.

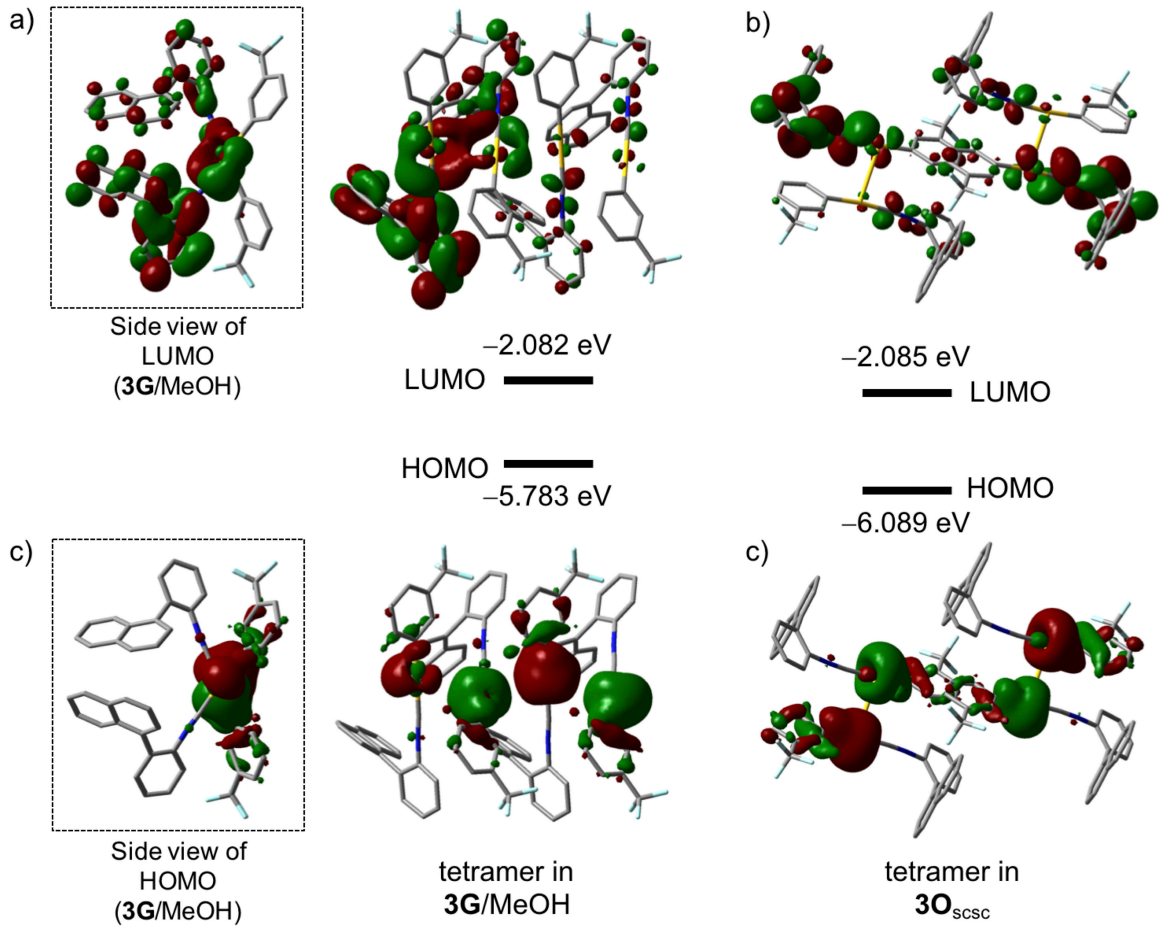

Figure S21. Energy levels and frontier orbitals of tetramer structures of **3G**/MeOH [(a): LUMO, (c): HOMO] and **3O**$_{scsc}$ [(b): LUMO, (d): HOMO]. All the H atoms are omitted for clarity.

Table S4. Selected singlet to singlet transitions of the tetramer in the crystal structure of **3G**/MeOH.

states	energy / eV	λ / nm	*f* / -	orbital transition	CI coefficients
S1	3.2199	385.05	0.2137	HOMO → LUMO	0.66654
				HOMO → LUMO+1	-0.17891
S6	3.7447	331.09	0.0578	HOMO → LUMO+4	-0.11984
				HOMO → LUMO+5	-0.26798
				HOMO → LUMO+6	0.56846
				HOMO → LUMO+7	0.14452

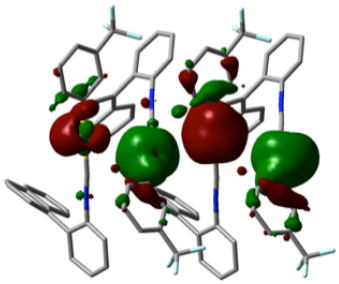

HOMO

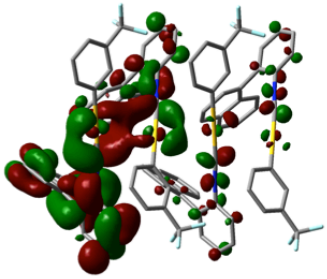

LUMO

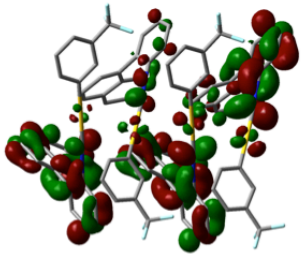

LUMO+1

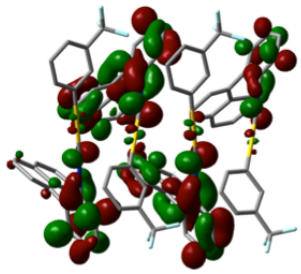

LUMO+4

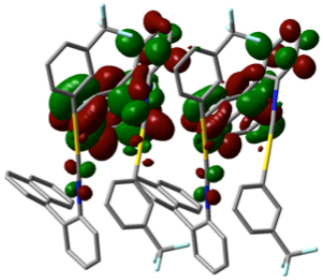

LUMO+5

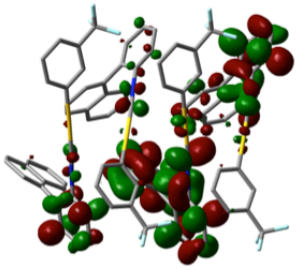

LUMO+6

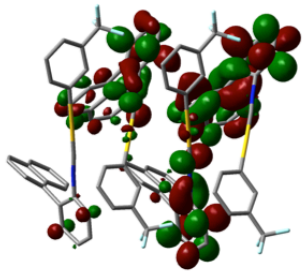

LUMO+7

Table S5. Selected singlet to singlet transitions of the tetramer in the crystal structure of **3O**$_{scsc}$.

states	energy / eV	λ / nm	*f* / -	orbital transition	CI coefficients
S1	3.3925	365.47	0.0001	HOMO−1 → LUMO+1	0.47887
				HOMO → LUMO	0.49849
S2	3.39947	365.23	0.0946	HOMO−1 → LUMO	0.48942
				HOMO → LUMO+1	0.48881
S30	4.2424	292.25	0.1252	HOMO−8 → LUMO+1	−0.11527
				HOMO−1 → LUMO+9	0.23128
				HOMO → LUMO+8	0.31991

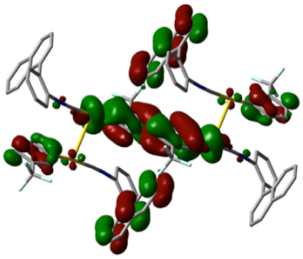

HOMO−8

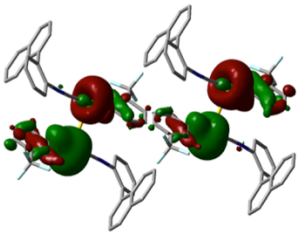

HOMO−1

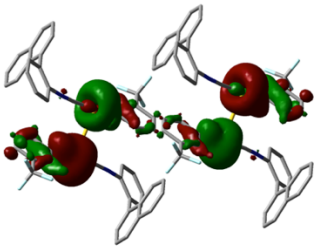

HOMO

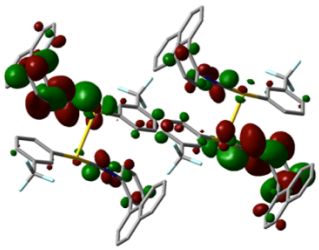

LUMO

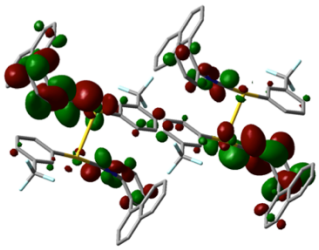

LUMO+1

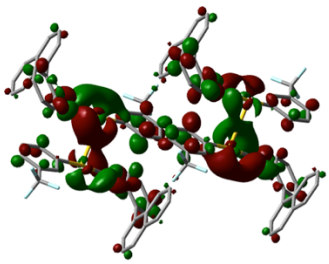

LUMO+8

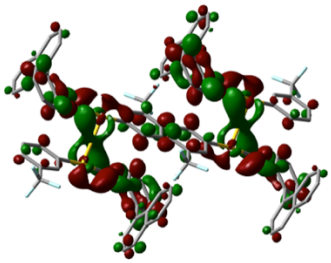

LUMO+9

Analysis of polarity in crystals 3G/MeOH and $3O_{scsc}$

All molecules in the crystals exhibit a dipole moment (blue arrows in Figure S21a, b, d, and e). When these molecules crystallize to form **3G**/MeOH with polar space group that does not contain an inversion center, the tetramer units in these crystals also exhibit a dipole moment (Figure S21c). Conversely, the dimer units in crystals of $\mathbf{3O}_{scsc}$, which crystallize in a space group with an inversion center, do not exhibit a dipole moment (Figure S21f).

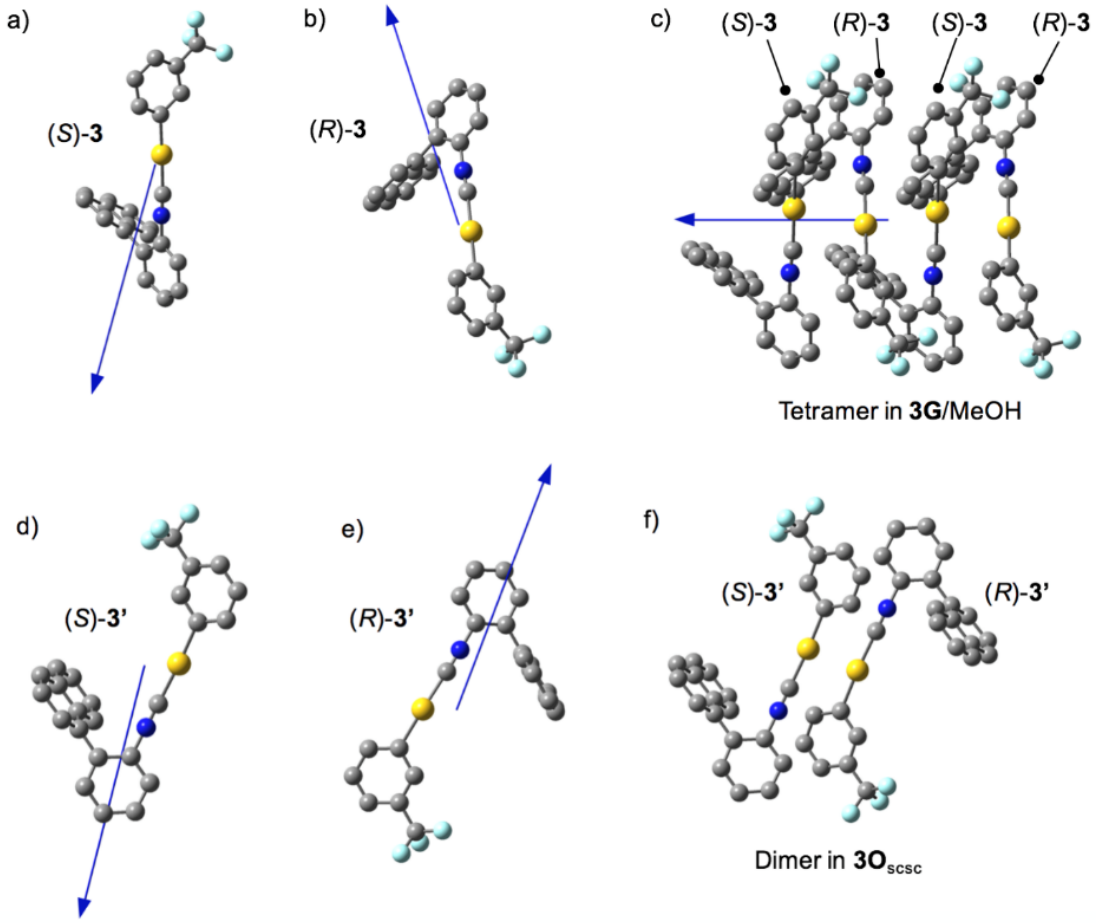

Figure S22. Representation of the dipole moments (blue arrows) of monomers, a dimer, and a tetramer in the crystals of **3G**/MeOH and $\mathbf{3O}_{scsc}$. Conformations of a) (*S*)-**3**, b) (*R*)-**3**, and c) a tetramer contained in the crystals of **3G**/MeOH. d) Conformations of d) (*S*)-**3'**, e) (*R*)-**3'**, and f) a dimer contained in the crystals of $\mathbf{3O}_{scsc}$. Blue arrows indicate the dipole moment obtained from DFT calculations at the B3LYP/SDD level of theory. All hydrogen atoms are omitted for clarity.

5.5. References

34. (a) Malwitz, M. A.; Lim, S. H.; White-Morris, R. L.; Pham, D. M.; Olmstead, M. M.; Balch, A. L. *J. Am. Chem. Soc.* **2012,** *134*, 10885. (b) Kiri, P.; Hyett, G.; Binions, R. *Adv. Mat. Lett.* **2010**, *1*, 86. (c) Wenger, O. S. *Chem. Rev.* **2013**, *113*, 3686. (d) Ciardelli, F.; Ruggeri, G.; Pucci, A. *Chem. Soc. Rev.* **2013**, *42*, 857. (e) Sagara, Y.; Kato, T. *Nat. Chem.* **2009**, *1*, 605. (f) Balch, A. L.; *Angew. Chem. Int. Ed.* **2009**, *48*, 2641. (g) Sagara, Y.; Yamane, S.; Mitani, M.; Weder, C.; Kato, T. *Adv. Mater.* **2016**, *28*, 977.
35. Park, S. K.; Cho, I.; Gierschner, J.; Kim, J. H.; Kim, J. H.; Kwon, J. E.; Kwon, O. K.; Whang, D. R.; Park, J.-H.; An, B.-K.; Park, S. Y. *Angew. Chem. Int. Ed.* **2016,** *55,* 203.
36. (a) Mutai, T.; Satou, H.; Araki, K. *Nat. Mater.* **2005,** *4*, 685. (b) Li, F. F.; Zhang, L.; Gong, L. L.; Yan, C. S.; Gao, H. Y.; Luo, F. *Dalton Trans.* **2017,** *46*, 338. (c) Lim, S. H.; Olmstead, M. M.; Balch, A. L. *Chem. Sci.* **2013**, *4*, 311. (d) Zeng, M.-H.; Tan, Y.-X.; He, Y.-P.; Yin, Z.; Chen, Q.; Kurmoo, M. *Inorg. Chem.*, **2013**, *52*, 2353. (e) Huang, R.-W.; Wei, Y.-S.; Dong, X.-Y.; Wu, X.-H.; Du, C.-X.; Zang, S.-Q.; Mak, T. C. W. *Nat. Chem.* **2017,** *9*, 689. (f) Lim, S. H.; Olmstead, M. M.; Balch, A. L. *J. Am. Chem. Soc.* **2011**, *133*, 10229. (g) Seki, T.; Sakurada, K.; Muromoto, M.; Ito, H. *Chem. Sci.* **2015**, *6*, 1491.
37. (a) Naumov, P.; Bharadwaj, P. K. *CrystEngComm* **2015,** *17*, 8775. (b) Chaudhary, A.; Mohammad, A.; Mobin, S. M. *Cryst. Growth Des.* **2017,** *17*, 2893.
38. (a) Ito, H.; Muromoto, M.; Kurenuma, S.; Ishizaka, S.; Kitamura, N.; Sato, H.; Seki, T. *Nat. Commun.* **2013,** *4*, 2009. (b) Seki, T.; Sakurada, K.; Ito, H. *Angew. Chem. Int. Ed.* **2013,** *52*, 12828. (c) Seki, T.; Sakurada, K.; Muromoto, M.; Seki, S.; Ito, H. *Chem.-Eur. J.* **2016**, *22*, 1968. (d) For an example of a mechanical-stimulation-triggered SCSC that is not accompanied by an emission change, see: Liu, G.; Liu, J.; Liu, Y.; Tao, X. *J. Am. Chem. Soc.* **2014**, *136*, 590. and Liu, J.; Liu, G.; Liu, Y.; Zheng, X.; Han, Q.; Ye, X.; Tao, X. *Chem. Asian J.* **2016**, *11*, 1682. (e) For a report of mechanosalient molecular crystals with reversion by heating the daughter phase, see: Karothu, D. P.; Weston, J.; Desta, I. T.; Naumov, P. *J. Am. Chem. Soc.* **2016**, *138*, 13298.
39. (a) Liu, G. F.; Liu, J.; Ye, X.; Nie, L. N.; Gu, P. Y.; Tao, X. T.; Zhang, Q. C. *Angew. Chem. Int. Ed.* **2017,** *56,* 198. (b) Takamizawa, S.; Miyamoto, Y. *Angew. Chem. Int.*

Ed. **2014,** *53,* 6970. (c) Takasaki, Y.; Takamizawa, S. *Chem. Commun.* **2015**, *51*, 5024. (d) Takamizawa, S.; Takasaki, Y. *Angew. Chem. Int. Ed.* **2015,** *54,* 4815.

40. Seki, T.; Takamatsu, Y.; Ito, H. *J. Am. Chem. Soc.* **2016**, *138*, 6252.
41. Crystals in the same dish that were not cut did not show a change of the emission color when **3O**$_{scsc}$ spontaneously appeared.
42. ^{1}H NMR spectroscopic, elemental, and thermogravimetric (TGA) analyses of **3O** obtained from recrystallization did not support the inclusion of any solvent in the crystal (Figures S9 and S10, as well as Table S2). The ^{1}H NMR spectrum of **3G**/MeOH indicated the inclusion of MeOH in the crystal (Figure S9).
43. τ_{av} is defined as: $\tau_{av} = \Sigma \tau_n A_n^2 / \Sigma \tau_n A_n$
44. Hong, Y.; Lam, J. W. Y.; Tang, B. Z. *Chem. Soc. Rev.* **2011**, *40*, 5361.
45. The resulting orange-emitting sample of a crystalline powder showed an emission change to yellow under concomitant formation of a distinct crystalline structure, which is not consistent with that of **3G**/MeOH, as evident from the powder XRD analysis (Figures S16-18).
46. Seki, T.; Tokodai, N.; Omagari, S.; Nakanishi, T.; Hasegawa, Y.; Iwasa, T.; Taketsugu, T.; Ito, H. *J. Am. Chem. Soc.* **2017**, *139*, 6514.
47. The long emission lifetimes (14.6 and 331.1 μs) suggest that solid-state luminescence occurs from the triplet excited state. It would thus be feasible to assume that the structure relaxation during the excitation–emission process should cause the red-shifted emission of **3O** relative to that of **3G**/MeOH.
48. When **3O**$_{scsc}$ was contacted to a droplet of liquid MeOH, only the domain in which MeOH liquid directly contacted exhibited emission change from orange to green under ambient air. This result indicates that the contact of the crystal and MeOH is prerequisite for the phase transition from **3O**$_{scsc}$ to **3G**$_{re}$/MeOH.
49. (a) Centore, R.; Fusco, S.; Capone, F.; Causà, M. *Cryst. Growth Des.* **2016,** *16*, 2260. (b) Myerson, A. S. Molecular Modeling Applications in Crystallization, Cambridge University Press, Cambridge, 1999; pp 207–209.
50. Seki, T.; Takamatsu, Y.; Ito, H. *J. Am. Chem. Soc.* **2016**, *138*, 6252.
51. Sheldrick, G. M. SHELXT, Program for the Refinement of Crystal Structures; University of Göttingen, Göttingen, Germany, **2015**.
52. Gaussian 09, Revision C.01, Frisch, M. J.; Trucks, G. W.; Schlegel, H. B.; Scuseria, G. E.; Robb, M. A.; Cheeseman, J. R.; Scalmani, G.; Barone, V.; Mennucci, B.;

Petersson, G. A.; Nakatsuji, H.; Caricato, M.; Li, X.; Hratchian, H. P.; Izmaylov, A. F.; Bloino, J.; Zheng, G.; Sonnenberg, J. L.; Hada, M.; Ehara, M.; Toyota, K.; Fukuda, R.; Hasegawa, J.; Ishida, M.; Nakajima, T.; Honda, Y.; Kitao, O.; Nakai, H.; Vreven, T.; Montgomery, J., J. A.; Peralta, J. E.; Ogliaro, F.; Bearpark, M.; Heyd, J. J.; Brothers, E.; Kudin, K. N.; Staroverov, V. N.; Kobayashi, R.; Normand, J.; Raghavachari, K.; Rendell, A.; Burant, J. C.; Iyengar, S. S.; Tomasi, J.; Cossi, M.; Rega, N.; Millam, N. J.; Klene, M.; Knox, J. E.; Cross, J. B.; Bakken, V.; Adamo, C.; Jaramillo, J.; Gomperts, R.; Stratmann, R. E.; Yazyev, O.; Austin, A. J.; Cammi, R.; Pomelli, C.; Ochterski, J. W.; Martin, R. L.; Morokuma, K.; Zakrzewski, V. G.; Voth, G. A.; Salvador, P.; Dannenberg, J. J.; Dapprich, S.; Daniels, A. D.; Farkas, Ö.; Foresman, J. B.; Ortiz, J. V.; Cioslowski, J.; Fox, D. J.; Gaussian, Inc., Wallingford CT, 2009.

53. Spartan ’10; Wavefunction, Inc.: Irvine, CA.

Chapter 6.

Thermo-Responsive Phosphorescence Control Mediated by Molecular Rotation and Aurophilic Interactions in Amphidynamic Crystals of Phosphane-Gold(I) Complex

5.1. Introduction

The precise control of luminescent properties in solid-state materials has attracted much attention because of their potential for the development of sophisticated functional materials such as sensors, transducers and external field-sensitive devices.[1] A concept that has attracted a great deal of attention in this context is the development of aggregation induced emission (AIE), pioneered by Tang and co-workers. In this case, it has been shown that the rotation of conjugated groups within certain chromophores result in emission quenching as the excited state is able to decay through a conical intersection (CI).[2] Therefore, while the AIE chromophores are non-emissive and are free to explore their torsional space in solution, aggregation and crystallization suppress their rotational freedom and prevents access to the CI, such that emission can be turned on in the solid state.

In order to further develop the field of functional luminescent materials, in addition to having binary systems with one state described by molecules that are free to rotate in solution and another one where molecules are aggregated in the solid state, it would be advantageous to control luminescence efficiency by affecting the rate of rotation in the solid state.[3] To accomplish that, we propose the use of amphidynamic crystals based on elements of molecular and crystal engineering to produce materials that combine luminescence and rotational motion.[4] One of the most robust and general architectures for the formation amphidynamic molecular crystals is based on the use of dumbbell shaped molecular rotors, as illustrated in Figure 1a and 1b.[5] These molecular *rotors* consist of a central phenylene *rotator* (shown in red) that is axially linked by triple bonds, or *axle*, to two bulky groups that play the role of a *stator* (shown blue in figure 1b). These structures are able to generate crystals with a relatively low packing density near the zone of the rotator in an otherwise densely-packed environment. For the objectives of this work, we recognized that the luminescence of crystalline gold(I) complexes can be highly sensitive to external stimuli, such as exposure to solvent vapor, changes in temperature, and mechanical stress, which often result in large changes in emission properties.[6] It is well known that these changes are the result of subtle structural changes around the gold complexes, which are highly sensitive to their environment, primarily as a result of their large and highly polarizable *d*-orbitals. Thus, their electronic environment can easily be influenced by internal or external changes, molecular conformations, the dipole moment of neighboring systems, and alternative molecular arrangements.[6] Furthermore, a tendency to form aurophilic interactions (Au–Au < 3.5 Å) can be used both as a crystal engineering synthon and as an emission tool with higher emission intensities and lower HOMO-LUMO energy gap.[7]

Taking dumbbell shaped molecular rotors as a model structure, we decided to incorporate the desired gold(I) atoms by taking advantage of complexation with the *p*-dialkynyl-phenylene rotator and a tri-(*p*-fluorophenyl)phosphane stator to form gold complex **1** in Figure 1 and Scheme 1 (R=H). Analog **2** (Scheme 1, R=Me), with a hindered *p*-dialkynyl-tetra-methylphenylene that is unable to rotate in the crystal was also prepared to conduct control experiments. With these structures, we set out to (1) expand the scope of amphidynamic materials using gold(I) complexes, (2) determine changes in emission properties in terms of rotational frequencies as a function of temperature, and (3) look for a possible correlation between emission and rotational frequency. We hypothesized that rotational motion in crystals of **1** would be relatively fast at high temperatures, which would lead to emission quenching while low temperatures should slow down the molecular rotor allowing for higher emission (Figure 1c). By contrast, we expected crystals of **2** with a static tetra-methylphenylene to show no changes in emission as a function of temperature. As described below, the general concepts formulated for this work were realized. The desired structures were obtained, changes in emission and rotational motion in the case of **1** were observed as a function of temperature, and a general correlation such as that predicted in Figure 1c was observed.

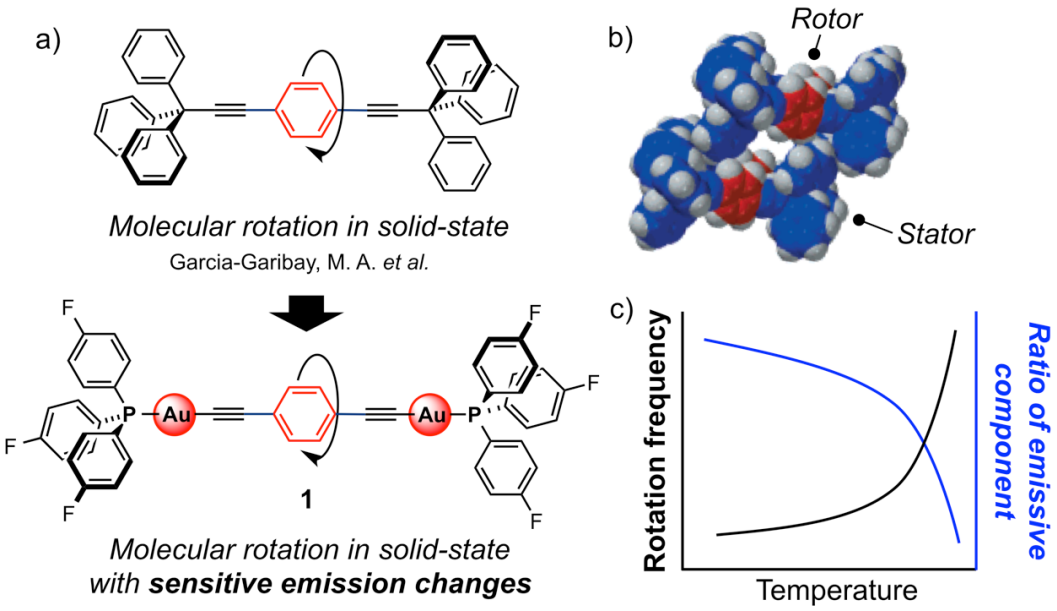

Figure 1. a) Molecular design based on the substitution of the triphenylmethane by a triarylphosphane gold(I) complex in a 1,4-bis(triphenylpropynyl)benzene. b) The dumbbell shaped molecular rotors with *rotor* and *stator* indicates in the crystal. c) Expected relation between rotation frequency and emission properties.

5.2. Results and Discussion

5.2.1. Synthesis and Characterization

Dumbbell-shaped gold complexes **1**, **1-*d*$_4$** and **2** were synthesized from derivatives of 1,4-diethynylbenzene and tris(4-fluorophenyl)phosphane gold(I) chloride using standard alkynylation conditions, as illustrated in Scheme 1.[8] Crystallization was accomplished by layering hexane as a poor solvent on top of a solution of the rotor complex in chloroform (typically, 10 mg of the complex in 2 ml of chloroform), which afforded green yellowish crystals (below 0.3 mm in size) subsequently shown to emit green light. No solvent inclusion was observed by either X-Ray diffraction or thermogravimetric analysis (TGA) (Figure S1). The samples were characterized by ^{1}H and ^{13}C nuclear magnetic resonance (NMR) spectroscopy, high-resolution mass spectrometry, elemental analysis, TGA, and single crystal X-ray diffraction (XRD) analyses (see the experimental section).

Scheme 1. Synthesis of the gold(I) phosphane complexes **1**, **1-*d*$_4$**, and **2**

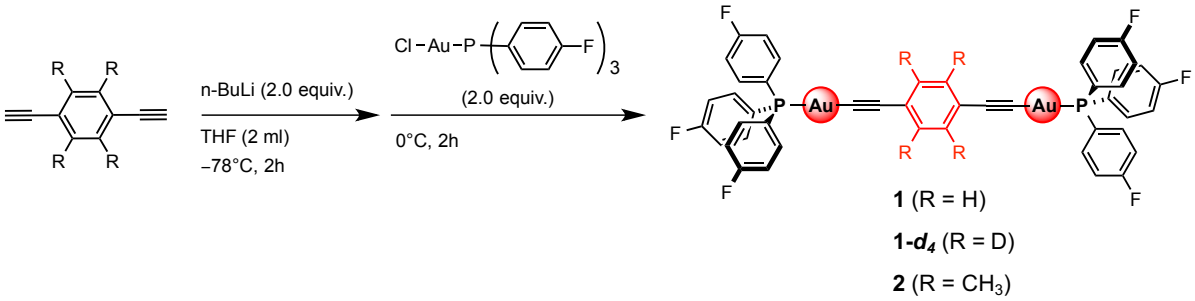

5.2.2. Single Crystal X-Ray Diffraction and Thermal Analyses of 1 and 2.

To obtain precise structural information, we performed single crystal XRD analysis of complexes **1** and **2**. Gold(I) complex **1** crystallized in the triclinic space group *P*-1 with two distinct half molecules per asymmetric unit, each occupying a crystallographic inversion center, so that two full molecules are generated per unit cell (*Z*=2) (Table S1). The desired structure was confirmed, as illustrated in Figure 2a, and the expected inter-molecular aurophilic interactions between neighboring molecules (Au–Au distance: 3.05 Å) were shown to occur as dimers (Figure 2b). Phenylene rotators are surrounded by fluorophenyl groups from the phosphane stators of neighboring molecular rotors displaying T-shaped CH-π interaction (Figure 2b). Interestingly, two dimeric aurophilic interactions at the ends of the central diethynyl benzene lead to the formation of infinite zigzag chains, as shown in Figure 2c and S2.

Gold(I) complex **2** with a bulky tetramethyl benzene group was prepared to investigate the emission properties of an isostructural non-rotating structure (Figure 3a). Crystals of **2** were obtained in the monoclinic space group *C*2/*c* with several characteristics that are common to those found in crystals of **1** (Table S1). There are two distinct half molecules per asymmetric unit with coinciding molecular and crystallographic inversion centers, such that there are two sets of four crystallographically distinct molecules per unit cell (*Z*=8) (Table S1). While the crystal system and packing structure of **2** are different from those of **1**, they have similar intermolecular aurophilic interactions with neighboring molecules experiencing Au–Au distances of 3.36 Å, as shown in Figure 3b. The tetramethyl phenylene rotator of **2** is surrounded by the fluorophenyl groups of neighboring stators, but in this case presenting nearly parallel π–π interactions (Figure 3b), instead of the CH-π interactions observed in the case of **1** (Figure 2b). The robust nature of these supramolecular crystal-guiding interactions was also shown by the formation of intermolecular zigzag chains that are very similar to those in crystal **1** (Figure 3c and S3–4), except that tetramethyl phenyl rotator **2** is more densely packed and less likely to display fast molecular rotation (Figure 3c and S3).

Single crystal XRD data were collected for both crystals in the range 123–298 K with five intermediate steps (193, 213, 233, 253, and 273 K). No phase transitions and no collapse of the intermolecular networks were observed, with only small changes in crystal dimensions and volume noted (Figure S5–8 and Table S1). Differential scanning calorimetry (DSC) profiles of the crystal **1** and **2** showed no peaks in the range 193–298 K, indicating that there are no phase transitions in this temperature range (Figures S9).

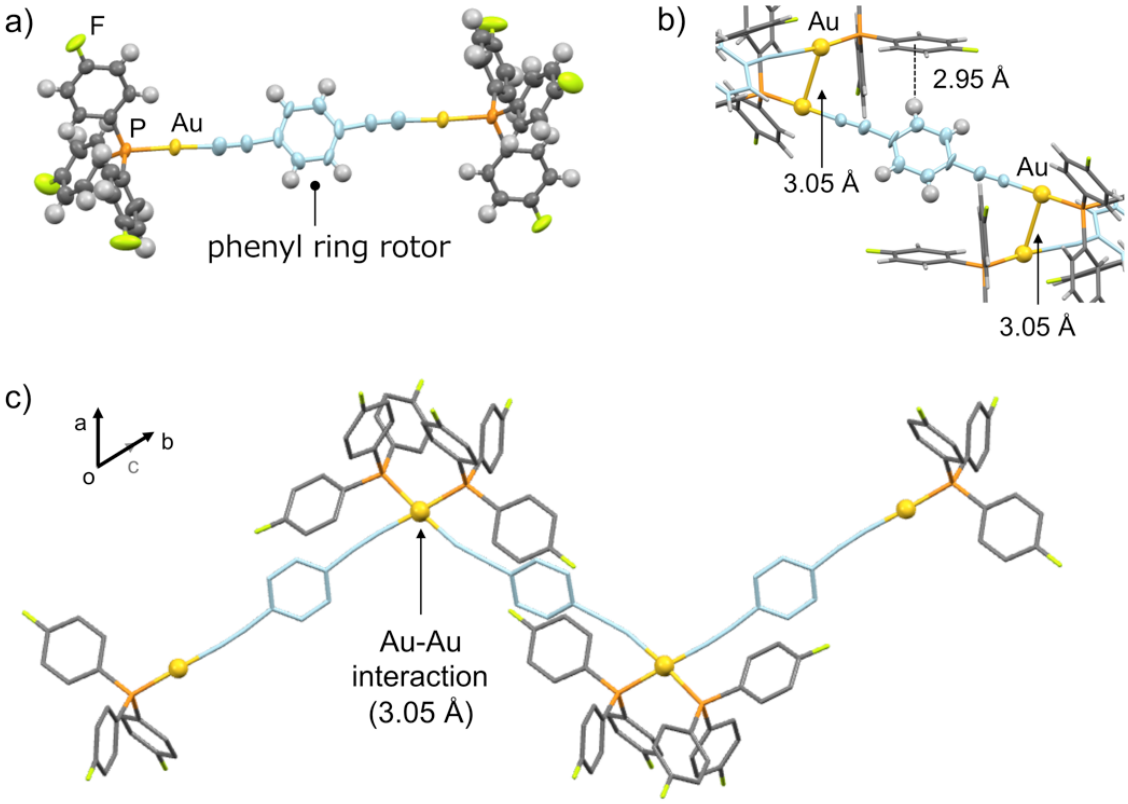

Figure 2. a) Structure of dinuclear gold(I) complex **1** at 123 K. b) Dimeric aurophilic interactions between neighboring molecular rotors. c) Zig-zag chains of molecular rotors formed by dimeric aurophilic interactions.

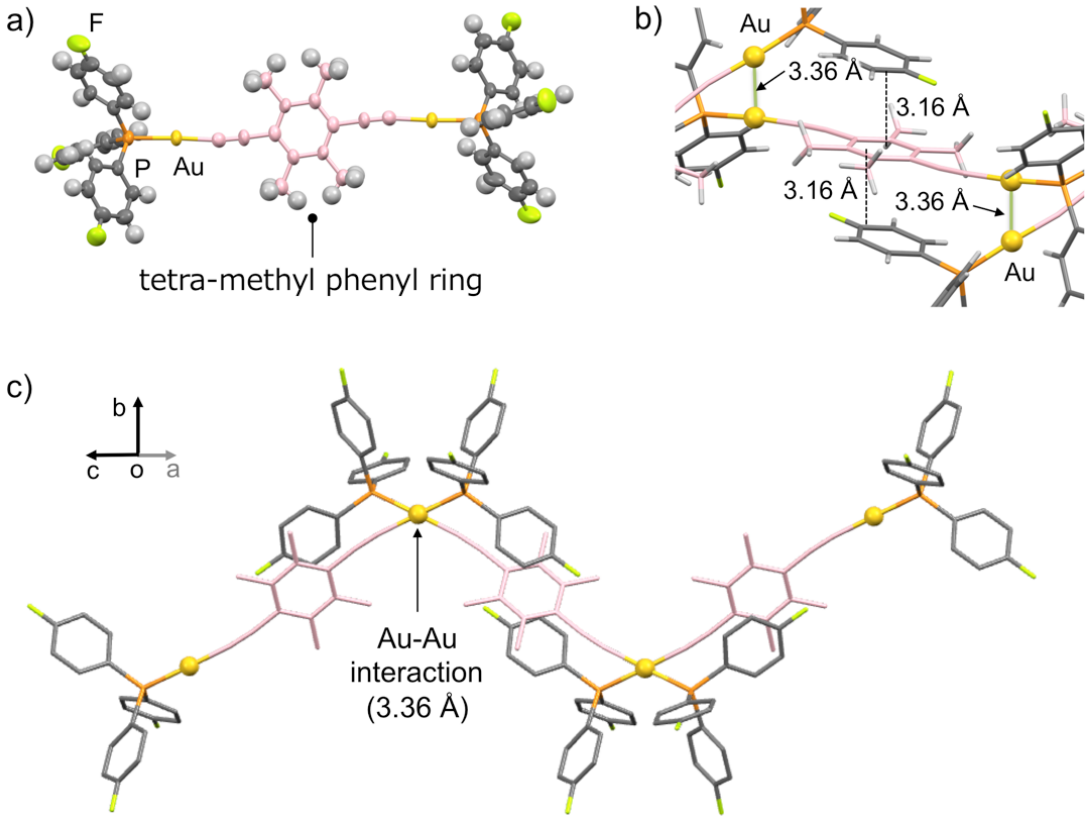

Figure 3. a) Structure of dinuclear gold(I) complex **2** at 123 K. b) Dimeric aurophilic interactions between neighboring molecules. c) Zig-zag chains of molecular rotors formed by dimeric aurophilic interactions.

5.2.3. Crystallinity and Phase Identity of Powdered Samples.

Knowing that mechanical forces may cause changes in the structure and photophysical properties of gold(I) complexes, we determined the crystallinity and phase identity of our powdered samples before turning our attention to rotational dynamics and emission measurements.[7] Figure 4 displays the experimental powder XRD patterns for samples of molecular rotors **1** and **2**. The top two diffractograms depict the experimental powder sample of rotor **1** and the one calculated from its single-crystal structure, respectively. The fact that two diffractograms have similar peak positions and intensities suggest that the powder sample is in fact crystalline and in the same polymorph as the single crystalline specimens. Analogous studies performed with molecular rotor **2** (bottom two diffractograms) indicate a similar result, with the experimental powder sample of the tetramethylated rotor giving the same PXRD as the single crystal.

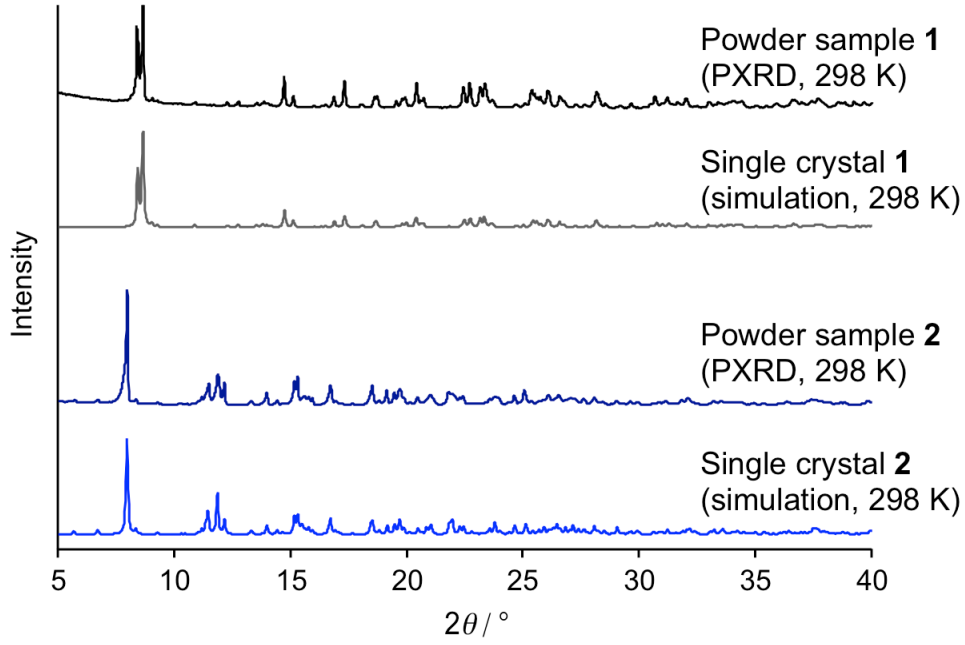

Figure 4. Powder XRD patterns of the crystalline samples of **1** and **2** obtained by the powder XRD (PXRD) and simulations from the single crystal XRD.

5.2.4. Variable Temperature Solid State NMR Studies of 1-d_4 and 2.

In order to investigate the rotational dynamics of gold(I) rotor **1**, we performed solid state (SS) ^{2}H NMR spin- echo measurements and line shape simulations. This is a relatively simple and widely used technique to analyze internal dynamics of deuterium-enriched groups in the dynamic window of $10^3 - 10^8$ Hz.[9] The variable temperature (VT) SS ^{2}H NMR spin-echo measurements were performed on polycrystalline powders of **1-*d*$_4$** to determine the rotational frequency of the central phenylene rotator as a function of temperature.

Figure 5a and S10 shows the experimental line shapes observed in the temperature range between 318 and 193 K in solid black lines. The line shapes obtained by simulation provided a reasonably good match with those obtained in the experiment (red dotted lines) using a quadrupolar coupling constant (QCC) of 180 kHz,[9] characteristic of aromatic deuterons, a cone angle of 60° formed between the rotational axis and C-D bond vector, and Brownian jumps of 180° about a two-fold potential energy profile, in agreement with the crystal structure where two degenerate minima can be expected. Line shape simulations required site exchange frequencies that expand the entire dynamic range of the method.[5a] The line shape at 318 K is close to the fast exchange regime and a good match was obtained with a 12.5 MHz rotational frequency. At ambient temperature (298 K), the line shape suggests rotational motion in the intermediate exchange regime with a frequency of ca. 4.0 MHz. The experimental spectra measured at temperatures of 273, 253, 233, 213, and 193 K, were simulated with rotational exchange frequencies of ca. 2.50, 1.41, 0.35, 0.15, and below 0.01 MHz, respectively. An Arrhenius plot constructed from the rotational exchange frequencies for **1-*d*$_4$** (Figure 5b) indicates a relatively low activation energy of E_a = 5.21 kcal/mol and a pre-exponential factor of $A = 5.8 \times 10^{10}$ s^{-1}, which is somewhat smaller that the value expected for an elementary torsional mode of ca. 10^{12} s^{-1}.

Expecting a much slower rotational motion for the tetramethyl phenylene rotator of **2** we decided to explore its motion using VT ^{13}C CPMAS (Figure 5c and S11). This experiment is analogous to VT measurements carried out in solution where signals broaden, coalesce, collapse, and sharpen as the rate of site exchange changes from much slower to much faster than the value corresponding to the chemical shift difference between the exchanging groups. For that reason, the dynamic range of the method is relatively slow and generally limited to site exchange in the ca. 10-10^4 Hz. The temperature range explored for the VT CPMAS ^{13}C NMR experiment was the same as that analyzed in the VT SS ^{2}H NMR spin-echo experiment for **1-*d*$_4$**, between 318 K and 193 K. We assigned the resonance signals of methyl groups in

the hindered rotator moiety to peaks observed at ca. 16–18 ppm, which are marked with an asterisk in Figure 5c. It should be noted that methyl groups related by 180° rotation in **2** are expected to have different chemical shifts as a result of their crystallographically and magnetically different environments. Notably, there was no change in the width or position of the methyl group signals at 16 and 18 ppm as a function of temperature, indicating that there is no rotational site exchange in the dynamic range given by their frequency difference of $\Delta\nu$ = 300 Hz (coalescence would occur at a rate of ca. k = 2.22 x 300 Hz = 666 Hz). As illustrated in Figure 5d, we conclude that the time constant for rotational motion of the phenylene rotator in crystals of **1** at ambient temperature (ca. 0.25 μs) should be in reasonable proximity to the time constants which are typical in the phosphorescence time window (see below). By contrast, the tetramethyl phenylene rotator of **2** is essentially static, even at the highest temperatures analyzed.

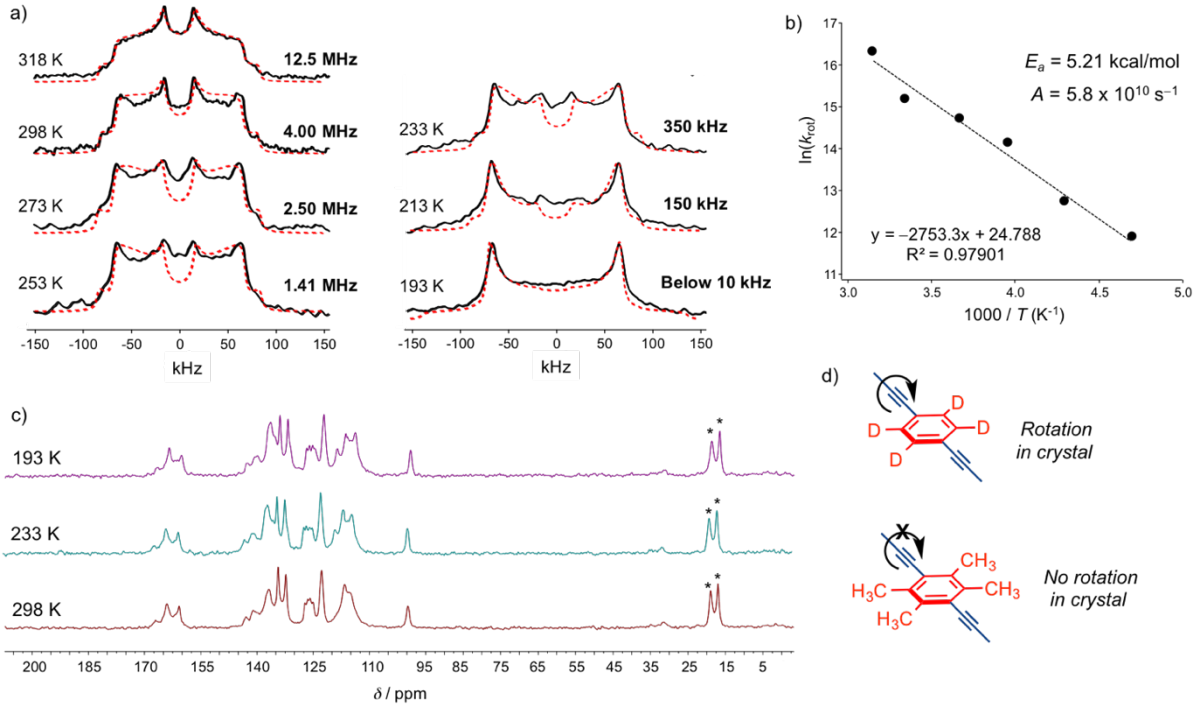

Figure 5. Variable temperature (VT) solid-state (SS) NMR studies of **1** and **2**. a) Experimental (black solid line) and simulated (red dashed line) SS ^{2}H NMR spectra of crystal **1**. b) Arrhenius plot of phenyl ring rotor dynamics in crystal **1**. c) SS ^{13}C CPMAS spectra of crystal **2** acquired at 150 MHz. * indicates peaks from the methyl group of tetra-methyl phenyl moiety. d) Schematic representation of the results of VT SS NMR studies of **1** and **2**.

5.2.5. Emission properties of 1 and 2.

Crystalline samples of complexes **1** and **2** were found to exhibit green and yellow emission, respectively, under UV light excitation (λ_{ex} = 370 nm) at 298 K (Figures 6a and 7a). The emission intensities of **1** and **2** in dilute $CHCl_3$ solution were very weak as compared to those in the solid state (Figure S12-13), as expected for a long-lived triplet emission that is highly susceptible to quenching.[10] The complex emission lifetimes in the microsecond regime described below confirmed that the crystalline state emission can be assigned as phosphorescence. Crystal **1** showed reversible visual changes in emission from green to yellow as the temperature changes from 298 to 193 K (Figure 6a). The temperature range of these changes matches well the temperature range where the thermally activated molecular rotator varies from highly dynamic to nearly static. The emission spectrum of **1** consists of a sharp, well resolved peak at 498 nm, followed by a several less resolved peaks and shoulders with a λ_{max} = 543 nm, suggesting a relatively rich vibronic structure. Lowering the temperature from 298 to 193 K resulted in the relative increase in intensity of the lower energy bands, which is responsible for the visual changes in emission going from green to yellow (Figure 6b).

The solid state emission of the static molecular rotor **2** shown in Figure 7 does not have the vibrational resolution of the unsubstituted compound, and there are no visual or spectral changes as a function of temperature from 298 K to 193K. The spectrum has a λ_{max} = 545 nm with an envelop that spans from ca. 490 nm to 700 nm, covering the same energy range as **1**, but lacking a strong 0-0 transition and displaying significant broadening of the lower energy bands. To suggest an explanation for the observations shown in Figure 6 and 7, we propose assignments for the emissions of **1** and **2**, consider the photophysical properties of conjugated arylene-ethynylenes as a function of rotation, and explore the role of the gold(I) centers in the electronic communication among the diethynylphenylene rotors in the crystal.

We first note that the emission spectrum of **1** is consistent with the phosphorescence of an isolated π-conjugated diethynyl arene chromophore.[10,11] This includes a vibronic structure that includes a strong 0-0 transition and a rich vibrational progression that arises from several C-H stretching and bending modes.[10,12] The spectrum of **2**, by contrast, is consistent with a similar diethynyl arene chromophore under conditions of co-facial aggregation,[12,14] which tends decrease the intensity of the 0-0 band while broadening the rest of the spectrum. [12,14] These assignments are also consistent with structural parameters available from the corresponding crystal structures, which show the central aromatic ring to have a T-shaped C-H-π interaction with neighboring molecules in the case of **1** and co-facial π–π interactions in the case of **2**.

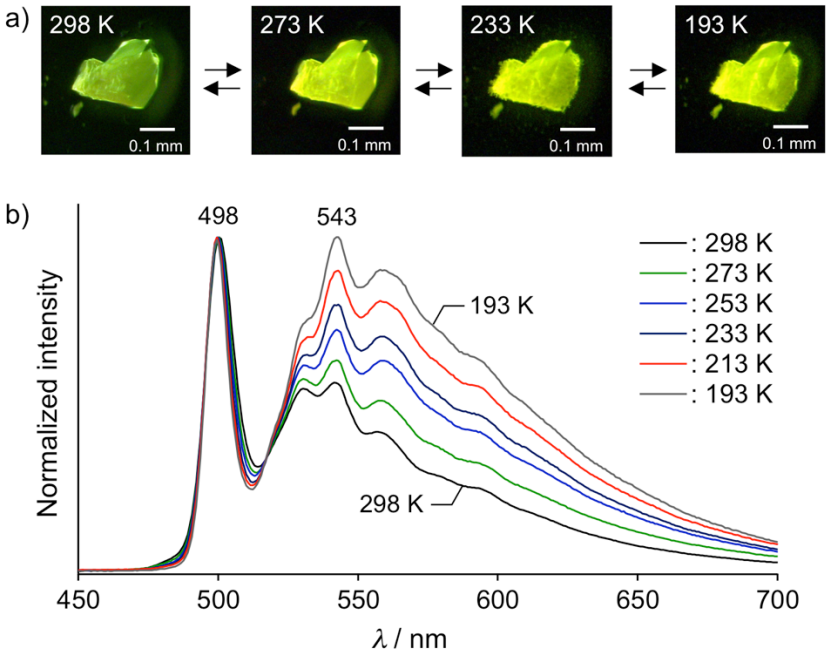

Figure 6. a) Photographs of emission color changes of **1** under UV irradiation by cooling or heating. b) Emission spectra of **1** in various temperatures.

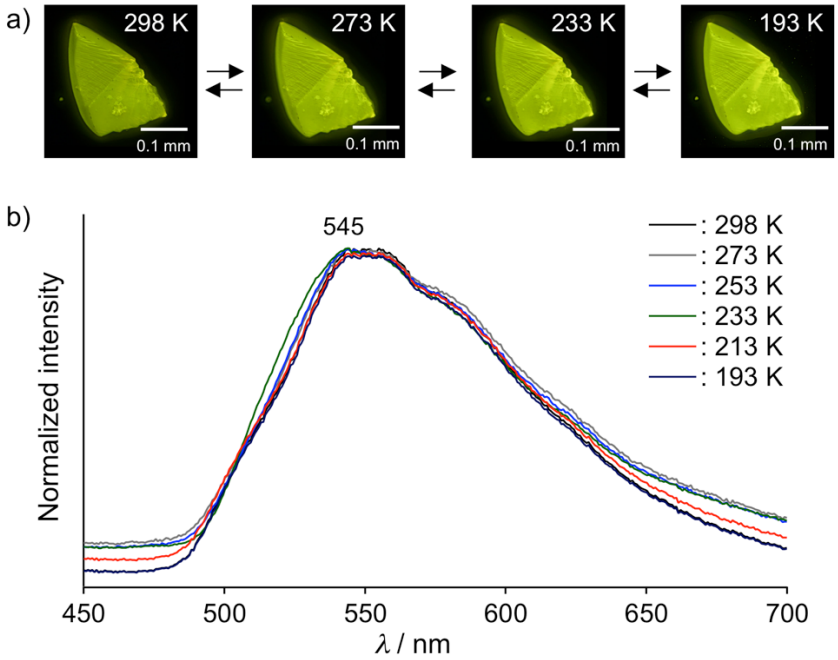

Figure 7. a) Photographs of no emission color changes of **2** under UV irradiation. b) Emission spectra of **2** in various temperatures.

Spectral changes as a function of rotational angle have been well documented for π-conjugated chromophores that are linked by triple bonds, such as tolane,[13] bis(phenylethynyl)benzene (Scheme 2a), [12,14] and numerous structures where electronic interactions are determined by metal centers.[10b-c,15] While rotation of aromatic groups relative to each other does not affect the ground state potential energy profile, electronic excitation causes changes in bond order with single and triple bonds acquiring cumulene character, which makes the excited state energies sensitive to twist angles of arene groups.[12,14] Thus, coplanar structures are fully delocalized in the ground and excited states (shown in red in the top frame of Scheme 2a), such that they tend to absorb and emit at lower energies as compared to the analogous twisted structures. In fact, twisting restricts conjugation in the excited state (Scheme 2a, bottom frame) so that those structures have greater excitation energies. Differences in the twist angle result in differences in the position of the spectrum, and in the relative intensity of the vibronic components, as shown with several linearly conjugated chromophores,[10,12] including a series of pentiptycenes that illustrate this effect remarkably well.[16] Another key feature of the π-conjugated chromophores is that phosphorescence tends to be more efficient from the twisted structures, which tend have an efficient intersystem crossing mechanism that leads to the population of the phosphorescent state.[13,16]

In order to extend the model shown in Scheme 2a to a chromophores such as the diethynylbenzene of **1** with a single aromatic group flanked by triple bonds that are coordinated to metal centers, we propose to take advantage of electronic interactions between neighboring molecular rotors that are made possible by Au–Au contacts. As shown in the top frame of Scheme 2b, we propose that parallel orbital alignment between the Au–Au bond and the π-system of the central aromatic phenylene can delocalize the wave function beyond a single chromophore, such that excitation in conformers with parallel aromatic rings can be shared between adjacent rotors, as illustrated by red color in the top structure in Scheme 2b.

In order to test this hypothesis, we carried out time-dependent (TD) DFT calculations using a dimer with coordinates taken from single-crystal structure of **1** at 193 K (Figure 8, S14–15, and Table S2–5). The results of these calculations confirm that rotation of the phenyl ring within the reference frame given by the direction of the Au–Au bond of adjacent complexes can affect their electronic communication (Figure 8 and S15). In addition to the equilibrium geometry of the test Au–Au dimer present in the crystal, we carried out B3LYP/SDD calculations with a model where the central phenylenes were rotated by 90° (Table S3–4). The excitation energy calculated for the crystal structure had a relatively good

agreement with the value obtained from the experimental phosphorescence excitation spectrum (Figure S14). Furthermore, the frontier molecular orbitals for the dimer with the crystal conformation indicated that the HOMO was distributed over the two diethynylbenzenes with a small density localized in the gold atoms of the dimer (Figure 8 and S15).[17] On the other hand, the HOMO of the dimer with the phenyl rings rotated by 90° was localized on a diethynylbenzene monomer, which is very similar to the bottom structure in Scheme 2b. The LUMOs of the two structures were mainly located on the tris(4-fluorophenyl)phosphane moiety in the complex (Figure 8 and S15). Furthermore, the HOMO-LUMO gaps were significantly different, suggesting that the two extreme structures should have distinct absorption and emission spectra. Results from calculations performed using a dimer of hindered rotor **2** were analogous to those from **1** (Figure S15 and Table S5), suggesting that changes in emission would also take place in **2** if rotation of the central tetra-methylphenylenes were possible in the corresponding crystals.

Scheme 2

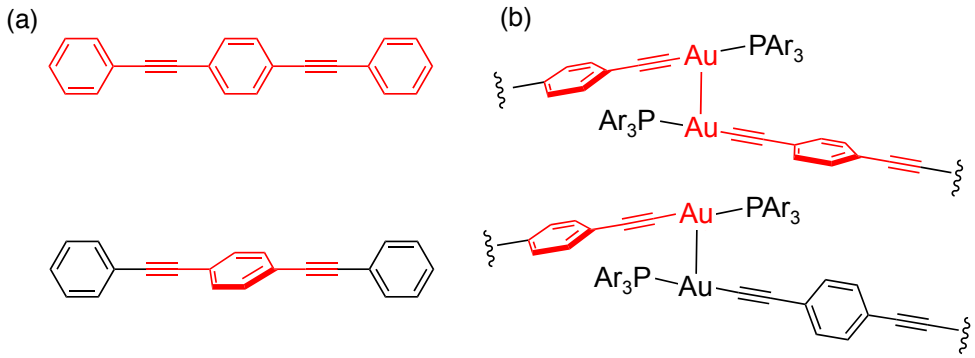

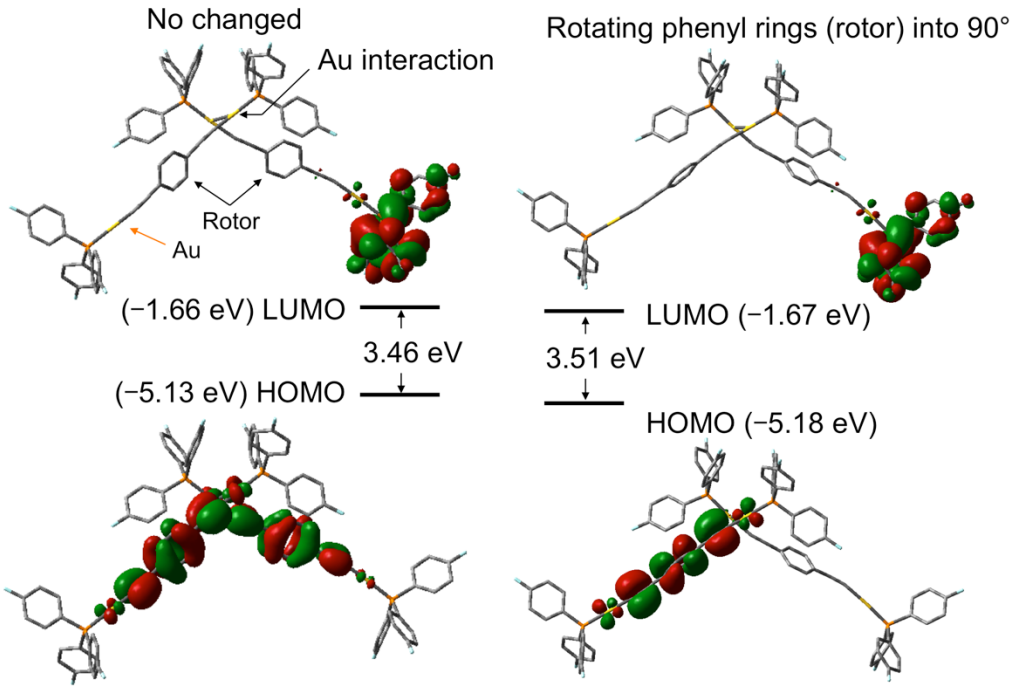

Figure 8. Frontier molecular orbitals and the corresponding energy levels obtained by TD-DFT calculations (B3LYP/SDD, singlet) of dimer in the crystal structures of **1** (left) and 90° rotated phenyl ring geometry (right).

5.2.6. Potential Correlation between Triplet Decay and Rotational Dynamics.

In search of a qualitative correlation between the emission changes of **1** and the rotational frequency determined by solid-state NMR, we measured the phosphorescence decays of crystalline **1** and **2** at 498 and 543 nm at temperatures ranging from 195 to 298 K (Figure 9 and S16–17). The two data sets revealed high heterogeneities that depart significantly from single exponential functions with decays that span a time window from ca. 100-200 μs in the case of **1**, and ca. 2 ms in the case of **2**. Significantly, only the decay kinetics of dynamic rotors **1** displayed high temperature dependence and measurements carried out by detection at 498 and 543 nm resulted in different decays, highlighting the spectral heterogeneity and complexity of the solid state emission (Figure S16). Considering that reasonable decay models required multiple exponential functions with varying lifetimes (τ_n) and pre-exponentials (A_n), we calculated the weighted average from all the components for each sample ($\tau_{av} = \Sigma A_n \tau_n$) at every temperature, as shown for **1** in Table 1 and S6–7. Decay fits in the case of **2** (Table S8) require as many as four exponential functions leading to an average temperature-independent time constant of 56.6±7.5 μs. In the case of **1** we were able to use double exponential functions with varying pre-exponentials of short- (ca. 10 μs) and long-lived components (ca. 38 μs) in the temperature interval of 213–298 K (Table 1 and S6). However, measurements at 195 K required a small amount (ca. 10%) of an additional much longer component (110 μs, Table 1 and S6), which led to average time constants between ca. 11 μs to 32 μs in the range of 298 and 193 K. We note that excited state decay occurs within the range of the time constants for rotation (0.25 μs to 100 μs), which may help explain the high kinetic heterogeneity of the observed emission. One may visualize spectral changes in Figure 6 as resulting from a superposition of a vibrationally resolved spectrum of **1**, from a rotational minimum, combined with increasing contributions from a broad spectrum that arises from components experiencing increasingly large vibrations and rotational motion as the temperature increases. A plot illustrating the variation in k_{rot} and τ_{av} as a function of temperature is shown in Figure 10.

While the data shown in Figures 5–9 support the role of phenylene rotation as the cause for the observed changes in emission, one should consider the fact that aurophilic interactions defined by Au–Au distances < 3.5 Å may also affect luminescent properties.[7] For example, the deformation of aurophilic interactions, which include changes in the Au–Au distance, can affect the delocalization and energetics of molecular orbitals, which in turn may also alter excitation energies and emission properties.[7] We found upon inspection of the XRD structures that changes in the Au–Au distances in the range of 193–298 K for **1** and **2** are not sufficient

to explain the different trends in their corresponding emission properties (Figure S8). The Au–Au distances of **1** and **2** increased upon heating to 298 K, and their corresponding changes were 0.042 and 0.054 Å, respectively, with a greater change observed for the complex that presents no changes in emission. Based on these observations, we conclude that the phosphorescence changes upon cooling and heating are not correlated with aurophilic interactions but are more likely the result changes in electronic communication that occur when the central phenylene vibrates and rotates in the crystal.

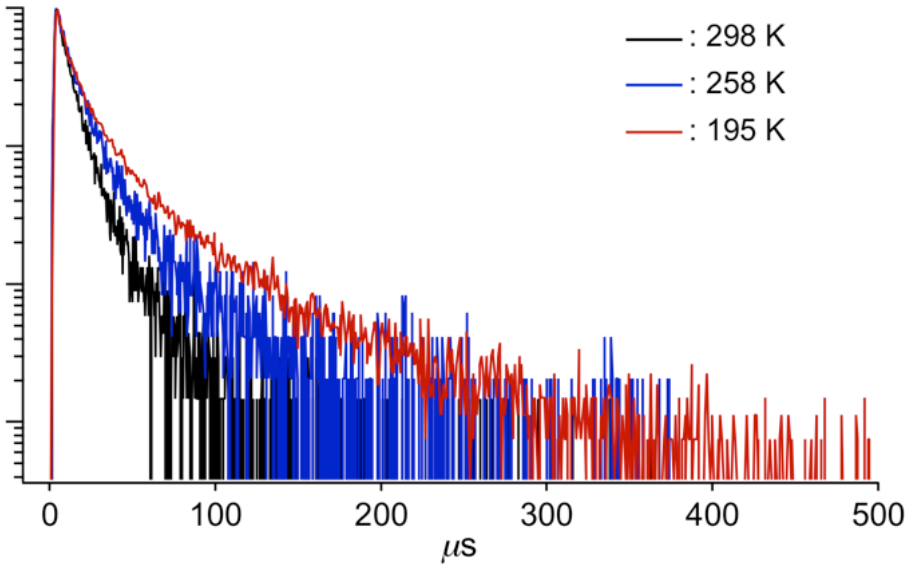

Figure 9. Emission decay of the crystalline **1** observed at 543 nm in various temperatures.

Table 1. Emission lifetimes of the crystalline 1 at 543 nm in various temperatures.[a]

Temp. / K	τ_1 (A_1) /μs (-)	τ_2 (A_2) /μs (-)	τ_3 (A_3) /μs (-)	τ_{av}[b] /μs
298	10.0 (0.95)	38.3 (0.05)	-	11.4
273	10.2 (0.91)	38.2 (0.09)	-	12.6
253	10.1 (0.73)	38.4 (0.27)	-	17.7
233	10.1 (0.67)	38.9 (0.33)	-	19.7
213	10.0 (0.61)	38.8 (0.39)	-	21.1
195	10.1 (0.49)	38.8 (0.41)	111.0 (0.10)	32.0

[a]Results from measurements obtained with crystals of **2** are included in table S4. [b] $\tau_{av} = \Sigma\ \tau_n A_n$, obtained by tail fitting (λ_{ex} = 370 nm).

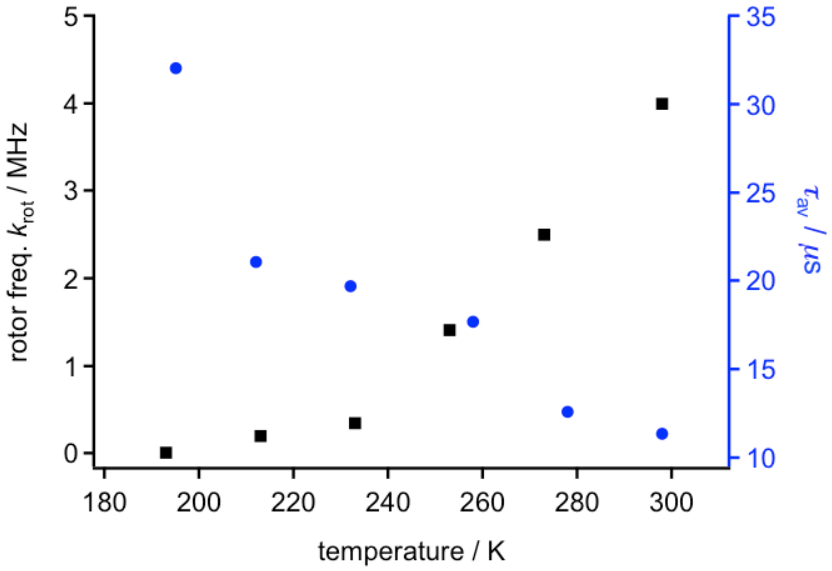

Figure 10. Qualitative correlation between the average emission lifetime (τ_{av}) at 540 nm and the rotation frequency of **1** ($k_{rot.}$).

5.3. Summary

In this work, we described the first example of a crystalline material where changes in phosphorescence appear to be the result of changes in the rotational motion of an aromatic chromophore that is part of dumbbell-shaped gold(I) complex **1.** Changes in emission properties and rotational frequency exhibited a reasonable correlation, and TD-DFT studies revealed that conformational changes of the phenylene rotator can cause changes in the electronic communication between adjacent chromophores. Furthermore, gold(I) complex **2** with a sterically hindered tetramethylphenylene rotator provided us with an excellent control sample where no changes in emission color and no rotational motion can be detected in its crystals. These results strongly indicate that the luminescence properties of bulk materials can be tuned by taking advantage of amphidynamic crystals that allow for structurally-controlled rotational motion.

5.4. Experimental Section

5.4.1. General

All commercially available reagents and solvents are reagent grade and were used without further purification unless otherwise noted. Solvents for the synthesis were purchased from commercial suppliers, degassed by three freeze-pump-thaw cycles and further dried over molecular sieves (4 Å). NMR spectra were recorded on a JEOL JNM-ECX400P or JNM-ECS400 spectrometer (^{1}H: 400 MHz; ^{13}C: 99.5 MHz) using tetramethylsilane and $CDCl_3$ as internal standards, respectively. Solid-state NMR spectra were acquired on a Bruker DRX 300 instrument (^{2}H: 46.07 MHz; 13C: 75.47 MHz). Emission spectra were recorded on a Hitachi F-7000 spectrometer. Absorption spectra were recorded on the basis of synchronous fluorescence spectroscopy using a Hitachi F-7000 spectrometer equipped with an integrating sphere. Fluorescence microscopic spectra were recorded on a Photonic Hamamatsu PMA-12 Multichannel Analyzer. The emission quantum yields of the solid samples at room temperature were recorded on a Hamamatsu Quantaurus-QY spectrometer with an integrating sphere. Variable temperature emission decay measurements were obtained using an FLS 920 spectrometer from Edinburgh Instruments equipped with a micro halogen lamp (μF). Elemental analyses and low- and high-resolution mass spectra were recorded at the Global Facility Center at Hokkaido University. Photographs were obtained using Olympus BX51 or SZX7 microscopes with Olympus DP72, Nikon D5100 digital cameras. Thermal gravimetric analysis profiles were recorded on Bruker TG-DTA2010SAT. Differential Scanning Calorimetry (DSC) profiles were measured on Perkin Elmer DSC8000 with an Intracooler II. The raw data files were plotted on Igor Pro Version 6.37

5.4.2. Synthesis

Synthesis of **1**

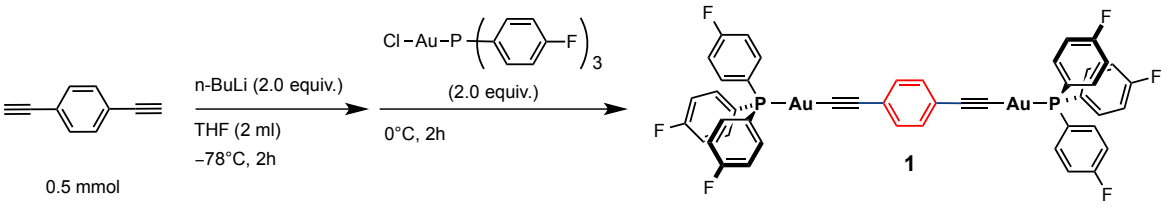

A powder of 1,4-diethynylbenzene (0.063 g, 0.50 mmol) was placed in an oven-dried two neck flask. The flask was connected to vacuum/nitrogen manifold through a rubber tube. It was evacuated and then backfilled with nitrogen. This process was repeated three times. Dry THF (3.0 ml) was then added to the flask under nitrogen atmosphere. After cooling to –78 °C, *n*-BuLi in Hexane (0.61 ml, 1.00 mmol, 1.63 M) was added to the mixture dropwise and stirred for 2 h. The suspended THF solution was added tris(4-fluorophenyl)phosphane gold(I) complex[18] (0.549 g, 1.00 mmol), and the reaction was performed under 0 °C for 2 h. The reaction was quenched by addition of a phosphate buffer solution and then extracted with $CHCl_3$ three times and washed with H_2O and brine. The organic layers were collected and dried over $MgSO_4$. After filtration, the solvent was removed *in vacuo*. Further purification by filtration washed with Et_2O and recrystallization using $CHCl_3$/Hexane gave analytically pure green crystals of **1** with green emission under UV light. (0.449 g, 0.39 mmol, 78 %). ^{1}H NMR (400 MHz, $CDCl_3$, δ): 7.18 (dt, J = 4.4 Hz, 12.1 Hz, 12H), 7.38 (s, 4H), 7.50–7.56 (m, 12H). ^{13}C NMR (100 MHz, $CDCl_3$, δ): 104.6, 116.8–117.2 (m), 123.2, 125.3 (d, J = 58.2 Hz), 132.1, 136.4–136.6 (m), 165.0 (d, J = 256.0 Hz). MS-ESI (*m*/*z*): calculated for $C_{46}H_{28}Au_2F_6P_2$, 1151.09350; found, 1151.09797. Anal. Calcd for $C_{46}H_{28}Au_2F_6P_2$: C, 48.02; H, 2.45; Found: C, 48.83; H, 2.33.

Synthesis of **1-*d*$_4$**

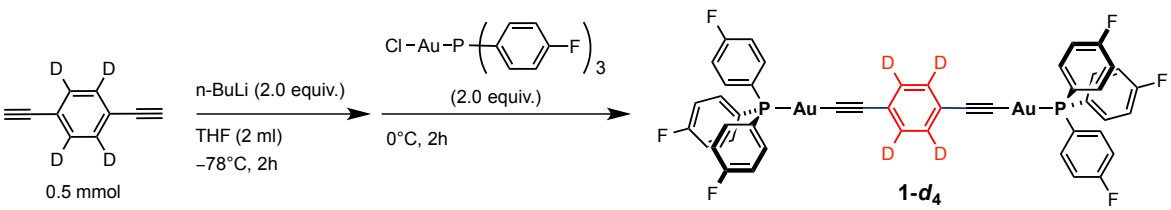

1-*d*$_4$ was prepared from 1,4-diethynyl-C_6D_4[19] (0.065 g, 0.50 mmol) according to the procedure similar to that described for the preparation of **1**. Yield: 82 % (0.473g, 0.41 mmol, green solid). ^{1}H NMR (400 MHz, $CDCl_3$, δ): 7.18 (dt, J = 4.3 Hz, 12.1 Hz, 12H), 7.50–7.56 (m, 12H). ^{13}C NMR (100 MHz, $CDCl_3$, δ): 104.5, 116.8–117.2 (m), 123.0, 125.3 (d, J = 57.8 Hz), 131.7 (t, J

= 25.2 Hz), 136.3–136.6 (m), 165.0 (d, J = 259.1 Hz). MS-ESI (m/z): calculated for $C_{46}H_{24}D_4Au_2F_6P_2$, 1155.11861 (49.8 %); found, 1155.12308. Anal. Calcd for $C_{46}H_{24}D_4Au_2F_6P_2$: C, 47.85; H, 2.79; Found: C, 47.83; H, 2.37.

Synthesis of **2**

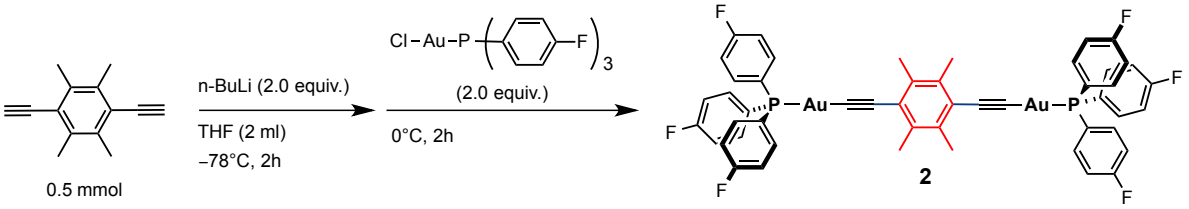

2 was prepared from 1,4-diethynyl-tetramethylbenzene[20] (0.091 g, 0.50 mmol) according to the procedure similar to that described for the preparation of **1**. Yield: 71 % (0.428g, 0.36 mmol, yellow solid). ^{1}H NMR (400 MHz, $CDCl_3$, δ): 2.52 (s, 12H), 7.19 (dt, J = 4.4 Hz, 12.1 Hz, 12H), 7.51–7.58 (m, 12H). ^{13}C NMR (100 MHz, $CDCl_3$, δ): 19.2, 103.0, 116.7–117.1 (m), 123.6, 125.6 (d, J = 55.3 Hz), 135.6, 136.4–136.7 (m), 165.0 (d, J = 258.5 Hz). MS-ESI (m/z): calculated for $C_{50}H_{36}Au_2F_6P_2$, 1207.15610 (54.1%); found, 1207.16057 Anal. Calcd for $C_{50}H_{36}Au_2F_6P_2$: C, 49.77; H, 3.01; Found: C, 49.33; H, 2.97.

5.4.3. TGA of 1 and 2

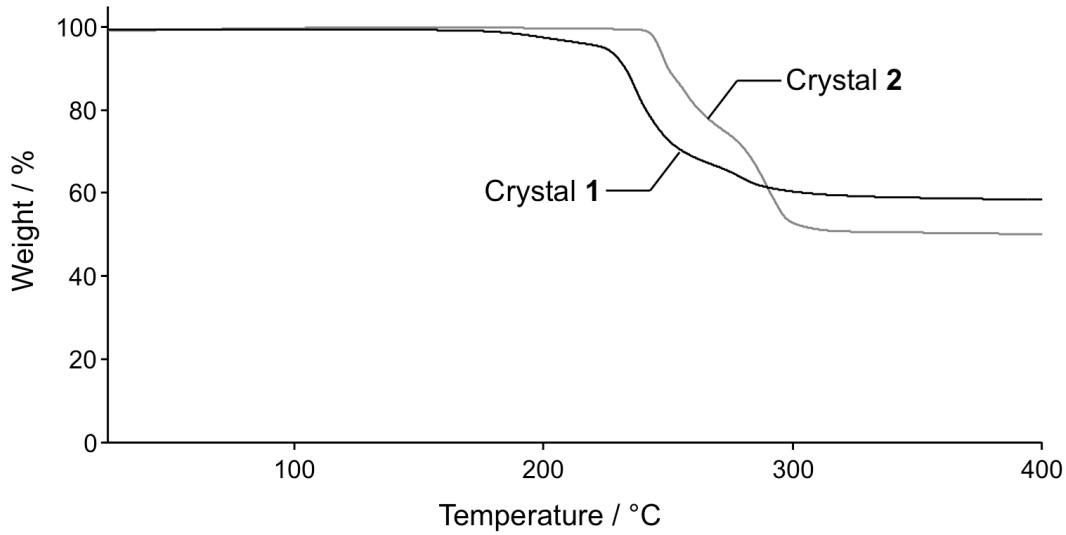

Figure S1. TGA profiles of the crystal **1** and **2** (black bold line and gray bold line, respectively). The heating rate is 5 °C/min. There was no decrease of weight percent of the samples until decomposition. These results indicate that both samples do not include solvent molecules in the crystals.

5.4.4. Data for Single-Crystal X-Ray Structural Analyses

Single-crystal X-ray structural analyses were carried out on a Rigaku R-AXIS RAPID diffractometer using graphite monochromated Mo-K□ radiation. The structure was solved by direct methods and expanded using Fourier techniques. Non-hydrogen atoms were refined anisotropically. Hydrogen atoms were refined using the riding model. All calculations were performed using the CrystalStructure crystallographic software package except for refinement, which was performed using SHELXL-2013.[21]

Table S1 Summary of X-ray crystallographic data of the crystal **1** and **2**.

compound	**1** at 123 K	**1** at 193 K	**1** at 213 K
CCDC Number	1568271	1568265	1568266
Empirical Formula	$C_{46}H_{28}Au_2F_6P_2$	$C_{46}H_{28}Au_2F_6P_2$	$C_{46}H_{28}Au_2F_6P_2$
Formula Weight	1150.60	1150.60	1150.60
Crystal System	triclinic	triclinic	triclinic
Crystal Size / mm	0.138×0.076×0.051	0.141×0.081×0.056	0.088×0.143×0.067
a / Å	11.9234(11)	11.9564(13)	11.9603(16)
b / Å	14.1307(12)	14.1676(17)	14.179(2)
c / Å	14.1890(11)	14.2228(15)	14.2356(19)
α / °	68.637(2)	69.048(3)	68.990(3)
β / °	67.907(2)	67.782(3)	67.695(4)
γ / °	65.678(2)	65.550(4)	65.533(4)
V / Å^3	1955.5(3)	1971.7(4)	1974.0(5)
Space Group	P-1(#2)	P-1(#2)	P-1(#2)
Z value	2	2	2
D_{calc} / g cm^{-3}	1.954	1.938	1.936
Temperature / K	123	193	213
$2\theta_{max}$ / °	55.0	55.0	55.0
μ(Mo K$_\alpha$) / cm^{-1}	76.639	76.007	75.919
No. of Reflections	Total: 19295 Unique: 8875 R_{int} = 0.0897	Total: 19553 Unique: 8990 R_{int} = 0.0918	Total: 19475 Unique: 8982 R_{int} = 0.0965
R_1[a]	0.0883	0.0929	0.1027
wR_2[b]	0.3233	0.3064	0.3774
GOF[c]	0.869	1.079	1.086
Max./Mini. peak I[d] / Å^3	2.58 e$^-$/−4.00 e$^-$	2.52 e$^-$/−3.91 e$^-$	2.58 e$^-$/−4.00 e$^-$

[a]:$I > 2.00\sigma(I)$. [b]:All reflections. [c]:Goodness of Fit Indicator. [d]: in Final Diff. Map.

compound	**1** at 233 K	**1** at 253 K	**1** at 273 K	**1** at 298 K
CCDC Number	1568267	1568268	1568269	1568270
Empirical Formula	$C_{46}H_{28}Au_2F_6P_2$	$C_{46}H_{28}Au_2F_6P_2$	$C_{46}H_{28}Au_2F_6P_2$	$C_{46}H_{28}Au_2F_6P_2$
Formula Weight	1150.60	1150.60	1150.60	1150.60
Crystal System	triclinic	triclinic	triclinic	triclinic
Crystal Size / mm	0.145×0.090×0.069	0.146×0.092×0.070	0.148×0.095×0.072	0.151×0.098×0.076
a / Å	11.9857(16)	12.001(2)	12.061(3)	12.0427(18)
b / Å	14.187(2)	14.205(2)	14.190(4)	14.236(2)
c / Å	14.267(2)	14.266(2)	14.292(4)	14.3149(19)
α / °	69.105(4)	69.224(4)	69.463(8)	69.614(3)
β / °	67.658(4)	67.495(4)	67.245(8)	67.344(4)
γ / °	65.451(4)	65.403(4)	65.456(6)	65.315(4)
V / Å^3	1983.3(5)	1986.7(6)	1998.4(10)	2005.7(5)
Space Group	*P*-1(#2)	*P*-1(#2)	*P*-1(#2)	*P*-1(#2)
Z value	2	2	2	2
D_{calc} / g cm^{-3}	1.927	1.923	1.912	1.905
Temperature / K	233	253	273	298
$2\theta_{max}$ / °	55.0	55.0	55.0	55.0
μ(Mo K$_\alpha$) / cm^{-1}	75.565	75.432	74.993	74.719
No. of Reflections	Total: 19627 Unique: 9004 R_{int} = 0.1006	Total: 19611 Unique: 9011 R_{int} = 0.1007	Total: 19718 Unique: 9078 R_{int} = 0.1147	Total: 19774 Unique: 9106 R_{int} = 0.1013
R_1[a]	0.0887	0.0983	0.0877	0.0938
wR_2[b]	0.3413	0.3645	0.3429	0.3550
GOF[c]	0.966	1.022	0.922	0.815
Max./Mini. peak I[d] / Å^3	1.96 e$^-$/−3.34 e$^-$	1.83 e$^-$/−3.03 e$^-$	2.05 e$^-$/−1.80 e$^-$	1.62 e$^-$/−2.23 e$^-$

compound	**2** at 123 K	**2** at 193 K	**2** at 213 K	**2** at 233 K
CCDC Number	1568253	1568255	1568260	1568261
Empirical Formula	$C_{50}H_{36}Au_2F_6P_2$	$C_{50}H_{36}Au_2F_6P_2$	$C_{50}H_{36}Au_2F_6P_2$	$C_{50}H_{36}Au_2F_6P_2$
Formula Weight	1206.71	1206.71	1206.71	1206.71
Crystal System	monoclinic	monoclinic	monoclinic	monoclinic
Crystal Size / mm	0.175×0.170×0.065	0.175×0.170×0.065	0.176×0.171×0.066	0.205×0.192×0.067
a / Å	30.890(2)	31.070(3)	31.171(2)	31.370(8)
b / Å	14.5763(9)	14.5498(11)	14.5681(8)	14.641(3)
c / Å	19.1589(12)	19.1760(14)	19.2032(11)	19.272(4)
α / °	90	90	90	90
β / °	97.7949(15)	97.356(2)	97.2997(16)	97.170(4)
γ / °	90	90	90	90
V / Å^3	8546.8(10)	8597.5(12)	8649.5(9)	8782(3)
Space Group	*C2/c*(#15)	*C2/c*(#15)	*C2/c*(#15)	*C2/c*(#15)
Z value	8	8	8	8
D_{calc} / g cm^{-3}	1.875	1.864	1.853	1.825
Temperature / K	123	193	213	233
$2\theta_{max}$ / °	55.0	55.0	55.0	55.0
μ(Mo K$_\alpha$) / cm^{-1}	70.186	69.772	69.352	68.307
No. of Reflections	Total: 61543 Unique: 9759 R_{int} = 0.1205	Total: 39622 Unique: 9849 R_{int} = 0.0892	Total: 63130 Unique: 9890 R_{int} = 0.1152	Total: 40716 Unique: 9941 R_{int} = 0.0866
R_1[a]	0.0610	0.0583	0.0627	0.0606
wR_2[b]	0.1822	0.1796	0.1890	0.1809
GOF[c]	1.023	1.017	1.074	1.048
Max./Mini. peak I[d] / Å^3	2.28 e$^-$/−2.38 e$^-$	2.12 e$^-$/−2.57 e$^-$	1.80 e$^-$/−1.95 e$^-$	2.14 e$^-$/−1.78 e$^-$

[a]:$I > 2.00\sigma(I)$. [b]:All reflections. [c]:Goodness of Fit Indicator. [d]: in Final Diff. Map.

compound	**2** at 253 K	**2** at 273 K	**2** at 298 K
CCDC Number	1568262	1568263	1568264
Empirical Formula	$C_{50}H_{36}Au_2F_6P_2$	$C_{50}H_{36}Au_2F_6P_2$	$C_{50}H_{36}Au_2F_6P_2$
Formula Weight	1206.71	1206.71	1206.71
Crystal System	monoclinic	monoclinic	monoclinic
Crystal Size / mm	0.184×0.172×0.067	0.203×0.201×0.071	0.206×0.195×0.070
a / Å	31.287(2)	31.368(3)	31.414(3)
b / Å	14.5786(10)	14.5952(10)	14.5653(13)
c / Å	19.1847(13)	19.2014(14)	19.2042(17)
α / °	90	90	90
β / °	97.1376(18)	97.0338(18)	96.824(2)
γ / °	90	90	90
V / Å^3	8682.7(10)	8724.6(11)	8724.8(14)
Space Group	*C2/c*(#15)	*C2/c*(#15)	*C2/c*(#15)
Z value	8	8	8
D_{calc} / g cm^{-3}	1.846	1.837	1.837
Temperature / K	253	273	298
$2\theta_{max}$ / °	55.0	55.0	55.0
μ(Mo K$_\alpha$) / cm^{-1}	69.088	68.756	68.754
No. of Reflections	Total: 66125 Unique: 9926 R_{int} = 0.1330	Total: 65971 Unique: 9905 R_{int} = 0.1258	Total: 66790 Unique: 9979 R_{int} = 0.1332
R_1[a]	0.0621	0.0648	0.0646
wR_2[b]	0.1774	0.1959	0.2038
GOF[c]	0.968	1.015	0.972
Max./Mini. peak I[d] / Å^3	1.79 e$^-$/−1.51 e$^-$	1.62 e$^-$/−1.25 e$^-$	1.53 e$^-$/−1.32 e$^-$

[a]:$I > 2.00\sigma(I)$. [b]:All reflections. [c]:Goodness of Fit Indicator. [d]: in Final Diff. Map.

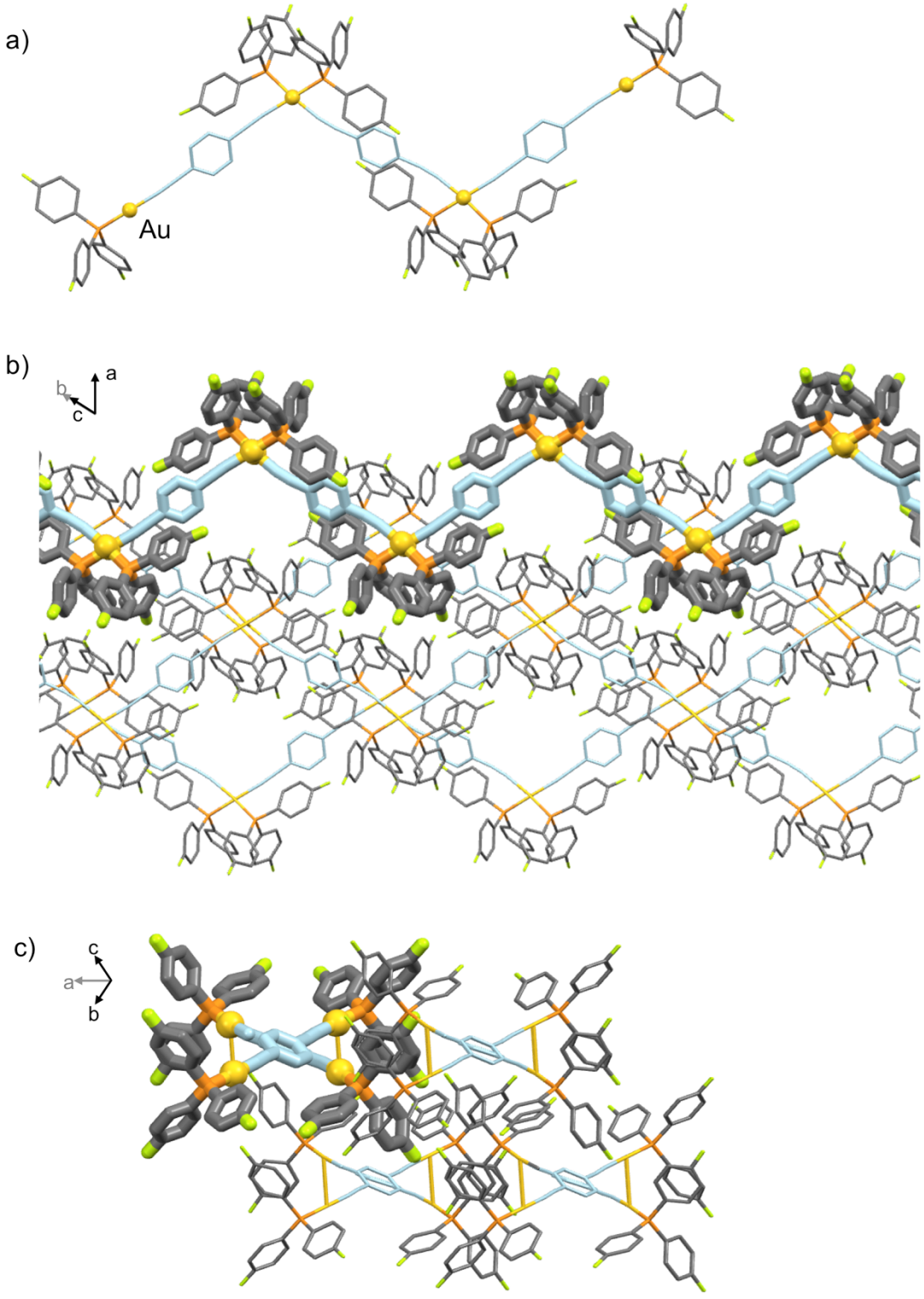

Figure S2. a-c) Single crystal structure of **1** at 123 K. All the H atoms are omitted for clarity.

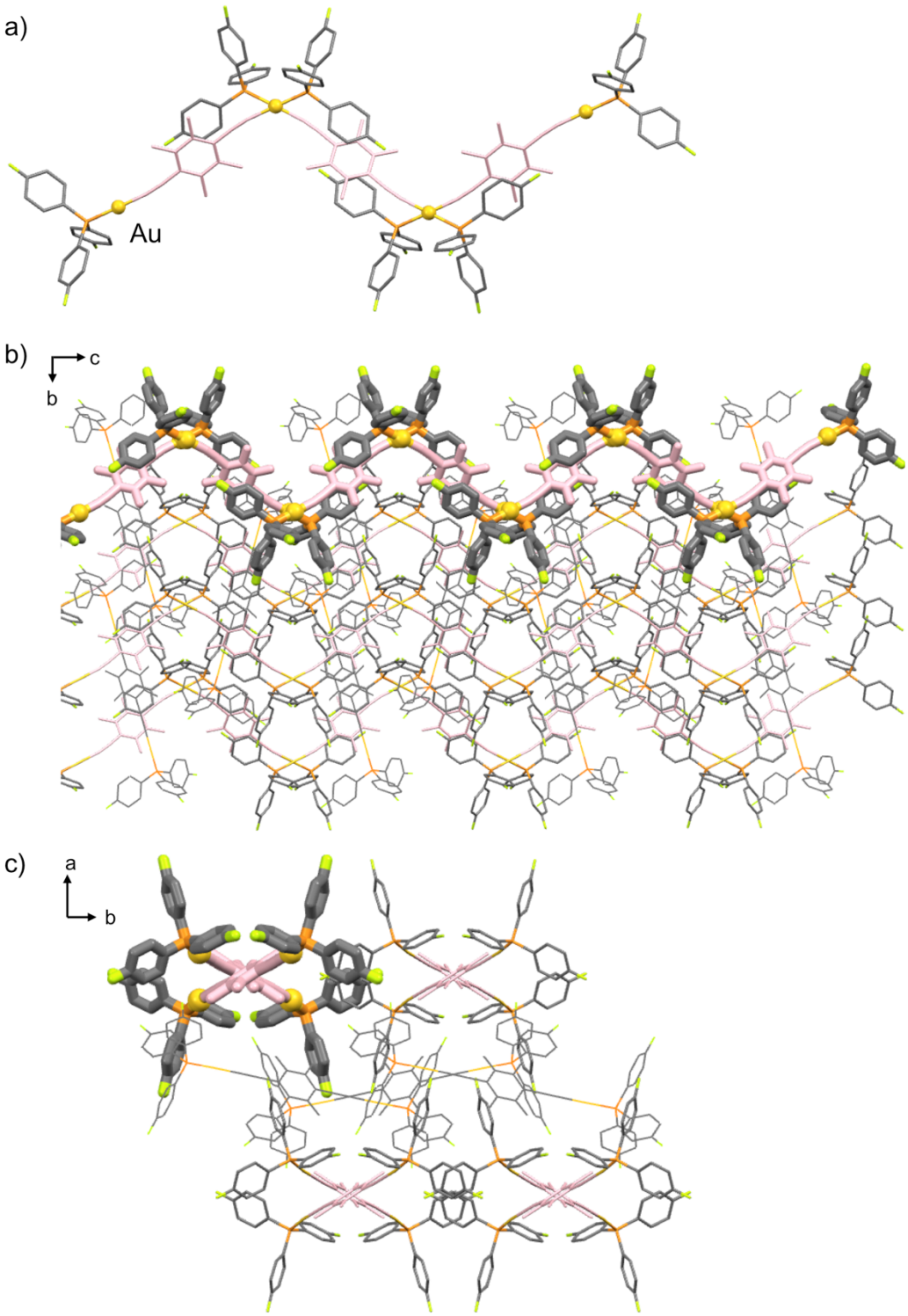

Figure S3. a-c) Single crystal structure of **2** at 123 K. All the H atoms are omitted for clarity.

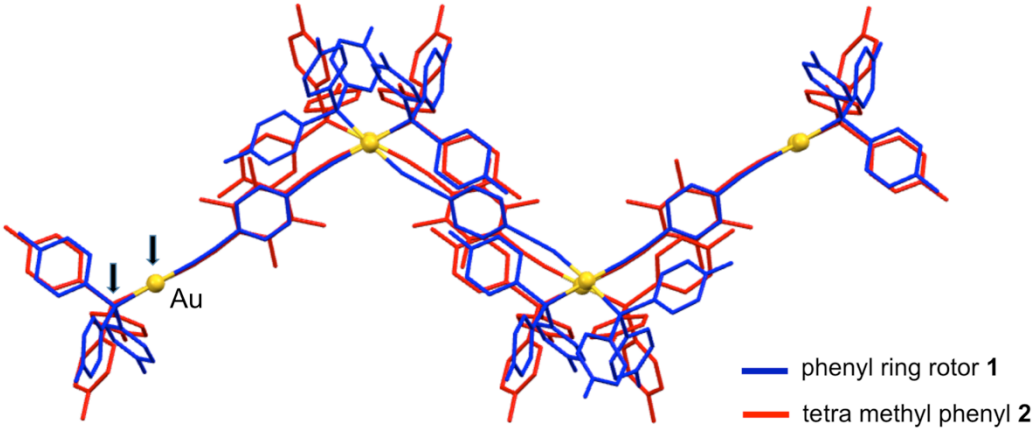

Figure S4. Superimposition of the intermolecular networks in the crystal **1** and **2** obtained at 123 K.

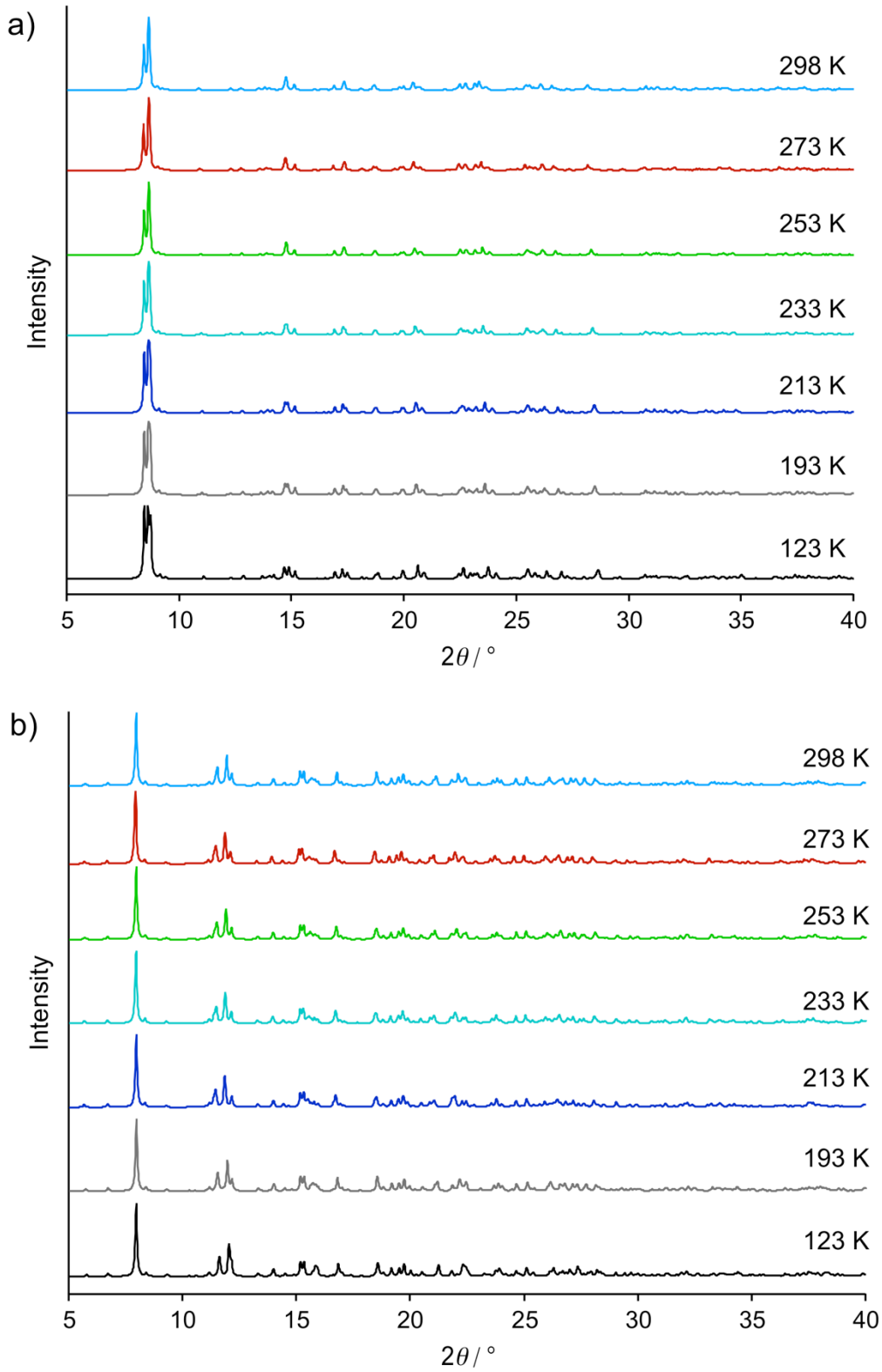

Figure S5. Simulation PXRD patterns from the VT-single crystal XRDs of a) **1** and b) **2** taken at 123 K to 298 K.

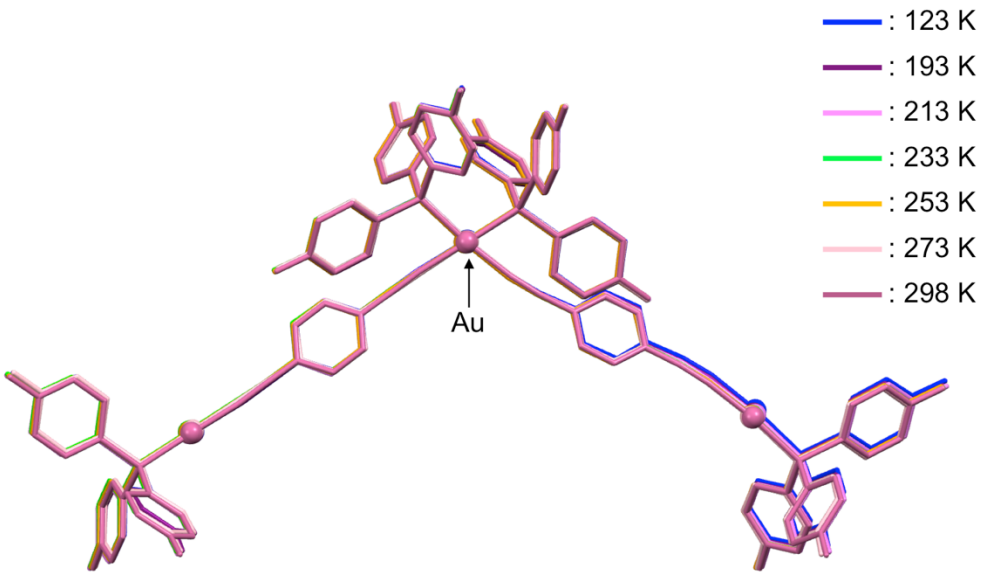

Figure S6. Superimposition of the dimers in the crystal **1** obtained at 123 K to 298 K.

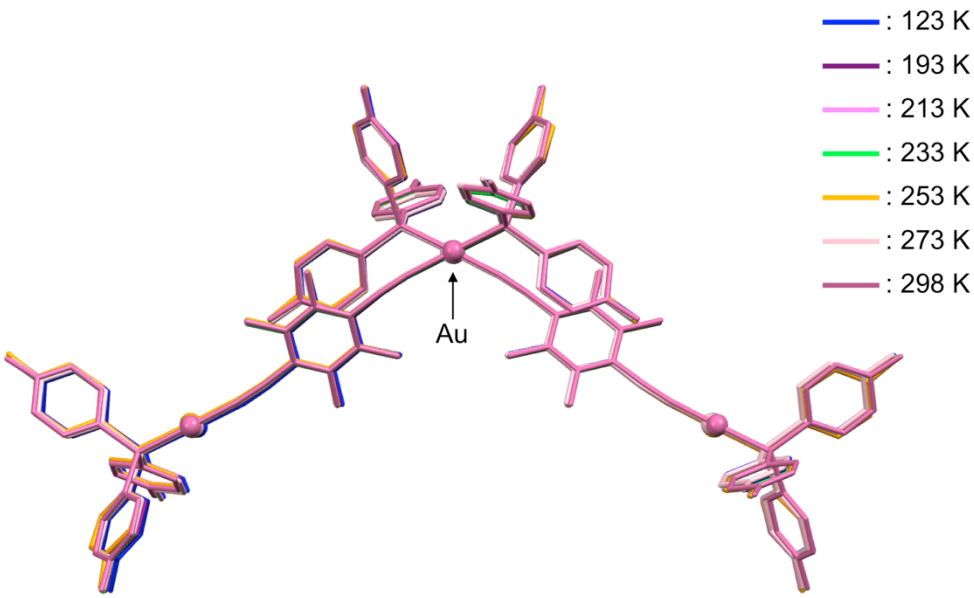

Figure S7. Superimposition of the dimers in the crystal **2** obtained at 123 K to 298 K.

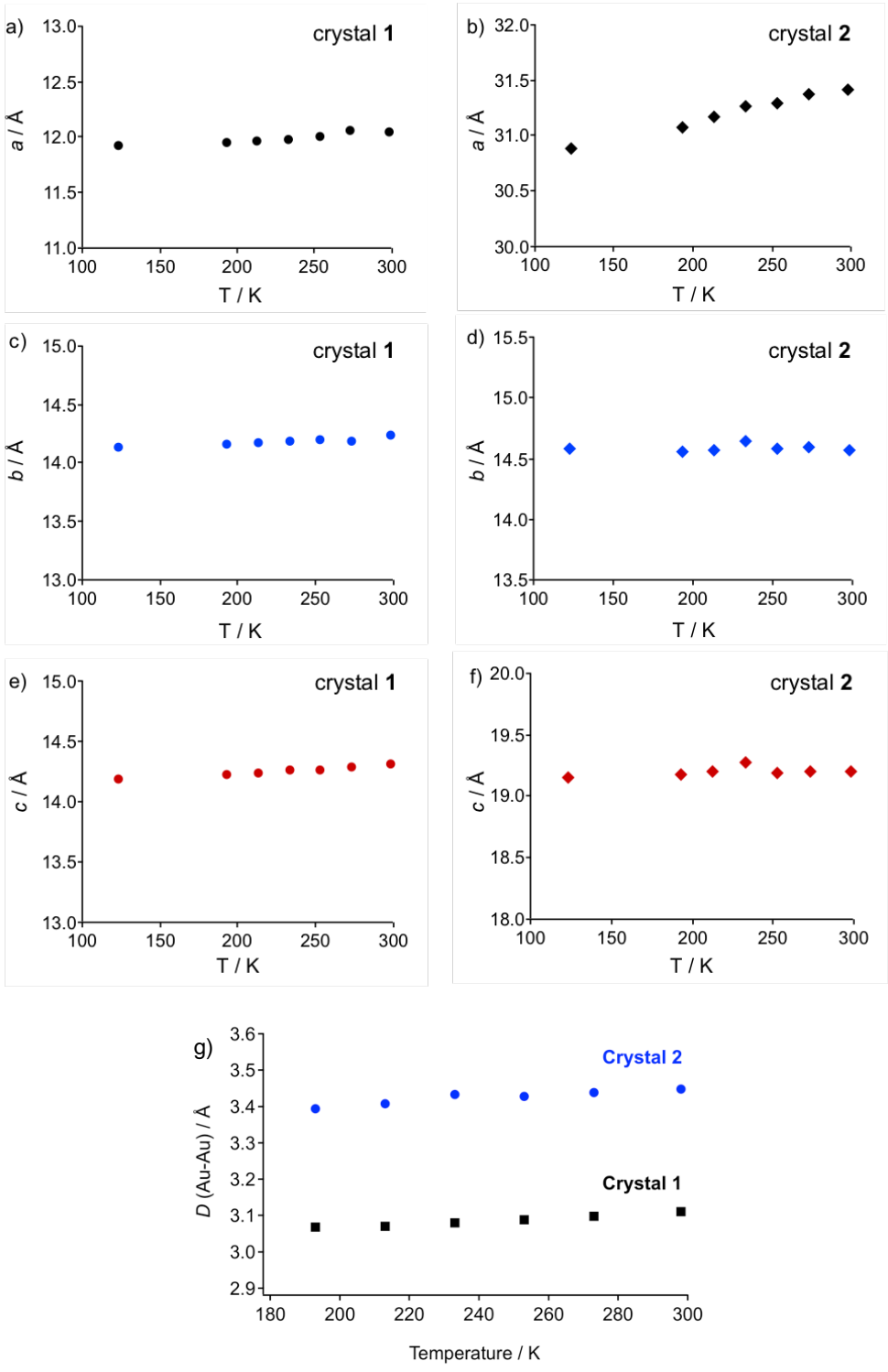

Figure S8. Plots of the cell parameters (*a*, *b*, *c*) of the crystal **1** (a, c, e) and **2** (b, d, f), and g) Au-Au [*D*(Au-Au)] in the crystal **1** (blue circle) and **2** (black square) with the measurement temperatures.

5.4.5. DSC of 1 and 2

Differential Scanning Calorimetry (DSC) profiles were measured on Perkin Elmer DSC8000 with an Intracooler II.

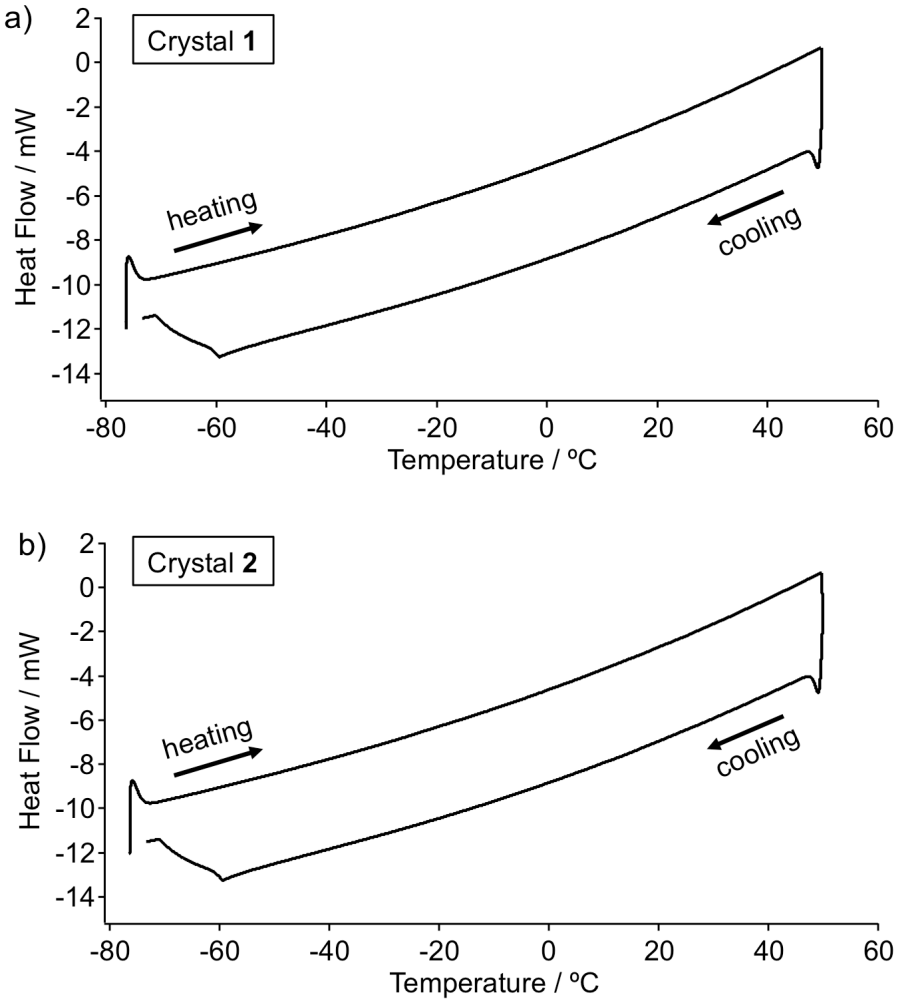

Figure S9. DSC profiles of a) the crystal **1** and b) **2**. Heating and cooling rates were 5 °C / min, respectively. There were no exo- or endothermic peaks in the both crystalline samples.

5.4.6. Solid-State NMR Studies of 1 and 2

5.4.6.1. Solid-state ^{2}H NMR Spin-echo Experiments

Solid-state ^{2}H NMR spectra were acquired on a Bruker DRX 300 instrument at ^{2}H frequency of 46.07 MHz. In the spin-echo experiments, a quadrupolar-echo sequence with phase cycling was used to suppress undesired single- and double-quantum coherence-transfer artifacts. A pulse of 50 μs with a refocusing delay of 42 μs was used in the sequence. The spectrometer produced 2.5-μs ^{2}H 90-degree pulses (46.07 MHz) with recycle delays of 20 s between pulses inside the coil. Variable temperature experiments were performed between 193 K and 318 K. For all these experiments, ca. 50 mg solid sample was placed inside a borosilicate glass NMR tube between two glass rods and sealed with Teflon tape. After performing high temperature or low temperature experiments, the samples were cooled/warmed back to the starting temperature and a ^{2}H NMR spectrum taken again to ensure that no irreversible transition had occurred during the VT experiments. The number of scans to obtain spectra with decent signal to noise ratio ranges from a few hundred to a few thousand. The data was processed with a line broadening of 5 kHz.

5.4.6.2. Simulation of the Experimental Spectra

All simulation was performed utilizing the online program offered by professor H. W. Spiess.[22] The spectra obtained for **1**-d_4 (crystalline sample) were identified to be the result of simple 2-fold rotations (Figure S10).

5.4.6.3. Solid-state Cross Polarization Magic Angle Spinning ^{13}C NMR (CP-MAS ^{13}C NMR)

CP-MAS ^{13}C NMR spectra of the crystalline sample **2** was recorded on a ^{1}H 300 MHz spectrometer at ^{13}C frequency of 75.47 MHz, with ^{1}H broadband decoupler in a 4 mm broadband probe. A spinning frequency of 10 kHz was used for the removal of spinning sidebands and a cross polarization contact time of 5 ms was used. Approximately 80 mg of the crystalline solid were gently ground using a mortar and pestle and packed in a 4 mm wide ZrO_2 rotor with a KelF cap. Variable temperature experiments were performed between 193 K and 298 K (Figure S11).

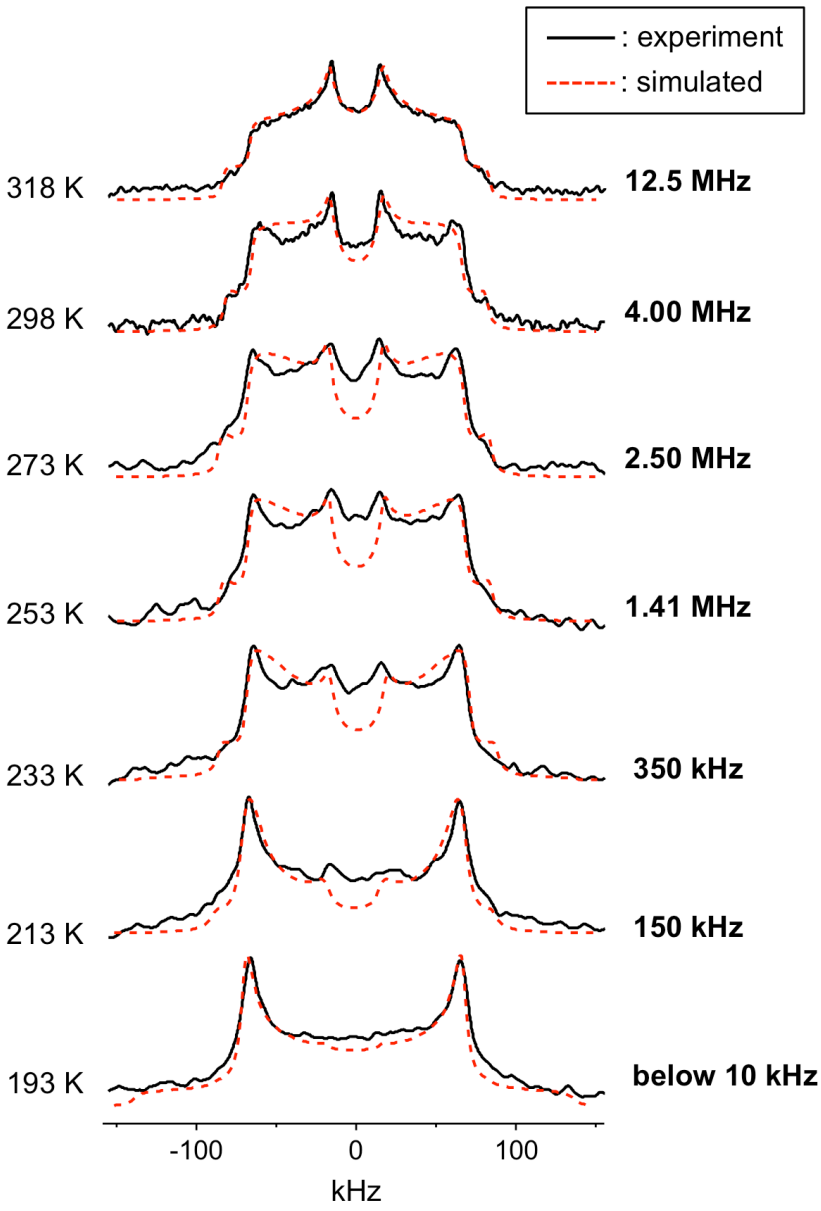

Figure S10. Variable temperature (VT) solid-state ^{2}H NMR spin-echo spectra of the crystal **1** obtained from the experiment (black solid line) and the simulations (red dashed line).

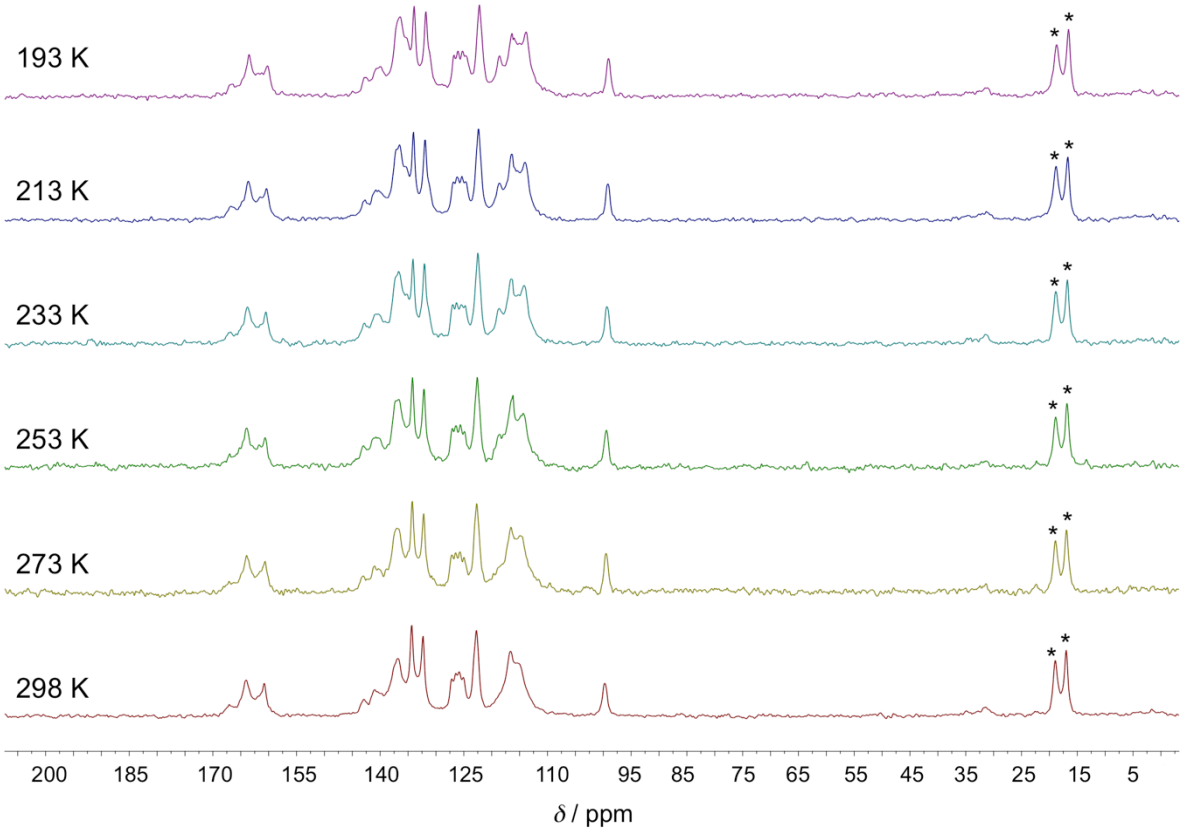

Figure S11. Variable temperature (VT) solid-state CP-MAS ^{13}C NMR spectra of the crystal **2**. * indicates peaks from the methyl group of tetra-methyl phenyl moiety.

5.4.7. Optical Properties of Solution Phase

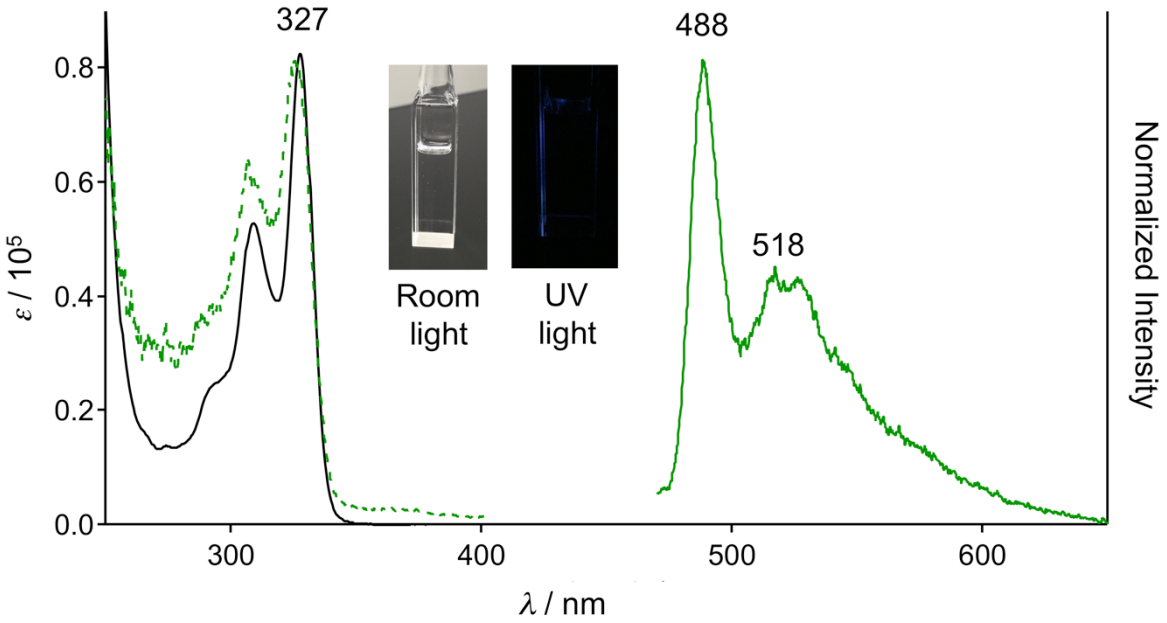

Figure S12. UV/vis absorption (black solid line), excitation (green dotted line, λ_{em} = 488 nm), and emission spectra (green solid line, λ_{ex} = 327 nm) of **1** in $CHCl_3$ (c = 4.6 × 10^{-6} M) at room temperature. The solution of **1** in $CHCl_3$ exhibited very weak emission under UV light.

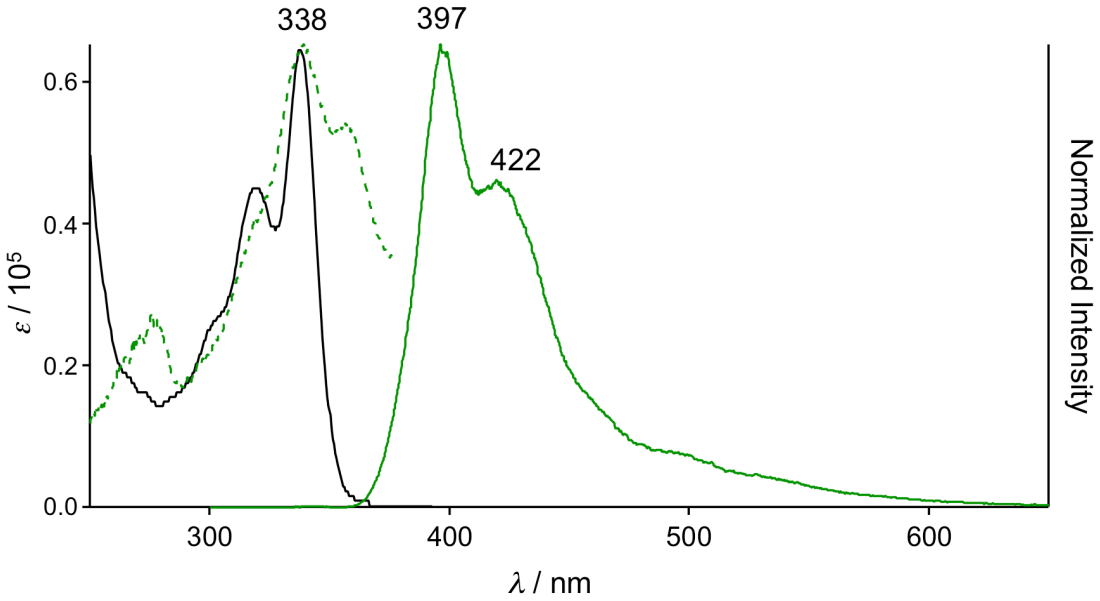

Figure S13. UV/vis absorption (black solid line), excitation (green dotted line, λ_{em} = 397 nm), and emission spectra (green solid line, λ_{ex} = 338 nm) of **2** in $CHCl_3$ (c = 1.5 × 10^{-6} M) at room temperature. The solution of **2** in $CHCl_3$ exhibited very weak emission under UV light.

5.4.8. TD-DFT Calculations

All calculations were performed using the Gaussian 09W (revision C.01 and E.01) and Gaussian 09 (revision C.01 and E.01) program package.[23] The singlet state TD-DFT calculations of the dimer of the crystal **1** were performed with the goal of understanding the origin of its emission properties. In the calculations, the B3LYP functional and the SDD basis set with an effective core potential were used. The geometries of the dimer with no rotated phenyl ring rotor were taken from the single crystal structure of **1** at 193 K. And, the dimer possessing the rotated phenyl rings into 90° from the initial geometry were prepared. Moreover, the calculation using the dimer taken from the single crystal of **2** at 193 K were performed. The positions of heavy atoms were fixed and only the positions of H atoms were optimized using the Spartan'10 MMFF force-field calculations before TD-DFT calculations.[24] The simulated UV/vis absorption spectra and the excitation spectra from the experiments exhibited the similar traces (Figure S14). Thus, the results of TD-DFT calculations give us reasonable mechanistic insight for studying the correlation between rotor rotations and the emission properties of the crystal **1**.

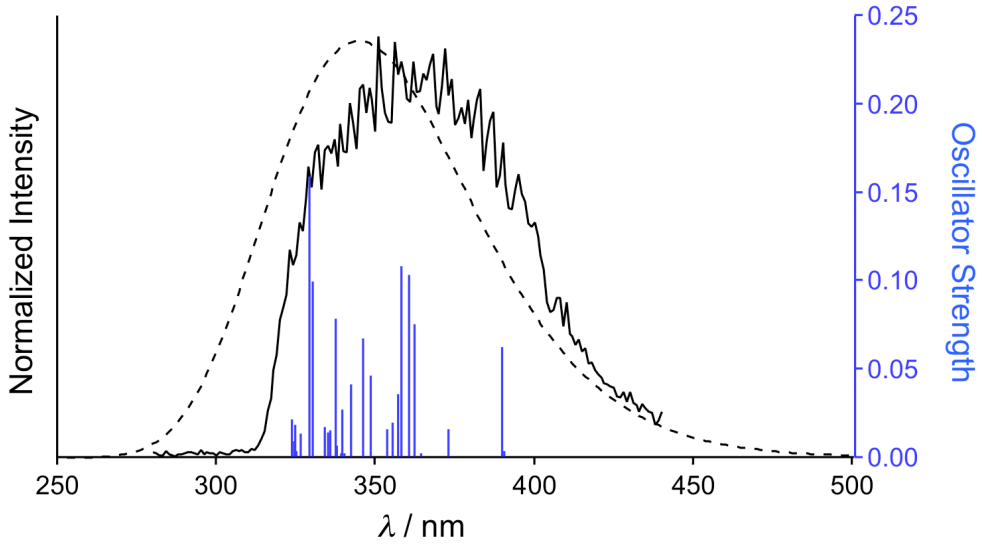

Figure S14. Comparison of experimental and theoretical studies on emission properties of the crystal **1**. Excitation spectra of the crystal **1** (black solid line) obtained at 195 K. Simulated UV/vis absorption spectra of the dimer in the crystal **1** (black dashed line) and oscillator strengths (blue sticks) based on the singlet state TD-DFT calculations of the dimer with no rotated phenyl ring rotor derived from the single crystalline structures of **1** measured at 193 K (B3LYP/SDD).

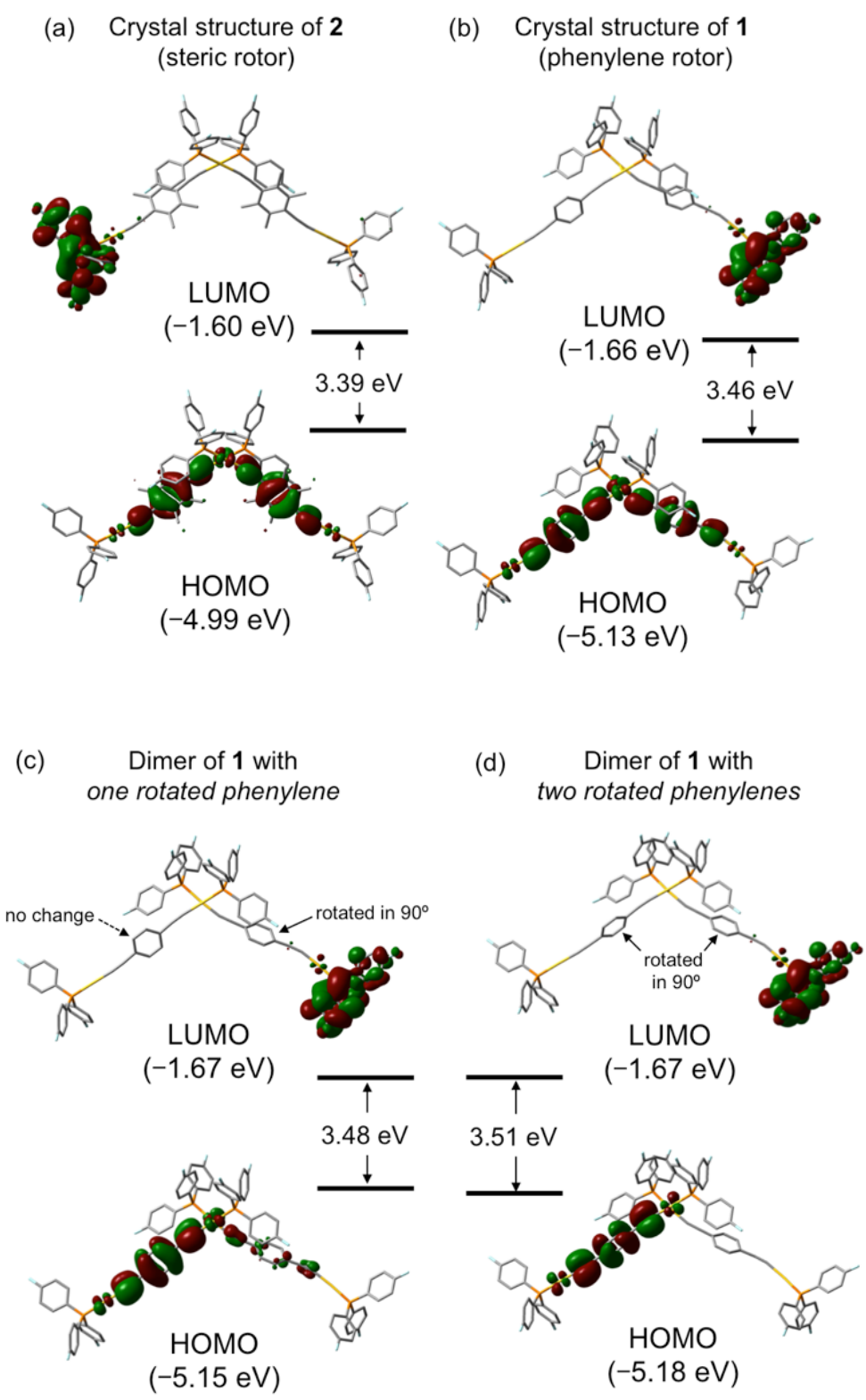

Figure S15. Energy levels and frontier orbitals of HOMO and LUMO of the dimer models.

Because the full optimization of the crystal structures including heavy metals (Au) requires high calculation costs, we used the model geometries taken from the single crystals of **1** and **2** without optimization other than C–H bonds. Because of the use of the non-full optimization models, the imaginary frequencies with small absolute value were observed in the vibration calculations.

Table S2. Selected singlet to singlet transitions of dimer in the crystal structure of **1**

states	energy / eV	λ / nm	*f* / -	orbital transition	CI coefficients
S1	3.176	390.38	0.0039	HOMO−1 → LUMO	−0.43677
				HOMO → LUMO	0.54618
S2	3.1793	389.97	0.0628	HOMO−1 → LUMO+1	0.31342
				HOMO → LUMO+1	0.62289
S8	3.4604	358.29	0.1084	HOMO−1 → LUMO+2	−0.29972
				HOMO−1 → LUMO+3	0.22766
				HOMO−1 → LUMO+4	0.12212
				HOMO−1 → LUMO+6	−0.11141
				HOMO → LUMO+2	−0.22644
				HOMO → LUMO+3	0.32795
				HOMO → LUMO+4	−0.27659
				HOMO → LUMO+6	0.25976

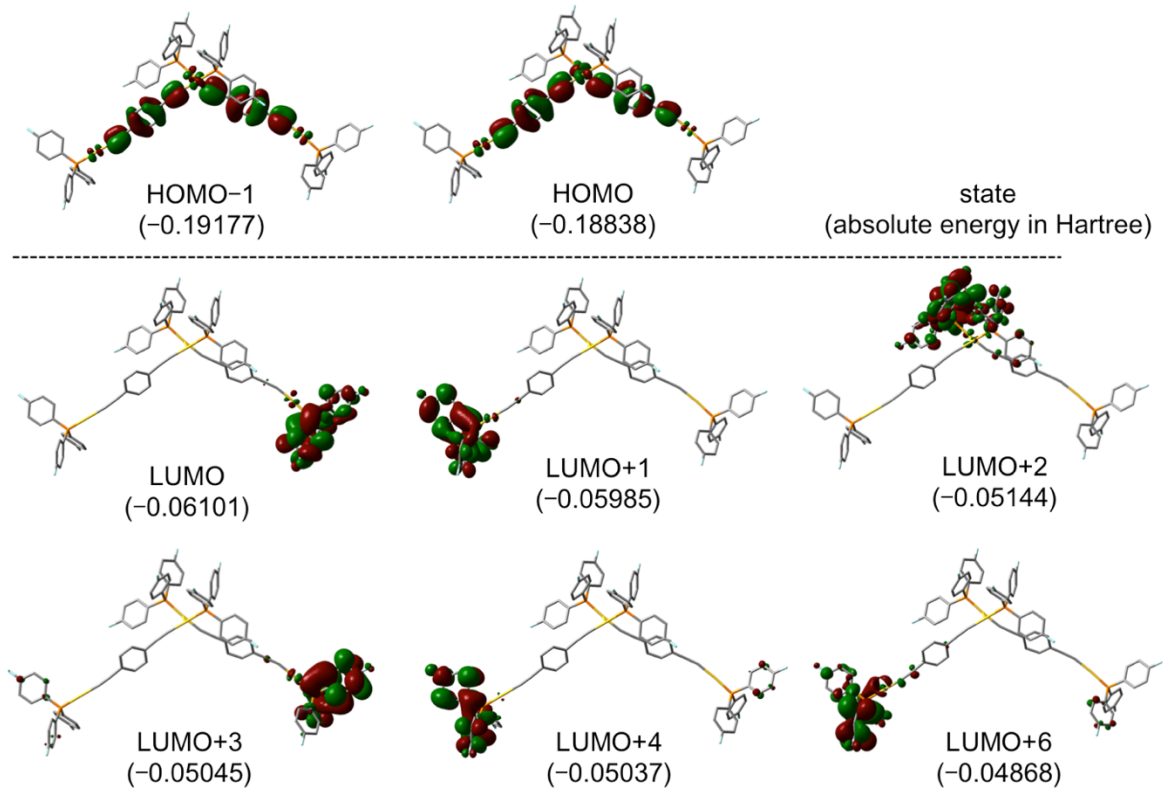

Table S3. Selected singlet to singlet transitions of dimer of **1** with *one rotated central phenylene*

states	energy /eV	λ / nm	*f* / -	orbital transition	CI coefficients
S1	3.1837	389.43	0.0675	HOMO−1 → LUMO+1	−0.14045
				HOMO → LUMO+1	0.68618
S2	3.2123	385.86	0.0587	HOMO−1 → LUMO	0.62751
				HOMO → LUMO	0.31600
S7	3.4624	358.09	0.1424	HOMO−1 → LUMO+2	0.62826
				HOMO−1 → LUMO+7	−0.14103
				HOMO → LUMO+4	−0.15765
				HOMO → LUMO+6	0.12204
				HOMO → LUMO+7	−0.13142

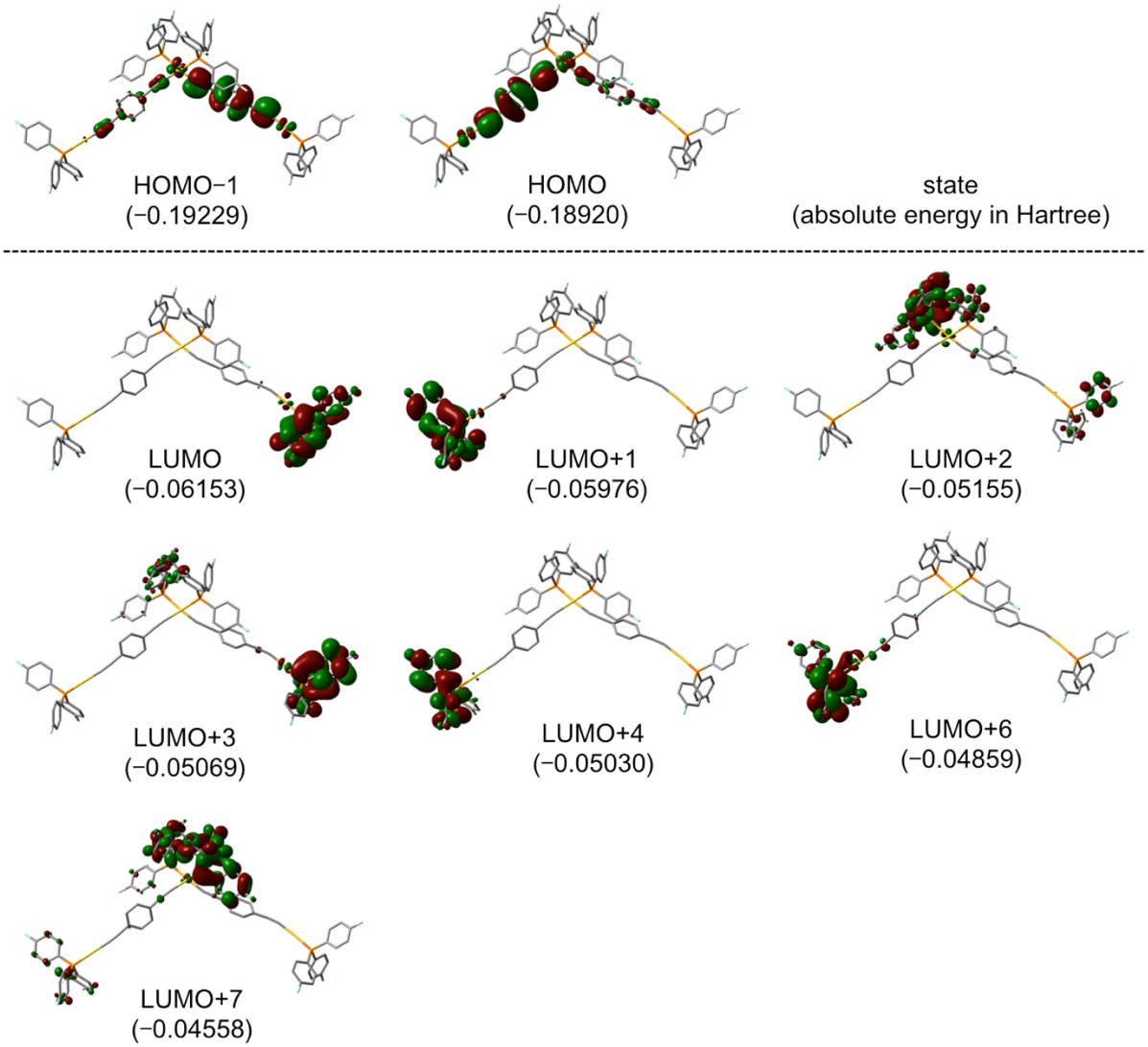

Table S4. Selected singlet to singlet transitions of dimer of **1** with *two rotated central phenylenes*

states	energy / eV	λ / nm	*f* / -	orbital transition	CI coefficients
S1	3.2041	386.95	0.0055	HOMO → LUMO+1	0.70049
S2	3.2168	385.43	0.0630	HOMO−1 → LUMO	0.70188
S6	3.4474	359.65	0.1679	HOMO−1 → LUMO+2	0.66552
				HOMO−1 → LUMO+6	−0.15625
				HOMO → LUMO+4	−0.10104
S8	3.506	353.64	0.1533	HOMO−1 → LUMO+3	−0.18322
				HOMO → LUMO+4	−0.20191
				HOMO → LUMO+6	0.63306

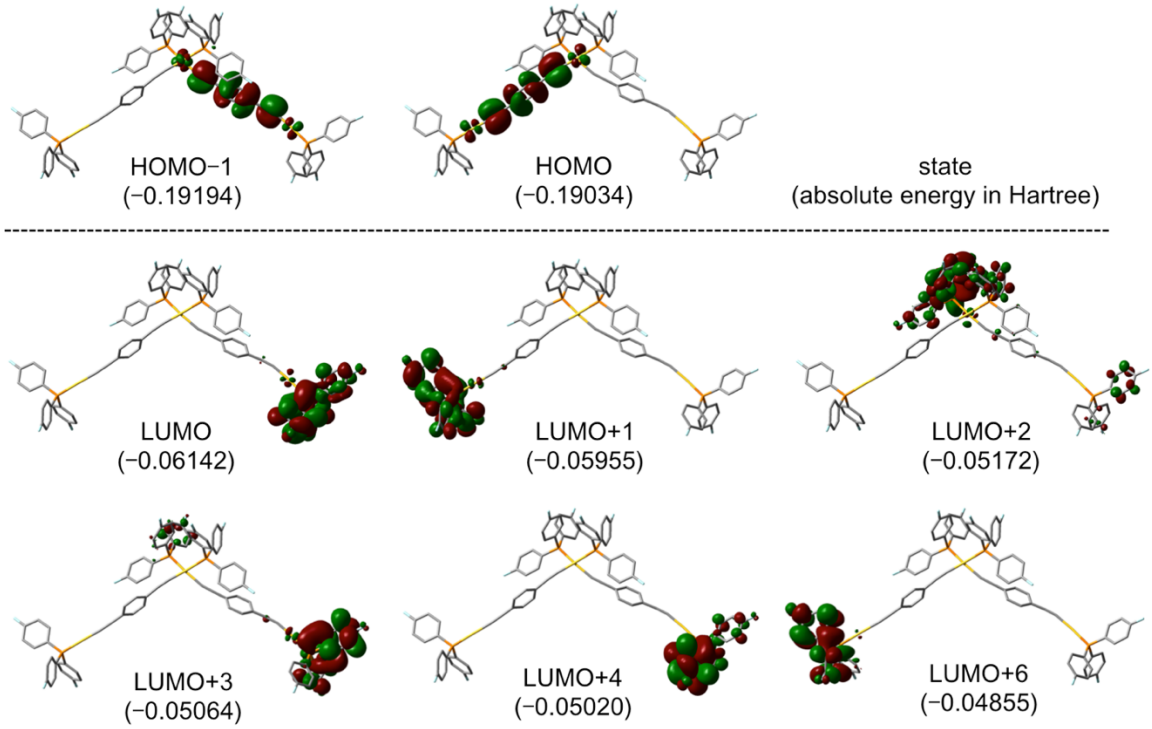

Table S5. Selected singlet to singlet transitions of dimer in crystal structure of **2** (steric rotor)

states	energy / eV	λ / nm	*f* / -	orbital transition	CI coefficients
S1	3.0831	402.14	0.0029	HOMO−1 → LUMO	−0.34354
				HOMO−1 → LUMO+1	−0.18459
				HOMO → LUMO	0.57125
				HOMO → LUMO+1	−0.12034
S3	3.1501	393.59	0.1496	HOMO−1 → LUMO+3	0.37694
				HOMO → LUMO+2	0.58834
S13	3.3748	367.39	0.0901	HOMO−1 → LUMO+11	−0.23983
				HOMO → LUMO+7	−0.11294
				HOMO → LUMO+10	0.62009

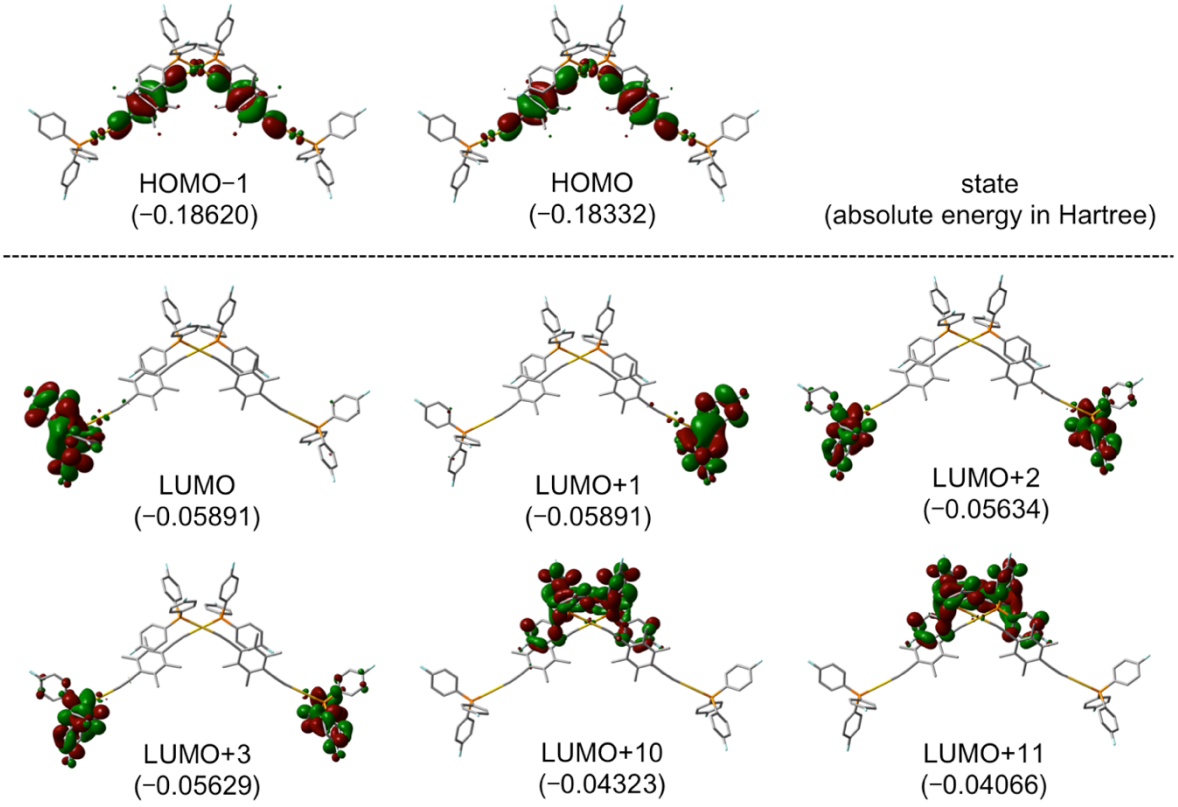

5.4.9. Photophysical Properties

Emission spectra and decay traces were obtained using an FLS 920 spectrometer from Edinburgh Instruments equipped with a micro halogen lamp (μF). For phosphorescence emission spectra, we used 370 nm as the excitation wavelength and detected emission from 400 nm to 700 nm. For phosphorescence decay trace, we used 370 nm as the excitation wavelength and detected kinetic traces at 498 nm and 543 nm. For low temperature measurements, we used a custom made NMR tube Dewar to vary the temperature using different cooling baths. Approximately 8 mg of the solid sample, which was grinded to a find powder, was placed inside an NMR tube and the NMR tube was placed inside the Dewar for low temperature measurements.

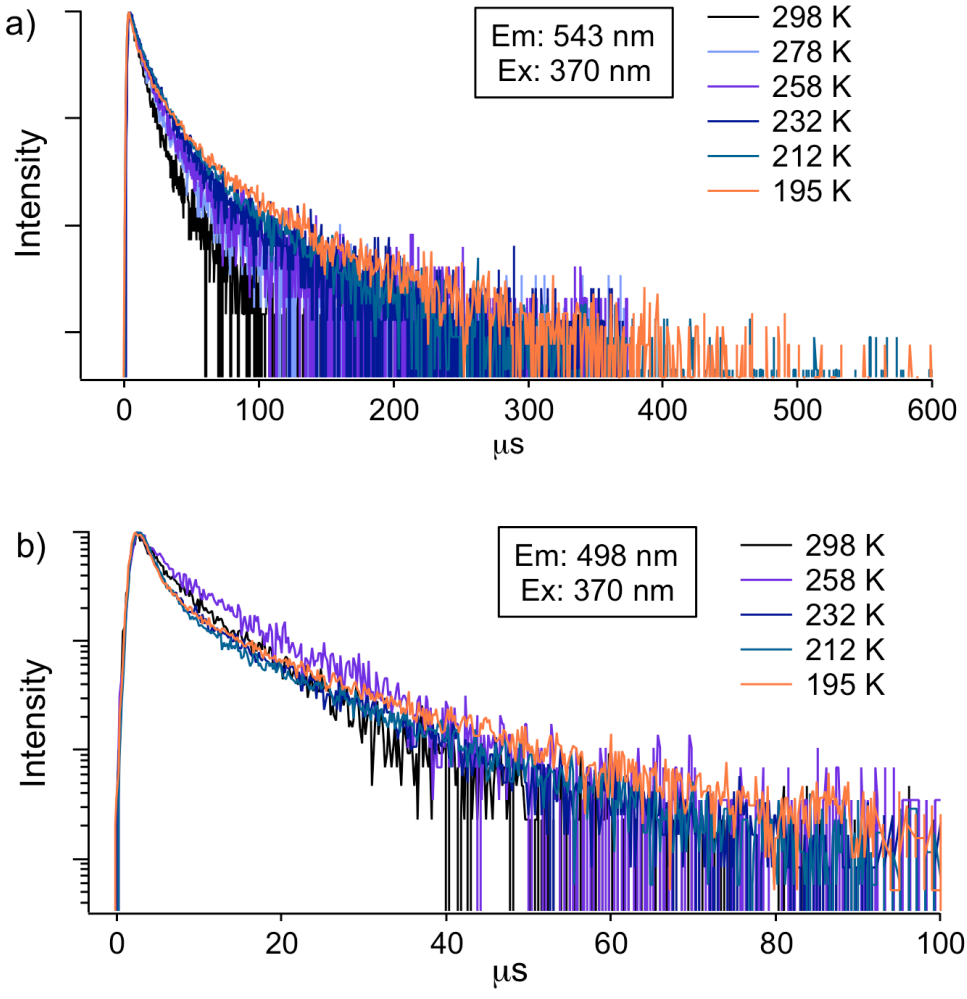

Figure S16. Emission decay profiles of the crystal **1** in various temperatures. The emission decays were monitored at a) 543 nm and b) 498 nm.

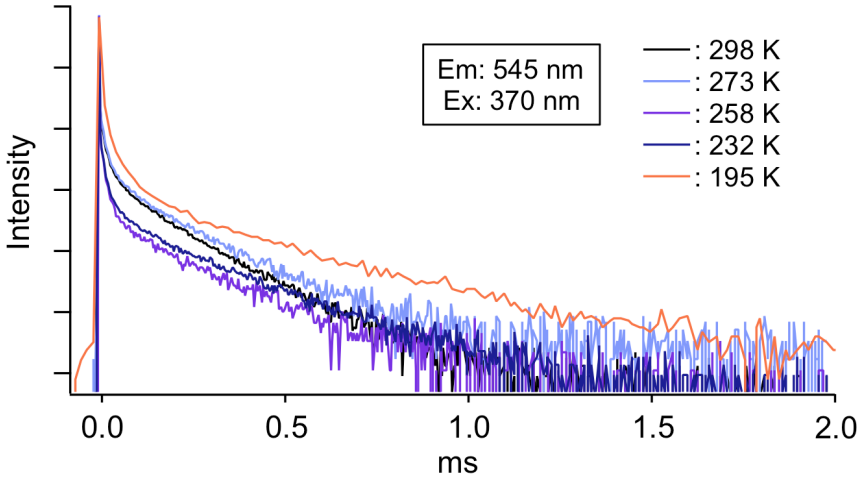

Figure S17. Emission decay profiles of the crystal **2** in various temperatures. The emission decays were monitored at 545 nm.

Table S6 Emission lifetimes fitted from the emission decays of the crystal **1** monitored at 543 nm.

Tem. / K	τ_{av} / μs[a,b]	τ_1 / μs[a] (A / -)	τ_2 / μs[a] (A / -)	τ_3 / μs[a] (A / -)	CHI
298	11.4	10.0 (0.95)	38.3 (0.05)	-	1.001
278	12.6	10.2 (0.91)	38.2 (0.09)	-	0.999
253	17.7	10.1 (0.73)	38.4 (0.27)	-	0.972
233	19.7	10.1 (0.67)	38.9 (0.33)	-	1.013
213	21.1	10.0 (0.61)	38.8 (0.39)	-	0.960
195	32.0	10.1 (0.49)	38.8 (0.41)	111.0 (0.10)	1.005

[a]: λ_{ex} = 370 nm, λ_{em} = 543 nm. [b]: $\tau_{av} = \Sigma \tau_n A_n$. All emission decay was fitted by tail fitting.

Table S7 Emission lifetimes fitted from the emission decays of the crystal **1** monitored at 498 nm.

Tem. / K	τ_{av} / μs[a,b]	τ_1 / μs[a] (A / -)	τ_2 / μs[a] (A / -)	CHI
298	7.34	2.44 (0.30)	8.05 (0.70)	0.981
253	8.58	2.10 (0.13)	9.51 (0.87)	1.027
233	8.16	2.07 (0.35)	11.5 (0.65)	0.995
213	8.94	2.10 (0.39)	13.3 (0.61)	1.053
195	11.65	2.37 (0.30)	15.7 (0.70)	1.159

[a]: λ_{ex} = 370 nm, λ_{em} = 498 nm. [b]: $\tau_{av} = \Sigma \tau_n A_n$. All emission decay was fitted by tail fitting.

Table S8 Emission lifetimes fitted from the emission decays of the crystal **2** monitored at 545 nm.

Tem. / K	τ_{av} / μs[a,b]	τ_1 / μs[a] (A / -)	τ_2 / μs[a] (A / -)	τ_3 / μs[a] (A / -)	τ_4 / μs[a] (A / -)	CHI
298	52.0	2.65 (0.21)	10.8 (0.33)	51.1 (0.19)	141.6 (0.27)	1.010
278	61.4	3.66 (0.19)	11.4 (0.32)	50.6 (0.18)	154.5 (0.31)	0.931
253	48.9	3.02 (0.29)	10.6 (0.37)	46.3 (0.10)	163.9 (0.24)	0.740
233	67.2	3.20 (0.25)	10.7 (0.33)	58.0 (0.15)	197.5 (0.27)	0.924
195	53.5	7.64 (0.55)	26.2 (0.23)	82.1 (0.10)	284.0 (0.12)	0.915

[a]: λ_{ex} = 370 nm, λ_{em} = 545 nm. [b]: $\tau_{av} = \Sigma \tau_n A_n$. All emission decay was fitted by tail fitting.

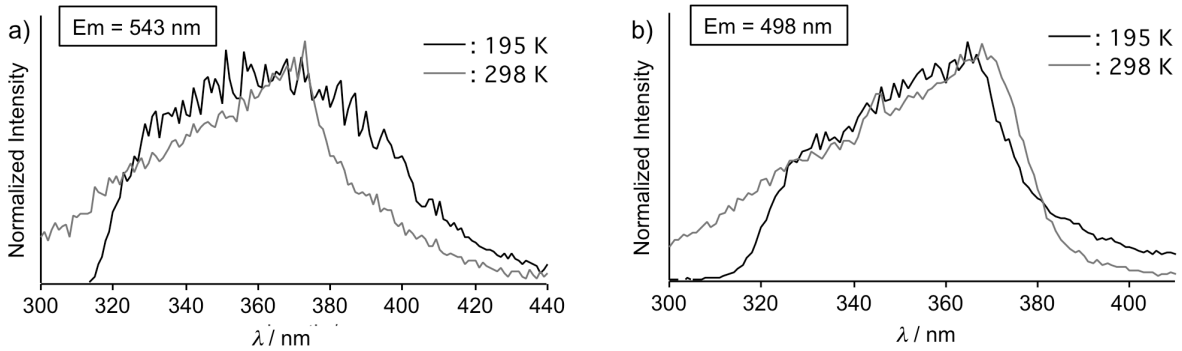

Figure S18. Excitation spectra of the crystalline sample 1 monitored at a) 543 nm and b) 498 nm. The excitation spectra were measured in variable temperatures, 298 K (gray bold line) and 195 K (black bold line).

5.5. References

54. (a) Yan, D.; Evans, D. G. *Mater. Horiz.* **2014**, *1*, 46. (b) Friend, R. H.; Gymer, R. W.; Holmes, A. B.; Burroughes J. H.; Marks, R. N. *Nature*, **1999**, *397*, 121. (c) Mutai, T.; Satou, H.; Araki, K. *Nat. Mater.* **2005**, *4*, 685. (d) Sagara, Y.; Yamane, S.; Mitani, M.; Weder, C.; Kato, T. *Adv. Mater.* **2016**, *28*, 977.
55. Hong, Y.; Lam, J. W. Y.; Tang, B. Z. *Chem. Soc. Rev.* **2011**, *40*, 5361.
56. (a) Shustova, N. B.; McCarthy, B. D.; Dincă, M. *J. Am. Chem. Soc.* **2011**, *133*, 20126. (b) Shustova, N. B.; Ong, T.-C.; Cozzolino, A. F.; Michalis, V. K.; Griffin, R. G.; Dincă, M. *J. Am. Chem. Soc.* **2012**, *134*, 15061. (c) Hughs, M.; Jimenez, M.; Khan, S. I.; Garcia-Garibay, M. A. *J. Org. Chem.* **2013**, *78*, 5293.
57. (a) Vogelsberg, C. S.; Garcia-Garibay, M. A. *Chem. Soc. Rev.* **2012**, *41*, 1892. (b) Khuong, T. A. V.; Nuñez, J. E.; Godinez, C. E.; Garcia-Garibay, M. A. *Acc. Chem. Res.* **2006**, *39*, 413. (c) Horansky, R. D.; Clarke, L. I.; Winston, E. B.; Price, J. C.; Karlen, S. D.; Jarowski, P. D.; Santillan, R.; Garcia-Garibay, M. A. *Phys. Rev. B* **2006**, *74*, 054306. (d) Shima, T.; Hampel, F.; Gladysz, J. A. *Angew. Chem., Int. Ed.* **2004**, *43*, 5537. (e) Lang, G. M.; Shima, T.; Wang, L.; Cluff, K. J.; Skopek, K.; Hampel, F.; Blümel, J.; Gladysz, J. A. *J. Am. Chem. Soc.* **2016**, *138*, 7649. (f) Setaka, W.; Yamaguchi, K. *J. Am. Chem. Soc.* **2012**, *134*, 12458. (g) Setaka, W.; Yamaguchi, K. *J. Am. Chem. Soc.* **2013**, *135*, 14560. (h) Akutagawa, T.; Koshinaka, H.; Sato, D.; Takeda, S.; Noro, S.-I.; Takahashi, H.; Kumai, R.; Tokura, Y.; Nakamura, T. *Nat. Mater.* **2009**, *8*, 342. (i) Yao, Z. S.; Yamamoto, K.; Cai, H. L.; Takahashi, K.; Sato, O. *J. Am. Chem. Soc.* **2016**, *138*, 12005.
58. (a) Dominguez, Z.; Khuong, T. A. V.; Sanrame, C. N.; Dang, H.; Nuñez, J. E.; Garcia-Garibay, M. A. *J. Am. Chem. Soc.* **2003**, *125*, 8827. (b) Dominguez, Z.; Dang, H.; Strouse, M. J.; Garcia-Garibay, M. A. *J. Am. Chem. Soc.* **2002**, *124*, 2398. (c) Godinez, C. E.; Zepeda, G.; Garcia-Garibay, M. A. *J. Am. Chem. Soc.* **2002**, *124*, 4701. (d) Jarowski, P. D.; Houk, K. N.; Garcia-Garibay, M. A. *J. Am. Chem. Soc.* **2007**, *129*, 3110.
59. Jobbaǵy, C.; Deaḱ, A. *Eur. J. Inorg. Chem.* **2014**, *2014*, 4434.
60. (a) Balch, A. L. *Gold Bull.* **2004**, *37*, 45. (b) Pyykkö, P. *Angew. Chem., Int. Ed.* **2004**, *43*, 4412. (c) Katz, M. J.; Sakai, K.; Leznoff, D. B. *Chem. Soc. Rev.* **2008**, *37*, 1884. (d) Schmidbaur, H.; Schier, A. *Chem. Soc. Rev.* **2008**, *37*, 1931. (e) Laguna, A.

Modern Supramolecular Gold Chemistry; Wiley-VCH; John Wiley distributor: Weinheim, Germany, **2008**. (f) Chen, Y.; Cheng, G.; Li, K.; Shelar, D. P.; Lu, W.; Che, C.-M. *Chem. Sci.* **2014**, *5*, 1348. (g) Ito, H.; Muromoto, M.; Kurenuma, S.; Ishizaka, S.; Kitamura, N.; Sato, H.; Seki, T. *Nature Communications* **2013**, *4*, 2009.

61. Zalesskiy, S. S.; Sedykh, A. E.; Kashin, A. S.; Ananikov, V. P. *J. Am. Chem. Soc.* **2013**, *135*, 3550.
62. Macho, V.; Brombacher, L.; Spiess, H. W. *Appl. Magn. Reson.* **2001**, *20*, 405.
63. (a) Laposa, J.D.; Singh, H. *Chem. Phys. Lett*. **1969**, *4*, 288. (b) Emmert, L.A.; Choi, W.; Marshal, J.A.; Yang, Y.; Meyer, L.A.; Brozic, J.A. *J. Phys. Chem. A* **2003**, *107*, 11340. (c) Chao, H.Y.; Lu, W.; Li, Y.; Chan, M.C.W.; Che, C.-M.; Cheung, K.-K.; Zhu, N. *J. Am. Chem. Soc*. **2002**, *124*, 14696.
64. It has been shown that structures analogous to **1** can display phosphorescence emission in solution by photoactivated removal of oxygen: Wan, S.; Lu, W. *Angew. Chem. Int. Ed*. **2017**, *56*, 1784.
65. Levitus, M.; Zepeda, G.; Dang, H.; Godinez, C.; Khuong, T. A. V.; Schmieder, K.; Garcia-Garibay, M.A. *J. Org. Chem*. **2001**, *66*, 3188.
66. Krämer, M.; Bunz, U.H.F.; Dreuw, A. *J. Phys. Chem. A*, **2017**, *121*, 946.
67. (a) Levitus, M.; Schmieder, K.; Ricks, H.; Shimize, K.D.; Bunz, U.H.F; Garcia-Garibay, M.A. *J. Am. Chem. Soc*. **2001**, *123*, 4259. (b) Levitus, M.; Garcia-Garibay, M.A. *J. Phys. Chem. A* **2000**, *104*, 8632, (c) Yang, J.-S.; Yan, J.L.; Hwang, C.-Y; Chiou, S.-Y.; Liau, K.-L.; Tsai, H.H.G. Lee, G.S.; Peng, S.M. *J. Am. Chem. Soc*. **2001**, *123*, 4259.
68. Cardolaccia, T.; Li, Y.; Schanze, K.S. *J. Am. Chem. Soc*. **2008**, *130*, 2535.
69. Yang, J.-S.; Yan, J.L.; Liau, K.-L.; Tsai, H.H.G.; Hwang, C.-Y. J. *Photochem. Photobiol. A: Chemistry*, **2009**, *207*, 38.
70. Wang, L.; Li, Y.; Zhang, Y.; He, H.; Zhang, J. *Spectrochim. Acta Mol. Biomol. Spectrosc.* **2015**, *137*, 259.
71. Zalesskiy, S. S.; Sedykh, A. E.; Kashin, A. S.; Ananikov, V. P. *J. Am. Chem. Soc.* **2013**, *135*, 3550.
72. Gardinier, J. R.; Pellechia, P. J.; Smith, M. D. *J. Am. Chem. Soc.* **2005**, *127*, 12448.
73. Xia, W. S.; Schmehl, R. H.; Li, C. J. *Tetrahedron* **2000**, *56*, 7045.
74. Sheldrick, G. M. SHELXL-2013, Program for the Refinement of Crystal Structures; University of Göttingen, Göttingen, Germany, **2013**.

75. Macho, V.; Brombacher, L.; Spiess, H. W. *Appl. Magn. Reson.* **2001**, *20*, 405. For the online program, visit: http://weblab.mpip-mainz.mpg.de/weblab/
76. Gaussian 09, Revision C.01, Frisch, M. J.; Trucks, G. W.; Schlegel, H. B.; Scuseria, G. E.; Robb, M. A.; Cheeseman, J. R.; Scalmani, G.; Barone, V.; Mennucci, B.; Petersson, G. A.; Nakatsuji, H.; Caricato, M.; Li, X.; Hratchian, H. P.; Izmaylov, A. F.; Bloino, J.; Zheng, G.; Sonnenberg, J. L.; Hada, M.; Ehara, M.; Toyota, K.; Fukuda, R.; Hasegawa, J.; Ishida, M.; Nakajima, T.; Honda, Y.; Kitao, O.; Nakai, H.; Vreven, T.; Montgomery, J., J. A.; Peralta, J. E.; Ogliaro, F.; Bearpark, M.; Heyd, J. J.; Brothers, E.; Kudin, K. N.; Staroverov, V. N.; Kobayashi, R.; Normand, J.; Raghavachari, K.; Rendell, A.; Burant, J. C.; Iyengar, S. S.; Tomasi, J.; Cossi, M.; Rega, N.; Millam, N. J.; Klene, M.; Knox, J. E.; Cross, J. B.; Bakken, V.; Adamo, C.; Jaramillo, J.; Gomperts, R.; Stratmann, R. E.; Yazyev, O.; Austin, A. J.; Cammi, R.; Pomelli, C.; Ochterski, J. W.; Martin, R. L.; Morokuma, K.; Zakrzewski, V. G.; Voth, G. A.; Salvador, P.; Dannenberg, J. J.; Dapprich, S.; Daniels, A. D.; Farkas, Ö.; Foresman, J. B.; Ortiz, J. V.; Cioslowski, J.; Fox, D. J.; Gaussian, Inc., Wallingford CT, 2009.
77. Spartan ’10; Wavefunction, Inc.: Irvine, CA.

Conclusion of the Dissertation

The Ph D. studies presented in this dissertation have focused on controlling and generating new types of external stimuli-responsive luminescent molecular crystalline materials through several molecular design. One of strategy is taking advantaging of various conformation of biaryl groups. Chapter 2 describes from those molecular design to the result that biphenyl gold(I) isocyanide complex formed dozen different crystal structure when just used different recrystallization solvents. Also, the photophysical properties of the crystals were different. From single crystal XRD analysis of the crystals, introducing biphenyl group was acted as key factor for forming various conformation of gold complex in the crystals. Molecular design of chapter 3 and 4 was focused on using chirality of crystal through axial chirality of molecule. Through chapter 3, it is proposed that homo-chiral crystal and racemic crystal can be used as fine tuning mechano-responsive luminescence of crystalline materials. Also, chapter 4 suggested that interconversion between chiral and achiral (or racemic) crystals could be one of important concept for generating and controlling external stimuli-responsive luminescence of solid state materials. The molecular design in chapter 5 have achieved the first example of reversible single-crystal-to-single-crystal (SCSC) phase transition with emission change triggered by mechanical stimulations and vapor addition. The designed gold(I) complex have possessed high dipolar moiety and formed polar crystals including MeOH molecules which is polar solvent. Cutting the crystal induced SCSC transition and the result crystal had not included MeOH in the crystal. The molecules were packed in non-polar space group. High vapor pressure of MeOH induced phase reversion into the initial crystal as SCSC transition. The result indicated that proper approach of dipolar moment in molecule could be one of method for constructing stimuli-responsive properties even in the case of crystalline materials. The chapter 6 had challenged to invent a new concept through hybrid molecular rotation in crystals and luminescent gold complex toward the controlling solid-state emission properties. Fortunately, dumbbell-shaped gold(I) phosphane complex formed luminescent amphidynamic crystals and the emission properties were corresponded with the molecular rotation. Especially, the molecular rotation was controlled by temperature change from 333 K to 123 K. The phosphorescent component of the crystal was altered through the temperature change with alteration of the molecular rotation. The Ph. D. dissertation have described several challenges of material design concept toward novel stimuli-responsive luminescence and novel phenomenon on solid-state materials.

Acknowledgment

The Ph D. studies presented in this dissertation have been performed under the direction of Professor Hajime Ito, Associate Professor Tatsuo Ishiyama, and Assistant Professor Tomohiro Seki, Division of Faculty of Engineering, Hokkaido University, Since April 2014 to September 2018. The author is deeply grateful to Professor Hajime Ito for his permissive direction and continuous encouragement throughout these works. The author wishes to express his sincere gratefulness to Assistant Professor Tomohiro Seki for his valuable suggestions and patient teaching. The author deeply feels indebted to Professor Miguel A. Garcia-Garibay, Department of Chemistry & Biochemistry, University of California Los Angeles, for his grateful supervising during the collaborations. The author would also like to acknowledge Associate Professor Tatsuo Ishiyama, Ms. Chiharu Yotumoto and Ms. Miyakawa for their kindness supports. The author feels sincere grateful to Professor Kazuki Sada and Professor Masako Kato, Department of Chemistry, Faculty of Science, Hokkaido University, for their kind advices. The author enjoyed working with colleagues because the friendship and good mode of the laboratory created a pleasant and stimulating environment. He thanks all members of Professor Ito's group. The author is very grateful to Ambitious Leading Program in Hokkaido University and JSPS Research Fellowship for Young Scientists (DC2) during the author's Ph D. program.

Finally, the author would like to express his deep gratitude for his family for their kind understanding, support, and encouragement throughout his whole of life.

September, 2018

Mingoo Jin